Probing the CP nature of the Higgs coupling to top quarks with the ATLAS experiment at the LHC

Emanuel Demétrio Mendes Gouveia

UMinho | 2021

Universidade do Minho
Escola de Ciências

Emanuel Demétrio Mendes Gouveia

Probing the CP nature of the Higgs coupling to top quarks with the ATLAS experiment at the LHC

Agosto de 2021

Universidade do Minho
Escola de Ciências

Emanuel Demétrio Mendes Gouveia

Probing the CP nature of the Higgs coupling to top quarks with the ATLAS experiment at the LHC

Tese de Doutoramento
Física

Trabalho realizado sob a orientação de

Professor Doutor António Joaquim Onofre Abreu Ribeiro Gonçalves

Professor Doutor José Ricardo Morais Silva Gonçalo

Agosto de 2021

DIREITOS DE AUTOR E CONDIÇÕES DE UTILIZAÇÃO DO TRABALHO POR TERCEIROS

Acknowledgements

I have been fortunate to find myself surrounded by excellent people during the period of this PhD. To them, a note of gratitude is in order.

My supervisors António Onofre and Ricardo Gonçalo, for being extremely supportive, for trusting me with a great deal of autonomy and for the many motivation-boosting conversations.

My colleagues Ana Luísa Carvalho and Luís Coelho, who have been very dependable, kind, and overall great to work with.

The ATLAS $t\bar{t}H$ group at Manchester, and Nicolas Scharmberg in particular, from whom I learned a lot in a long-lasting collaboration.

The ATLAS $t\bar{t}H(b\bar{b})$ analysis team and the ATLAS jet trigger group, where I always found forums of interested discussion, which pushed me to continuously learn and improve.

My colleagues at LIP Minho, for coming up with new interesting discussions every day, physics-related and otherwise. In particular, I thank Nuno Castro and Henrique Carvalho for making sure that we always have the best working conditions at the office.

LIP, for hosting me and for the opportunities to present my results in conferences and workshops. These frequent contacts with experts, inside and outside the institute, really provided a sense of community and surely had a positive impact on my work and training.

The IDPASC network, for the opportunity to attend a school and several workshops and to be exposed to colleagues from closely related fields.

My fiancée Eduarda, for supporting me every day and for having just the best sense of humour.

My family, for their care and patience.

My friends, for many memorable journeys and laughs.

Financial support

This work was financed by Portuguese national funds through FCT - Fundação para a Ciência e a Tecnologia, I.P., in the scope of grant PD/BD/128231/2016 and projects CERN/FIS-PAR/0002/2019 and FCT, COMPETE2020-Portugal2020, FEDER, POCI-01-0145-FEDER-007334.

STATEMENT OF INTEGRITY

I hereby declare having conducted this academic work with integrity. I confirm that I have not used plagiarism or any form of undue use of information or falsification of results along the process leading to its elaboration.

I further declare that I have fully acknowledged the Code of Ethical Conduct of the University of Minho.

Medida da natureza $\mathcal{CP}$ do acoplamento do bosão de Higgs aos quarks top com a experiência ATLAS no LHC

Resumo

Desde que o bosão de Higgs com uma massa de 125 GeV foi descoberto pelas experiências ATLAS e CMS, no CERN, o estudo das propriedades desta partícula tem sido uma prioridade no programa de física do Grande Colisor de Hadrões (LHC). As interacções do bosão de Higgs com outras partículas fundamentais são previstas pelo Modelo Padrão da física de partículas e podem ser medidas com uma precisão sem precedentes usando os dados da Run 2 do LHC. Os acoplamentos de Yukawa entre o bosão de Higgs e os fermiões podem sofrer efeitos observáveis se o sector do Higgs for estendido para incluir interacções adicionais em que ocorra violação da simetria $\mathcal{CP}$ (conjugação de carga e paridade), um ingrediente necessário para explicar o desequilíbrio observado entre matéria e anti-matéria no Universo. O acoplamento de Yukawa mais forte é o do quark top, o que o torna experimentalmente mais acessível e lhe confere um papel de destaque em questões teóricas como a naturalidade da massa do bosão de Higgs e a estabilidade do vácuo. Actualmente, a melhor via directa para medir o acoplamento de Yukawa do quark top é a produção, no LHC, de bosões de Higgs associados a pares de quarks top ($t\bar{t}H$).

Nesta tese, são apresentadas duas análises de acontecimentos $t\bar{t}H$ com leptões no estado final e em que o bosão de Higgs decai para um par de quarks bottom. São utilizados dados recolhidos pela experiência ATLAS durante a Run 2 do LHC, perfazendo uma luminosidade integrada de 139 fb^{-1} de colisões protão-protão com uma energia de centro de masssa de 13 TeV. A primeira análise é uma medida da secção eficaz de produção de $t\bar{t}H$, que resulta numa força de sinal observada de $0.43^{+0.36}_{-0.33}$. A segunda análise é uma medida da estrutura $\mathcal{CP}$ do acoplamento de Yukawa do quark top, na qual o ângulo de mistura $\mathcal{CP}$ observado é $\alpha = 4^{\circ}{}^{+52^{\circ}}_{-60^{\circ}}$. Ambos os resultados são compatíveis com as previsões do Modelo Padrão, embora a taxa de sinal observada neste estado final em particular não seja suficiente para constituir evidência da produção de $t\bar{t}H$ nem para excluir um acoplamento puramente $\mathcal{CP}$-ímpar com um nível de confiança de 95%.

Probing the $\mathcal{CP}$ nature of the Higgs coupling to top quarks with the ATLAS experiment at the LHC

Abstract

Since the Higgs boson with a mass of 125 GeV was discovered by the ATLAS and CMS experiments at CERN, the study of the properties of this particle has been a priority of the Large Hadron Collider (LHC) physics programme. The interactions of the Higgs boson with other elementary particles are predicted by the Standard Model of particle physics and can be measured with unprecedented precision using data from the Run 2 of the LHC. The Yukawa couplings between the Higgs boson and fermions may suffer observable effects if the Higgs sector is extended to include additional interactions which violate the symmetry under $\mathcal{CP}$ (charge conjugation and parity), an ingredient required to explain the observed imbalance between matter and anti-matter in the Universe. The strongest Yukawa coupling is that of the top quark, which makes it more easily accessible experimentally and also grants it a special role in theoretical issues, such as the naturalness of the Higgs boson mass and the stability of the vacuum. Currently, the best direct probe to measure the top quark Yukawa coupling is the production, at the LHC, of Higgs bosons in association with top quark pairs ($t\bar{t}H$).

In this thesis, two analysis are presented of $t\bar{t}H$ events in final states with leptons and in which the Higgs boson decays to a pair of bottom quarks. Data collected by the ATLAS experiment during the Run 2 of the LHC is used, making up a total integrated luminosity of 139 fb^{-1} of proton-proton collisions with a centre-of-mass energy of 13 TeV. The first analysis is a measurement of the $t\bar{t}H$ production cross-section, resulting in the observed signal strength $0.43^{+0.36}_{-0.33}$. The second analysis is a measurement of the $\mathcal{CP}$ structure of the top quark Yukawa coupling, in which the observed $\mathcal{CP}$ mixing angle is $\alpha = 4^{\circ}{}^{+52^{\circ}}_{-60^{\circ}}$. Both results are compatible with the Standard Model predictions, although the observed signal rate in this particular final state is not enough to establish evidence for $t\bar{t}H$ production nor to exclude a pure $\mathcal{CP}$-odd coupling with a 95% confidence level.

Contents

Outline of the thesis

The low rate at which violation of the $\mathcal{CP}$ symmetry occurs in the Standard Model (SM) is a hint of its incompleteness, when contrasted with the observed asymmetry between matter and anti-matter in the Universe. Many models of physics beyond the Standard Model (BSM) provide additional sources of $\mathcal{CP}$ violation in extended Higgs sectors, possibly with observable impacts on the 125 GeV Higgs boson, discovered by the ATLAS [1] and CMS [2] collaborations in 2012. In this sense, precision measurements of the Higgs boson provide a doorway to exploration of new physics scenarios. With the currently available integrated luminosity of proton-proton (pp) collisions surpassing what was used for discovery by more than one order of magnitude, the Run 2 of the Large Hadron Collider (LHC) marked the advent of the Higgs precision era.

Electroweak symmetry breaking (EWSB) predicts that the Higgs boson interacts with other particles with an interaction strength determined by their mass. In particular, the Higgs boson is coupled to fermions via Yukawa terms proportional to the fermion masses. This prediction can currently be tested at the LHC for the third generation of fermions and even for muons, which presents a crucial test to the EWSB mechanism. In the presence of BSM sources of $\mathcal{CP}$ violation in the Higgs sector, the structure of Yukawa couplings may deviate from the SM prediction. Depending on the model, such couplings may be the preferred probe to the presence of $\mathcal{CP}$ violation. The Yukawa coupling of the top quark is expected to be the largest among all fermions. Being close to unity, it plays a special role in fundamental theoretical issues of the SM, such as the naturalness of the Higgs boson mass and the stability of the vacuum. The best direct probe of the top-Higgs interaction is the production of a Higgs boson in association with a top quark pair at the LHC.

This thesis presents two analyses of $t\bar{t}H$ events in the final state with leptons and in which the Higgs boson decays to a $b\bar{b}$ pair, using the dataset collected by the ATLAS experiment during the full Run 2 of the LHC. The first analysis is a measurement of the $t\bar{t}H$ production inclusive cross-section, and the second is a measurement of the $\mathcal{CP}$ properties of the top quark Yukawa coupling. In this introductory section, I provide an outline of the thesis and explain my contributions to the works presented.

Chapter 1 presents an overview of the Standard Model of particle physics, with focus on the Brout-Englert-Higgs mechanism, and discusses $\mathcal{CP}$ violation, in the Standard Model and beyond it. In Chapter 2, the state of the art in the most relevant top quark and Higgs boson properties is presented. Special attention is given to processes sensitive to the top-Higgs interaction, in particular $t\bar{t}H$ production.

Chapter 3 is a discussion of the physics of $t\bar{t}H$ production in the presence of a $\mathcal{CP}$-odd component in the top quark Yukawa coupling. Several expected differences in cross-section and kinematics between the $\mathcal{CP}$-even and $\mathcal{CP}$-odd scenarios are presented, and an attempt is made to give some insight about their origin, based on theoretical considerations. The discussion about contributions from different t-channel diagrams to the $t\bar{t}H$ cross-section and their expected effect on kinematics based on the corresponding propagators are originally presented in this thesis. I was one of the authors of the results discussed in Section 3.2.4, published in Ref. [3]. In particular, I originally found the differences between $\mathcal{CP}$ scenarios in the angles measured in the $t\bar{t}H$ rest frame between the top quarks and the Higgs boson in $t\bar{t}H$ events. This motivated a discussion with theorists, leading to the study of other observables in the $t\bar{t}H$ rest frame. For the published results, I produced the histograms at reconstruction level and computed the confidence levels for excluding the $\mathcal{CP}$-odd scenario with luminosities up to $3\,\mathrm{ab}^{-1}$. The study shown in Section 3.3 is also my own work, which was presented at the TOP2018 conference [4] and included in the CERN "Report on the Physics at the HL-LHC and Perspectives for the HE-LHC" [5]. In that study, I combined results from previous studies to obtain a projection of future sensitivity to $\mathcal{CP}$-odd $t\bar{t}H$ production using the $H \to b\bar{b}$ final states.

Chapter 4 gives a brief description of the ATLAS detector at the LHC. In order to qualify as an ATLAS author, I performed technical work in the ATLAS jet trigger. The most relevant studies carried out in that context are presented in Chapter 5. Different strategies were investigated, all targeting a reduction of trigger inefficiencies in single-jet triggers with low energy thresholds.

The remaining chapters are dedicated to the $t\bar{t}H$ analyses. Common elements of the two analyses are described in Chapters 6 and 7. The first addresses the definition of detector objects, the data and Monte Carlo (MC) samples used, background modelling, systematic uncertainties and the statistical model. The second describes the common analysis strategy, including region definition, kinematic reconstruction and the discrimination between signal and backgrounds.

Chapter 8 discusses the analysis used for the measurement of the inclusive $t\bar{t}H$ cross-section, which is published in Ref. [6]. The dedicated strategy for this analysis is presented and motivated, expected and observed results are discussed, and comparisons are shown between data and the pre- and post-fit predictions. I joined this analysis effort a few months before its previous installment, published in Ref. [7]. For that round, I performed studies of small backgrounds in the dilepton channel. For the more recent version of the analysis, I was one of the main analysers in the single-lepton channel. I contributed to the processing of common samples used by the analysis team and performed comparisons between data and MC that motivated the choice of nominal background predictions. I did many fit tests which contributed to various decisions in the course of the analysis development, including region definition, systematics model, splitting/merging of samples, histogram smoothing algorithms and observables used in the fit. I made a few contributions also to the development of the analysis software.

The measurement of the $\mathcal{CP}$ structure of the top quark Yukawa coupling is presented in Chapter 9. The signal modelling as a function of the coupling parameters is described, as well as the specific analysis strategy for this measurement. This includes the region definition and the set of $\mathcal{CP}$ discriminants used in the fit. Expected and observed results are shown, and comparisons are made between data and the pre- and post-fit predictions. I was the main analyser and developer of this analysis in the single-lepton channel. Before the official ATLAS samples were available for $\mathcal{CP}$-odd scenarios of the signal, I generated private samples and ran them through a fast detector simulation with the DELPHES package [8]. In order to obtain significant statistics in all analysis regions with these samples, I developed a tag rate function tool with support for multiple b-tagging working points. The DELPHES samples were important for the team to make progress in the analysis strategy while the request for official samples was ongoing. Regarding the $\mathcal{CP}$ discriminants used in the analysis, I introduced the modification described in Section 9.2 to the angular observables defined in Ref. [9]. In the modified version, top quarks are labelled according to their angular separation with respect to the Higgs boson, and not according to their charge, which produced variables with higher $\mathcal{CP}$-discriminating power. I contributed to the definition and implementation of the parameterisation of the signal model in terms of the coupling parameters, as well as for the definition of signal modelling uncertainties where they are different from the ones used in the cross-section measurement. I developed new features in the fitter and analysis software frameworks, according to the specific needs of this measurement.

Conclusions and ideas for future measurements of $t\bar{t}H$ and related processes are presented in Chapter 10.

Chapter 1

Theoretical introduction

This chapter provides an introductory overview of theoretical aspects necessary to give context to the measurements presented in later chapters. Section 1.1 presents the Standard Model of particle physics, highlighting the role of the mechanism for EWSB, responsible for the prediction of the Higgs boson. In section 1.2, $\mathcal{CP}$ violation is explained. An example is given of $\mathcal{CP}$ violation beyond the Standard Model, in the Higgs sector, that could be probed via the top-Higgs coupling.

1.1 Standard Model of particle physics

Elementary particle physics has the ambitious goal of describing nature in terms of its most fundamental constituents. From this endeavour, a theoretical framework has come together, incrementally, in a succession of experimental and theoretical breakthroughs across the last century. This theory is known as the Standard Model (SM) of particle physics [10, 11, 12]. It is a quantum field theory that provides a description of all particles presently believed to be elementary, and the interactions among them. The gravitational interaction is not included in the SM because it lacks an adequate quantum mechanical description, but gravity is extremely weak compared to all the other forces, making it irrelevant in the systems studied by particle physics.

1.1.1 Particle content

In the SM, matter is made up of elementary fermions, which may be divided into quarks and leptons. At a first approximation, only three elementary fermions would be required to describe the atoms and molecules that constitute ordinary matter: the electron (e^-), which is a lepton with electric charge -1, and the up (u) and down (d) quarks, with electrical charges $2/3$ and $-1/3$, respectively [1]. These two quarks are the building blocks of protons and neutrons, which in turn are bound together to form

[1] Electric charges are expressed in units of the absolute value of the electric charge of the electron.

atomic nuclei. An additional lepton, the electron neutrino (ν^e), which is electrically neutral, is necessary to account for radioactive decays of some nuclei. This picture presented so far is an incomplete one, as it represents only the first generation of quarks and the first generation of leptons. In fact, three generations of quarks and three generations of leptons are established. Each of the additional generations can be seen as a replica of the first generation, in which particles have the same charges as their counterparts in the first generation. The second generation of quarks consists of the charm (c) and strange (s) quarks, while the top (t) and bottom (b) quarks make up the third generation. Each of these quarks is more massive than the analogous quark in the previous generations. Charged leptons also observe such a mass hierarchy, with the muon (μ) in the second generation and the tau lepton (τ) in the third generation. They have as partners the muon neutrino (ν^μ) and tau neutrino (ν^τ).

Interactions in the SM are generated by imposing local gauge symmetries on the lagrangian density[2] of the theory, which requires the introduction of gauge fields. The particles associated with these gauge fields are called gauge bosons, and can be regarded as the carriers of the corresponding forces. The gauge bosons of the SM are spin-1 particles. The photon (γ) is massless, electrically neutral and is responsible for carrying the electromagnetic force, thus interacting with all electrically charged particles. Gluons (g) are also massless and electrically neutral, and mediate the strong force. Gluons interact with all particles carrying colour charge. This includes all quarks, but also gluons themselves. The weak force carriers are the Z and the $W^\pm$ bosons. The Z boson is electrically neutral, while the $W^\pm$ bosons have charge ± 1. They are massive particles, which explains the short range of the weak force.

The Higgs boson is the only scalar (i.e., spin-0) fundamental particle in the SM. It is electrically neutral and is not a gauge boson. Instead, it is an inevitable consequence of the mechanism of EWSB, a feature that enables the generation of masses for elementary particles in the SM. A summary of the particle content of the SM is shown in Figure 1.1 [13].

[2]Usually just called 'lagrangian' for brevity.

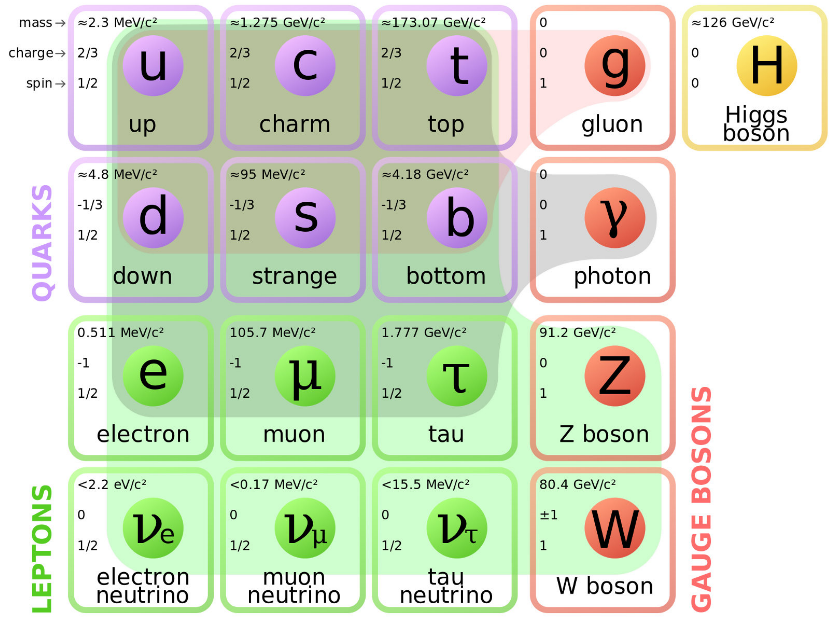

Figure 1.1: Summary of the particle content of the SM. Shaded areas surround each gauge boson and the fermions that interact with it [13]. Upper limits on the neutrino masses are to be interpreted with care, since the flavour eigenstates are strongly mixed with respect to the mass eigenstates.

Relativistic quantum mechanics predicts, for every elementary particle, the possibility of a corresponding anti-particle, with the same mass and opposite-sign charges. The W^+ and the W^- bosons are the anti-particle of each other, while neutral bosons are their own anti-particles. In the case of fermions, anti-particles are additional fields, resulting in twice as many fermion fields as those presented above. For example, the anti-particle of the electron is the positron (e^+), which was the first discovered anti-particle [14].

1.1.2 Standard Model lagrangian

The SM is based on the local gauge symmetry $SU(3)_C \times SU(2)_L \times U(1)_Y$. This symmetry group is the product of the group of strong interactions – $SU(3)_C$ – and the group of electroweak interactions – $SU(2)_L \times U(1)_Y$. The gauge fields corresponding to the $SU(3)_C$ group are G^a_μ ($a = 1, ..., 8$), which can be identified with the eight independent gluon fields. On the electroweak side, the gauge fields associated with the $SU(2)_L$ group are W^i_μ ($i = 1, 2$ or 3) and the field corresponding to $U(1)_Y$ is B_μ. After the EWSB, they are mixed into the photon, Z boson and $W^\pm$ bosons – electromagnetic and weak interactions are unified in the SM.

The full SM lagrangian can be written in condensed form as

$$\mathcal{L}_{SM} = \mathcal{L}_f + \mathcal{L}_{Gauge} + \mathcal{L}_{SSB} + \mathcal{L}_{Yukawa}. \tag{1.1}$$

The first term, $\mathcal{L}_f$, contains the kinetic energies of the fermions and their interactions with the gauge bosons. Interactions are obtained by starting from the free fermion lagrangian, and imposing the local gauge symmetries. Interaction terms arise between the gauge fields and the fermions that are transformed by the respective group. Conversely, the representation of a fermion under each gauge group can be chosen to reproduce the observed interactions. The L in $SU(2)_L$ stands for "Left", meaning that only left-handed chirality fermions transform as doublets under the action of the group[3]. Right-handed fermions transform as singlets and, as a result, they do not interact with the W^i_μ fields. After the EWSB, this leads to the observed feature that only left-handed fermions are subject to weak interactions. Quarks transform as triplets of colour under $SU(3)_C$, thus acquiring interaction terms with gluons. Leptons, on the other hand, transform as singlets. Separating $\mathcal{L}_f$ in terms that make evident the allowed interactions, it can be written as:

$$\begin{aligned} \mathcal{L}_f = &\bar{\psi}\gamma^\mu (i\partial_\mu - g'\frac{Y}{2}B_\mu)\psi \\ &-\bar{\psi}_L\gamma^\mu (g\boldsymbol{I}\cdot\boldsymbol{W_\mu})\psi_L \\ &-\bar{q}\gamma^\mu (g_s\boldsymbol{T}\cdot\boldsymbol{G_\mu})q, \end{aligned} \tag{1.2}$$

where ψ, ψ_L and q are spinor fields, and sums over the fermions are implicit: ψ runs over all fermions, ψ_L runs over those with left-handed chirality

[3]Spinor fields have two possible chirality states, arising from the possible representations of the Lorentz group. The right-handed and left-handed components are eigenstates of the chirality operator γ_5, with eigenvalues $+1$ and -1, respectively.

and q runs over all quarks. Each interaction is associated with a coupling constant and with an operator – a generator of the corresponding gauge group. The first term accounts for the kinetic energy and for the interaction with the B_μ field, where g' is the coupling constant and Y is the hypercharge operator. Interaction with the W^i_μ fields is described by the second term, where the coupling constant is g and $\boldsymbol{I}$ is the isospin operator. The last term in $\mathcal{L}_f$ contains the interaction with the gluon fields G^a_μ, in which the strong coupling constant is g_s, and the corresponding operator is $\boldsymbol{T}$. Table 1.1 lists the isospin (total and third components), hypercharge and the electric charge eigenvalues of elementary fermions.

Table 1.1: Quantum numbers of elementary fermions [10]: I and I_3 are the total isospin and the third component of the isospin, respectively, Y is the hypercharge and Q is the electric charge. The symbol e^- stands for any charged lepton, ν for any neutrino, u for any up-type quark and d for any down-type quark.

Fermion	I	I_3	Y	Q
ν_L	$\frac{1}{2}$	$\frac{1}{2}$	-1	0
e^-_L	$\frac{1}{2}$	$-\frac{1}{2}$	-1	-1
e^-_R	0	0	-2	-1
u_L	$\frac{1}{2}$	$\frac{1}{2}$	$\frac{1}{3}$	$\frac{2}{3}$
d_L	$\frac{1}{2}$	$-\frac{1}{2}$	$\frac{1}{3}$	$-\frac{1}{3}$
u_R	0	0	$\frac{4}{3}$	$\frac{2}{3}$
d_R	0	0	$-\frac{2}{3}$	$-\frac{1}{3}$

The second term of the SM lagrangian, $\mathcal{L}_{Gauge}$, contains the kinetic and self-interacting terms of the gauge fields:

$$\mathcal{L}_{Gauge} = -\frac{1}{4}G^a_{\mu\nu}G_a^{\mu\nu} - \frac{1}{4}W^i_{\mu\nu}W_i^{\mu\nu} - \frac{1}{4}B_{\mu\nu}B^{\mu\nu}. \tag{1.3}$$

This is written in terms of the field strength tensors

$$G^a_{\mu\nu} = \partial_\mu G^a_\nu - \partial_\nu G^a_\mu + g_s f^{abc} G^b_\mu G^c_\nu \tag{1.4}$$

$$W^i_{\mu\nu} = \partial_\mu W^i_\nu - \partial_\nu W^i_\mu + g\epsilon^{ijk} W^j_\mu W^k_\nu \tag{1.5}$$

$$B_{\mu\nu} = \partial_\mu B_\nu - \partial_\nu B_\mu, \tag{1.6}$$

where f^{abc} and ϵ^{ijk} are the structure constants of the respective groups. They are necessary in order to preserve gauge invariance whenever the generators of a group do not commute. The terms in which the structure constants appear are responsible for the self-interactions of gauge bosons. In particular, the self-interaction of gluons is responsible for complex phenomena in quantum chromodynamics (QCD), such as the confinement of quarks.

The partial lagrangian $\mathcal{L}_f + \mathcal{L}_{Gauge}$ already accounts for all kinetic energies and interactions of gauge bosons and fermions. However, all the fields considered so far remain massless. If mass terms are directly added to the lagrangian, gauge symmetry is no longer preserved and divergences that cannot be renormalised appear in the amplitudes of certain loop diagrams.

1.1.3 Brout-Englert-Higgs mechanism

Masses for gauge bosons may be generated without explicitly introducing mass terms in the lagrangian. This is possible with spontaneous symmetry breaking, leading to a vacuum that does not share the full symmetry of the fundamental lagrangian. The mass terms arise when writing the lagrangian in terms of vacuum expectation values (vev) plus perturbations. They are no longer problematic since this form of the lagrangian is not expected to be invariant under the gauge group of the fundamental theory.

Historically, an important obstacle to the introduction of a spontaneous symmetry breaking mechanism in electroweak theory was the Goldstone theorem: spontaneously breaking continuous symmetries introduces new massless boson states (Goldstone bosons) in the theory [15, 16, 17]. Such particles are not observed, making this an undesirable feature of the mechanism. This picture changed in 1964, when three independent groups (Peter Higgs [18, 19, 20]; Robert Brout and François Englert [21]; Gerald Guralnik, Carl Richard Hagen and Tom Kibble [22, 23]) proposed a solution to circumvent the Goldstone theorem while spontaneously breaking a gauge symmetry. They introduced a scalar field with a non-zero expectation value in the vacuum, now called the Higgs field. Coupling this scalar field to the gauge bosons ensures that the degrees of freedom of the Goldstone bosons are not physical particles. Instead, they are "absorbed" by the longitudinal polarisation states of the vector bosons, which become available as the bosons acquire mass. The total number of degrees of freedom introduced exceeds by one the number of degrees of freedom absorbed by the vector bosons. The remaining degree of freedom corresponds to the Higgs boson, a massive scalar particle predicted by the mechanism. After the proposal of this mechanism, Abdus Salam and Steven Weinberg [24, 25] showed how it could be applied to the unified electroweak theory of Sheldon Glashow [26]. Decisive proof that the resulting electroweak theory is renormalisable came only later, from Gerard 't Hooft and Martinus Veltman [27].

In the following, the main ideas of the Brout-Englert-Higgs mechanism applied to the SM are presented and the terms contributing to $\mathcal{L}_{SSB}$ are explained. The $SU(2)_L \times U(1)_Y$ symmetry of the electroweak interactions can be broken into the observed $U(1)_{EM}$ symmetry in a minimal way through the introduction of an $SU(2)_L$ doublet ϕ of complex scalar fields, with hypercharge Y =1. It can be written as

$$\phi = \frac{1}{\sqrt{2}} \begin{pmatrix} \phi_1 + i\phi_2 \\ \phi_3 + i\phi_4 \end{pmatrix}, \tag{1.7}$$

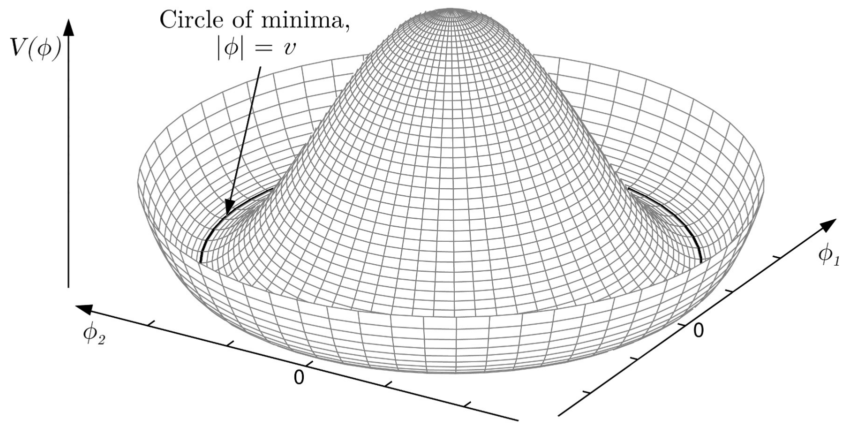

Figure 1.2: Projection of the Higgs potential $V(\phi)$ on the (ϕ_1, ϕ_2) plane, with $\phi_3 = \phi_4 = 0$.

where ϕ_1, ϕ_2, ϕ_3 and ϕ_4 are real. This field is used to build $\mathcal{L}_{SSB}$:

$$\mathcal{L}_{SSB} = \left| \left(i\partial_\mu - g\boldsymbol{I} \cdot \boldsymbol{W}_\mu - g' \frac{1}{2} B_\mu \right) \phi \right|^2 - V(\phi). \tag{1.8}$$

The first term includes the kinetic energy of ϕ and its interactions with the electroweak gauge bosons, and it can be obtained by imposing gauge invariance. The second term $V(\phi)$ is called the Higgs potential, introduced to enable the spontaneous symmetry breaking:

$$V(\phi) = \mu^2 \phi^\dagger \phi + \lambda (\phi^\dagger \phi)^2, \text{ with } \lambda > 0, \tag{1.9}$$

which is clearly gauge invariant. If $\mu^2 > 0$, the vacuum will correspond to $\phi = 0$, also trivially gauge invariant. More interestingly, when $\mu^2 < 0$, the vacuum must verify

$$\phi^\dagger \phi = \frac{1}{2}(\phi_1^2 + \phi_2^2 + \phi_3^2 + \phi_4^2) = -\frac{\mu^2}{2\lambda} \equiv \frac{v^2}{2}. \tag{1.10}$$

Any particular vacuum satisfying this equation is not invariant under the full symmetry group. Figure 1.2 shows a projection of this potential on the (ϕ_1, ϕ_2) plane, for $\phi_3 = \phi_4 = 0$. One adequate choice for the vev ϕ_0 is:

$$\phi_0 = \frac{1}{\sqrt{2}} \begin{pmatrix} 0 \\ v \end{pmatrix}. \tag{1.11}$$

Now, to show that masses are generated for the vector bosons, the lagrangian should be re-written, with ϕ replaced by an expansion around ϕ_0. One such way to write ϕ is

$$\phi = \frac{1}{\sqrt{2}} e^{i\boldsymbol{I}\cdot\boldsymbol{\theta}/v} \begin{pmatrix} 0 \\ v+h \end{pmatrix}, \tag{1.12}$$

where the fields h, θ_1, θ_2 and θ_3 are real. This parameterisation can describe a fully generic deviation from ϕ_0 in all the degrees of freedom of ϕ (two real and two imaginary, as made evident in Equation 1.7). Excitations on three of those degrees of freedom could in principle be identified with Goldstone bosons. However, the lagrangian was forced to have local $SU(2)_L$ symmetry. Because $\boldsymbol{\theta}$ parameterises a generic $SU(2)_L$ transformation, this guarantees that the deviations from ϕ_0 other than h are not physical, and correspond only to the freedom of gauge fixing. Therefore, the re-written $\mathcal{L}_{SSB}$ can be obtained by making the replacement

$$\phi = \frac{1}{\sqrt{2}} \begin{pmatrix} 0 \\ v+h \end{pmatrix}. \tag{1.13}$$

In particular, the mass terms of the vector bosons can be obtained by replacing ϕ by ϕ_0 in the interaction term between ϕ and the electroweak bosons:

$$\left| \left(-g\boldsymbol{I} \cdot \boldsymbol{W_\mu} - g'\frac{1}{2}B_\mu \right) \phi_0 \right|^2. \tag{1.14}$$

The physical fields are defined as linear combinations:

$$W^\pm_\mu = \frac{W^1_\mu \pm iW^2_\mu}{\sqrt{2}}, A_\mu = \frac{g'W^3_\mu + gB_\mu}{\sqrt{g^2+g'^2}}, Z_\mu = \frac{gW^3_\mu - g'B_\mu}{\sqrt{g^2+g'^2}}. \tag{1.15}$$

Taking these fields and putting them back in Equation 1.14 ultimately gives:

$$m_W^2 W_\mu^+ W^{-\mu} + \frac{1}{2} m_Z^2 Z_\mu Z^\mu + \frac{1}{2} m_A^2 A_\mu A^\mu, \tag{1.16}$$

$$\text{with } m_W = \frac{vg}{2}, m_Z = \frac{v\sqrt{g^2 + g'^2}}{2}, m_A = 0. \tag{1.17}$$

The model built so far has massive vector bosons, a massless photon and a Higgs boson, but still carries massless fermions. A term $m\bar{\psi}\psi$ is not gauge invariant because of the chiral nature of fermions. Conveniently, the Higgs doublet introduced to break the electroweak symmetry can also be used to generate fermion masses, by adding Yukawa couplings between the Higgs doublet and the fermion fields. This is the content of $\mathcal{L}_{Yukawa}$, which can be written as

$$\mathcal{L}_{Yukawa} = -(k_d \bar{Q}_L \phi d_R + k_u \bar{Q}_L \phi^c u_R + k_e \bar{L}_L \phi e_R + \text{h.c. (hermitian conjugate)}), \tag{1.18}$$

where $\phi^c = -i2I_2\phi^*$, d_R runs over all right-handed down-type quarks, u_R runs over all right-handed up-type quarks, e_R runs over all right-handed charged leptons, while Q_L and L_L are left-handed doublets of quarks and leptons, respectively, of the same generation as the right-handed signlet in each term. Each of k_u, k_d and k_e represents three free parameters of the theory, corresponding to the three generations of quarks or leptons. When the scalar field acquires a non-zero vev, the term for a fermion field ψ becomes

$$-m\bar{\psi}\psi - \frac{m}{v}\bar{\psi}\psi h. \tag{1.19}$$

As expected, the fermion mass is generated, with m depending on the k_u, k_d or k_e in the unbroken lagrangian. In this form, an interesting prediction of the SM becomes apparent: there is an interaction between each fermion and the Higgs boson, with strength proportional to the fermion mass.

The masses of neutrinos were left out of this discussion because neutrinos are canonically considered massless in the SM. It is known that neutrino masses must be non-zero to accommodate the experimental observation of neutrino oscillations, first announced by the Super-Kamiokande and SNO collaborations [11, 28]. Mass terms for neutrinos can be generated through $\mathcal{L}_{Yukawa}$ just like for any other fermion. This requires the inclusion of right-handed chirality neutrinos in the theory. However, neutrinos are only produced and detected through weak interactions, such that this hypothetical right-handed component would not be observable. There are other possibilities for generating neutrino masses. One that does not require adding unobserved particles is through Majorana mass terms, which can be used below the electroweak scale to generate neutrino masses solely with the v_L field [29]. An experimental signature of Majorana masses would be neutrinoless double beta decay, a nuclear decay in which two electrons would be emitted without the accompanying anti-neutrinos, thus violating lepton number conservation. In certain SM extensions, very small neutrino masses are naturally generated by the addition heavy neutrinos with Majorana mass terms, in the so-called 'see-saw' mechanism [30].

1.1.4 Success and shortcomings

The SM is a successful theory, proven to make accurate predictions at different energy scales, spanning several orders of magnitude. One remarkable result of quantum electrodynamics (QED) is the accurate prediction of the electron magnetic moment. This quantity has been computed with a precision of 0.72×10^{-12} [31] and measured with an uncertainty of 0.25×10^{-12} [32]. The central values between prediction and measurement differ merely by 1.30×10^{-12}. At a completely different energy scale, the masses of the Z and $W^{\pm}$ bosons were accurately predicted using observed parameters of the weak interactions, but before the actual bosons were observed [33].

In spite of its success, the SM leaves outside its scope three crucial ingredients of the cosmological-scale Universe: gravity, dark matter and dark energy. Besides that, even within the range of phenomena it aims to describe, there are questions that remain at least partially unanswered, of which a non-exhaustive list is presented below.

The SM is remarkably minimal, considering the abundance of predictions it delivers. However, it could be expected from such a fundamental theory that the number of parameters it requires were even smaller. In particular, there are 9 independent Yukawa couplings and 4 quark-mixing parameters. If neutrino masses and mixing are to be included, that means 7 additional parameters. The origin of these parameters is not addressed by the SM, although the hierarchy in the Yukawa couplings and the quark-mixing structure seem to demand some deeper level of explanation.

Another puzzling issue is the naturalness of the Higgs boson mass. The SM predicts corrections to the Higgs boson mass that are quadratic on a cut-off scale parameter of the theory, while all other masses in the SM only get logarithmic corrections. If the SM is a complete theory up to the Planck scale ($M_P = 1.22 \times 10^{19}\,\mathrm{GeV}$), these corrections are many orders of magnitude above the observed Higgs boson mass, which lies in the weak scale ($\sim 10^2\,\mathrm{GeV}$). For this to be the case, the bare Higgs mass squared, which is a free parameter of the theory, must nearly cancel the quadratic corrections. This requires a fine adjustment of this parameter down to one part in 10^{36}, which can be regarded as 'unnatural'. Instead, if the cut-off scale is chosen at a few TeV, the required adjustment would be brought to the percent or per-mille level. The choice of a lower energy cut-off is only justifiable if new physical processes beyond the Standard Model (BSM) are introduced at this scale, with additional symmetries "protecting" the Higgs boson mass from larger corrections. In fact, this motivates BSM theories such as supersymmetry (SUSY) [34], technicolour [35], and theories with extra dimensions [36].

One major issue of observational nature is the abundance of matter and scarcity of anti-matter in the Universe. Assuming that equal amounts of matter and anti-matter existed immediately after the Big Bang, $\mathcal{CP}$-violating interactions are a necessary condition for one of them to dominate later in the lifetime of the Universe [37, 38]. The problem is that, in the SM, $\mathcal{CP}$ violation occurs only at very small rates, not sufficient to generate the currently observed asymmetry. This discrepancy serves as a motivation for the remainder of this chapter and for the analysis discussed in Chapter 9, which attempts to probe sources of $\mathcal{CP}$ violation through a measurement of the interaction between the Higgs boson and the top quark.

1.2 $\mathcal{CP}$ violation

1.2.1 $\mathcal{C}$ and $\mathcal{P}$ symmetries

The charge conjugation transformation $\mathcal{C}$ relates every particle to its anti-particle [39]. As mentioned already in Section 1.1.1, the electric charge of an anti-particle is the symmetric of the charge of the particle, and the same is true about other quantum numbers, such as baryon number and lepton number. The mass of the particle and of the anti-particle is the same. In a system with symmetry under $\mathcal{C}$, every process is as likely to happen as the process obtained by exchanging every particle by its anti-particle in the initial and final states.

A particle can only be an eigenstate of $\mathcal{C}$ if it is its own anti-particle, like the photon or the neutral pion π^0. Since $\mathcal{C}^2$ must be equal to 1, each particle that is a $\mathcal{C}$ eigenstate has an eigenvalue ($\mathcal{C}$ number) of 1 or -1. In multi-particle systems, the $\mathcal{C}$ number is given by the product of the $\mathcal{C}$ numbers of the constituent particles. A change in this number during a certain process is an indication of $\mathcal{C}$ violation.

The parity transformation $\mathcal{P}$ is a discrete transformation that, acting upon a physical system, transforms the vectors of spatial coordinates as $\vec{r} \to -\vec{r}$. Symmetry of physical laws under the parity transformation is well established in classical systems. Linear momentum $\vec{p}$ transforms like the spatial coordinates and changes sign under $\mathcal{P}$. On the other hand, angular momentum $\vec{J} = \vec{r} \times \vec{p}$ remains unchanged under $\mathcal{P}$. Vectors which flip sign under $\mathcal{P}$, like $\vec{r}$ and $\vec{p}$, are called polar vectors, or simply vectors if there is no ambiguity. Vectors which are invariant under $\mathcal{P}$, like $\vec{J}$, are called axial vectors or pseudovectors. Physical quantities described by a single component and invariant under $\mathcal{P}$ are scalars, while those that change sign under $\mathcal{P}$ are pseudoscalars. When there is symmetry under $\mathcal{P}$, an elementary physical process is just as likely to occur as its mirror image. The action of $\mathcal{P}$ on spinors is such that fermions with left-handed chirality are transformed into fermions with right-handed chirality, and vice-versa. A quantity related to chirality that is extensively used in particle physics is helicity:

$$h = \frac{\vec{s} \cdot \vec{p}}{p}, \tag{1.20}$$

where $\vec{s}$ is the spin of the particle. Simply put, it is the projection of the particle's spin along its direction of motion. This quantity is clearly a pseudoscalar, since it results from the inner product between a pseudovector and a vector. In general, states with a definite chirality can have positive and negative helicity components. However, in the ultra-relativistic or massless limit ($p \gg m$), there is a coincidence of positive helicity with right-handed chirality, and of negative helicity with left-handed chirality[4]. Since these limits are often applicable, helicity is useful to probe the degree of parity symmetry (or parity violation) in particle interactions.

The assignment of $\mathcal{P}$ eigenvalues to particles is conventional. Normally, fermions are assigned positive parity, which determines negative parity for anti-fermions. The parity of a state is obtained by multiplying the parity numbers of all particles (intrinsic parity) and the parity number associated with the orbital angular momentum ℓ of the state, which is $(-1)^\ell$ (extrinsic parity).

1.2.2 Violation of $\mathcal{C}$, $\mathcal{P}$ and $\mathcal{CP}$ in weak interactions

$\mathcal{C}$ and $\mathcal{P}$ symmetries hold exactly for the electromagnetic and strong interactions. The same is not true for weak interactions. Parity viola-

[4]Positive and negative helicities are also referred to as right- and left-handed helicities, respectively.

tion was decisively discovered in the β decay of ^{60}Co by Chien-Shiung Wu and collaborators, in 1957 [40]. In the experiment, a magnetic field and low temperatures were used to polarise the nuclei. An excess of β^- radiation along the direction opposite to the applied magnetic field was observed. Since the applied field $\vec{B}$ is a pseudovector and the momentum $\vec{p}$ of an emitted electron is a vector, the product $\vec{B} \cdot \vec{p}$ is a pseudoscalar. The observation of its non-zero expectation value was evidence of parity violation. Subsequent experiments have shown that weak charged currents are maximally parity-violating, in the sense that the mirror image of any possible process mediated by a weak charged current is forbidden. Interestingly, maximal $\mathcal{C}$ violation also occurs in weak interactions, and in such a way that weak processes exhibit near-perfect symmetry under $\mathcal{CP}$, the combined action of the $\mathcal{C}$ and $\mathcal{P}$ transformations.

It was only later discovered that $\mathcal{CP}$ symmetry is also violated, albeit at a small rate, in processes involving the weak interaction [41]. For this discovery, the Nobel Prize in Physics of 1980 was awarded to James Cronin and Val Fitch. Their experiment was related to the decay of the neutral kaon K_L, where the subscript L stands for “long”, referring to its long lifetime, compared to the shorter-lived K_S. The fact that both K_L and K_S can decay to a two-pion final state which has definite $\mathcal{CP}$ is proof of $\mathcal{CP}$ violation. In a $\mathcal{CP}$-conserving world, K_L and K_S would have definite $\mathcal{CP}$ themselves, and their decays would conserve $\mathcal{CP}$, resulting in non-overlapping final states.

1.2.3 $\mathcal{CP}$ violation in the SM

The way $\mathcal{CP}$-violating interactions arise in the SM is not obvious from a first look at the lagrangian discussed in Sections 1.1.2 and 1.1.3. A lagrangian containing only $\mathcal{L}_f + \mathcal{L}_{Gauge}$ is necessarily $\mathcal{CP}$ invariant. The $\mathcal{L}_{SSB}$ term, which includes a single scalar doublet, also ensures $\mathcal{CP}$ symmetry. Ultimately, the sector described by $\mathcal{L}_{Yukawa}$, in coexistence with weak charged currents from $\mathcal{L}_{Gauge}$, is responsible for $\mathcal{CP}$ violation in the

SM. This term, as already written in Equation 1.18, is

$$\mathcal{L}_{Yukawa} = -(k_d \bar{Q}_L \phi d_R + k_u \bar{Q}_L \phi^c u_R + k_e \bar{L}_L \phi e_R + \text{h.c.}).$$

The fact that k_d, k_u and k_e are used means that a convenient choice of basis is made implicitly, in which the quarks and leptons are states of definite mass. However, the different generations of quarks and leptons can mix, and there is in fact no reason for the mass basis to be the one that also diagonalises weak interactions. Taking this into account, the lagrangian for weak charged currents involving quarks may be written in terms of the mass states:

$$\mathcal{L}_W = \frac{g}{\sqrt{2}}(W_\mu^+ \bar{u}_L \gamma^\mu V d_L + W_\mu^- \bar{d}_L \gamma^\mu V^\dagger u_L), \tag{1.21}$$

where the basis transformation is encoded in the matrix V, known as the Cabbibo-Kobayashi-Maskawa (CKM) matrix [42]. An equivalent of this matrix for leptons does not exist in the SM with massless neutrinos. In SM extensions accounting for the observed massive neutrinos, such a matrix exists and is called the Pontecorvo-Maki-Nakagawa-Sakata (PMNS) matrix [43]. The most immediate consequence of the existence of a non-trivial CKM matrix is the mixing of generations, allowing transitions between quark generations via weak charged currents and decays of the W boson into a quark and anti-quark of different generations. The observation of these phenomena, namely the non-conservation of strangeness[5] in certain decays, lead to the proposal by Nicola Cabibbo [44] of a mixing angle which was the two-generation analogue of the later introduced CKM matrix.

By performing a $\mathcal{CP}$ transformation on the lagrangian of Equation 1.21 and comparing it to the original lagrangian, it can be shown that, for the weak charged currents to be $\mathcal{CP}$ conserving, it should be possible to express the CKM matrix as a real matrix. The CKM matrix is a 3×3 unit-

[5]The strangeness of a hadron is given by the number of s quarks minus the number of $\bar{s}$ anti-quarks in its content.

ary matrix, in general parameterised by nine parameters. However, five of those may be attributed to the five global phase differences between quark fields that can be changed without physical consequence. Four parameters remain, three of which can be identified with the Euler angles needed to describe a three-dimensional rotation. The existence of the fourth parameter is the soure of $\mathcal{CP}$ violation in the SM because it means that the CKM matrix is in general not real. This parameter is often described by the Jarlskog invariant [45], which is the imaginary part of the product of four CKM matrix elements of the form $V_{\alpha i} V_{\beta j} V^*_{\alpha j} V^*_{\beta i}$. Its value is the same regardless of which up-type quarks α, β and down-type quarks i, j are considered (provided that $i \neq j$ and $\alpha \neq \beta$).

1.2.4 $\mathcal{CP}$ violation beyond the SM

The small rates of $\mathcal{CP}$ violation observed in kaon and B-meson decays [11] are indicative of a small $\mathcal{CP}$-violating phase in the CKM matrix. Additional sources of $\mathcal{CP}$ violation beyond the SM are required to account for the observed asymmetry between matter and anti-matter in the Universe, assuming a symmetric initial-state Universe. [37, 38]. This is accomplished in many BSM theories, among which SUSY receives a large share of attention, due to its promise to address many of the limitations of the SM. The minimal supersymmetric model requires the existence of two scalar doublets, instead of one. This is a requirement also appearing in other extensions of the SM, which motivates the study of two-Higgs-doublets models (2HDM) in general [46, 47]. In such models, a rich Yukawa sector and scalar self-interactions provide many possible $\mathcal{CP}$ violation sources. Spontaneous $\mathcal{CP}$ symmetry breaking, in particular, is only possible with at least two Higgs doublets.

In 2HDM, there are two fundamental scalar $SU(2)$ doublets, ϕ_1 and ϕ_2. They can always be expressed in a basis, called the Higgs basis, as:

$$H_1 = \begin{pmatrix} G^+ \\ \frac{1}{\sqrt{2}}(v + \chi_1 + iG^0) \end{pmatrix}, \quad H_2 = \begin{pmatrix} H^+ \\ \frac{1}{\sqrt{2}}(\chi_2 + i\chi_3) \end{pmatrix}. \tag{1.22}$$

In this basis, all the Goldstone bosons (G^0 and $G^{\pm}$) appear in H_1, which is also the only doublet that gets a (real and positive) vev. Five physical degrees of freedom remain: two charged ($H^{\pm}$) and three neutral, two of which are $\mathcal{CP}$-even (χ_1 and χ_2) and one which is $\mathcal{CP}$-odd (χ_3). These neutral degrees of freedom are not necessarily mass states, and can be related to three mass states h_1, h_2, h_3 by an orthogonal matrix R. The fact that the matrix R is allowed to mix $\mathcal{CP}$-even and $\mathcal{CP}$-odd states provides a source of $\mathcal{CP}$ violation. This source is useful to illustrate how, if the physical Higgs bosons are not states of definite $\mathcal{CP}$, that may become evident through couplings to fermions. For example, it is relevant to focus on the coupling between an up-type quark u and the lightest Higgs boson h_1. When building Yukawa terms in 2HDM, a discrete symmetry is usually introduced to avoid flavour-changing neutral currents at tree level, which are highly constrained by experiment [11]. To conform to this symmetry, each set of fermions – charged leptons, up-type quarks and down-type quarks – must couple only to one of the fundamental doublets. Up-type quarks are conventionally coupled to ϕ_2. It is possible to pick all the ϕ_2 contributions to h_1, such that the coupling to u becomes:

$$-\frac{m_u}{v}\frac{1}{\sin\beta}\left[(R_{11}\sin\beta + R_{12}\cos\beta - iR_{13}\cos\beta)\,\bar{u}_L\phi_2^c u_R + \text{h.c.}\right], \tag{1.23}$$

where β is a mixing angle used to define the Higgs basis with respect to the fundamental doublets and R_{ij} is the element of the matrix R mixing the mass state h_i and the Higgs-basis state j. For simplicity, coupling modifiers with respect to the SM may be defined as

$$\kappa_u \equiv \frac{R_{11}\sin\beta + R_{12}\cos\beta}{\sin\beta}, \quad \tilde{\kappa}_u \equiv -\frac{R_{13}\cos\beta}{\sin\beta}. \tag{1.24}$$

Substituting in Equation 1.23, the coupling reduces to

$$-\frac{m_u}{v}\bar{u}(\kappa_u + i\gamma_5\tilde{\kappa}_u)u, \tag{1.25}$$

after using the equality $\gamma_5 = P_R - P_L$, where P_R and P_L are the right-and left-handed chirality projectors, respectively. The key indicator of $\mathcal{CP}$ violation in this interaction is the term proportional to γ_5, which is a pseudoscalar. This means that the lagrangian of 1.25 is not $\mathcal{CP}$-invariant. Not necessarily every process involving this coupling would be $\mathcal{CP}$-violating. However, any observation confirming that both κ_u and $\tilde{\kappa}_u$ are non-zero would be proof of $\mathcal{CP}$ violation in the Higgs sector.

Chapter 2

Top quark and Higgs boson

This chapter discusses the physics of the top quark and of the Higgs boson, with focus on processes where the interaction between the two is relevant. Properties of the top quark are discussed in Section 2.1, while the state of the art in Higgs boson properties is given in Section 2.2. In Section 2.3, several processes and observations sensitive to the top-Higgs coupling are addressed. Associated production of the Higgs boson with top quarks at the LHC is presented as the best direct probe of this interaction. The most relevant measurements of this process made so far are discussed.

2.1 Top quark

Makoto Kobayashi and Toshihide Maskawa were the first to theoretically propose the existence of the top and bottom quarks. When they introduced the CKM matrix as a possible source of the observed $\mathcal{CP}$ violation in weak interactions [42], only two generations of quarks had been experimentally observed. Top quark production was first observed in 1995 at the Tevatron by the D∅ and CDF experiments [48, 49]. The top quark is the most massive elementary particle in the SM. Measurements of its mass have been performed by the ATLAS [50] and CMS [51] collaborations at the LHC, combining different final states and using the full dataset of the LHC Run 1, with the results

$$\text{ATLAS: } m_t = 172.69 \pm 0.25_{\text{(stat.)}} \pm 0.41_{\text{(syst.)}}\,\text{GeV}, \tag{2.1}$$

$$\text{CMS: } m_t = 172.44 \pm 0.13_{\text{(stat.)}} \pm 0.47_{\text{(syst.)}}\,\text{GeV}. \tag{2.2}$$

Due to its large mass, the top quark can decay through the charged current $t \to W^+b$ ($\bar{t} \to W^-\bar{b}$) [52]. The final states Ws and Wd are also allowed, but very suppressed by the non-diagonal terms of the CKM matrix, such that the branching ratio to Wb is very close to 1. The large available phase-space in that channel results in a lifetime close to 5×10^{-25} s, much shorter than that of any other quark and shorter than the hadronisation time scale ($\sim 3 \times 10^{-24}$ s). As a result, the top quark is the only quark that decays from its "bare" state, instead of hadronising. The top quark decay is categorised according to the decay of the resulting W boson. If the W decays into a lepton and a neutrino, which occurs 33% of the time, the decay of the parent top quark is said to be leptonic, and if the W decays to a quark and anti-quark pair, which happens 67% of the time, it is said to be hadronic.

The short decay time of the top quark ensures that its spin state can be measured from the decay products. In the leptonic decay in particular, the resulting lepton in the final state preserves most of the spin information of the decaying top quark. This is unique to the top quark, since for any other quark the spin information is quickly degraded during hadronisation. At hadron colliders, top quarks resulting from $t\bar{t}$ production are unpolarised. However, the spins of the $t\bar{t}$ pair are strongly correlated. Spin correlation measurements in $t\bar{t}$ production have been performed by ATLAS [53] and CMS [54] using $36\,\text{fb}^{-1}$ of data from the Run 2 of the LHC, focusing on the dileptonic final state. The two experiments report observations compatible with the expectation from the SM. However, an interesting result from both experiments was the distribution of the azimuthal angle difference between the two leptons ($\Delta\phi_{\ell\ell}$). The degree of spin correlation measured in this distribution is higher than what is expected from most of the predictions available, a result which has driven state-of-the-art high-order calculations for this process [55].

2.2 Higgs boson

2.2.1 Higgs boson physics at the LHC

Searching for the Higgs boson was one of the goals for the operation of the LHC [56] and of the general-purpose LHC experiments ATLAS [57] and CMS [58]. The Higgs boson production in pp collisions at the LHC was expected to occur through four main processes [59]: gluon fusion (ggF), vector boson fusion (VBF), associated vector boson production (VH, with $V = Z$ or $V = W$) and associated top quark pair produc-

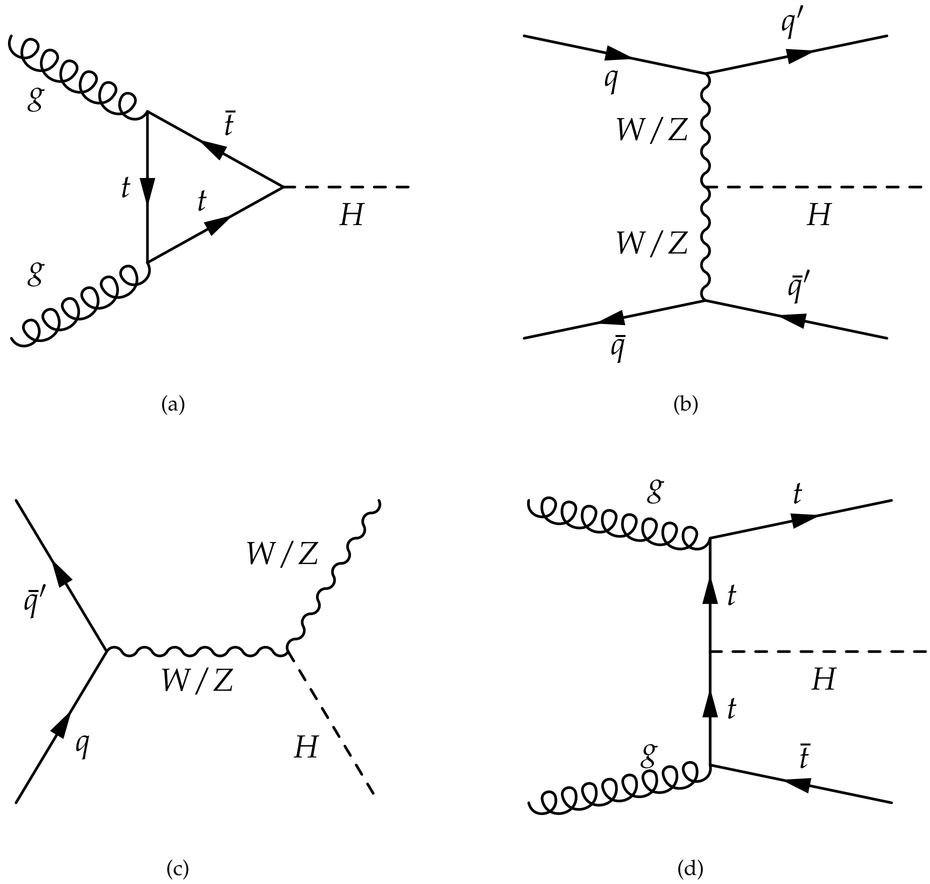

Figure 2.1: Example of leading-order diagrams for the main Higgs boson production processes at the LHC. (a) Gluon fusion (ggF). The top quark loops dominate, but there are contributions from loops of every quark. (b) Vector boson fusion (VBF). (c) Vector boson associated production (VH). (d) Top quark pair associated production ($t\bar{t}H$).

tion ($t\bar{t}H$). Examples of production diagrams at leading order are shown in Figure 2.1.

For a light Higgs boson ($m_H \lesssim 130\,\text{GeV}$), the dominant decay channel is $H \to b\bar{b}$, but it is not necessarily the most sensitive channel for searches or measurements at the LHC. Due to the phenomenon of confinement in strong interactions, quarks in the final state hadronise: quark/anti-quark pairs are created from the vacuum, forming bound states with each other and with the initial "bare" quarks, until only colour-neutral stable hadrons remain. If the original quark travels with enough momentum, the cascade of particles thus generated forms a 'jet' with approximately conical shape, which may be reconstructed in the detectors. In hadron colliders, the most common hard inelastic process is the production of two or more jets, each initiated by a gluon or a light-flavour quark. This overwhelming multijet background, several orders of magnitude more abundant than Higgs boson production, can only be removed from the $b\bar{b}$ final state to a very limited extent. That limitation can be partially overcome if the analysis is performed in one of the less common production channels – VBF, VH or $t\bar{t}H$ – resulting however in a much smaller number of signal events. In any case, jets are the objects measured with worst energy resolution by experiments, which propagates to the reconstructed Higgs boson mass. The channel $H \to WW$ may have one or both of the W bosons decaying leptonically, which provides a cleaner final state. However, the neutrinos in the final state make it impossible to fully reconstruct the Higgs boson. The decay channels $H \to \gamma\gamma$ and $H \to ZZ^* \to 4\ell$ (4ℓ means two pairs of leptons, only considering e and μ, where leptons within each pair have the same flavour and opposite charge) produce unique final states, with leptons and photons, particles which are detected with better energy resolution. Therefore, $H \to \gamma\gamma$ and $H \to ZZ^* \to 4\ell$ were expected to provide the best resolution in Higgs boson mass, possibly allowing the new particle to be observed as a peak in the reconstructed mass distribution, over a smooth background. However, they are particularly rare channels, which made them less sensitive than $H \to WW$ in the first Higgs boson searches at the LHC.

In July 2012, both ATLAS and CMS collaborations announced, the discovery of a new resonance with mass close to 125 GeV, consistent with the Higgs boson predicted by the SM [1, 2]. Following the discovery, the 2013 Nobel Prize in Physics was granted to Peter Higgs and François Englert for the theoretical discovery of the EWSB mechanism [60]. The Higgs boson discovery was the crucial piece of evidence for the mechanism that allows a world governed by gauge symmetries to bear massive particles. It represented the largest step towards a better understanding of the EWSB, and a doorway to open problems, such as the Higgs mass naturalness and the need for additional sources of $\mathcal{CP}$ violation.

2.2.2 Higgs boson properties

Assuming a SM Higgs boson with a mass of 125 GeV, numerical predictions can be obtained for its production cross-sections at the LHC and for its branching fractions. In Figure 2.2, the cross-section for each production process is plotted as a function of the centre-of-mass energy [59]. Table 2.1 shows theoretical values for the most important branching ratios [59].

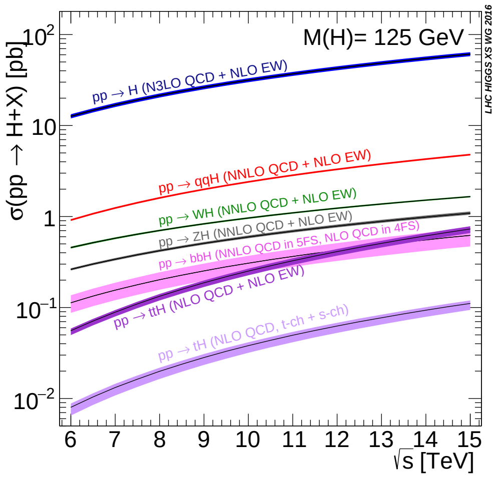

Figure 2.2: Cross-sections for the production processes of a 125 GeV SM Higgs boson in pp collisions as a function of the centre-of-mass energy [59]. $pp \to H$ means ggF and $pp \to qqH$ means VBF.

Table 2.1: Higgs boson branching ratios for a 125 GeV SM Higgs boson [59].

Decay channel	BR (%)
$b\bar{b}$	58.2
WW	21.4
gg	8.19
$\tau\tau$	6.27
$c\bar{c}$	2.89
ZZ	2.62
$\gamma\gamma$	0.227
Others	< 0.2

Following discovery, the properties of the newly discovered particle have been studied. The mass value of 125 GeV sits in a region that makes the Higgs boson physics at the LHC particularly rich. With such a mass, many production and decay channels are sufficiently abundant to have become feasible targets for analyses. Production cross-sections and decay branching ratios have been measured and compared with SM predictions. Alternative scenarios regarding properties such as spin and parity have been tested. The results of some of these measurements are presented below. All of them show consistency with the SM predictions, progressively building confidence that the 125 GeV boson is an SM-like Higgs boson.

For this reason, it will be referred to as simply 'the Higgs boson' in the rest of this document.

Higgs boson mass measurements have been made in the $\gamma\gamma$ and $ZZ^* \to 4\ell$ channels. The most precise measurement from ATLAS was obtained by analysing the $ZZ^* \to 4\ell$ channel alone, using the full Run 2 dataset, corresponding to 139 fb^{-1} [61]. CMS combined measurements of the two decay channels, using the Run 1 dataset together with 35.9 fb^{-1} of data from Run 2 [62]. The obtained mass values were

$$\text{ATLAS: } m_H = 124.92 \pm 0.19_{\text{(stat.)}}{}^{+0.09}_{-0.06}{}_{\text{(syst.)}}\,\text{GeV}, \tag{2.3}$$

$$\text{CMS: } m_H = 125.38 \pm 0.11_{\text{(stat.)}} \pm 0.08_{\text{(syst.)}}\,\text{GeV}, \tag{2.4}$$

which bring to an impressive precision, at the per-mille level, the knowledge of a fundamental parameter that just before 2012 was completely unknown.

Measurements of Higgs boson production and decay rates were performed by ATLAS [63] and CMS [64], using data from the LHC Run 2. These measurements consist of combinations of several analyses, each targeting a subset of production processes and decay modes of the Higgs boson. For a particular combination of a production process i and decay channel f, a signal strength parameter can be defined as

$$\mu_{i,f} = \frac{\sigma_i}{\sigma_i^{\text{SM}}} \frac{\text{BR}_f}{\text{BR}_f^{\text{SM}}}, \tag{2.5}$$

where σ_i and BR_f are the production cross-section and branching ratio, respectively, that best adjust to the data. The denominators σ_i^{SM} and BR_f^{SM} refer to the corresponding SM predictions. Both ATLAS and CMS measured several signal strengths in Higgs boson processes. In one particular measurement, the signal strength is assumed to be the same across all production and decay channels. By fitting this single parameter μ, called the global signal strength, the obtained values were:

$$\begin{aligned} \text{ATLAS: } \mu &= 1.06 \pm 0.07 \qquad (2.6) \\ &= 1.06 \pm 0.04_{\text{(stat.)}} \pm 0.03_{\text{(exp.)}}{}^{+0.05}_{-0.04}{}_{\text{(sig. th.)}} \pm 0.02_{\text{(bkg. th.)}}, \\ \text{CMS: } \mu &= 1.02^{+0.07}_{-0.06} \qquad (2.7) \\ &= 1.02 \pm 0.04_{\text{(stat.)}} \pm 0.04_{\text{(exp.)}} \pm 0.04_{\text{(th.)}}, \end{aligned}$$

which shows remarkable agreement with the SM.

Measuring the global signal strength provides a test to deviations from the SM in which there is an overall increase or decrease of the production rate of Higgs bosons at the LHC. In order to probe scenarios in which the deviations of the Higgs couplings may be such that they cancel out in the total rate, a more flexible fit model can be built using the so-called 'κ framework'. In this framework, coupling modifiers κ_j are defined such that

$$\kappa_j^2 = \frac{\sigma_j}{\sigma_j^{\text{SM}}} \text{ and } \kappa_j^2 = \frac{\Gamma_j}{\Gamma_j^{\text{SM}}}, \qquad (2.8)$$

where σ_j and Γ_j are, respectively, the production cross-section and the partial decay width governed by the Higgs boson coupling to the particle j. The photon and the gluon are massless, thus not coupling to the Higgs boson at tree level, but only through loops. In this framework, κ_γ and κ_g may be treated in two different ways. They can be considered as effective coupling modifiers, independent from the other κ_j, or they may be expressed in terms of the other κ_j, assuming that the loop contributions to the photon and gluon couplings to the Higgs boson are the ones predicted by the SM. The latter can be expected to yield more precise values of κ_j, with the caveat of assuming no BSM effects contributing to the loops.

Both experiments made fits using at least one of the prescriptions, obtaining results compatible with the SM in all cases. CMS results are shown in Figure 2.3a, for which κ_γ and κ_g are kept as effective couplings. The EWSB mechanism predicts the proportionality between the coupling of a particle to the Higgs boson and the particle mass, in the

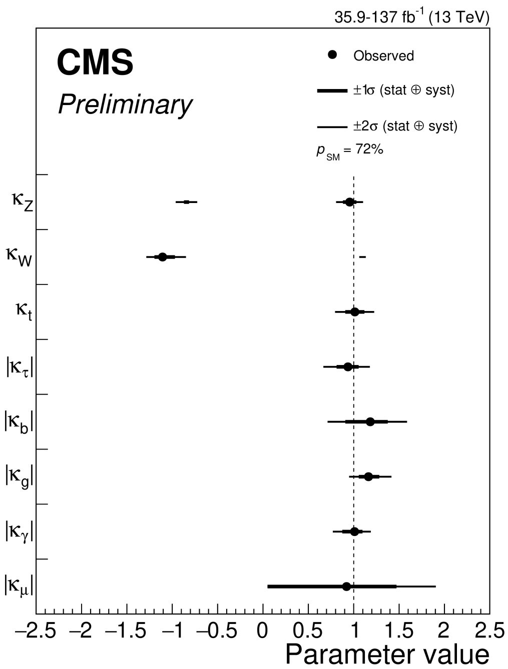

(a)

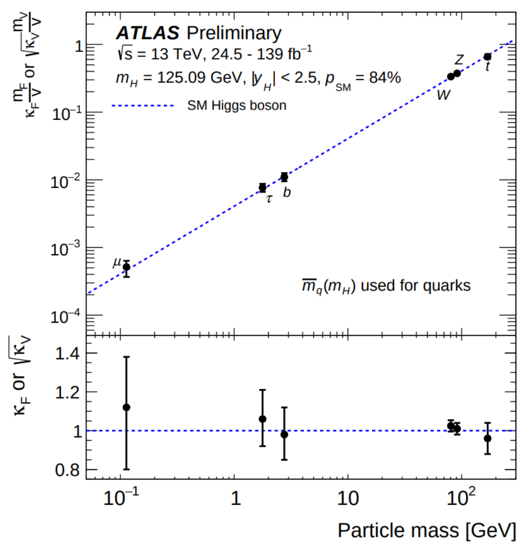

(b)

Figure 2.3: (a) Coupling modifiers κ_j measured by CMS, using effective coupling modifiers for photons and gluons [64]. (b) Reduced couplings ($y_F = \kappa_F \frac{m_F}{v}$ for fermions and $y_V = \sqrt{\kappa_V}\frac{m_V}{v}$ for vector bosons) measured by ATLAS, as a function of the corresponding particle mass [63]. The loop-induced κ_γ and κ_g were defined as functions of the other κ_j. The dashed line indicates the SM prediction.

case of fermions, or mass squared, in the case of vector bosons. 'Reduced couplings' are defined as $\kappa_F \frac{m_F}{v}$ for each fermion F and $\sqrt{\kappa_V}\frac{m_V}{v}$ for each vector boson V, such that they are both predicted to be proportional to the corresponding particle mass. The ATLAS result in Figure 2.3b, shows reduced couplings as a function of particle mass, from a fit in which κ_γ and κ_g are expressed in terms of other κ_j.

In the SM, the Higgs boson is a spin-0, $\mathcal{CP}$-even particle ($J^{\mathcal{CP}} = 0^+$). For the Higgs boson discovered at the LHC, the spin-1 scenario is excluded by the observation of the diphoton decay, which is forbidden for a massive spin-1 particle. Measurements have been performed by ATLAS [65] and CMS [66] to exclude other scenarios of spin and parity, using the whole dataset of LHC Run 1 (approximately 5 fb^{-1} of data at $\sqrt{s} = 7$ TeV and 20 fb^{-1} at $\sqrt{s} = 8$ TeV). Both analyses focused on the final states $\gamma\gamma$, 4ℓ and $WW^* \rightarrow \ell\nu\ell\nu$. The SM hypothesis was tested against several BSM scenarios, including various spin-2 scenarios and a negative parity spin-0 scenario. All the spin-2 hypotheses were excluded at confidence levels greater than 99% and the pure pseudoscalar hypothesis was excluded with confidence levels above 99.9% by both experiments.

Anomalous couplings between the Higgs boson and vector bosons, including $\mathcal{CP}$-violating terms, were also studied [65, 66, 67, 68, 69, 70, 71]. All the measurements reported consistency with SM predictions and stringent limits have been put on anomalous $\mathcal{CP}$-odd interactions. For example, the CMS analysis of Ref. [70] combines measurements of VBF Higgs boson production (with $H \rightarrow \tau\tau$) and of the $H \rightarrow 4\ell$ channel (ggF, VBF and VH production modes) to probe the anomalous couplings. It sets an upper limit on the anomalous $\mathcal{CP}$-odd cross-section fraction f of 0.092 with a 95% confidence level. Although the limits on $\mathcal{CP}$-odd couplings between the Higgs boson and vector bosons are strong, this does not translate trivially into a statement about the $\mathcal{CP}$ nature of the 125 GeV Higgs boson. A $\mathcal{CP}$-odd Higgs boson is not allowed to couple at tree level to gauge bosons [72], which means that decays of such a particle into WW and ZZ, as well as production via VH and VBF, can only occur through loops and are expected to be highly suppressed when compared to the $\mathcal{CP}$-even scenario. Thus, a large $\mathcal{CP}$-odd component to the 125 GeV Higgs boson could in principle exist, while leaving the couplings to vector bosons very SM-like. Couplings to fermions, on the other hand, are allowed at tree level for $\mathcal{CP}$-even and $\mathcal{CP}$-odd states alike, thus providing an irreplaceable test to the nature of the Higgs boson.

2.3 Probing the top-Higgs interaction

The top quark, being the most massive fermion, is expected to have the largest coupling to the Higgs boson, making it a preferred candidate for probing the Yukawa sector. In the κ framework, the interaction between the top quark and the Higgs boson can be written as

$$\mathcal{L}_{Ht\bar{t}} = \frac{m_t}{v}\kappa_t \bar{t}tH. \tag{2.9}$$

Well motivated new physics models may result in a top quark Yukawa coupling to the 125 GeV Higgs boson with $\mathcal{CP}$-even and $\mathcal{CP}$-odd components, as was shown in Section 1.2.4. One possible generalisation of the SM interaction that accommodates both components is

$$\begin{aligned} \mathcal{L}_{Ht\bar{t}} &= \frac{m_t}{v}\bar{t}(\kappa_t + i\tilde{\kappa}_t\gamma_5)tH, &(2.10)\\ &= \frac{m_t}{v}\kappa_t'\bar{t}(\cos\alpha + i\sin\alpha\gamma_5)tH, &(2.11) \end{aligned}$$

where the two lines correspond to different parameterisations describing the same space of physics scenarios. In the first parameterisation, κ_t and $\tilde{\kappa}_t$ are real coupling modifiers of the $\mathcal{CP}$-even and $\mathcal{CP}$-odd components of the coupling, respectively. The SM coupling is recovered by setting $\kappa_t = 1$ and $\tilde{\kappa}_t = 0$, a pure $\mathcal{CP}$-odd coupling has $\kappa_t = 0$ and $\tilde{\kappa}_t \neq 0$, and a $\mathcal{CP}$-mixed coupling has both $\kappa_t \neq 0$ and $\tilde{\kappa}_t \neq 0$. In the second parameterisation, κ_t' is a modifier affecting both the $\mathcal{CP}$-even and $\mathcal{CP}$-odd components of the coupling, and α is a $\mathcal{CP}$-mixing angle. The SM scenario corresponds to $\kappa_t' = 1$ and $\alpha = 0$, a pure $\mathcal{CP}$-odd scenario is obtained with $\alpha = \pm\pi/2$ and $\kappa_t' \neq 0$. A $\mathcal{CP}$ mixture will occur whenever α is not an integer multiple of $\pi/2$, with maximal $\mathcal{CP}$-violation when $\alpha = \pi/4 + k\pi/2$, with integer k. In this document, both parameterisations are used because either one or the other may provide more clarity, depending on the context.

The large top quark Yukawa coupling is a privileged probe into the Higgs boson $\mathcal{CP}$ nature, if α is universal or similar across all fermions. However, it is in principle possible that the size of $\mathcal{CP}$-odd contributions is different for different fermions, and the couplings of all fermions to the Higgs boson should be addressed. Before focusing exclusively on the top quark, a complementary process worth mentioning here is the already observed decay of the 125 GeV Higgs boson to τ leptons. This decay provides direct access to the τ Yukawa coupling, and its $\mathcal{CP}$ nature has some observable impact on the final state. The CMS collaboration measured directly the $\mathcal{CP}$ nature of this coupling, by analysing $H \to \tau\tau$ events in the full Run 2 dataset [73]. Angular correlations between the decay planes of the τ leptons were used to obtain sensitivity to the $\mathcal{CP}$-mixing angle, which was measured to be $4 \pm 17°$. The pure $\mathcal{CP}$-odd scenario was excluded with a significance of 3.2 standard deviations.

2.3.1 $t\bar{t}H$ production

The most relevant process that allows direct measurement of the top quark Yukawa coupling at the LHC is $t\bar{t}H$ production. In this process, there is always one vertex of interaction between the Higgs boson and a t or $\bar{t}$ in the leading production diagrams. It is a relatively rare process at the LHC, with a predicted SM production cross-section of 507 fb at $\sqrt{s} = 13\,\text{TeV}$ [59].

Search and cross-section measurements

Both ATLAS and CMS collaborations observed the $t\bar{t}H$ production process at the LHC [74, 75], when combining results of several analysis channels from the LHC Runs 1 and 2. The channels contributing to the combination are similar across the experiments: the $b\bar{b}$ channel, which targets the Higgs decay into $b\bar{b}$; the multilepton channel, which focuses on final states where the Higgs decays either into τ leptons or bosons, the latter decaying at least partially into leptons, and the rare $\gamma\gamma$ channel, which nevertheless provides a clean final state for detection. In broad terms, the strategies used in each channel are also not very different and are briefly described here.

Analyses of the multilepton channel rely on several final states, categorised by number of electrons and muons (referred to just as leptons) and by number of (hadronically-decaying) τ leptons. By requiring that the number of leptons and τ leptons combined is at least three or that there is a same-sign lepton pair, background events with leptons from the $t\bar{t}$ decay alone are mostly rejected, and the categories are enriched in leptonic decays of the Higgs boson. All final states are also required to have additional jets identified as resulting from the hadronisation of b quarks (b-tagged jets), expected from the $t\bar{t}$ decay. The downside of high lepton multiplicity is that this channel becomes sensitive to the background due to fake and non-prompt leptons. Fake leptons are objects mistakenly identified as electrons (narrow jets or photons) or muons (jet constituents punching through the calorimeters into muon detectors). Non-prompt leptons are true leptons originating from secondary processes irrelevant for the analysis, such as leptonic decays of hadrons or photon conversions.

The $H \to b\bar{b}$ channel is mainly divided in categories depending on the number of leptons (e or μ): zero (in the CMS analysis only), one, or two, respectively targeting the $t\bar{t}$ fully-hadronic, semileptonic and dileptonic decays. Events are selected with at least 3 b-tagged jets. Within the semileptonic final state, ATLAS includes an additional 'boosted' category, targeting Higgs bosons produced with high transverse momentum (p_T) that decay into a pair of b quarks with small angular separation. Both experiments make use of the b-tagging discriminant scores of the jets. Those values, together with kinematic variables, are used to build one or more layers of multivariate methods with the purpose of separating signal from backgrounds. The main background for this channel is $t\bar{t}$ production in association with additional jets ($t\bar{t}$ + jets). The component in which at least one of the additional jets is initiated by a b quark ($t\bar{t} + \geq 1b$) dominates in the signal-rich phase-space. Modelling of the $t\bar{t} + \geq 1b$ background is particularly challenging, and constitutes the main source of uncertainty in this measurement.

The $H \to \gamma\gamma$ channel divides its $t\bar{t}H$-enriched categories into leptonic and hadronic, to target the different $t\bar{t}$ decays. The leptonic category is obtained by requiring, besides the diphoton signature, at least one prompt lepton (e or μ). In both categories, additional jets are required. Signal sensitivity is enhanced by using multivariate methods. A fit is performed to the diphoton invariant mass distribution of events, in which analytical functions are used to parameterise the background continuum and the signal peak. The parameters of these functions are extracted directly from the data, making the $\gamma\gamma$ channel less dependent on physics modelling by MC event generators than other channels. This results in relatively small systematic uncertainties which, together with the small BR of $H \to \gamma\gamma$, make this channel statistically dominated, thus expected to greatly improve in sensitivity as data taking continues.

In the combination of all channels at $\sqrt{s} = 13\,\text{TeV}$, the ATLAS collaboration observed the $t\bar{t}H$ process [74]. The distribution of the diphoton invariant mass in the $H \to \gamma\gamma$ events used in the combination is shown in Figure 2.4a, where weights are applied to data according to the signal purity of the category into which they are selected. The leading systematic uncertainty sources to the ATLAS observation were the modelling of $t\bar{t} + \geq 1b$, the modelling of $t\bar{t}H$ signal, the estimate of backgrounds due to fake and non-prompt leptons, and the jet energy scale and resolution. In a more recent result, using up to 139 fb^{-1} of Run 2 data and simultaneously measuring the signal strengths of several Higgs production processes, ATLAS measured a $t\bar{t}H + tH$ signal strength of $1.10^{+0.16}_{-0.15}{}_{\text{(stat.)}}{}^{+0.14}_{-0.13}{}_{\text{(syst.)}}$ [63].

The CMS collaboration observed $t\bar{t}H$ production already with the Run 1 and Run 2 results combined [75]. When combining several channels and datasets, a fit is performed to many binned distributions, where bins may be regarded as analysis categories with varying signal-to-background ratios. Figure 2.4b shows data, signal and background yields in all the analysis categories combined, binned by signal-to-background ratio of the category. The leading sources of systematic uncertainty in the measurement include b-tagging, identification of leptons, energy scales of jets and τ leptons, modelling of $t\bar{t}$ production in association with W, Z, b and c, and modelling of the $t\bar{t}H$ signal. In a later analysis, using a larger dataset for measuring Higgs boson production rates, CMS reported a $t\bar{t}H$ signal strength of $1.14 \pm 0.13_{\text{(stat.)}}{}^{+0.17}_{-0.15}{}_{\text{(syst.)}}$ at $\sqrt{s} = 13\,\text{TeV}$ [64].

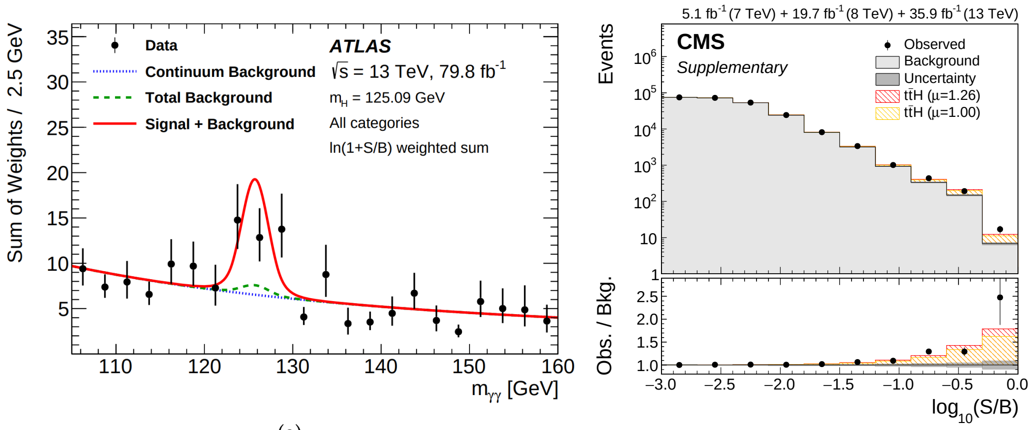

(a)

(b)

Figure 2.4: (a) Invariant mass of the diphoton system in the $H \to \gamma\gamma$ events used in the ATLAS combination [74]. Events are weighted by $\ln(1 + S/B)$, where S and B are the signal and background yields in the smallest mass window containing 90% of signal in the category into which the event is selected. Lines show the fitted functions used to model the background and signal components. (b) Data, signal and background yields in all the analysis categories combined by CMS [75], binned by logarithm of the signal-to-background ratio of the category. Two signal hypotheses are shown: with the SM expected strength ($\mu = 1$) and with the best-fit strength ($\mu = 1.26$).

$\mathcal{CP}$ measurements in $H \to \gamma\gamma$

Direct measurements of the $\mathcal{CP}$ nature of the top quark Yukawa coupling have been performed by the ATLAS and CMS collaborations in $t\bar{t}H$ production, with the Higgs boson decaying into two photons [76, 77]. The analysis strategies adopted by the two experiments are similar enough to allow a common description.

As in the cross-section measurement, the analyses start from a diphoton selection and a classification of events into leptonic and hadronic categories. In the hadronic category, both experiments use a boosted decision tree (BDT) to identify jet triplets as compatible with resulting from a top quark decay. Classification BDTs are also used for discriminating signal from backgrounds, with dedicated training in each category. The main backgrounds present in the signal-enriched phase-space are $\gamma\gamma$+jets and $t\bar{t} + \gamma\gamma$. Events with a low score of the signal/background classification BDT are removed. In the remaining signal-rich regions, an additional

BDT, called $\mathcal{CP}$ BDT, is used to discriminate between $\mathcal{CP}$-even and $\mathcal{CP}$-odd signal hypotheses. Events are further divided into categories, in two splittings made in succession, the first based on the signal/background BDT score and the second based on the $\mathcal{CP}$ BDT score.

In order to perform the measurement, the $t\bar{t}H$ estimate is parameterised in terms of the coupling $\mathcal{CP}$ structure using MC samples. Both experiments include an estimate for the Higgs boson production in association with a single top or anti-top quark (tH) and also parameterise its rate in terms of the coupling. ATLAS also parameterises the shape and includes this process in the training of the $\mathcal{CP}$ BDT. In the CMS measurement, the exclusion of the region with negative κ_t is not pursued, and that parameter is only allowed to be positive. A fit is performed simultaneously to the diphoton mass distribution using all categories. Signal and background distributions are parameterised by analytical functions.

Both experiments report 0 as the best-fit value for α. The observed exclusion significances of the $\mathcal{CP}$-odd scenario were 3.9 and 3.2 standard deviations in the ATLAS and CMS measurements, respectively. The ranges of α excluded with a 95% confidence level (CL) were $\alpha > 43^\circ$ and $\alpha > 55^\circ$ for ATLAS and CMS, respectively. In addition, ATLAS reported its first upper limit on the tH production signal strength, at 12 times the SM prediction with a 95% CL. These measurements are statistically dominated. Figure 2.5a summarises the ATLAS result in the $(\kappa_t, \tilde{\kappa}_t)$ plane, where the SM prediction and best-fit point are represented, as well as exclusion contours at different significance levels. Figure 2.5b shows distributions of the $\mathcal{CP}$ BDT used by CMS, for the observed data and for the $\mathcal{CP}$-even and $\mathcal{CP}$-odd signal hypotheses, and the log-likelihood profile of a parameter equivalent to $\sin^2\alpha$.

2.3.2 Beyond $t\bar{t}H$ production

An intriguing feature of the top quark Yukawa coupling is that it may have a determinant role in the stability of the vacuum. If the SM is assumed to be a valid theory for energies up to the order of the Planck scale,

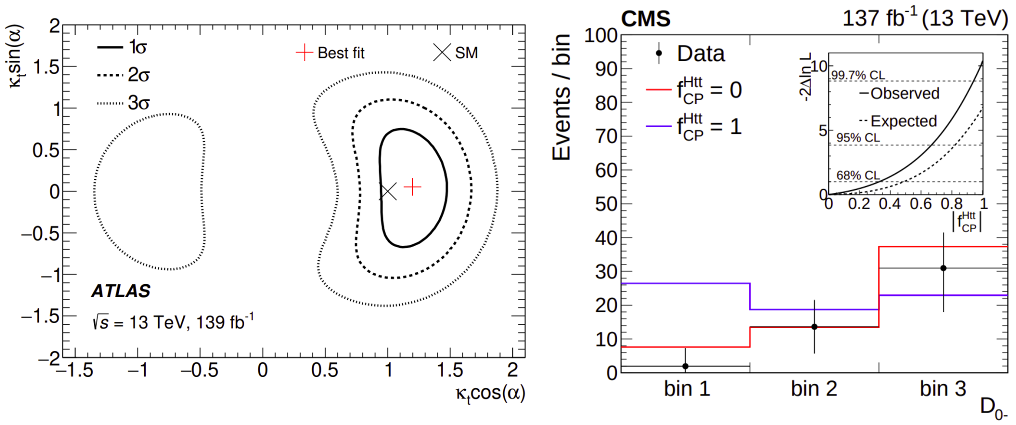

(a) (b)

Figure 2.5: Results of the direct measurements of the $\mathcal{CP}$ nature of the top quark Yukawa coupling in $t\bar{t}H$ production, with $H \to \gamma\gamma$. (a) ATLAS results in the $(\kappa_t, \tilde{\kappa}_t)$ plane, together with the SM point [76]. The best-fit point is shown, as well as the exclusion contours at significances of 1, 2 and 3 standard deviations. (b) Distributions of the $\mathcal{CP}$ BDT used by CMS, for the observed data and for the $\mathcal{CP}$-even and $\mathcal{CP}$-odd signal hypotheses, and the log-likelihood profile of a parameter equivalent to $\sin^2\alpha$.

the Higgs quartic self-coupling λ, as defined in Section 1.1.3, must be corrected for loop contributions, which become more and more important at higher energy scales [78]. In particular, this running value of λ is very sensitive to the mass of the Higgs boson and to the top quark Yukawa coupling, since it is the only Yukawa coupling of order unity. For corrections near the Planck scale, a large top Yukawa coupling could drive λ to zero and even negative values. This change of sign has a qualitative impact on the Higgs potential $V(\phi)$. Depending on λ, the SM vacuum could either be stable (i.e., a global minimum of $V(\phi)$), metastable (a local minimum) or unstable (not a minimum at all). The requirement that the SM vacuum is a stable one results in a constraint between the Higgs boson and the top quark masses. The currently measured mass values are compatible with the stability constraint within uncertainties, but the central values fall into the metastable region. It is unsettling to conceive the known Universe as living in a metastable vacuum. In that scenario, it could in principle evolve via tunneling into another, more stable, vacuum, with destructive consequences. This existential concern is an additional motivation for precise determination of the Higgs boson mass and of the top quark Yukawa coupling.

There are indirect constraints on the $\mathcal{CP}$-odd component of the top quark Yukawa coupling. One of them comes from the precise measurement of the electric dipole moment (EDM) of the electron [79]. If the Higgs field couples both to the top quark and to the electron, the electron is expected to have contributions to its EDM proportional to $\tilde{\kappa}_t \kappa_e$ and $\kappa_t \tilde{\kappa}_e$. Assuming an SM-like electron Yukawa coupling, only the former contribution remains. Making that assumption, the very stringent upper limit $\tilde{\kappa}_t < 0.01$ has been set [79]. Since then, the electron EDM has been measured with precision improved by nearly one order of magnitude by the ACME collaboration [80], which brings the upper limit on $\tilde{\kappa}_t$ closer to 0.001. Of course, it is possible to make different assumptions on the Yukawa couplings or to include additional sources of $\mathcal{CP}$ violation that remove this constraint. In particular, the Higgs boson couplings to the first generation of fermions have not yet been directly constrained.

Processes at the LHC, other than $t\bar{t}H$, can be explored as probes to the top quark Yukawa coupling. One such process, which is directly dependent on the top quark Yukawa coupling, just like $t\bar{t}H$, is tH production. It has the unique feature of being sensitive to the relative sign of the coupling with respect to the HWW coupling, due to destructive interference between production diagrams with a top-Higgs vertex and those with a W-Higgs vertex. Interfering diagrams are depicted in Figure 2.6a [81]. This process is flavour-violating and thus much less likely to occur than $t\bar{t}H$, with a cross-section of merely 77.1 fb at $\sqrt{s} = 13\,\text{TeV}$ [59]. The CMS collaboration searched for tH production and measured the ratio between the top quark Yukawa coupling and its SM prediction [83]. The result was the exclusion with a 95% CL of values outside the intervals $[-0.9, -0.5]$ and $[1.0, 2.1]$. The interference between diagrams is nearly maximally destructive in the SM scenario, such that in the presence of a $\mathcal{CP}$-odd coupling, the tH production cross-section can be significantly enhanced. This behaviour, which is just the opposite from $t\bar{t}H$, can be exploited by analyses sensitive to both processes to improve the constraint on the $\mathcal{CP}$-

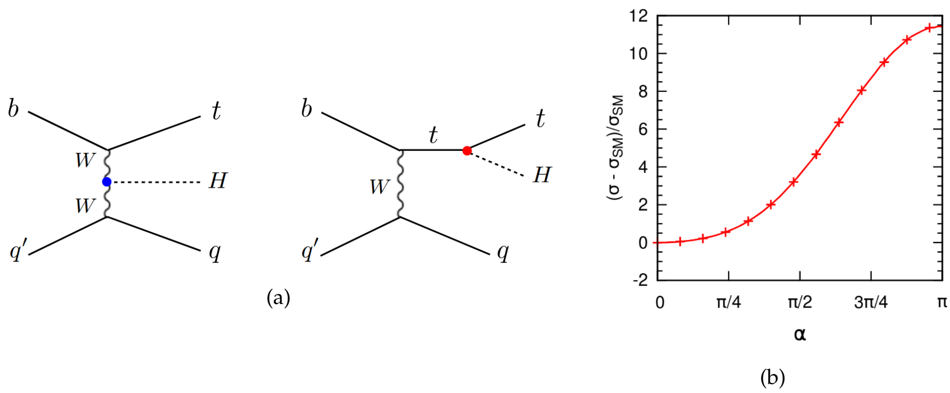

Figure 2.6: (a) Diagrams which interfere destructively in $tH/\bar{t}H$ production, with the WH vertex in blue and the top quark Yukawa vertex in red [81]. (b) Expected enhancement of the $tH/\bar{t}H$ production cross-section as a function of α in the 14 TeV LHC [82].

odd contribution. The expected cross-section enhancement at 14 TeV as a function of α is depicted in Figure 2.6 [82]. Asymmetries sensitive to the top quark polarisation in tH have shown potential for measuring α [82]. Combining the $H \to b\bar{b}$ and $H \to \gamma\gamma$ channels, such a method can be used to exclude $\alpha > \pi/4$ at the 2σ level using $3\,\mathrm{ab}^{-1}$ of data from the LHC.

The large top quark Yukawa coupling ensures that the dominant Higgs production channel at the LHC, ggF, gets its main SM contribution from top quark loops. However, because it is loop-induced, this process cannot be used to measure the top quark Yukawa coupling directly. Any measurement in that process is indirect, in the sense that it requires some assumptions about relative contributions to the loop, not only from SM sources, but also from possible BSM ones. Examples of such measurements are the results in the κ framework of Refs. [63] and [64], in which κ_g is written in terms of other κ_j. Measurements of this process, as well as other Higgs boson production and decay modes at the LHC, also provide indirect constraints on the $\mathcal{CP}$ nature of the top quark Yukawa coupling. In Ref. [72], the authors combine the allowed intervals of Higgs boson signal strengths and decay rates reported by ATLAS and CMS after the full LHC Run 1, as well as those obtained by the Tevatron experiments.

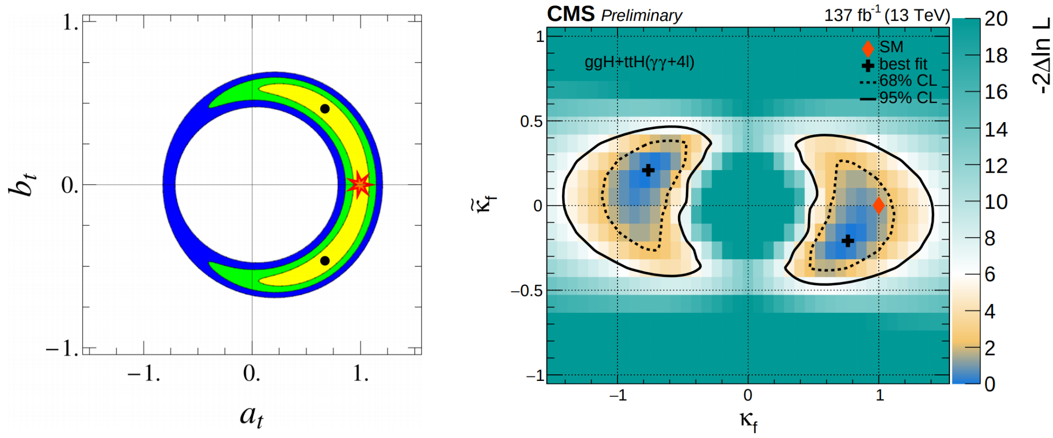

(a) (b)

Figure 2.7: (a) Allowed scenarios in the $(\kappa_t, \tilde{\kappa}_t)$ plane – labelled (a_t, b_t) – obtained from a fit to LHC Run 1 and Tevatron Higgs production and decay rate results [72]. The black points indicate best-fit scenarios, the star is the SM scenario, and the yellow, green and blue areas are the allowed regions with a 68%, 95% and 99.7% CL, respectively. (b) κ_t and $\tilde{\kappa}_t$ measured by CMS, from the combination of ggF production (with $H \to 4\ell$) and $t\bar{t}H$ $(\gamma\gamma)$ $\mathcal{CP}$ measurements, using the full Run 2 dataset [71].

The effective Higgs couplings to gluons and photons are modified by factors expressed in terms of κ_t and $\tilde{\kappa}_t$, assuming no BSM particles in the loop. Fixing all the other couplings to be SM-like, κ_t and $\tilde{\kappa}_t$ are fitted simultaneously. The result is summarised in Figure 2.7a, where it can be seen that a wide range of values for $\tilde{\kappa}_t$ is still allowed. Although this fit includes $t\bar{t}H$ signal strength measurements, it is dominated by the measurements of ggF production signal strength and $H \to \gamma\gamma$ decay rate. The CMS collaboration used $H \to 4\ell$ events, mostly from ggF production, to indirectly constrain the $\mathcal{CP}$ properties of the top quark Yukawa coupling, assuming the SM loop structure in the production [71]. The full Run 2 dataset was used and sensitivity was greatly enhanced by combining this measurement with the direct measurement made in $t\bar{t}H$ $(H \to \gamma\gamma)$ $\mathcal{CP}$ analysis from Ref. [77]. Figure 2.7b shows the results in the $(\kappa_t,\tilde{\kappa}_t)$ plane. Higgs production via ggF has also been studied by the ATLAS collaboration with the purpose of constraining the $\mathcal{CP}$ of the top quark Yukawa coupling [84]. The analysis focused on the WW final state, using kinematic distributions of additional jets in the event as discriminant

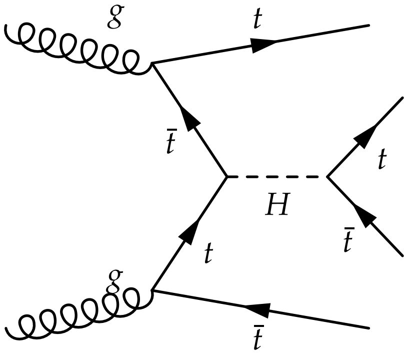

(a)

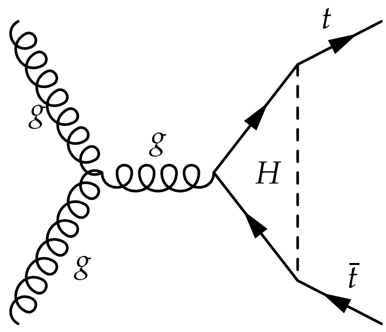

(b)

Figure 2.8: Processes at the LHC, besides Higgs boson production processes, that are sensitive to the top quark Yukawa coupling. Examples of Feynman diagrams in which the Yukawa coupling is relevant are shown. (a) $t\bar{t}t\bar{t}$ production. (b) $t\bar{t}$ production.

observables. Analysing 36.1 fb^{-1} of Run 2 data, and using both rate and shape information to constrain the mixing angle, the observed $\tan\alpha$ was $0.0 \pm 0.4_{\text{(stat.)}} \pm 0.3_{\text{(syst.)}}$.

Sensitivity to the top-Higgs interaction is also provided by the extremely energetic process of four top quark ($t\bar{t}t\bar{t}$) production. Among the Feynman diagrams contributing to the process, some involve a Higgs boson propagator between top quark lines, as can be seen in Figure 2.8a. The amplitude of such diagrams depends quadratically on the coupling (whereas in $t\bar{t}H$ production they are proportional), providing extra sensitivity to large deviations from the SM. The ATLAS collaboration found evidence for $t\bar{t}t\bar{t}$ production at the LHC, by analysing multilepton final states in the full Run 2 dataset [85]. The measured cross-section was 24^{+7}_{-6} fb, corresponding to an exclusion significance of the background-only hypothesis of 4.3 standard deviations. The CMS collaboration also searched for this process and interpreted the results in terms of the top quark Yukawa coupling [86]. No evidence for signal was found and upper limits were set with a 95% CL: 22.5 fb for the cross-section and 1.7 for the absolute value of the ratio between the Yukawa coupling and its expectation in the SM. Production of $t\bar{t}t\bar{t}$ is also affected by the $\mathcal{CP}$ nature of the top quark Yukawa coupling. The rising of the cross-section as a function of the Yukawa coupling is much faster for the $\mathcal{CP}$-odd component than for the $\mathcal{CP}$-even component [87]. Using that cross-section dependence, the CMS upper limit on the cross-section can be naively interpreted as an upper limit on $\tilde{\kappa}_t$ of 0.96.

Production of $t\bar{t}$ pairs, a relatively common process at the LHC, also allows studies of the top quark Yukawa coupling. The exchange of virtual Higgs bosons between the produced top quarks is governed by that coupling, as shown in the Feynman diagram of Figure 2.8b. The presence of these interactions has observable effects on kinematics of the top quarks and their decay products. CMS measured a coupling strength (ratio to the SM prediction) by searching for those effects in the dilepton final state. The obtained result was $1.16^{+0.24}_{-0.35}$ with a 68% CL, and the interval $[0, 1.62]$ with a 95% CL [88].

Chapter 3

$\mathcal{CP}$-odd $t\bar{t}H$ production

As discussed in Section 2.3.1, production of $t\bar{t}H$ is the preferred direct probe to the top quark Yukawa coupling at the LHC. This chapter presents a summary of the observable effects in this process when in the presence of a $\mathcal{CP}$-odd component in the coupling, and an attempt is made at providing physics arguments that motivate their use. Section 3.1 provides theoretical considerations about the different diagrams contributing to $t\bar{t}H$ production that lead to expected differences in kinematics between the $\mathcal{CP}$ scenarios. Candidate $t\bar{t}H$ observables to be used in analyses of the top-Higgs coupling $\mathcal{CP}$ structure are presented in Section 3.2. Finally, Section 3.3 shows a projection of future sensitivity to this $\mathcal{CP}$ structure using only the $H \to b\bar{b}$ analyses.

3.1 Diagram contributions

In quark(qq)-initiated production at the LHC, the impact of the $\mathcal{CP}$ nature of the Higgs boson in the kinematics of $t\bar{t}H$ production can be understood from an argument of conservation of angular momentum and parity. This argument has been made for the very similar process of $t\bar{t}H$ production at e^+e^- colliders [89]. The diagram for qq-initiated production is represented in Figure 3.1a. In this process, the intrinsic parity of the initial state is $(+1) \times (-1) = -1$. The intrinsic parity of the final state is -1 or $+1$, depending on the Higgs boson being a scalar or pseudoscalar, respectively. If parity conservation is imposed, any change in intrinsic parity must be accompanied by a change in extrinsic parity, which is realised by an odd transition in orbital angular momentum. Very close to the production energy threshold, this implies that the $t\bar{t}H$ system will have orbital angular momentum 0 and 1, in the scalar and pseudoscalar scenarios, respectively. The result is that, for a pseudoscalar, the cross-section rises more softly with the deviation from threshold.

At the LHC, qq-initiated production is less important than gluon(gg)-initiated production, which includes a gluon-mediated s-channel and a top-mediated t-channel. All leading-order diagrams for $t\bar{t}H$ production

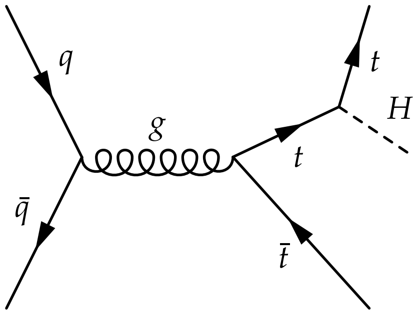

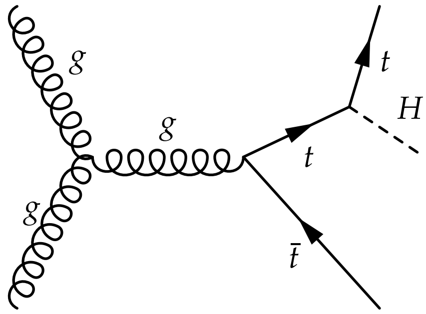

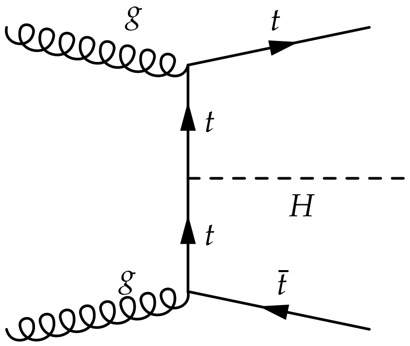

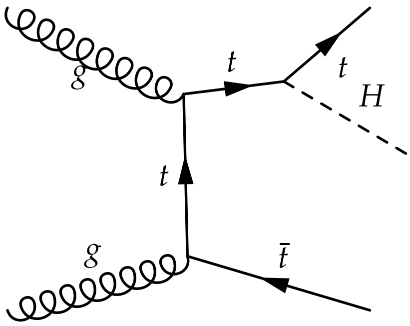

Figure 3.1: Leading order diagrams for $t\bar{t}H$ production at the LHC. All possible diagrams can be obtained from particle/anti-particle exchanges and the exchange of gluon lines in the t-channel. (a) qq-initiated production. (b) gg-initiated s-channel production. (c) t-channel production, with the Higgs boson being radiated off by the top quark exchanged in the t-channel (internal). (d) t-channel production, with the Higgs boson being radiated off by the external top quark (external)

at the LHC are represented in Figure 3.1, considering implicitly those obtained from exchanging particles for anti-particles and exchanging the gluon lines in the t-channel. Interestingly, the gluon-initiated s-channel displays the same kind of suppression close to threshold as the quark-initiated production, while the gluon-initiated t-channel does not [72]. Within t-channel diagrams, a relevant distinction can be made between those in which the Higgs is radiated off by the top exchanged in the t-channel (Figure 3.1c) and those in which it is radiated off by one of the "external" top quark lines (Figure 3.1d). Those will be referred to as in-

Table 3.1: Relative contributions of the different diagrams to the $t\bar{t}H$ production cross-section, in the $\mathcal{CP}$-even and $\mathcal{CP}$-odd scenarios. Cross-sections were computed at leading order, using MadGraph5_aMC@NLO [90] with the HC UFO model [91, 92], for the 13 TeV LHC. The results among the interfering gg diagrams should only be taken qualitatively: they are affected in unknown proportion by the interference terms and may not be gauge invariant.

	Contribution to $\sigma_{t\bar{t}H}$ (%)	
Diagram	$\mathcal{CP}$-even	$\mathcal{CP}$-odd
qq	29	9
gg s-channel	4	1
gg t-channel internal	18	67
gg t-channel external	49	23

ternal and external, respectively. An indication of the relative importance of each diagram to the total cross-section can be obtained from a calculation at leading order (LO), using MadGraph5_aMC@NLO [90] with the Higgs Characterisation (HC) UFO model [91, 92]. The extent to which the quantitative results among gg diagrams can be interpreted is limited: the distribution of the interference terms across the resulting fractions is not known and the fractions themselves are not guaranteed to be gauge invariant. The results of such a calculation are shown in Table 3.1. The suppression of s-channel production near threshold has a large impact on the overall contribution of s-channel production, which drops from 33% in the $\mathcal{CP}$-even scenario to 10% in the $\mathcal{CP}$-odd scenario. Besides that, the two scenarios also display very different relative contributions of the t-channel internal and external components. In case of a $\mathcal{CP}$-odd coupling, t-channel production is dominated by internal diagrams. This is in opposition to the $\mathcal{CP}$-even scenario, in which external diagrams dominate.

How the fractions in Table 3.1 are related to the differences in kinematics between $\mathcal{CP}$-even and $\mathcal{CP}$-odd $t\bar{t}H$ prodution can be partially understood by examining the amplitudes of each of these diagrams, published in Ref [93]. Let s be the squared centre-of-mass energy, g_1 and g_2 the four-momenta of the initial gluons, and k, $\bar{k}$ and h the final state four-momenta of t, $\bar{t}$ and H, respectively. The amplitudes are found to have the following dependences:

$$M_{s\text{-channel}} \propto \frac{1}{s}\frac{1}{2h \cdot k + m_H^2} + [k \leftrightarrow \bar{k}] \tag{3.1}$$

$$M^{\text{internal}}_{t\text{-channel}} \propto \frac{1}{k \cdot g_1}\frac{1}{\bar{k} \cdot g_2} + [g_1 \leftrightarrow g_2] \tag{3.2}$$

$$M^{\text{external}}_{t\text{-channel}} \propto \frac{1}{2h \cdot k + m_H^2}\frac{1}{\bar{k} \cdot g_2} + [k \leftrightarrow \bar{k}, g_1 \leftrightarrow g_2]. \tag{3.3}$$

The terms inside square brackets are used to abbreviate additional terms, obtained from exchanging the indicated momenta in the given expressions. The inner product of two four-momenta is minimised when the space components are parallel. It follows that s-channel production is enhanced when one of the final-state top quarks travels with a small angle with respect to the Higgs boson. On the other hand, t-channel production favours having at least one of the top quarks travelling close to the beam axis. In the case of the internal diagram, production is enhanced when both top quarks travel close to the beam axis, in opposite directions. In the external diagram, the preference is for one of the top quarks to travel close to the beam axis, and the other close to the Higgs boson. Bringing this together with the information from Table 3.1, some features can be expected in the kinematics of $\mathcal{CP}$-odd $t\bar{t}H$ production with respect to the $\mathcal{CP}$-even case: higher relative importance of the internal t-channel enhances the production of top quark pairs travelling closer to the beam axis in opposite directions, and suppression of s-channel production close to the energy threshold results in a higher fraction of events in which the final state particles have high momentum. In the transverse plane, this higher momentum is expected to be most evident for the Higgs boson, as the top quarks travel closer to the beam axis. The expectations drawn from the arguments presented above are confirmed by differential distributions obtained from calculations and event generation. Numerous studies have put forward proposals for observables that could be used in a measurement of the top-Higgs coupling $\mathcal{CP}$ in $t\bar{t}H$ production. Choosing observables from the different studies based on their potential for experimental use is not always possible, since the studies consider varying levels of experimental realism when drawing their conclusions. The discussion for the rest of this chapter is rather guided by the primary concern of representing the various motivations and techniques for building the observables.

3.2 Observable effects

3.2.1 Inclusive cross-section

The decrease in production cross-section is the most immediately recognisable effect of a non-zero α in the coupling, assuming that κ_t' is fixed. Figure 3.2a shows the relative cross-section dependence with $|\alpha|$, for the $H \to \gamma\gamma$ and $H \to b\bar{b}$ final states and for several pp centre-of-mass energies [94]. For computing the $H \to \gamma\gamma$ decay rate, the Higgs coupling to the W is assumed to be proportional to κ_t. Assuming κ_t' fixed to 1, a $t\bar{t}H$ cross-section measurement at the SM value with 20% uncertainty at 14 TeV would imply the constraint $|\alpha| < \pi/6$ [81]. Measuring the total production cross-section is obviously not enough to constrain two parameters of the coupling at the same time. It is only useful to constrain α assuming a fixed value of κ_t', which merely consists of reinterpreting a signal strength measurement, rather than probing any structure in the coupling. Instead, two parameters can be constrained simultaneously by exploiting asymmetries or distribution shapes of observables in $t\bar{t}H$ production that are sensitive to the relative $\mathcal{CP}$-even and $\mathcal{CP}$-odd contributions. The cross-section of $t\bar{t}H$ production contains terms proportional to $\kappa_t^2 + \tilde{\kappa}_t^2$ and terms proportional to $\kappa_t^2 - \tilde{\kappa}_t^2$ [95]. Separately enhancing sensitivity to the two kinds of terms allows a measurement of the sizes of κ_t and $\tilde{\kappa}_t$.

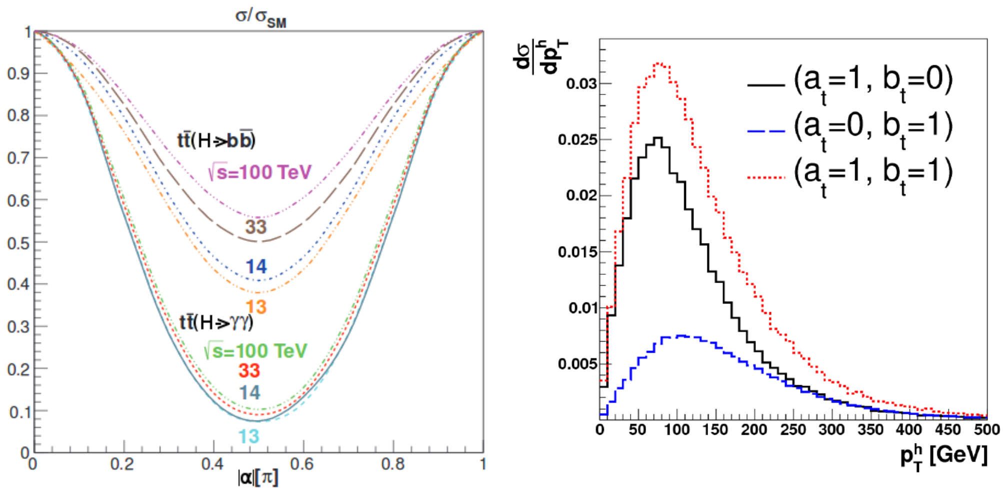

(a)

(b)

Figure 3.2: (a) $t\bar{t}H$ production cross-section relative to the SM as a function of $|\alpha|$, for the $H \to \gamma\gamma$ and $H \to b\bar{b}$ final states and for several pp centre-of-mass energies [94]. For the $H \to \gamma\gamma$ decay, the Higgs coupling to the W is assumed to be proportional to κ_t. (b) Distributions of Higgs boson p_T revealing differences of behaviour near threshold in $t\bar{t}H$ production at the 14 TeV LHC, for the $\mathcal{CP}$-even ($a_t = 1, b_t = 0$), $\mathcal{CP}$-odd ($a_t = 0, b_t = 1$) and maximally $\mathcal{CP}$-mixed ($a_t = 1, b_t = 1$) scenarios [72]. The parameters a_t and b_t correspond exactly to κ_t and $\tilde{\kappa}_t$, defined previously in the text.

3.2.2 Suppression near threshold

Different behaviours near threshold are captured in the distribution of $m_{t\bar{t}H}$, which is the invariant mass of the $t\bar{t}H$ system [72, 81]. Because it may not always be possible to correctly reconstruct the full system in experiment, an alternative to probe this behaviour is the Higgs boson p_T [72, 96]. The distribution of the Higgs boson p_T in $t\bar{t}H$ production at the 14 TeV LHC is shown in Figure 3.2b, where the $\mathcal{CP}$-even and $\mathcal{CP}$-odd scenarios can be compared (as well as a mixed scenario) [72]. Suppression near threshold is evident in the much slower rise of the distribution for the $\mathcal{CP}$-odd case. Remarkably, the distributions become nearly indistinguishable for a Higgs boson p_T above 200 GeV. Because the Higgs boson recoils against the $t\bar{t}$ system in the transverse plane, it is expected that a higher p_T of the Higgs boson is correlated with a smaller azimuthal angular difference between the top quarks. Indeed, this azimuthal angle difference, called $\Delta\phi(t, \bar{t})$ has also been proposed as a $\mathcal{CP}$-discriminating observable [72]. This correspondence between a feature in a p_T distribution and a feature in an angle could be advantageous, since angular quantities are less affected by the experimental uncertainties in the energy of jets.

3.2.3 Top quark polar separation

Regarding the enhanced separation between the top quarks in polar angle (measured with respect to the conventionally positive side of the beam axis) in $\mathcal{CP}$-odd production, it is exploited by the observable $\Delta\eta_{t\bar{t}}$, the absolute pseudorapidity difference between the top quarks [96] [1]. Figure 3.3a shows normalised distributions of this observable, for $\mathcal{CP}$-even, $\mathcal{CP}$-odd and $\mathcal{CP}$-mixed scenarios at the 13 TeV LHC [96]. In the dileptonic final state of $t\bar{t}$, the presence of two neutrinos makes it difficult to reconstruct the top quarks, and alternatives that do not require reconstruction, such as $\Delta\eta_{\ell\ell}$ (absolute pseudorapidity difference between leptons), may also be explored. An asymmetry built from $\Delta\eta_{\ell\ell}$ could be useful, around a value close to 1.5 that maximises sensitivity to the $\mathcal{CP}$ nature of the coupling [97].

Several products of top quark momentum projections have been suggested as observables for separating $\mathcal{CP}$-even and $\mathcal{CP}$-odd $t\bar{t}H$ production [95]. The ones found to be most discriminant are defined as:

$$b_2 = \frac{\vec{p}_{Tt} \cdot \vec{p}_{T\bar{t}}}{p_t p_{\bar{t}}}, \tag{3.4}$$

$$b_4 = \frac{p_t^z p_{\bar{t}}^z}{p_t p_{\bar{t}}}. \tag{3.5}$$

Both observables are able to capture the effect of enhanced polar separation between the top quarks. For top quarks with a larger longitudinal

[1]Pseudorapidity, denoted by η, is defined as $-\ln(\tan(\theta/2))$, where θ is the polar angle. A central direction corresponds to η close to 0, while a very forward (backward) direction corresponds to large positive (negative) η. In the massless or ultra-relativistic limit, the pseudorapidity difference of two particles, denoted $\Delta\eta$, is invariant under boosts of the two-particle system along the beam axis.

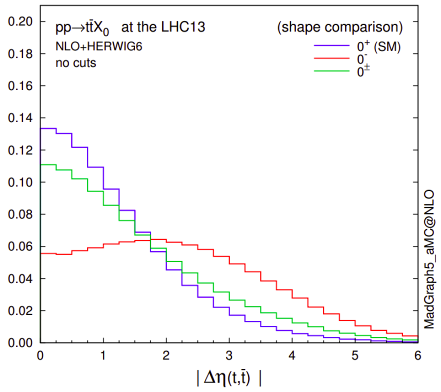

(a)

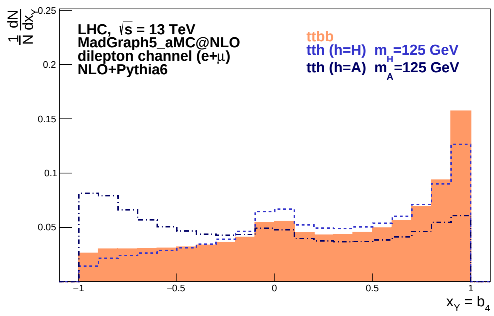

(b)

Figure 3.3: Enhanced top quark polar separation in $\mathcal{CP}$-odd production. (a) Normalised distributions of $\Delta\eta$ between the top quarks in $t\bar{t}H$ production at the 13 TeV LHC, for the $\mathcal{CP}$-even (0^+), $\mathcal{CP}$-odd (0^-) and maximally $\mathcal{CP}$-mixed ($0^\pm$) scenarios [96]. (b) Normalised distributions of b_4, for $t\bar{t}H$ ($H \to b\bar{b}$) and $t\bar{t} + b\bar{b}$ events, in the $t\bar{t} \to$ dilepton channel [9]. The $t\bar{t}A$ scenario means pure $\mathcal{CP}$-odd production.

component of momentum, the magnitude of b_2 is smaller, while that of b_4 is larger. Furthermore, the sign of b_4 is negative whenever those longitudinal components have opposite signs, and is positive otherwise. The sign of b_2, on the other hand, depends on whether $\Delta\phi(t,\bar{t})$ is above or below $\pi/2$. Due to this dependence, b_2 is not only sensitive to the effect of enhanced top quark polar separation, but also to the suppression of production near threshold.

Normalised distributions of b_4 are shown in Figure 3.3b, for $\mathcal{CP}$-even and $\mathcal{CP}$-odd $t\bar{t}H$ production at the 13 TeV LHC, as well as for the $t\bar{t} + b\bar{b}$ process, which is the dominant background in the $H \to b\bar{b}$ final state [9]. In this final state, the average of the b_4 distribution was found to provide enough discrimination to expect evidence of an $\alpha = 0.3\pi$ scenario already with 300 fb^{-1} of LHC data, considering only the semileptonic channel [94].

3.2.4 Role of the $t\bar{t}H$ rest frame

In pp collisions at the LHC, only a constituent from each proton (a quark or a gluon) participates in the initial state of the high-energy process, carrying a fraction of the longitudinal momentum of the proton. Thus, the longitudinal momentum of the initial state in pp collisions varies widely. Distributions of final state kinematic features evaluated in the lab reference frame carry an implicit integration over all possible values of this initial longitudinal momentum. This may dilute effects such as the ones discussed so far about the production kinematics of $t\bar{t}H$ in the different $\mathcal{CP}$ scenarios. One possible way to avoid this loss of information is to evaluate the relevant quantities in the $t\bar{t}H$ rest frame. Doing so makes the observables also more robust with respect to additional high-p_T radiation, which would degrade the same features were they to be measured in the lab frame.

In Ref. [3], the possibility of using observables evaluated in the $t\bar{t}H$ rest frame for determining the $\mathcal{CP}$ nature of the top quark Yukawa coupling was studied. Samples for $\mathcal{CP}$-even and $\mathcal{CP}$-odd $t\bar{t}H$ (both with $\kappa_t' = 1$), as well as for $t\bar{t} + b\bar{b}$ production, were generated at NLO accuracy with MadGraph5_aMC@NLO, using the HC UFO model for the $t\bar{t}H$ processes. Distributions with NLO accuracy including parton shower (PS) effects were obtained by retrieving the four-momenta of top quarks, H, and b quarks (for $t\bar{t} + b\bar{b}$) from the step in the MC event history after the PS, but before the decay/hadronisation of the respective particle.

In Figure 3.4, angular separations between the Higgs boson and the top quarks, in the $t\bar{t}H$ rest frame, are represented in two-dimensional distributions. The x axis corresponds to the angle between the Higgs boson and the near top quark – t or $\bar{t}$, the one whose direction makes the smallest angle with that of the Higgs boson in the $t\bar{t}H$ rest frame. The y axis corresponds to π minus the angle between the Higgs boson and the far top quark. As expected from the discussion about the LO $t\bar{t}H$ production diagrams, in the case of $\mathcal{CP}$-even production, the Higgs boson tends to be produced very close to one of the top quarks and almost back-to-back to the other one. For the $\mathcal{CP}$-odd signal, the Higgs boson is found to have a wider distribution of angular distances with respect to both top quarks. The observation of these clear differences when the angles are evaluated in the $t\bar{t}H$ rest frame motivated the search for other

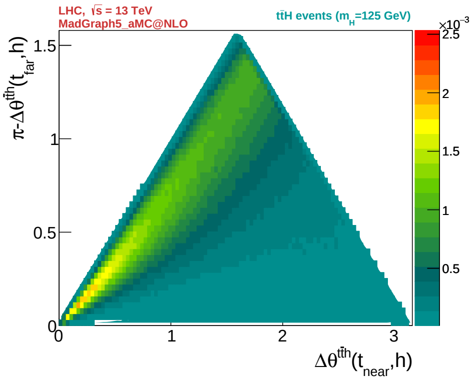

(a)

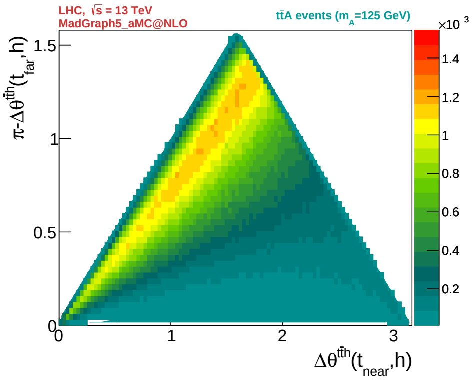

(b)

Figure 3.4: Normalised two-dimensional distributions at NLO including shower effects, of the angle between the Higgs boson and the near top quark (x-axis) and the angle between the Higgs boson and the far top quark (y-axis), both measured in the $t\bar{t}H$ rest frame. (a) $\mathcal{CP}$-even $t\bar{t}H$. (b) $\mathcal{CP}$-odd $t\bar{t}H$ (labelled $t\bar{t}A$).

distributions in which the boost to the $t\bar{t}H$ rest frame were beneficial to the determination of the $\mathcal{CP}$ nature of the top quark Yukawa coupling.

All observables from Ref. [95] were studied in the $t\bar{t}H$ rest frame. The $\mathcal{CP}$ discrimination provided by the distributions of b_2, and to a smaller extent b_4, is enhanced with respect to the lab frame versions. Figure 3.5 shows distributions of b_2 at NLO with PS effects, without any selection cuts, in the laboratory and $t\bar{t}H$ frames, for $\mathcal{CP}$-even and $\mathcal{CP}$-odd $t\bar{t}H$ scenarios, as well as for the dominant background $t\bar{t}+b\bar{b}$.

The dileptonic final state of $t\bar{t}$, with H decaying to $b\bar{b}$, was considered to study the sensitivity of the observables defined in the $t\bar{t}H$ rest frame. An analysis was implemented, where event generation, simulation and kinematic reconstruction were performed for the conditions of LHC Run 2 pp collisions ($\sqrt{s}=13$ TeV). This analysis chain had previously been discussed in detail in Ref. [9]. In addition to the signal and $t\bar{t}+b\bar{b}$ samples presented above, backgrounds from $t\bar{t}+$jets (with up to 3 additional non-b jets), $t\bar{t}V$, single top quark, diboson (WW, WZ, ZZ), $W+$jets and $Z+$jets, were generated at LO accuracy in QCD with MadGraph5_aMC@NLO. The Delphes [8] program was used for a fast simulation of a general-purpose collider experiment, using the default

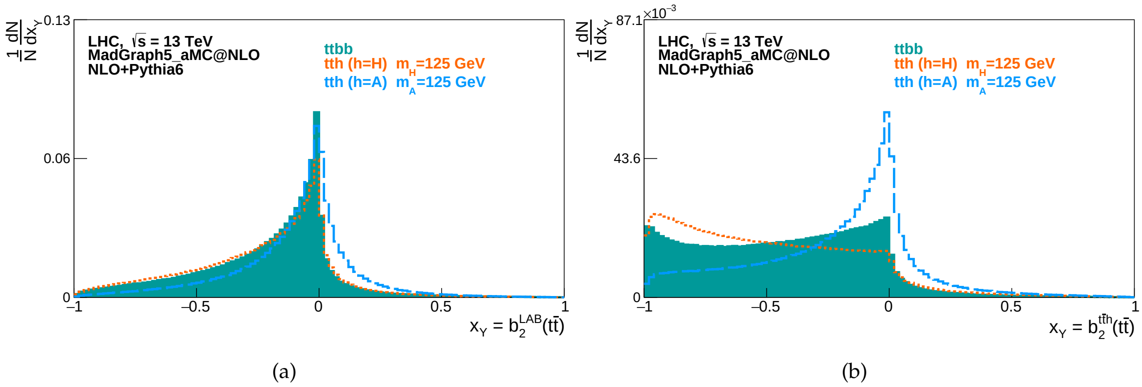

Figure 3.5: Normalised b_2 distributions at NLO including PS effects. The $t\bar{t}+b\bar{b}$ dominant background (shaded area), the $\mathcal{CP}$-even (dashed) and the $\mathcal{CP}$-odd (dotted, labelled $t\bar{t}A$) signals, are shown. (a) Lab reference frame. (b) $t\bar{t}H$ rest frame.

ATLAS parameter card. Observables boosted to the $t\bar{t}H$ rest frame require the full four-momenta reconstruction of the top quarks and Higgs boson. The reconstruction applied assumes that the total missing energy originates from the undetected neutrinos and uses a BDT to choose the most likely assignment between jets and partons. Events were selected with at least four jets, of which at least three must be b-tagged. Following the event selection and kinematic reconstruction, the distributions of different $\mathcal{CP}$-sensitive observables were obtained. Figure 3.6a shows the distributions of b_2 evaluated in the $t\bar{t}H$ rest frame. The number of events is scaled to an integrated luminosity of 100 fb^{-1}. The signal distributions are further scaled by a factor 40 for better visibility. Even after detector simulation and kinematic reconstruction, it is still possible to see distinct shape differences between the signals. The binned distributions of different observables were used to define a likelihood ratio between the $\mathcal{CP}$-even and $\mathcal{CP}$-odd hypotheses, considering information from both the shape and rate of the signal process. Only statistical uncertainties are considered for the result. This was used in pseudo-experiments to compute the CL with which the pure $\mathcal{CP}$-odd scenario can be excluded, assuming the true model is the SM. The expected exclusion CL was calculated as a function of the integrated luminosity from 100 fb^{-1} to 3 ab^{-1}, which is the

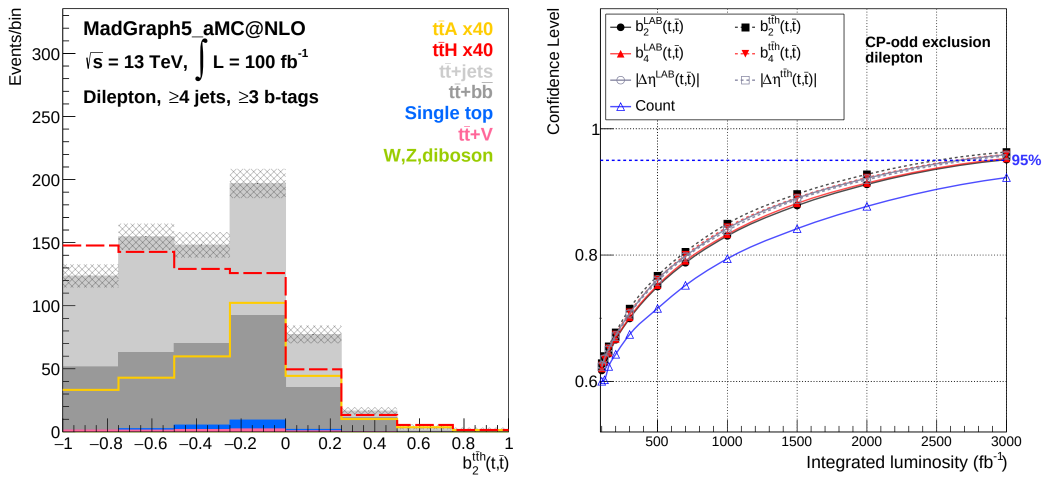

(a) (b)

Figure 3.6: Probing the $\mathcal{CP}$ nature of $t\bar{t}H$ events in the dilepton final state with four jets, three of which b-tagged. (a) Distributions of b_2 in the $t\bar{t}H$ rest frame. The $\mathcal{CP}$-even (red dashed) and $\mathcal{CP}$-odd (yellow solid, labelled $t\bar{t}A$) signals are scaled by a factor 40 for visibility. (b) Expected CLs for the exclusion of the pure $\mathcal{CP}$-odd scenario, given the observation of the SM scenario. Different curves correspond to different observables used for obtaining the used test statistic, including b_2 and b_4 in the lab and $t\bar{t}H$ rest frames. Only statistical uncertainties were considered.

expected integrated luminosity at the end of the High-Luminosity LHC (HL-LHC) programme. Figure 3.6b shows the expected CLs of exclusion of the pure $\mathcal{CP}$-odd scenario, for different observables. There is a visible improvement in sensitivity when the observables are evaluated in the $t\bar{t}H$ rest frame. For instance, b_2 requires roughly 250 fb^{-1} less luminosity to achieve the 90% exclusion CL, when evaluated in the $t\bar{t}H$ rest frame, with respect to the lab frame. The line labelled "Count" corresponds to the expectation from a rate measurement alone.

3.2.5 Spin correlations

As discussed in Section 2.1, the spins of the top and anti-top quarks are correlated in $t\bar{t}$ production at the LHC. This is also the case in $t\bar{t}H$ production and, considering the close relation between parity and an-

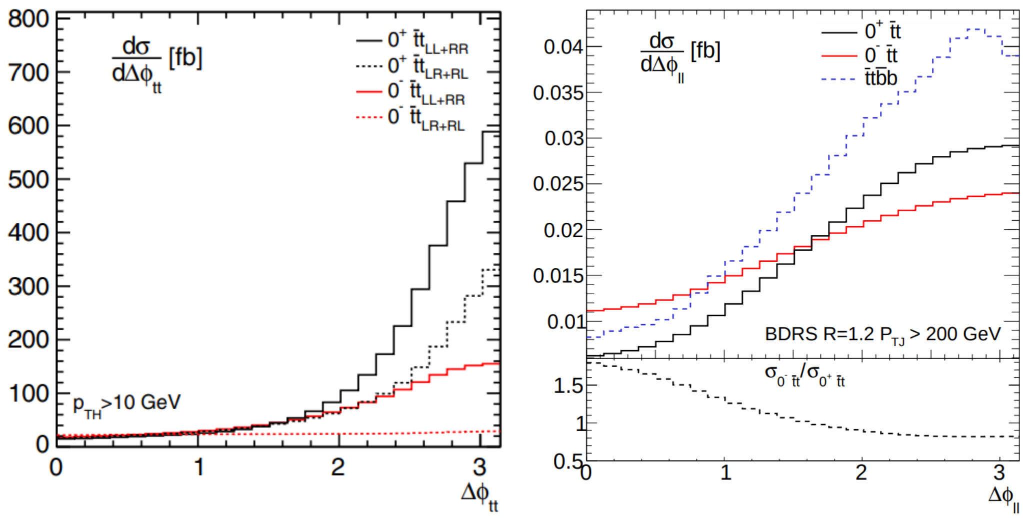

(a) (b)

Figure 3.7: Differential cross-sections sensitive to spin correlations in $t\bar{t}H$ production at the 13 TeV LHC [98]. (a) $\Delta\phi(t,\bar{t})$ for the $\mathcal{CP}$-even (0^+) and $\mathcal{CP}$-odd (0^-) scenarios, separately for like-helicity and opposite-helicity $t\bar{t}$ components. (b) $\Delta\phi(\ell^+,\ell^-)$, for the $\mathcal{CP}$-even and $\mathcal{CP}$-odd scenarios, as well as for $t\bar{t}+b\bar{b}$ production, after requiring $p_T > 200\,\text{GeV}$ for the reconstructed Higgs boson candidate.

gular momentum, it is not surprising that spin correlations are affected by the $\mathcal{CP}$ nature of the top quark Yukawa coupling. Figure 3.7a shows the $\Delta\phi(t,\bar{t})$ distributions for like-helicity and opposite-helicity top quark pairs in $t\bar{t}H$ production, for the $\mathcal{CP}$-even and $\mathcal{CP}$-odd scenarios [98]. The fact that opposite-helicity production is suppressed in the $\mathcal{CP}$-odd case, while it is a large contribution in the $\mathcal{CP}$-even case, proves that the $\mathcal{CP}$ of the coupling plays an important role in spin correlations. Relying on the fact that the top quark spin information is passed to its decay products, angular observables sensitive to spin correlations can be constructed.

In $t\bar{t}$ production, the azimuthal angle difference $\Delta\phi(\ell^+,\ell^-)$ in the dilepton channel is often considered, where the lepton momenta are evaluated in the lab frame. This observable can also be used in $t\bar{t}H$, although the recoil of the Higgs boson against the $t\bar{t}$ system in the transverse plane will have a smearing effect on spin correlations. One possibility to reduce this effect is to restrict the analysis to the high-p_T (boosted) Higgs boson regime [98]. A Higgs boson with $p_T > 200\,\text{GeV}$ decaying to $b\bar{b}$

can be required, using an algorithm that finds a large-radius jet with substructure (namely, two small-radius b-tagged jets). The requirement of the high-p_T Higgs boson enhances the $\mathcal{CP}$ discrimination provided by $\Delta\phi(\ell^+, \ell^-)$ and, as a side effect, increases the signal significance due to reduced backgrounds. Figure 3.7b shows normalised $\Delta\phi(\ell^+, \ell^-)$ distributions in $t\bar{t}H$ production, for the $\mathcal{CP}$-even and $\mathcal{CP}$-odd scenarios, as well as for the dominant background $t\bar{t} + b\bar{b}$, after applying the 200 GeV cut on the Higgs boson p_T [98].

Due to angular momentum conservation in particle decays, evaluating observables in frames other than the lab frame can enhance their sensitivity to spin correlations. The co-sine of the angle $\theta(\ell^+, \ell^-)$, measured between the ℓ^+ direction, in the t rest frame, and the ℓ^- direction, in the $\bar{t}$ rest frame, was proposed as a discriminant between $\mathcal{CP}$-even and $\mathcal{CP}$-odd $t\bar{t}H$ production [99]. The idea of considering directions of particles in the rest frames of other particles (or systems) preceding them in a decay chain is well motivated. Using the helicity formalism, cross-section dependences with the angles between such directions arise from imposing angular momentum conservation in the decays. A generalised form of this principle is applied to $t\bar{t}H$ in Refs. [9, 100]. A large set of angles was scanned in search for the ones for which the $\mathcal{CP}$-even and $\mathcal{CP}$-odd signal distributions were the most separated. The set was built from functions of the form $f(\theta_1)g(\theta_2)$, where the functions f and g are either sine or co-sine and the angles θ_1 and θ_2 are measured between the directions of two systems, each evaluated in the rest frame of a preceding system in the decay chain. For example, one of the observables proposed as a $\mathcal{CP}$ discriminant in the dilepton channel is $\sin(\theta_t^{t\bar{t}H})\sin(\theta_{W^+}^{H})$, where $\theta_t^{t\bar{t}H}$ is the angle between the t direction, evaluated in the $t\bar{t}H$ rest frame, and the direction of the $t\bar{t}H$ system in the lab frame, and $\theta_{W^+}^{H}$ is the angle between the H direction, in the $\bar{t}H$ rest frame, and the direction of W^+ in the H rest frame. Distributions of this particular observable are shown in Figure 3.8a, for $\mathcal{CP}$-even and $\mathcal{CP}$-odd $t\bar{t}H$ production and for the $t\bar{t} + b\bar{b}$ process, at the 13 TeV LHC [9].

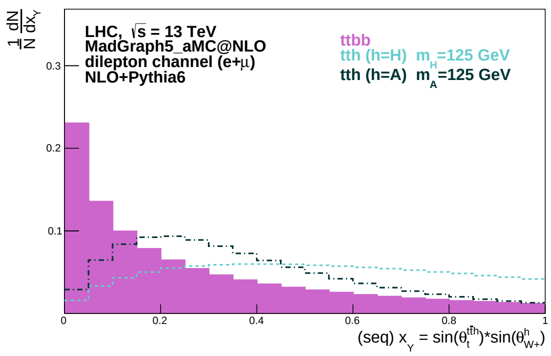

(a)

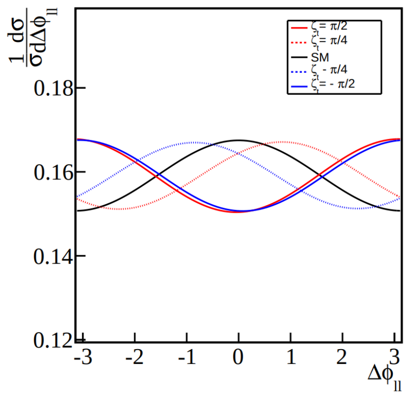

(b)

Figure 3.8: (a) Normalised distributions of $t\bar{t}H$ and $t\bar{t}+b\bar{b}$ events, in the $t\bar{t} \to$ dilepton channel, of $\sin(\theta_t^{t\bar{t}H})\sin(\theta_{W^+}^{H})$ [9]. The $t\bar{t}A$ scenario means pure $\mathcal{CP}$-odd production. b) Normalised distributions of $\theta^{\perp t}(\ell^+,\ell^-)$, multiplied by the sign of the pseudoscalar $\vec{p}_t \cdot (\vec{p_{\ell^-}} \times \vec{p_{\ell^+}})$, for $t\bar{t}H$ production at the 14 TeV LHC [81]. The symbol ζ_t corresponds to α as defined earlier, such that the scenarios considered are $\mathcal{CP}$-even, $\mathcal{CP}$-odd and maximal $\mathcal{CP}$-mixing with positive and negative relative signs of κ_t and $\tilde{\kappa}_t$.

3.2.6 $\mathcal{CP}$-odd observables

All the observables mentioned so far are sensitive to $t\bar{t}H$ cross-section terms with quadratic dependences on κ_t and $\tilde{\kappa}_t$. If both κ_t and $\tilde{\kappa}_t$ were found to be non-zero using those observables, that would already be a sign of $\mathcal{CP}$ violation in the Higgs sector. However, searching for $\mathcal{CP}$ violation in the $t\bar{t}H$ production process itself would also be interesting. That requires the construction of $\mathcal{CP}$-odd observables, sensitive to cross-section terms linear in $\tilde{\kappa}_t$ [72]. An observed non-zero asymmetry or mean value of such an observable would be evidence of $\mathcal{CP}$ violation in the $t\bar{t}H$ production process, and its sign would reveal the relative sign of κ_t and $\tilde{\kappa}_t$. One possibility to build such observables is by using triple products: inner products of a vector and a pseudovector with the same $\mathcal{C}$ parity, which result in $\mathcal{CP}$-odd quantities. An example is $\vec{p}_t \cdot (\vec{p_{\ell^-}} \times \vec{p_{\ell^+}})$, where the momenta are evaluated in the $t\bar{t}$ rest frame [81] . In order to obtain a full angular distribution, defined from $-\pi$ to π, the sign of this triple product is multiplied by the angle $\theta^{\perp t}(\ell^+,\ell^-)$, which means the angle between the leptons in the plane perpendicular to the t direction, all evaluated in the $t\bar{t}$ rest frame. Distributions of the resulting observable are shown in Figure 3.8b for the $t\bar{t}H$ production with different values of α: $0, \pm\pi/4, \pm\pi/2$. The distributions exhibit a smooth oscillation which, in the $\mathcal{CP}$-mixed cases, is phase-shifted with respect to the $\mathcal{CP}$-even case, with the sign of the phase shift depending on the sign of α.

3.3 Future sensitivity in $t\bar{t}H(b\bar{b})$

The analysis of the dilepton final state described in Section 3.2.4 and detailed in Ref. [9] was combined with a similar analysis of the single-lepton channel, detailed in Ref. [100], in order to obtain a projection of their future sensitivity to the $\mathcal{CP}$ nature of the top quark Yukawa coupling [4, 5].

In the single-lepton analysis, events were selected with a number of jets between 6 and 8 and a number of b-tagged jets between 3 and 4. The missing transverse energy was required to be above 20 GeV. Kinematic reconstruction of events was performed with the KLFitter package [101].

Expected CLs were computed for the exclusion of scenarios with a $\mathcal{CP}$-odd component in the coupling, assuming that the SM is the true model. The test statistic was based on binned distributions of various observables, considering both rate and shape of the signal process. Only the statistical uncertainty was considered. Figure 3.9 shows CLs as functions of integrated luminosity, up to $3\,\mathrm{ab}^{-1}$, the maximum expected at the HL-LHC. Figure 3.9a shows CLs for the exclusion of the $\mathcal{CP}$-odd scenario obtained from the combination of three different observables in each channel, and from the combination of the two channels. The observables within each channel were treated as uncorrelated. Figure 3.9b compares the CLs obtained, in the dilepton analysis alone and using $\Delta\eta_{\ell\ell}$ as the discriminant, for the exclusion of scenarios with different $\mathcal{CP}$-odd components, parameterised in terms of $\cos\alpha$. The single-lepton channel is much more sensitive than the dilepton channel, but the combination provides sizeable improvement. Besides, the introduction of systematic

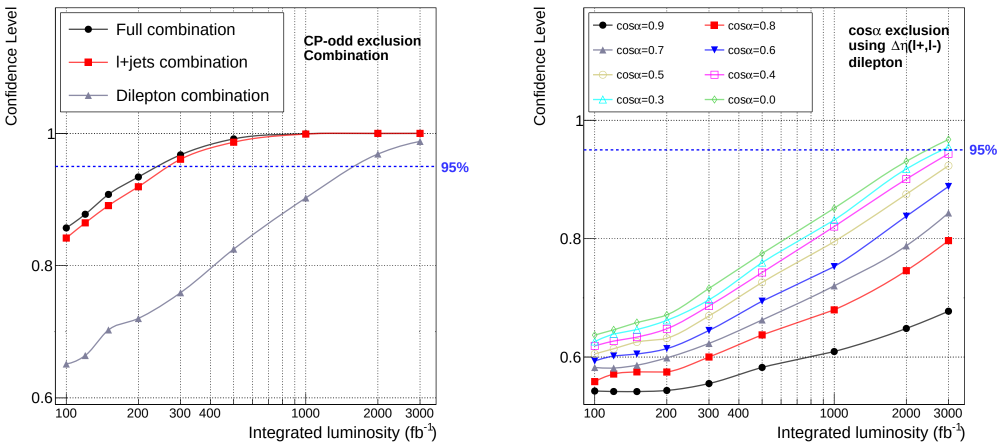

(a) (b)

Figure 3.9: Expected CLs, assuming the SM is the true model, as a function of the integrated luminosity. (a) Exclusion of pure $\mathcal{CP}$-odd scenario combining observables in each individual channel and combining both channels (the observables were treated as uncorrelated). (b) Exclusion of scenarios with different $\cos\alpha$ values, in the dilepton analysis alone, using $\Delta\eta_{\ell\ell}$ as the discriminant observable.

uncertainties is expected to affect more severely the channels with higher statistics, in relative terms, making the contributions to sensitivity more even, and urging the combination effort. The exclusion of a pure $\mathcal{CP}$-odd top quark Yukawa coupling at 95% CL may be within reach with ~ 250 fb^{-1} of LHC data, using only resolved $t\bar{t}(H \to b\bar{b})$ analyses with leptons. Excluding the maximal mixing scenario ($\cos\alpha = \sqrt{2}/2$) is expected to be much harder than excluding the pure $\mathcal{CP}$-odd scenario. For example, for the 80% CL, the required luminosity is roughly 3.5 times more than the one necessary for $\mathcal{CP}$-odd exclusion.

Chapter 4

ATLAS experiment

This chapter describes the experimental setup used to collect the data analysed in the measurements of the remaining chapters. Section 4.1 describes the LHC and Section 4.2 briefly describes the ATLAS detector, its main sub-detectors and the trigger system, with added focus on the jet trigger.

4.1 Large Hadron Collider

The LHC is the largest and highest-energy particle accelerator in the world [56] and is located at CERN, in Geneva, Switzerland. It is housed in a circular underground tunnel with 27 km of circumference, on average about 100 m below ground. This tunnel crosses the French-Swiss border and is the same tunnel where the Large Electron-Positron collider (LEP) operated. The accelerator relies on radiofrequency cavities to accelerate the particles and on superconducting electromagnets to guide them. Dipole magnets curve the particles into their circular trajectory, while quadrupole magnets keep them focused inside the beam pipe. The LHC is the last element of an accelerator chain in which every element plays the role of a pre-accelerator to the next. The beam pipes are kept at an ultra-high vacuum to ensure the beam quality, and operate at a temperature of 1.9 K to enable superconductivity in the magnets. This low temperature is maintained by a distribution system of liquid helium.

Inside the accelerator, two high-energy beams travel in opposite directions, in separate beam pipes. As the beams approach the detectors, they are radially confined and crossed to induce particle collisions in well-defined interaction points. Particles circulating in the LHC beam are packed in bunches along the beam direction. The LHC was designed to collide proton beams with a centre-of-mass energy $\sqrt{s}$ of up to 14 TeV and an instantaneous luminosity of $10^{34}\,\mathrm{cm}^{-2}\mathrm{s}^{-1}$.

The Run 1 of the LHC took place during 2011 and 2012. During this run, the general-purpose experiments ATLAS and CMS collected approximately $5\,\mathrm{fb}^{-1}$ of data at $\sqrt{s} = 7\,\mathrm{TeV}$ and $21\,\mathrm{fb}^{-1}$ at $\sqrt{s} = 8\,\mathrm{TeV}$. Between

February 2013 and March 2015, the LHC went through its first long shutdown period for maintenance and upgrade [102] [103]. A large engineering effort took place in order to strengthen the accelerator, with the main purpose being to consolidate the high-current connections between superconducting magnets. This renovation work made the LHC safer with respect to magnet quenching incidents. After the long shutdown, Run 2 ensued, extending from 2015 to 2018, with proton beams colliding at the unprecedented centre-of-mass energy of 13 TeV. During a large fraction of this period, the LHC reached double its design goal for instantaneous luminosity. The integrated luminosity suitable for physics analysis recorded by ATLAS and CMS from pp collisions over the full Run 2 was approximately 140 fb^{-1} [104, 105].

The high luminosity delivered by the LHC poses a challenge for the experiments. For a given event of interest resulting from a pp collision, the average number of additional inelastic pp interactions occurring in the same bunch crossing is large. Therefore, the response of detectors is not purely a result of the interesting event, but instead of the overlay of that event to the secondary collisions, which are known as pile-up. In Figure 4.1, distributions of the mean number of inelastic pp collisions per bunch crossing are shown, corresponding to the data collected by the ATLAS experiment during the LHC Run 2 [104]. The overall average number of collisions per bunch crossing in data collected during the LHC Run 2 was 33.7, while the corresponding design goal figure was 24. In pp collisions during the LHC Run 2, consecutive bunches crossed at the interaction points with time intervals as short as 25 ns between them. Given this short time interval and considerable restoration times of some sub-detector systems, the detector response to a given event may even be affected by collisions happening in the few previous bunch crossings. This effect is called out-of-time pile-up.

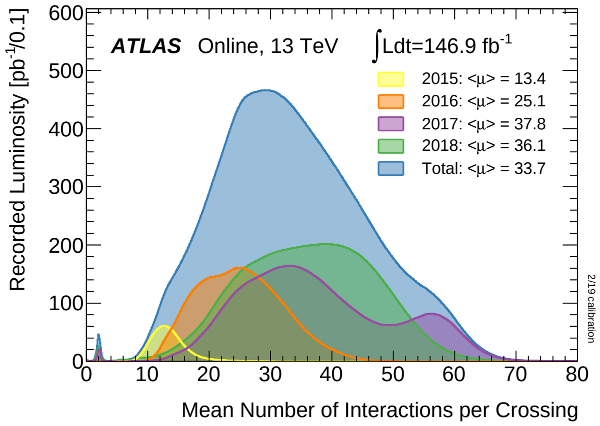

Figure 4.1: Distributions of the mean number of inelastic pp collisions per bunch crossing in data collected by ATLAS during the LHC Run 2, for the whole Run and separately for each year of data taking [104].

4.2 ATLAS detector

ATLAS was designed and built for probing pp and lead ion collisions, being able to perform a wide range of precise measurements and having sensitivity to new physics processes [57, 106]. New phenomena expected to occur at the TeV scale defined the requirements for the detector features.

The search for the SM Higgs boson established the minimum performance requirements for many sub-systems of ATLAS. The decay of the Higgs boson into a photon pair requires good electromagnetic calorimetry. On the other hand, the decay $H \to b\bar{b}$ requires good b-tagging efficiency, only attained with fine vertex reconstruction. In the case of final states with W bosons decaying leptonically, the presence of neutrinos adds the requirement of good reconstruction of missing transverse energy. Other physics goals that determined the ATLAS detector design included the searches for new heavy gauge bosons W' and Z', supersymmetric particles and experimental signatures of the existence of extra dimensions. The large amount of pile-up at the LHC requires mechanisms for resolving the different interaction vertices in a single bunch crossing, necessarily relying on high precision tracking.

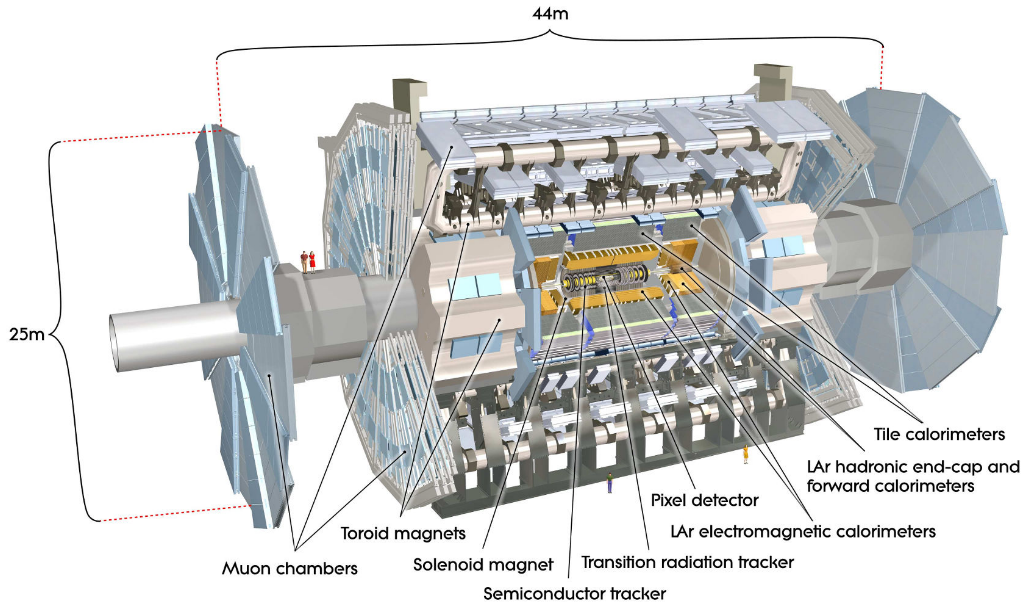

Figure 4.2: Cutaway view of the ATLAS detector [57]. The sub-detectors and main systems are identified, and two persons are visible on the image for scale.

The ATLAS detector is forward-backward symmetric and consists of multiple, approximately cylindrical, coaxial layers, covering the full solid angle. ATLAS is 25 m tall and 44 m long, with a mass close to 7000 tonnes. Its innermost sub-system is the inner detector (ID), which reconstructs tracks of charged particles. Outside the ID, there is the electromagnetic (EM) calorimeter, where photons and electrons are contained. Going outwards, next are the hadronic calorimeters, where hadrons are contained and deposit their energy. The muon-tracking chambers make up the outermost layer of ATLAS, which is immersed in a magnetic field created by toroid magnets. A cutaway view of the ATLAS detector with its sub-detectors exposed is shown in Figure 4.2. The performance goals imposed by the constraints mentioned above are summarised in Table 4.1.

4.2.1 Inner detector

The ID is a tracking system for charged particles that allows momentum measurements and precise reconstruction of interaction vertices.

Table 4.1: General performance goals of the ATLAS detector [57]. Energy (E) and p_T must be in GeV. The symbol $\oplus$ means a sum in quadrature.

Detector component	**Required resolution**	**η coverage**	
		Measurement	**Trigger**
Tracking	$\sigma_{p_T}/p_T = 0.05\%\ p_T \oplus 1\%$	± 2.5	
EM calorimetry	$\sigma_E/E = 10\%/\sqrt{E} \oplus 0.7\%$	$\pm$ 3.2	$\pm$ 2.5
Hadronic calorimetry (jets)			
barrel and end-cap	$\sigma_E/E = 50\%/\sqrt{E} \oplus 3\%$	$\pm$ 3.2	$\pm$ 3.2
forward	$\sigma_E/E = 100\%/\sqrt{E} \oplus 10\%$	$3.1 < \lvert\eta\rvert < 4.9$	$3.1 < \lvert\eta\rvert < 4.9$
Muon spectrometer	$\sigma_{p_T}/p_T = 10\%$ at $p_T = 1\,\mathrm{TeV}$	± 2.7	$\pm$ 2.4

The momentum measurement relies on the curvature of the particle trajectories, which are bent by a magnetic field peaking at 2 T and pointing along the z-axis[1], provided by a solenoid magnet placed immediately outside the ID. The ID is composed of three subcomponents: the pixel detector, the semiconductor tracker (SCT) and the transition radiation tracker (TRT), each with structures covering the barrel region and the end-cap regions. The ID is connected to over 80 million readout channels. Figure 4.3 shows a cutaway view of the ID.

The pixel and SCT along the barrel region are arranged in coaxial cylinders, starting as close as 31 mm from the beam axis. Inserting the innermost pixel layer, called the inner B-layer, was the main improvement made to the ATLAS experiment during the long shutdown after Run 1 [107]. In the end-cap region, pixels and SCT silicon strips are disposed in circular disks, perpendicular to the beam axis. The TRT is based on straw tube detectors with 4 mm in diameter with a gold-plated wire running inside. Each channel provides a drift time measurement, giving a spatial resolution of 170 µm per straw.

[1] ATLAS uses a right-handed reference system with its origin at the nominal interaction point in the centre of the detector and the z-axis along the beam pipe. The x-axis points from the origin to the centre of the LHC ring, and the y-axis points upward. Polar coordinates (r, ϕ) are used in the transverse plane, ϕ being the azimuthal angle around the beam pipe. Distances in (η, ϕ) space are given as $\Delta R = \sqrt{\Delta\phi^2 + \Delta\eta^2}$.

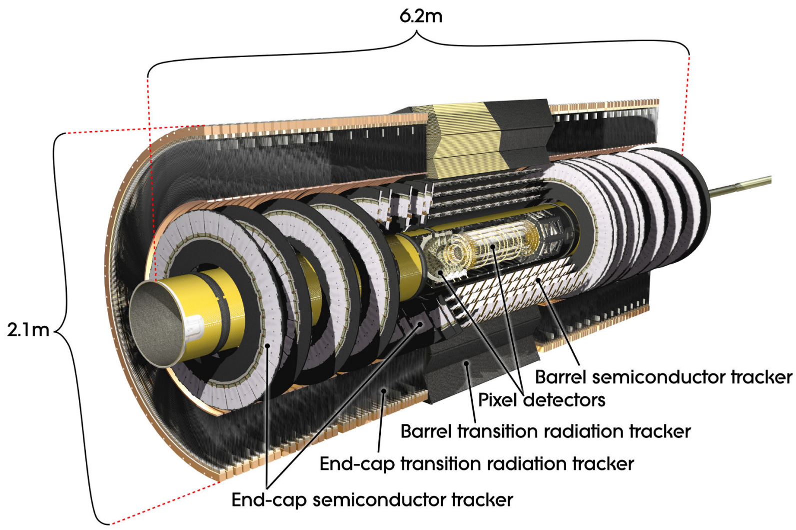

Figure 4.3: Cutaway view of the inner detector, with all of its components labeled [106]. The image portrays the ID before the insertion of the innermost pixel layer, the inner B-layer.

4.2.2 Electromagnetic calorimeter

The electromagnetic calorimeter is the detector layer where most photons and electrons are contained, and in which EM-interacting particles leave energy deposits. This calorimeter is composed of accordion-shaped layers of lead and liquid argon (LAr). The accordion geometry provides complete and symmetric coverage in ϕ, avoiding gaps. It is divided into a barrel part ($|\eta| < 1.475$) and two end-cap parts ($1.375 < |\eta| < 3.2$). In the barrel region, it consists of two half-barrels, where the low temperature for keeping the LAr is provided by the vacuum vessel shared with the central solenoid. In the end-caps, the EM calorimeter is made up from two coaxial wheels, joined at $|\eta| = 2.5$. Figure 4.4 shows a stack of accordion-shaped layers that belong to the barrel EM calorimeter.

The high-density lead plates act as absorber elements. They provide a large effective depth to the calorimeter, ranging between 2 and 4 radiation lengths, depending on η. Particle showers are induced in the absorber element, ensuring the energy dissipation of particles such as electrons

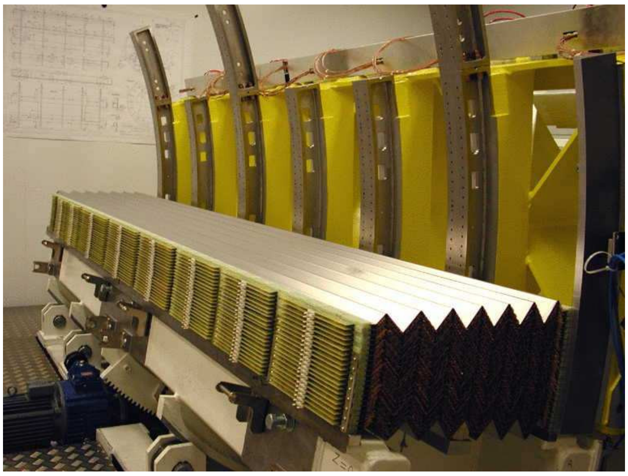

Figure 4.4: Photograph of a partially stacked barrel electromagnetic LAr module, where the accordion geometry is visible [57].

and photons and preventing them from punching through into the outer layers of the detector. As particles in the shower cross the LAr layers – the active element – they ionize the argon. The resulting electrons and ions drift, under the influence of an electric field, towards the electrodes. Only a fraction of the energy of the particles in the shower is deposited in this way. From this sample of deposited energy, the total energy and its spatial distribution are estimated.

4.2.3 Hadronic calorimeter

The hadronic calorimeter is the sub-detector where hadrons leaving the EM calorimeter are contained and deposit their energy, which is then measured through sampling. This calorimeter is composed by the tile calorimeter (TileCal), placed directly outside the EM calorimeter and covering the barrel region, and by two end-cap calorimeters: the LAr hadronic end-cap calorimeter, consisting of two wheels per end-cap, and the LAr forward calorimeter, a high density cylinder which provides both EM and hadronic calorimetry in a region of larger $|\eta|$.

The TileCal is divided in a central barrel and two extended barrels, together covering the range $|\eta| < 1.7$. The barrels are segmented azi-

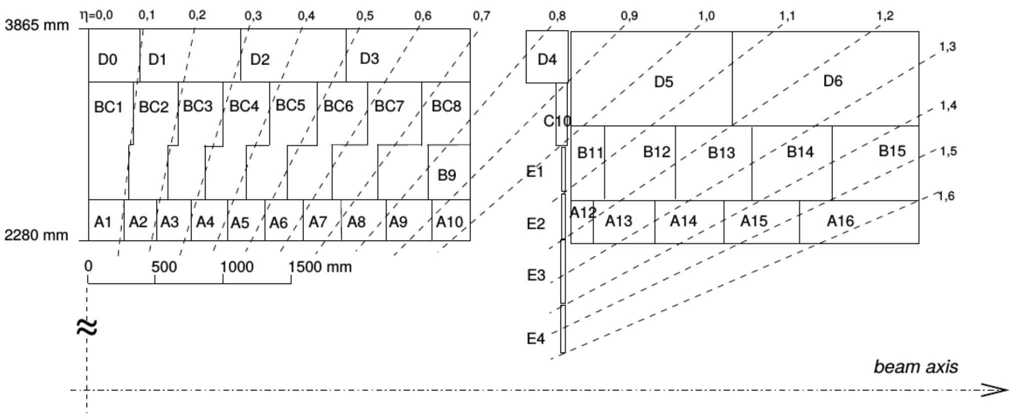

Figure 4.5: Segmentation in depth and η of the TileCal modules in the central (left) and extended (right) barrels [57].

muthally in 64 modules, and range from an inner radius of 2.28 m to an outer radius of 4.25 m. This calorimeter uses steel as the absorber medium and scintillating plastic tiles as the active material. It has a depth of at least 10 interaction lengths across most of its η range. The scintilating tiles emit light as they are crossed by ionising particles. Optical wavelength-shifting fibres at the edges of each tile collect the emmited light and shift the spectrum of the scintillator to match the sensitivity of the photomultiplier tubes (PMT) that generate the readout signal. Figure 4.5 shows the segments in a single module that are mapped to different PMTs. The segments are approximately projective towards the interaction point.

The central barrel and the extended barrels of the TileCal are necessarily separated due to cabling and services to the LAr calorimeter and to the inner detector. Three sets of additional cells are placed in the resulting gap: the Intermediate Tile Calorimeter (ITC) cells (D4 and C10 in Figure 4.5), the gap scintillators (E1 and E2) and the crack scintillators (E3 and E4). They help to compensate for the energy lost in the dead material and improve the uniformity of the calorimeter response to objects crossing the gap. ITC cells are standard TileCal cells covering the $0.8 < |\eta| < 1.0$ range, while gap and crack cells are plain scintillator plates, with respectively 12.7 mm and 6 mm thickness. The gap scintillators cover the surface of the extended barrel not covered by the ITC ($1.0 < |\eta| < 1.2$) and the crack scintillators are placed in front of the LAr end-cap calorimeter, covering the region $1.2 < |\eta| < 1.6$.

The two wheels in each end-cap of the LAr hadronic calorimeter share the same cryostat as the EM end-cap calorimeter and are placed directly behind it. They cover the region with $1.5 < |\eta| < 3.2$ and are composed of parallel copper plates alternated with LAr gaps, providing a depth of 12 interaction lengths. The LAr forward calorimeter is a cylindrical structure placed inside each of the end-cap wheels of the LAr hadronic calorimeter, sharing the same LAr cryostat. It provides coverage in the region with $3.1 < |\eta| < 4.9$ and a depth of 10 interaction lengths.

4.2.4 Muon spectrometer

The ATLAS muon system serves the purpose of tracking and measuring the momentum of muons, as they interact weakly with matter and are not contained by the calorimeters. It is based on a complex arrangement of toroid magnets which deflect the muon trajectories, high-precision tracking chambers and a dedicated muon trigger system.

There are three large air-core toroids in the ATLAS magnet system: the central barrel toroid and two end-cap toroids. Each of the toroids is composed of eight superconducting coils, assembled symmetrically in planes defined by fixed values of ϕ. The field produced in the central region is approximately 0.5 T on average and 3.9 T at its peak. In the end-caps, the field is approximately 1 T on average and 4.1 T at its peak. Figure 4.6 shows the 3D configuration of all the magnet coils in ATLAS.

The precision momentum measurement is performed by monitored drift tube (MDT) chambers, covering the pseudorapidity range $|\eta| < 2.7$. The chambers in the barrel region are placed in three coaxial cylindrical layers around the beam axis. In the two end-cap regions, muon chambers form large wheels, perpendicular to the z-axis and located at distances of up to 21.5 m from the interaction point. In the forward region ($2.0 < |\eta| < 2.7$), cathode-strip chambers (CSC) are used instead of MDT

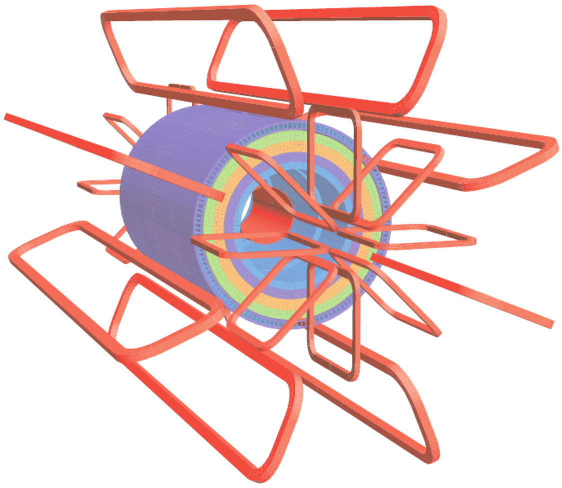

Figure 4.6: Geometry of magnet windings (in red) and TileCal steel. The eight toroidal coils in each end-cap are tilted relative to the barrel coils. The solenoid winding lies inside the calorimeter volume [57].

in the innermost layer, since they can handle higher hit rates and have finer time resolution. A projection of the ATLAS muon system on an axial plane is represented in Figure 4.7.

MDT chambers are composed of layers of drift tubes with an operation similar to the TRT in the inner detector, achieving an average resolution of about 35 μm per chamber. The CSC are multiwire proportional chambers in which cathode planes are segmented into strips running in perpendicular directions.

The precision tracking chambers are complemented by a system of fast trigger chambers. In the barrel region ($|\eta| < 1.05$) this is accomplished with resistive plate chambers (RPC), while in the end-cap ($1.05 < |\eta| < 2.4$) thin gap chambers (TGC) are used. The design goal was to minimise time contributions from signal propagation and electronics to allow efficient identification of the beam crossing. Both chamber types deliver signals with a spread of 15–25 ns, allowing each individual chamber to tag the bunch crossing with efficiency of at least 99%.

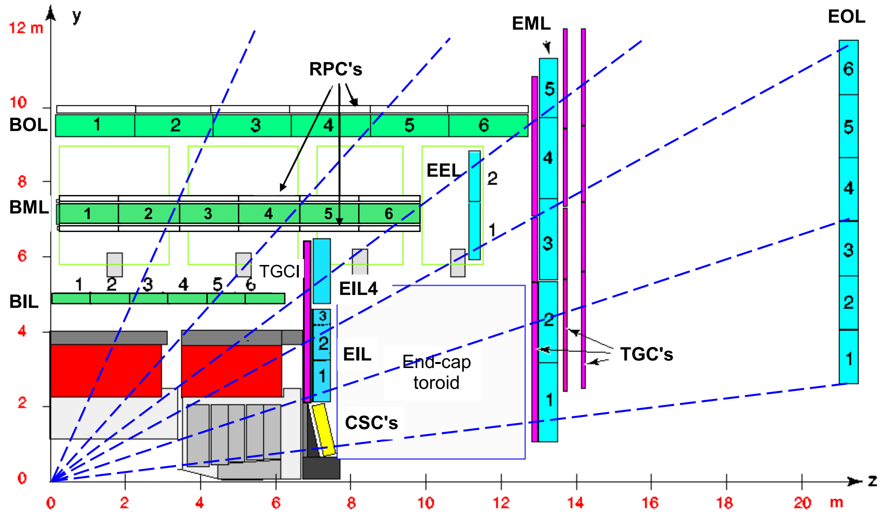

Figure 4.7: Labels: B/E - barrel/end-cap, I/M/O - inner/medium/outer, L - large. Cross-section of the muon system in a plane containing the beam axis. Straight trajectories are illustrated by the dashed lines and most likely traverse three muon stations [57].

4.3 ATLAS trigger system

At the LHC, the nominal bunch-crossing rate in pp collisions is 40 MHz. Although this rate was not reached during the Run 2 of the LHC, the individual runs with highest rate were close to 30 MHz. In contrast, the upper constraint on the average event recording rate in ATLAS is approximately 1.2 kHz. The orders of magnitude separating these rates require a fast decision system that rejects most of the large background rate in real time. Accomplishing this, while maximising the efficiency for accepting events that may be useful for physics, is the task of the ATLAS trigger system [108, 109]. The ATLAS trigger is structured in two levels: the Level-1 (L1) trigger and the high-level trigger (HLT).

The L1 trigger is the first rate-reducing step, based on custom-made electronics. It processes low-granularity information from calorimeters and muon trigger chambers, searching for features compatible with high-p_T muons, electrons, photons, jets or hadronically-decaying τ leptons. Global features such as large missing transverse energy and large total energy in the event are also targeted. This level takes up to 2.5 µs to select an event and to define regions of interest (RoI) in the detector, associated with the features found. The RoI information includes η and ϕ coordinates of the interesting feature, as well as the type of feature (electromagnetic, hadronic, muon...) and the highest reached threshold of energy/momentum, all of which are passed on to the HLT. The L1 trigger delivered an output event rate of up to 100 kHz during Run 2 of the LHC.

The HLT has access to higher-granularity information from the detector than L1. In particular, full information from all the detectors is available within the RoI defined by L1. This enables the accurate reconstruction of the features most likely to be relevant to the trigger decision, while requiring only a small fraction of the event data. The HLT reconstruction and selection are based on software similar to that implemented in offline analysis. Average processing times per event at this level are close to 200 ms and the final event size is approximately 1 MB. The average output rate of the HLT was 1.2 kHz during Run 2.

4.3.1 ATLAS jet trigger

Final states containing exclusively jets are possible in most production processes studied at the LHC. This is true for SM processes and is expected for production of BSM particles, such as heavier gauge or Higgs bosons, dark matter candidates and supersymmetric particles. The ATLAS jet trigger [108, 110, 111] selects events with jets in the final state. Besides being available for physics analyses, events selected by the jet trigger are also used in the performance studies that determine the jet reconstruction procedures and uncertainties used by the whole ATLAS collaboration. However, triggering on every event with jets is not feasible. In hadron colliders such as the LHC, every hard-scatter process can occur with the emission of additional jets with considerable p_T. Moreover, the majority of pile-up interactions correspond to QCD-mediated dijet production. The trade-off faced by the jet trigger is this: to keep as many events as possible from those that would be kept in offline physics analyses whose selection depends on jets, while meeting rate and bandwidth constraints. Doing so efficiently depends on reconstructing and calibrating jets at the trigger level as closely to offline jets as possible, using only the limited information available to the trigger. This should be achieved while ensuring that rates do not increase faster than linearly as a function of pile-up.

The jet trigger is made up from many trigger ‘chains’, each being just a sequence of selections based on calorimeter features, at L1, and on jets, at the HLT. All events passing any of the chains are recorded for offline analysis. The main selections used in the definition of jet trigger chains are: applying jet p_T cuts, requiring large jet multiplicities, combining tracking information to reduce the pile-up contribution, requiring basic kinematic selection on dijet systems or using jet substructure information. In case of need for a chain whose rate would be too large, the rate may be effectively reduced with a prescale factor N, meaning that only one random event out of every N is tested against the chain selection. Values of N vary widely depending on the expected unprescaled rate of the chains, and could be of order 10^7 for chains selecting events with at least one jet with low p_T.

Level-1 jet trigger

The L1 jet trigger is based on coarse granularity information from the calorimeters. Signals from the calorimeters are aggregated according to detector segments with approximate dimension 0.2×0.2 in the (η,ϕ) plane, called jet elements. These are built separately for the electromagnetic and hadronic calorimeters. RoIs are defined as windows of 4×4 jet elements around local maxima of transverse energy (E_T) if the total E_T inside the window passes a threshold. An additional algorithm is used to improve efficiency with respect to jets with a larger radius, resulting from hadronic decays of boosted heavy particles. Within a ΔR radius of 1.0 around each RoI, it searches for other RoIs and sums the E_T of such regions. The trigger selection is then applied based on these E_T sums.

High-level jet trigger

For the jet HLT, information with full calorimeter granularity is available. Taking the signals from calorimeter cells as input, a three-dimensional topological clustering algorithm is run. Jets are reconstructed with the anti-k_t jet-clustering algorithm [112] using the previously built topological clusters as input. For small-R jets, the R parameter that regulates the ΔR radius of the jet cone is set to 0.4, while large-R jets have $R = 1.0$.

A calibration sequence is applied to the reconstructed jets. The first calibration step applied in the trigger is the jet-area based pile-up subtraction, in which the contribution from the median p_T density in the event is removed from jets, proportionally to their area. The following step is the jet energy scale calibration, derived from MC events, which corrects the jet energy and η to those expected of a corresponding particle-level jet. Then, the global sequential calibration is applied. In offline analysis, this step combines calorimeter, tracking and muon-segment variables to account for the different detector responses to quark- or gluon-initiated jets. In the trigger, a reduced version is used, relying on calorimeter information only by default, and using tracks when available. The final step is the *in situ* calibration, applied only to data, in which remaining differences between data and MC are covered.

A different calibration sequence is applied to large-R jets, with just two steps. The first step is grooming, in which the least energetic constituents are removed from the large-R jet to reduce dependence on pile-up. The second step is an MC-based correction, which corrects the energy, η and mass of the jet.

Chapter 5

ATLAS jet trigger studies

This chapter presents studies performed in the ATLAS jet trigger. As a common goal, all studies tried to improve the efficiency of low E_T threshold single jet trigger chains, expected to be severely affected by increasing pile-up in future runs of the LHC. Section 5.1 presents a study addressing jets with energy deposits in the gap and crack calorimeter cells, particularly sensitive to pile-up. Several strategies for rejecting or correcting such jets were investigated. Section 5.2 shows additional strategies that could in the future be used for pile-up mitigation in the jet trigger.

5.1 Correction of trigger jets in the gap/crack region

The calorimeter layer comprising the gap and crack scintillators of the TileCal is referred to as 'TileGap3' in the rest of this section. The energy measurement from TileGap3 is used in offline analysis as a criterion to reject objects or even events altogether. An object with a large fraction of energy deposited in TileGap3 indicates that the energy lost in the dead material may be too large for the object to be reliably used in analysis. The TileGap3 cells show high sensitivity to the intensity of pile-up, with both the average response and the noise increasing with pile-up. A variation of the average number of collisions per bunch-crossing $\langle\mu\rangle$ from 8 to 33 leads to an increase of the average energy deposited per cell, as small as 2% for the cells farther from the beam, and as large as 90% for the cells closer to the beam. The gap and crack cells are, even under low pile-up ($\langle\mu\rangle = 4.8$), the noisiest group of cells of the TileCal.

Events recorded by the low E_T threshold jet trigger chains, especially during the first runs of each year of data taking, show an excess of jets with η close to that of the gap and crack scintillator tiles. A large fraction of such events is rejected by offline analyses when kinematic selection and pile-up mitigation tools relying on vertex identification are applied. This represents an undesirable waste of trigger rate. During the 2016 and

2017 data-taking periods, a small fraction of the runs and only the very lowest E_T threshold trigger chains were severely affected by this issue. In the worst cases, the excess represented up to 50% of the events recorded by the chain. Aiming to mitigate future occurrences of this issue, studies of possible corrections to be applied to trigger jets, based on the energy sampled by the TileGap3 scintillators, were performed.

The HLT chains mainly concerned in these studies are j15, j25, j35, j45 and j60 [110, 108]. The chain jx corresponds to the requirement of at least one jet with $|\eta| < 3.2$ and with E_T, expressed in GeV, equal to or greater than x. Chains j15 through j35 take as input a pure-prescale L1 trigger, while j45 and j60 are fed, respectively, by the L1 chains L1_J15 and L1_J20, where the number following J is the E_T threshold of the RoI, in GeV. Offline analyses using these trigger chains include the estimation of jet energy scale uncertainties and resolution [113] and the calibration of b-tagging techniques [114].

5.1.1 Excess of events

The histograms of Figure 5.1a show η distributions of the E_T-leading central ($|\eta| < 3.2$) HLT jet for events recorded by each of the chains during an early-year data-taking period (period B) of 2016. The excess of events in the pseudorapidity range $1.1 < |\eta| < 1.5$ is evident. It is very pronounced for j25, milder for j35 and barely visible for j45. The distributions for j15 and j60 are not shown, but are similar to those of j25 and j45, respectively. In order to study the role of the TileGap3 response in this excess, the quantity f_{TG3} is defined for jets as the fraction of the jet energy sampled at the TileGap3 calorimeter layer. In the following, a jet in which f_{TG3} is the largest among all sampling fractions from the various detector layers is defined as 'ugly'. The red histograms in Figure 5.1a show the η distributions only for events in which the E_T-leading central jet is not ugly. The remarkable reduction of the peaks hints at the importance of the TileGap3 response in this effect.

One of the tools used in offline analysis for pile-up mitigation is the

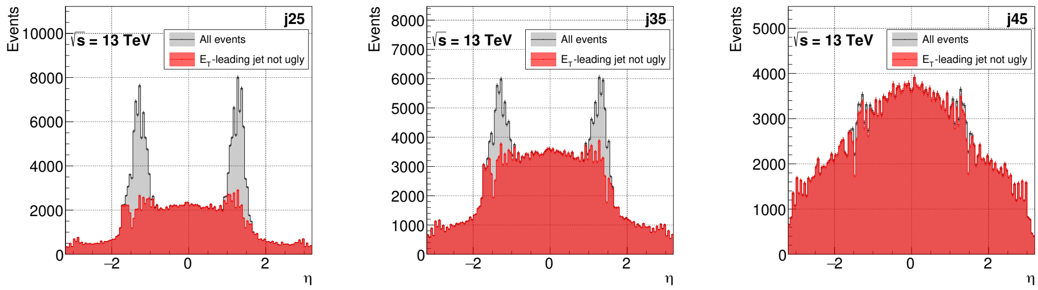

(a)

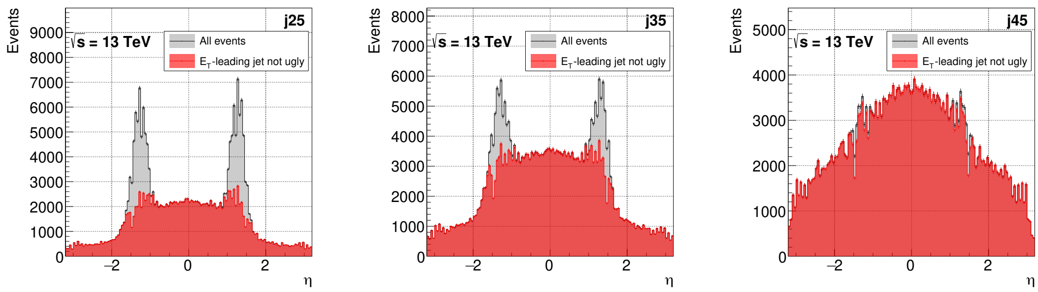

(b)

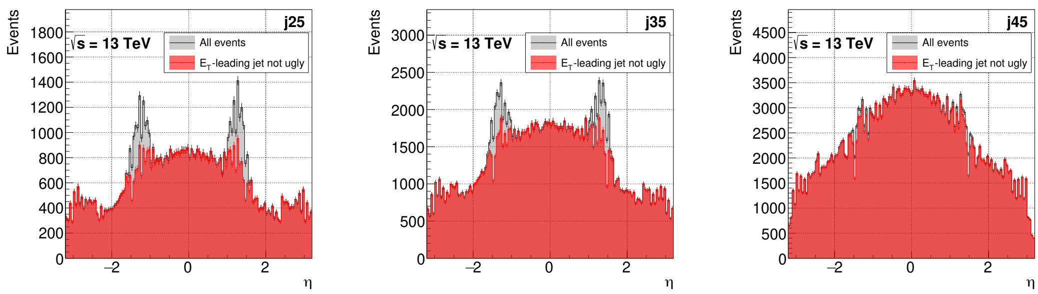

(c)

Figure 5.1: Distributions of η of the E_T-leading central jet in events passing j25, j35 and j45 in 2016 period B. The grey histograms show all events, while the red histograms are restricted to events in which the E_T-leading central jet is not ugly.(a) All events. (b) After requiring a matched offline jet. (c) After requiring a matched offline jet that passes JVT.

JetVertexTagger (JVT) [115], which uses tracks to associate jets to collision vertices and rejects the ones not associated to the primary vertex. In order to estimate the importance of pile-up in determining whether an event passes these chains, the effect of applying JVT prior to the chain selections was studied. As this tool is not available in the trigger, a match was attempted between the central E_T-leading trigger jet and an offline jet, using a ΔR criterion. The offline jet was then required to pass JVT, which was applied at a working point with 92% efficiency. It was only used in jets with p_T between 20 GeV and 60 GeV and $|\eta| \leq 2.4$, always rejecting jets with $p_T < 20$ GeV and always accepting jets with $p_T > 60$ GeV or $|\eta| > 2.4$. Figures 5.1b and 5.1c show the same η distributions as Figure 5.1a, with the additional requirements of a successful jet matching and of the offline jet passing JVT, respectively. In all cases, the requirement of a match to an offline jet has very small impact. On the other hand, the JVT requirement greatly reduces the fraction of events with leading ugly jets in j15 (not shown), j25 and j35. This confirms that ugly jets arise at least partially from pile-up and that a trigger-level analogous to JVT would be helpful to mitigate them. Besides that, the overall acceptance is also affected: the fraction of events in the most central bins that pass the JVT cut is close to 0.4, 0.5 and 0.9, respectively for j25, j35 and j45.

The excess of events with jets near the gap/crack region was found to be dependent on the bunch structure of the proton beams in 2015 and 2016 data: in general, shorter bunch trains resulted in larger peaks than longer bunch trains. This suggests that a role is played by out-of-time pile-up in this effect, since the amount of out-of-time pile-up is smaller in the first bunch crossings of each train than in the bulk. Figure 5.2 shows distributions of bunch-crossing ID (BCID) for all events (grey) and for events in which the E_T-leading central jet is not ugly (red), recorded by j25 in two different data-taking periods: the 2016 period B and the 2017 period B. In 2016 data, a dependence with BCID of the fraction of events with an ugly E_T-leading central jet is visible, with a larger fraction in the first bunches of each train. In 2017, this dependence disappears. The most likely reason for this was a change of the TileCal algorithm used

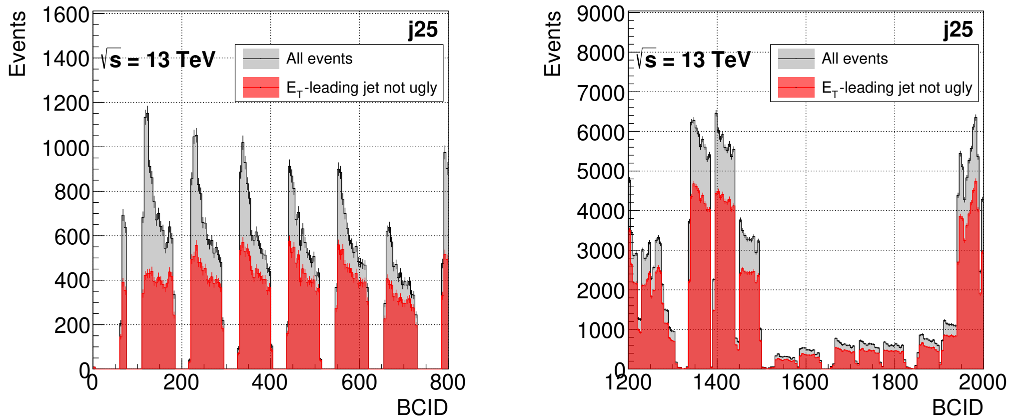

(a)

(b)

Figure 5.2: Distributions of BCID for events recorded by j25. The grey histograms show all events, while the red ones are restricted to those in which the E_T-leading central jet is not ugly. (a) 2016 period B. (b) 2017 period B.

to reconstruct signal pulses from the digital samples received from the cell electronics. The earlier algorithm used a pedestal subtraction, which assumes a stable pedestal value across the duration of each run. That correction was removed, and the later algorithm assigns instead negative weights to the peripheral samples, effectively subtracting a dynamical pedestal value. The result is a pulse reconstruction more robust with respect to variations such as those happening at the beginning of each bunch train.

5.1.2 Studied Corrections

Several correction strategies that may be applied to the jet collection prior to the chain selection were studied, as an attempt to minimise the impact of this problem:

- **Pre-calib**: take all jets at the EM scale (i.e., before calibration) and scale the four-momenta of all ugly jets by a factor 1-f_{TG3}. Calibrate all jets.

- **Post-calib**: scale the default calibrated four-momenta of all ugly jets by a factor 1-f_{TG3}.
- $\boldsymbol{f'}$ **event cut**: reject event if there is at least one jet with $f_{TG3} \geq f'$.
- **Ugly event cut**: reject event if there is at least one ugly jet.
- $\boldsymbol{f'}$ **jet cut**: remove all jets with $f_{TG3} \geq f'$ from the jet collection.
- **Ugly jet cut**: remove all ugly jets from the jet collection.

The pre- and post- calib corrections make the assumption that, whenever a jet is ugly, the response of the TileGap3 scintillators was noisy and thus attempt to remove the f_{TG3} contribution from the jet. In the post-calib correction, this is done simply by scaling the jets in the trigger jet collection. In the pre-calib correction, the EM-scale jets are corrected instead, and only then they are calibrated. The motivation for this is that, since the jet calibration is p_T-dependent, the jet input to the calibration should be already devoid of spurious contributions.

Figure 5.3 shows η distributions of the E_T-leading central jets of the jet collections modified by the pre-calib and post-calib corrections, for events that would be recorded by the modified j25 chain. The contribution of events with an ugly leading jet practically disappears and the peaks near the gap/crack region are reduced. The shapes of the distributions resulting from the two corrections are very similar in 2016 period B but quite different in 2017 period B, with the pre-calib correction being more effective in reducing the peaks.

The cut-based approaches do not attempt to correct jets with a relatively large f_{TG3}. Instead, they discard those jets or the corresponding event altogether. Because the low E_T threshold jet trigger chains are heavily prescaled, a large rejection factor could be accommodated by adjusting the prescale such that the overall chain rate is kept constant. The main drawbacks of these methods, which become more relevant as the cut becomes more aggressive, are its impacts on the analysis in which the jet energy scale and its uncertainty are derived. They can lead to a reduction

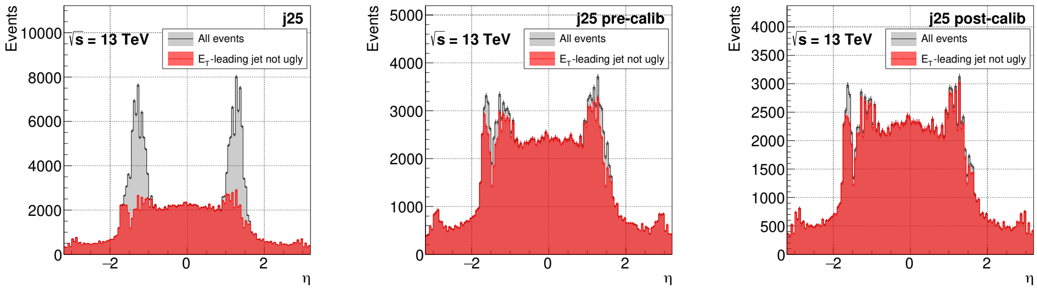

(a)

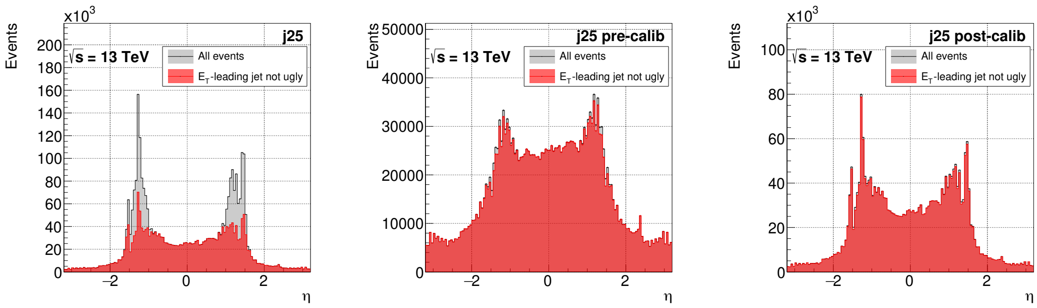

(b)

Figure 5.3: Distributions of η of the central jet leading in E_T in the original jet collection and in the collections modified by pre-calib and post-calib corrections, for events passing the modified j25 chain. The grey histograms show all events, while the red histograms are restricted to events in which the E_T-leading central jet of the modified chain is not ugly. (a) 2016 period B. (b) 2017 period B.

of statistics for events with jets in the η region of the gap/crack, resulting in a corresponding larger uncertainty in the calibration. Besides, a bias is introduced in the calibration, in the sense that f_{TG3} is correlated with pile-up and BCID, for instance. Thus, generalising a calibration derived using a selection based on f_{TG3}, while not applying the same selection in physics analysis, is an extrapolation which becomes less valid as the cut becomes more aggressive. The cuts can be parameterised by the threshold fraction f', with the jet or event being rejected when $f_{TG3} > f'$. The metric used for optimising this parameter was the fraction of events, among those accepted by the modified trigger chain, that are accepted after a baseline offline event selection. This was called the offline acceptance rate (OAR), and a higher value of this metric means a more efficient use of trigger rate. The offline selection used requires an offline jet with $|\eta| < 2.8$ and a p_T large enough for the unmodified trigger chain to be fully efficient. Offline analysis tools including JVT and jet cleaning – used to discard jets from non-collision sources – are also applied.

The OAR of each modified chain was computed as a function of f', for both the event cut and the jet cut corrections. Graphs of OAR as a function of f' for different chains are shown in Figure 5.4a for the 2016 period B. The low end of reasonable f' values (most aggressive cut) to test can be gauged by studying the shape of the η distributions of the E_T-leading central jet in events passing the modified chain, as f' is varied. Such η distributions are shown for j25 in Figure 5.4b. The point is to find the value for which the statistics in the gap/crack region starts to be compromised, i.e., the peaks turn into dips. Histograms resulting from applying an ugly event cut or an ugly jet cut are also drawn, in red.

In both cases it is evident that an aggressive cut with $f' \leq 0.2$ is necessary for a sizeable increase in OAR to be obtained. The event cut seems to yield a maximum OAR for most chains when f' is close to 0.2, while the jet cut shows an increasing OAR as the cut tightens, down to $f' \simeq 0$.

Regarding the η distributions for event cuts, there does not seem to be an f' for j15 (not shown) and j25 such that the peaks turn into dips, but they mostly disappear for $f' = 0.2$. For j35, j45 and j60 (not shown), $f' = 0.1$ clearly produces undesireable dips in the distribution. The ugly event cut appears to be a bad option for the lowest thresholds j15 and j25, where it retains most of the peaks, while sacrificing a large fraction of the events in the central region. For j45 and j60 it yields distributions very close to those from an $f' = 0.4$ event cut, while for j35 it is slightly less effective. With respect to jet cuts, both $f' = 0.2$ and the ugly jet cut perform well and consistently across the chains and in both periods.

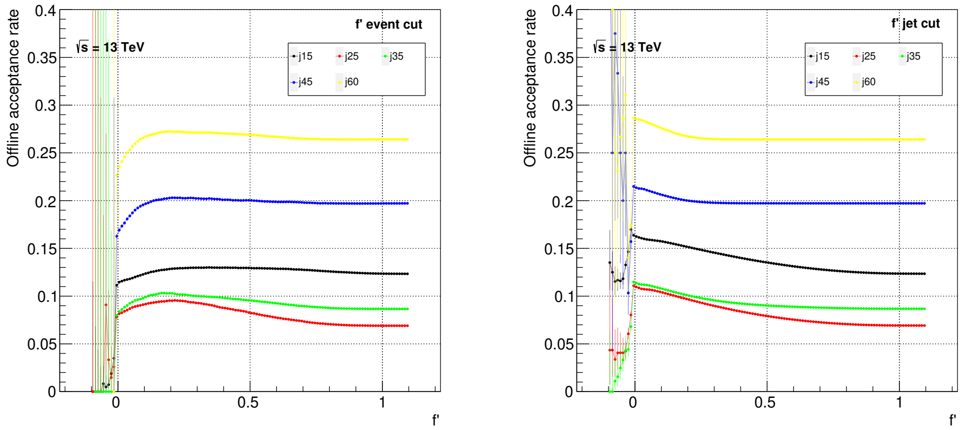

(a)

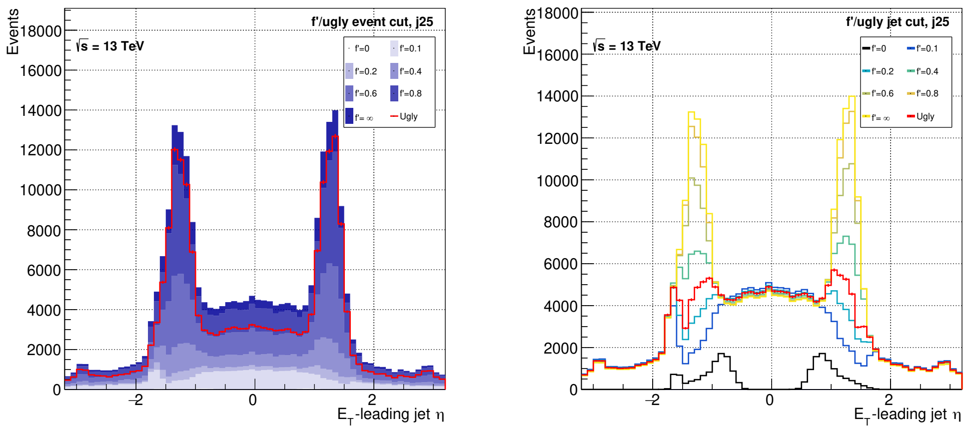

(b)

Figure 5.4: (a) OAR as a function of the threshold f' used in the event (left) or jet (right) cut applied to trigger jets for the various jet trigger chains in 2016 period B. (b) Distributions of E_T-leading central jet η for events passing the j25 chain modified by an event (left) or jet (right) cut. The results for different f' cuts are shown, as well as for the ugly cuts.

5.1.3 Expected impact on jet trigger

The OAR resulting from modifying the jet trigger chains by each one of the corrections was computed. Considering the discussion about the f' choice presented above, the event and jet cuts were tested for $f' = 0.2$ and $f' = 0.1$. Table 5.1 summarizes the results of these tests for 2016 period B and 2017 period B data. In addition to the expected OAR, the corresponding "potential savings" are also reported, which means the reduction in total rate, relative to the original chain, that could be accomplished in the modified chain, while keeping constant the amount of events passing the offline selection. Chains j45 and j60 were ommitted from this table because the changes in those are negligible.

Table 5.1: Impact of the corrections on the offline acceptance rate of the 2016 period B and 2017 period B events passing the modified chains. The numbers inside parentheses show the rate reduction that could be applied relative to the original chain while keeping constant the number of offline-accepted events.

	Offline acceptance rate[%] (potential savings[%])											
	2016 period B						2017 period B					
Correction	j15		j25		j35		j15		j25		j35	
None	12.3	-	6.88	-	8.65	-	15.5	-	5.31	-	7.75	-
Pre-calib	12.8	(3.78)	8.07	(14.7)	9.35	(7.5)	16.7	(7.21)	7.79	(31.8)	8.7	(11)
Post-calib	14.5	(14.9)	9.09	(24.3)	9.67	(10.6)	15.8	(1.86)	6.6	(19.4)	8.48	(8.57)
0.1 event cut	12.2	(-0.65)	9.08	(24.2)	9.78	(11.6)	10.4	(-48.8)	6.3	(15.7)	8.86	(12.6)
0.2 event cut	12.8	(3.84)	9.51	(27.6)	10.3	(16)	11.6	(-33.8)	6.42	(17.3)	9	(13.9)
Ugly event cut	12.9	(4.73)	9.31	(26)	10.1	(14.6)	12.4	(-25.3)	6.23	(14.7)	8.82	(12.1)
0.1 jet cut	15.7	(21.6)	10.4	(33.7)	10.8	(19.8)	16	(3)	7.59	(30)	9.39	(17.4)
0.2 jet cut	15.1	(18.6)	9.65	(28.7)	10.1	(14.2)	15.9	(2.62)	6.98	(23.9)	8.78	(11.7)
Ugly jet cut	14.7	(16.1)	9.14	(24.7)	9.69	(10.8)	15.9	(2.14)	6.59	(19.4)	8.48	(8.61)

The pre- and post-calib corrections provide significant improvement across chains and periods. The pre-calib correction is the best-performing option in 2017 data, being much less effective in 2016. Considering 2017 data only, it would allow for a reduction of the HLT rate in the range 11-32%, depending on the HLT chain (for j25 and j35), while keeping the offline rate fixed. The post-calib correction is slightly more effective in 2016 data than in 2017. Event cuts perform well for j25 and j35, but are ineffective and in some cases detrimental for j15. Jet cuts are the corrections yielding the highest OARs overall. In particular, the tighter 0.1 jet cut has the highest OAR for all chains in 2016 and is only slightly surpassed by the pre-calib correction in 2017. However, such an aggressive cut could compromise statistics and also bias the data used by offline analyses. The 0.2 jet cut could be the best compromise, since the η distributions in Figure 5.4 show that it would at least not harm statistics. With such a correction in place, the required HLT rate for a fixed offline rate could have a reduction in the range 11-29% (for j25 and j35).

In the short term, the modest gain from these methods was not considered enough to offset the concerns about potential biases introduced in the recorded data, which is used for jet energy scale and *b*-tagging calibrations. For this reason, the studied corrections were not included in the trigger menu for 2018 data taking. However, the results from this study could still be useful in the future, since the harsher pile-up during the LHC Run 3 is likely to enhance this issue.

5.1.4 Tag-and-probe methods

An alternative to the corrections presented above would be a correction that makes the best possible use of the TileGap3 sampling information to return the most likely "true" jet four-momentum. This is of particular interest for a subset of missing-E_T trigger chains that use jets above a certain E_T threshold as input to compute the missing E_T in each event.

A tag-and-probe method was studied using Z boson candidates decaying into muons as reference objects (tags), in events where an associated single jet is also produced. The associated jet is the probe, which is compared to the Z candidate, under the assumption of p_T balance, to study the effect of the response of TileGap3 scintillators on jets. The method relies on the fact that the momentum resolution of muons is much better than the energy resolution of jets. The events used were from 2017 periods B to F, recorded by a dimuon trigger, in order to reduce the bias with respect to the response of the calorimeters.

For the application of the tag-and-probe selection, the p_T-leading HLT jet is defined as the probe and is required to have $|\eta| < 2.5$. The Z

boson candidate is reconstructed by requiring two opposite-charge offline muons, each with $p_T > 20\,\text{GeV}$ and $|\eta| < 2.4$. Then, it is required to have an invariant mass within 66 GeV and 116 GeV and $p_T > 20\,\text{GeV}$. A correction to the p_T of the Z candidate is done according to

$$p_T^Z \to p_T^Z \times |\cos \Delta\phi(\text{probe}, Z)|,$$

in order to only consider the component which opposes the transverse direction of the probe. Because there is no JVT at the trigger level, collections of trigger jets typically have dozens of jets, even in events with low jet multiplicity from the hard-scatter process. A simple requirement of one trigger jet would largely reduce the analysed sample and would bias the selection towards events with untypically few pile-up events. The exclusive single jet selection is instead imposed by requiring $\Delta\phi(\text{probe}, Z) > 2.9$ and that the p_T-subleading HLT jet, if present, has $p_T < 0.4 \times p_T^Z$ and $p_T < 0.2 \times p_T^{\text{probe}}$.

Since the tag-and-probe method depends on the assumption of p_T balance, rejecting events in which the probe jet originates from pile-up is crucial. This was done by using the JVT tool to tag the offline jet matched to the probe jet. This allows two regions to be defined: a pile-up enriched region and a pile-up depleted region, depending on the outcome of the JVT. The histograms on Figure 5.5a show the normalised f_{TG3}^{probe} distributions for both regions, excluding events with $f_{TG3}^{\text{probe}} = 0$. A significant separation is visible between the pile-up enriched and pile-up depleted distributions.

Figure 5.5b shows the ratio $p_T^{\text{probe}}/p_T^{\text{tag}}$ as a function of f_{TG3}^{probe} for three different E_T^{probe} ranges, in the pile-up depleted region. The shaded bands indicate the standard deviation of $p_T^{\text{probe}}/p_T^{\text{tag}}$, while the vertical lines correspond to the uncertainty on its average value. In general, a larger f_{TG3} corresponds to larger values of the ratio. For $E_T^{\text{probe}} > 100\,\text{GeV}$, this dependence becomes less important and the standard deviation of the ratio decreases. This study was not pursued further, but results of this kind could be used to derive a correction for jets not believed to be spurious

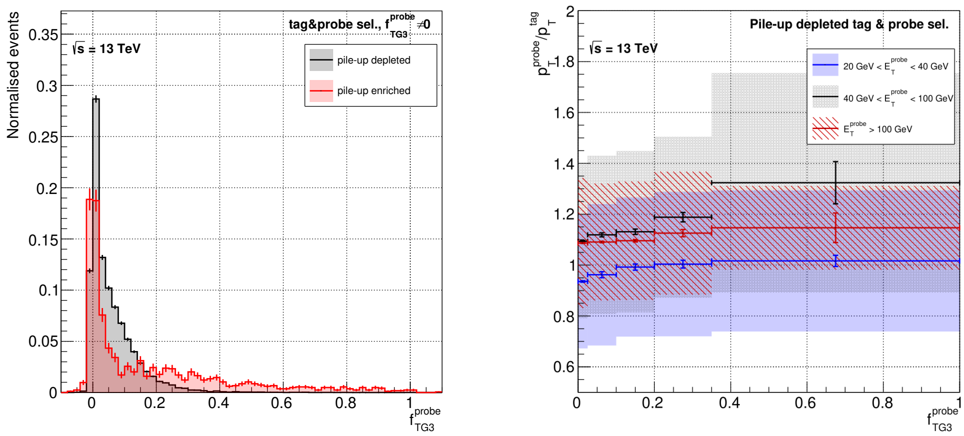

(a) (b)

Figure 5.5: (a) Normalised distributions of f_{TG3} of the probe in events passing the tag-and-probe selection, in the pile-up enriched (red) and pile-up depleted (grey) regions. Events with f_{TG3}^{probe} exactly equal to 0 are excluded from the histograms. (b) Average ratio $p_T^{\text{probe}}/p_T^{\text{tag}}$ as a function of f_{TG3}^{probe} for three different E_T^{probe} ranges in the pile-up depleted region. The shaded bands indicate the standard deviation of $p_T^{\text{probe}}/p_T^{\text{tag}}$, while the vertical lines correspond to the uncertainty on its average value.

and with $f_{TG3} \neq 0$. Functional fits to the points of each E_T^{probe} range, as well as an interpolation between different E_T^{probe} ranges, would be performed. Then, for a jet with given E_T and f_{TG3}, the average corresponding p_T^{tag} would be known. The f_{TG3} dependence could be removed by scaling the jet's four-momentum such that its corrected p_T would match the p_T^{probe} of a jet with $f_{TG3} = 0$ for the same p_T^{tag}.

5.2 Pile-up mitigation in low-E_T chains

5.2.1 Timing

Trigger jet timing was tested as a possible discriminant for flagging jets as originating from pile-up. Figure 5.6 shows distributions of timing for E_T-leading central HLT jets from 2017 period F data, for the j25 and j35 chains. Events are separated into those in which the offline jet matched to the HLT jet either passes ('good' jet) or fails ('bad' jet) the JVT and

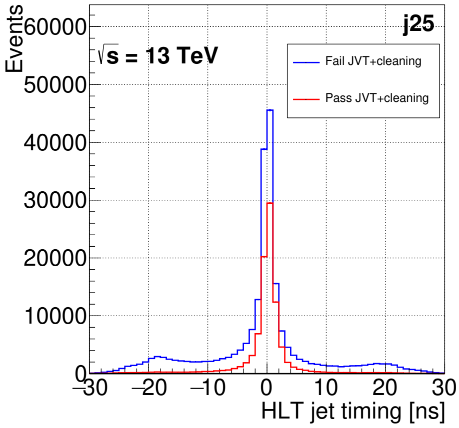

(a)

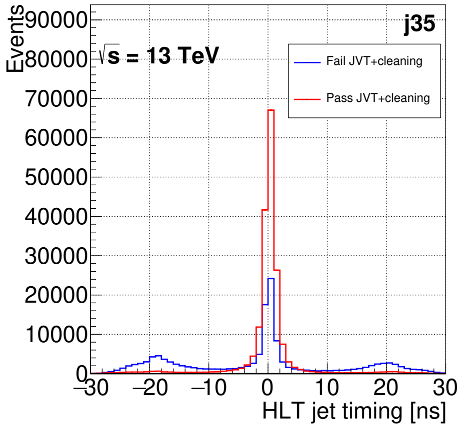

(b)

Figure 5.6: Distributions of timing of E_T-leading central HLT jets for events recorded by different jet trigger chains during 2017 period F. Events are separated into those in which the offline jet matched to the HLT jet either passes (red) or fails (blue) the JVT and jet cleaning requirements. (a) j25. (b) j35.

jet cleaning requirements. Timing information provides some discrimination: a rejection of trigger jets with absolute value of timing greater than 15 ns in j15 (j25, j35) would reject 14% (17%, 38%) of the bad jets and 4% (4%, 5%) of the good jets. Changing this timing threshold to 10 ns would result in a bad jet rejection rate of 22% (25%, 46%) and a good jet rejection rate of 7% (7%, 7%). For j25 and j35 in particular, there are visible bumps close to absolute values of timing of 20 ns. Considering that data was taken with a bunch-spacing of 25 ns, this corroborates the hypothesis that out-of-time pile-up contributes in part to the excess of events.

5.2.2 Fast TracKer

The Fast TracKer (FTK) is a highly parallel, hardware-based, tracking system that was planned to be implemented in the ATLAS trigger [116]. Its development has been abandoned during the second long shutdown of the LHC. FTK would deliver all tracks with p_T above 1 GeV for events passing L1, enabling improved HLT decisions on all final states where tracks can be used.

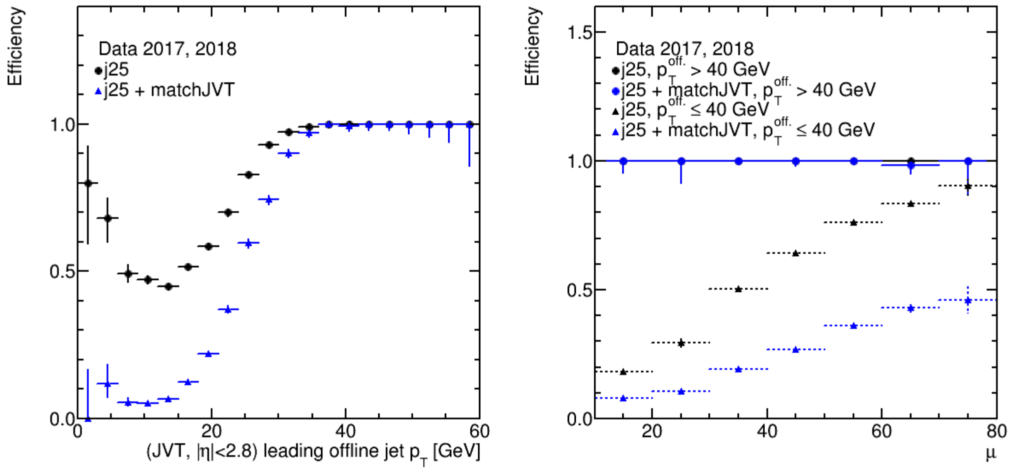

Figure 5.7: Efficiency of the original and modified (matchJVT) j25 chain. (a) As a function of p_T of the p_T-leading central ($|\eta| < 2.8$) offline jet. (b) As a function of the number of inelastic pp interactions μ.

For the jet trigger, one application would be the development of a trigger version of JVT, which would rely on FTK tracks to assign jets to either the primary or a secondary vertex. The low E_T threshold single jet chains discussed above would benefit from such a tagger, since they are affected by pile-up. An estimate of possible improvements in these chains was performed, by matching HLT jets to offline jets using a ΔR criterion and by assigning the offline JVT result to the corresponding HLT jet. Then, a modified version of the chains was created by removing jets failing the JVT from the jet collection prior to applying the default selection of the chain. Analysing data from 2017 and 2018, the expected rate reduction provided by such a modification of the chains would be approximately 10% for j15 and j45, 50% for j25 and j35, and below 2% for j60. On the other hand, a negligible impact was found on the amount of events selected by offline analyses targeting the phase-space in which the original chains would be fully efficient.

Figure 5.7a shows the efficiency of the original and modified j25 chains, as a function of p_T of the p_T-leading central ($|\eta| < 2.8$) offline jet. An ideal trigger would have as its efficiency curve a Heavyside function centred at the full-efficiency point (not necessarily equal to the nominal threshold). Any changes that bring the efficiency curve closer to that scenario are desirable. Because the jet p_T spectrum falls rapidly, decreasing efficiency below the full-efficiency point provides a disproportionately large decrease in rate. Figure 5.7b shows the pile-up dependence of the j25 trigger efficiency, separately for regions of E_T below and above 40 GeV, which is roughly the full-efficiency point. Both the original and modified chains are fully efficient above 40 GeV, regardless of the number of pp interactions per bunch crossing μ. On the contrary, the undesired efficiency below 40 GeV has a strong dependence on μ. The original chain is 90% efficient for large μ (between 70 and 80). The modified chain has approximately half of that efficiency, making it more robust for future runs with higher levels of pile-up.

Chapter 6

Features of $t\bar{t}H(H \rightarrow b\bar{b})$ analyses

The following chapters will focus on two analyses of $t\bar{t}H$ events in the final state with leptons and with the Higgs boson decaying to $b\bar{b}$. One is the inclusive cross-section analysis and the other is the $\mathcal{CP}$ properties analysis. This chapter introduces many important ingredients and procedures used in both. Section 6.1 defines the detector objects used and Section 6.2 describes the data and MC samples. In Section 6.3, the chosen background estimates are presented, with focus on the dominant background $t\bar{t} + \geq 1b$. The treatment of systematic uncertainties is explained in Section 6.4. Finally, in Section 6.5, the profile-likelihood fits used for the measurements are explained.

6.1 Object reconstruction

6.1.1 Electrons

The reconstruction of electrons starts from an energy cluster in the EM calorimeter. Information from ID tracks is used to distinguish them from photons. Electrons are required to have a matched track and photons are defined as not having a matched track or being matched to a e^-e^+ pair from a photon conversion. Identification of electrons relies on a likelihood discriminant combining information from the matched track and from the shower shape in the calorimeter. The energy of high-p_T electrons is obtained from the calorimeter measurement, while the direction is more precisely determined from the matched track. Electrons are required to have $p_T > 10$ GeV and $|\eta| < 2.47$. Candidates in the calorimeter barrel–end-cap transition region ($1.37 < |\eta| < 1.52$) are excluded. Electron tracks must match the primary vertex of the event.

6.1.2 Muons

Muon identification starts from the muon spectrometer, with track segments or full tracks. A match is attempted between these tracks and the tracks in the ID. If it is successful, combined tracks are reconstructed using the hits in both sub-detectors and taking into account energy losses in the calorimeters. The momentum measurements are performed using the resulting combined tracks. The spectrometer performance is optimal for muons with a p_T of 100 GeV. Below that, the combination of both systems is beneficial and below 30 GeV it is the ID that dominates the momentum resolution. Muons are required to have $p_T > 10$ GeV and $|\eta| < 2.5$. Muon tracks must match the primary vertex of the event.

6.1.3 τ leptons

Hadronically decaying τ leptons mostly give rise to a final state with one or three pions. In order to distinguish them from gluon- and quark-initiated jets, τ lepton identification relies on track multiplicity and on a multivariate discriminant based on the track collimation, jet substructure, and kinematic information. The τ lepton candidates are required to have $p_T > 25$ GeV and $|\eta| < 2.5$.

6.1.4 Small-R jets

Reconstruction of jets[1] relies on the anti-k_t jet clustering algorithm [112]. It takes as input three-dimensional topological energy clusters in the calorimeter [117]. The R parameter is set to 0.4. The reconstructed jets are then calibrated. Calibration steps include pile-up subtraction, jet energy scale and *in situ* corrections, the latter only applied to data in order to fix residual differences in jet responses with respect to simulation [113]. After calibration, jets are required to have $p_T > 25$ GeV and $|\eta| < 2.5$. In order to reduce the effect of pile-up, jets are required to pass the JVT (see Section 5.1.1). Finally, jet cleaning is applied, and events with at least one non-clean jet are rejected.

[1]In most analysis regions, small-R jets are the only jets used. For that reason they will often be referred to simply as jets.

6.1.5 *b*-tagging

The b-tagging procedure attempts to identify jets as originating from the hadronisation of a b quark. Tracks matched to jets may be used to produce variables which discriminate between different jet flavours. The b-tagging algorithm used in the analyses, the MV2 tagger [118], uses multivariate techniques to integrate information about the impact parameter of the tracks and their compatibility with a possible displaced secondary vertex or even a two-step decay chain within the jet. The tagger was trained on jets from simulated $t\bar{t}$ events, to discriminate b jets from background jets. In the particular variant of the tagger used, a mixture of 90% light-flavour jets (initiated by gluons or $u/d/s$ quarks) and 10% c jets was used as the background jet sample.

A cut performed on the MV2 score defines a b-tagging working point (WP), with a corresponding efficiency for correctly tagging b jets and rejection factors for light-flavour and c jets. In the analyses addressed here, a pseudo-continuous (PC) b-tagging method is used, which means that more than one WP is used simultaneously. The WPs available have efficiencies of 60%, 70%, 77% and 85%. The respective rejection rates are 1200, 300, 110 and 25 for light-flavour jets, and 23, 8.9, 4.9 and 2.7 for c jets. The PC b-tagging score of a jet is defined by the tightest WP at which the jet is tagged, such that a score of 1 corresponds to a jet not tagged by any of the WPs and 5 corresponds to a jet tagged by all the WPs, including the tightest one.

6.1.6 Overlap removal

To avoid the identification of a single detector response as more than one detector object, an overlap removal procedure is and applied to the reconstructed leptons and small-R jets. To prevent double-counting of electron energy deposits as jets, the closest jet within $\Delta R_y = \sqrt{(\Delta y)^2 + (\Delta\phi)^2} = 0.2$ of a selected electron is removed[2]. If,

[2]The rapidity is defined as $y = \frac{1}{2} \ln \frac{E+p_z}{E-p_z}$ where E is the energy and p_z is the longitudinal component of the momentum.

after that removal, there are electrons within the $\Delta R_y = 0.4$ cone of a jet, those electrons are discarded. Muons separated from a jet momentum vector by $\Delta R_y < 0.4$ are also removed, resulting in a reduction of the muon background from heavy-flavour decays inside jets. An exception is made if the jet has fewer than three associated tracks, in which case the jet is removed. This avoids an inefficiency for high-energy muons undergoing a significant energy loss in the calorimeter. A τ lepton candidate is rejected if it is separated by $\Delta R_y < 0.2$ from any selected electron or muon.

6.1.7 Missing E_T

In events resulting from hadron collisions, the vector sum of the transverse components of the outgoing particles must be zero. For this reason, it is interesting to define a missing E_T as the negative of the vector sum of the p_T of all particles produced at the primary vertex. First, this is computed using the selected objects as defined above. Then, an extra term is added to account for particles in the event not associated with any of the selected objects. This 'soft term' is calculated from ID tracks matched to the primary vertex, to avoid pile-up contamination. If there are energetic undetected particles in the event, such as neutrinos, the missing E_T should correspond to the transverse component of the vector sum of their momenta.

6.1.8 Boosted objects

Large-R jets

When a Higgs boson or a top quark with high p_T decay hadronically, the resulting showers may be very collimated. This feature is exploited by building a collection of large-R jets. With a large enough radius, large-R jets may be able to contain all the decay products from a boosted top quark or Higgs boson in signal events. The previously selected small-R jets are used as inputs for a jet reclustering technique [119] through an anti-k_t algorithm with a radius parameter of $R = 1.0$. Reclustered (RC) jets have the advantage of not needing additional calibration, because the input small-R jets are already calibrated. RC jets are required to have a reconstructed invariant mass higher than 50 GeV, $p_T > 200$ GeV and at least two constituent small-R jets.

Deep Neural Network

A multi-class deep neural network (DNN) was trained to identify the most likely origin of the RC jets, distinguishing between three categories: Higgs boson jets, top quark jets and QCD jets. The final layer of the DNN is a three-node output, corresponding to the inferred probabilities of the true jet category: $P(H)$, $P(t)$ and $P(q)$ for Higgs, top and QCD, respectively.

The DNN was trained jet by jet, using a sample of simulated $\mathcal{CP}$-even $t\bar{t}H$ events, after requiring two RC jets, at least one lepton and at least two small-R jets b-tagged with the 85% WP. The true categories of Higgs boson jet and top quark jet were obtained by matching the RC jets, within cones of $\Delta R = 0.4$, to hadronically decaying Higgs bosons or top quarks, respectively, at the generator level. All RC jets without a match were labelled as QCD jets. Input variables to the DNN include information about the RC jet constituents, such as p_T, angular separations and PC b-tagging scores, as well as variables describing the substructure of the RC jet, such as masses and number of constituents. For optimising the performance of the DNN, the metric used was the rate at which the true categories are correctly predicted, where the predicted category is that for which the output probability is highest. Identification of Higgs boson jets was given a higher priority in this optimisation.

Higgs candidate

From the DNN, a tagger for a particular category can be obtained by cutting on the corresponding probability. The distributions of $P(H)$, $P(t)$ and $P(q)$ are shown in Figure 6.1 for true Higgs boson jets and top quark jets. A threshold of 0.6 on $P(H)$ has been chosen for the definition of the

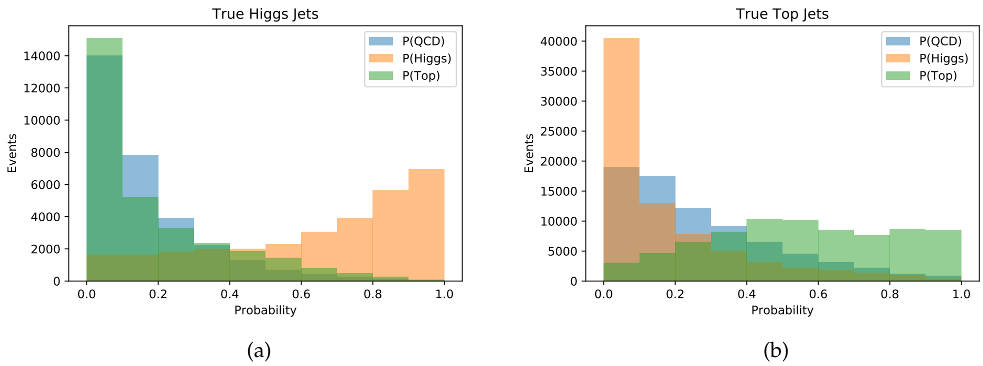

Figure 6.1: Distributions of the probabilities $P(H)$, $P(t)$ and $P(q)$. (a) Higgs boson jets. (b) Top quark jets.

Higgs tagger to be used in event selection. This working point sacrifices a large portion of Higgs jets ($\sim$ 40%) in exchange for a high rejection rate of top and QCD jets.

Boosted Higgs candidates are required to have $p_T > 300$ GeV and mass in the interval $[100, 140[$ GeV, to contain at least two constituent jets, among which exactly two b-tagged at the 85% WP, and to be Higgs-tagged by the DNN. If more than one boosted Higgs boson candidate is identified, the one with the mass closest to 125 GeV is selected.

6.2 Data and Monte Carlo samples

6.2.1 Data

The analyses discussed here use pp collision data collected from 2015 to 2018 by the ATLAS detector at $\sqrt{s}$ =13 TeV. This corresponds to the full Run 2 dataset, with a total integrated luminosity of 139.0 fb^{-1}. Selected events were recorded using unprescaled single-lepton triggers, fully efficient in the selected phase-space. Standard data taking quality requirements are applied, such as stable LHC beams and fully operational ATLAS detector conditions.

6.2.2 Monte Carlo

This section gives a description of features of the MC samples that are common to several processes, followed by a more detailed discussion, addressing each process individually. Additional technical aspects about event generation, such as mass parameters, parton density function (PDF) sets and scale choices, can be found in Appendix A.

For the analyses, several MC samples were produced using the full simulation of the ATLAS detector [120] based on GEANT4 [121], while others were produced using a faster method, where the simulation of the calorimeter is replaced by a detailed parameterisation of shower shapes [122]. Both simulations were found to give similar modelling.

To simulate the effects of pile-up, additional interactions were generated using PYTHIA8 [123] and overlaid to the simulated primary events. Event weights are used in simulation to make the distribution of the number of pile-up events per bunch crossing match the one observed in collision data. All simulated events are processed through the same reconstruction algorithms and analysis chain as the data.

For all samples generated using MADGRAPH5_aMC@NLO [90] for the matrix element (ME), top quarks, Z and W bosons are decayed at LO using MADSPIN [99] to preserve all spin correlations. In all samples involving Higgs boson production, the Higgs boson decay is handled by the PS generator, with all decay modes included. For t- and s-channel single top, tZq and $V+$jets production, only final states with at least one charged lepton are included. In tWZ, only Z boson decays to a pair of leptons are considered. For all other processes, all decay modes of the Z and W bosons are included.

Most of the samples were generated in the five flavour scheme (5FS), in which all the quarks, with the exception of the top quark, are treated as massless and are available in the PDFs, such that they may be taken directly from the proton to play the role of initial-state partons. In a few samples, the four flavour scheme (4FS) is used instead, in which effects due to the non-zero mass of the b quark are taken into account. One such case is that of the $t\bar{t}+b\bar{b}$ sample used to model the nominal prediction for $t\bar{t}+\geq 1b$, for which the choice of the 4FS will be motivated in detail in Section 6.3.2. Besides that, the 4FS is used for production processes of a single top quark in the t-channel, including in associated production with a Higgs or Z boson. What favours the choice of the 4FS for these processes is a much more accurate modelling of the kinematics of the associated (spectator) b quark [124]. The gluon splitting originating this b quark is modelled by the ME in MC generators using the 4FS, but it is modelled by the PS in the 5FS, leading to inaccuracies and large dependence on the PS model. Analyses depending on the discrimination between the t-channel process and other single top or $t\bar{t}$ processes rely crucially on features of the spectator b quark, and for that reason the 4FS prescription is adopted in the ATLAS collaboration.

$t\bar{t}H$

The $t\bar{t}H$ signal samples used for the nominal predictions in the cross-section analysis and in the $\mathcal{CP}$ analysis are different. The nominal sample for the cross-section analysis is obtained from a PowhegBox [125, 126] generator setup. In the $\mathcal{CP}$ analysis, the nominal samples used are generated with the MadGraph5_aMC@NLO generator. In both cases, the predictions have NLO precision in QCD and use the 5FS. The PS and hadronisation are modelled with Pythia8.

With the MadGraph5_aMC@NLO setup, besides the SM sample ($\alpha=0, \kappa_t'=1$), two samples of alternative $\mathcal{CP}$ scenarios are available, assuming a simple extension of the top-Higgs interaction Lagrangian, as described in Section 2.3. One has $\alpha=90°$ – corresponding to a pure $\mathcal{CP}$-odd interaction – and the other has $\alpha=45°$ – corresponding to maximal $\mathcal{CP}$ mixing. In both samples, κ_t' is set to 1. The generation of these samples relied on the HC UFO model [91, 92].

A sample produced from the same generated events as the PowhegBox+Pythia8 sample, but showered with Herwig7 [127] instead of Pythia8, is used to evaluate the impact of the PS and hadronisation model.

tH

Samples for associated production of a single top quark and a Higgs boson are also used. In the $t\bar{t}H$ cross-section measurement, this process is treated as background. However, in the $\mathcal{CP}$ analysis it must be taken as signal because the considered modification to the top-Higgs coupling inevitably affects both tH and $t\bar{t}H$ production. Two sub-processes – $tHjb$ and tWH – are generated using the MadGraph5_aMC@NLO generator at NLO in QCD. For $tHjb$, events are generated in the 4FS. The 5FS is used for the tWH simulation. In both processes, Pythia8 is used to handle the PS and hadronisation.

In addition to the SM $tHjb$ and tWH, multiple samples are also generated with different scenarios for the top-Higgs coupling, again using the HC UFO model that allows a $\mathcal{CP}$-odd component. For each of the processes, the following values of α and κ_t' are used:

- α from 15° to 90°, in steps of 15°, with $\kappa_t' = 1$
- $\alpha = 0$, with $\kappa_t' \in \{-1, 0.5, 2\}$
- $\alpha = 45°$, with $\kappa_t' = 2$

$t\bar{t}$ + jets

A $t\bar{t} + b\bar{b}$ sample generated at NLO in the 4FS was produced with the PowhegBoxRes [128] generator and OpenLoops [129, 130, 131], using a pre-release provided by the authors [132], and using Pythia8 for the PS and hadronisation. This sample is used as the nominal $t\bar{t} + \geq 1b$ prediction.

The inclusive production of $t\bar{t}$ events is modelled using the Powheg-Box [133] generator at NLO in QCD in the 5FS. Parton showers and hadronisation are simulated in Pythia8, with similar settings as for the PowhegBox+Pythia8 $t\bar{t}H$ samples. This sample is used for the nominal predictions of $t\bar{t}$ production with additional c jets ($t\bar{t} + \geq 1c$) and $t\bar{t}$ production with additional light-flavour jets ($t\bar{t}$ + light), as well as for uncertainty estimation in $t\bar{t} + \geq 1b$. Two additional samples are used to estimate the impact of modelling uncertainties: one is generated with a PowhegBox setup, like the nominal, but showered with Herwig7; the other is generated with a MadGraph5_aMC@NLO setup and showered with Pythia8.

Single top

Single top t-channel, s-channel, and tW production are modelled at NLO in QCD using the PowhegBox [124, 134, 135] generator. For t-channel production, events are generated in the 4FS and MadSpin is used to decay top quarks and W bosons. For s-channel and tW production, events are generated in the 5FS. For tW production, the diagram removal scheme [136] is employed to handle the interference with $t\bar{t}$ production. The events are showered with Pythia8.

For evaluating the impact of modelling uncertainties, additional samples are used. One set of samples has the same events generated in PowhegBox for the nominal samples, in which the PS is generated by Herwig7 instead of Pythia8. Another set consists of samples generated with MadGraph5_aMC@NLO, with NLO precision in QCD, in the 4FS for t-channel production, and in the 5FS for s-channel and tW production. Those events are showered with Pythia8. Finally, for tW production, an alternative sample is generated using the diagram subtraction scheme to estimate the uncertainty due to the interference with $t\bar{t}$ production.

Rare top processes

All samples used for nominal predictions of rare top processes are generated using the MadGraph5_aMC@NLO generator and are showered with Pythia8. The tZq samples are generated at LO in QCD, while the production of $t\bar{t}V$ (V is a W or Z boson), $t\bar{t}t\bar{t}$ and tWZ are modelled at NLO. The diagram removal scheme is applied to the tWZ sample to handle the interference with $t\bar{t}Z$.

For modelling uncertainty estimation, additional $t\bar{t}V$ samples are produced with the SHERPA generator, using the MEPS@LO prescription [137, 138] with up to one additional parton for the $t\bar{t}Z$ sample and two additional partons for the others. The CKKW merging scale of the additional emissions is set to 30 GeV.

Vector bosons

Samples of V+jets and diboson production are simulated with the SHERPA generator. The V+jets prediction is obtained from NLO-accurate MEs for up to two partons and LO-accurate MEs for up to four partons, calculated using the Comix [139] and OPENLOOPS libraries. The NLO MEs of a given jet multiplicity are matched to the PS using a variant of the MC@NLO algorithm [140]. Different jet multiplicities are then merged into an inclusive sample using the MEPS@NLO prescription [137, 138], with a merging cut at 20 GeV. In diboson samples, MEs corresponding to different numbers of parton emissions are also merged and matched to the SHERPA PS using the MEPS@NLO prescription.

6.3 Background modelling

6.3.1 $t\bar{t}$ + jets flavour classification

The $t\bar{t}$ + jets background is categorised according to the flavour of additional jets in the event. Generator-level particle jets are reconstructed from stable particles (lifetime longer than 3×10^{-11} s) using the anti-k_t algorithm with a radius parameter $R = 0.4$, and are required to have $p_T > 15$ GeV and $|\eta| < 2.5$. The flavour of a jet is determined by counting the number of b or c hadrons within $\Delta R < 0.4$ of the jet axis. Jets matched to at least one b hadron with p_T above 5 GeV are labelled b jets. Jets not labelled as b jets and matched to at least one c hadron with p_T above 5 GeV are labelled c jets. Events with at least one b jet besides the products of the $t\bar{t}$ decay are labelled as $t\bar{t} + \geq 1b$ and those with no b jets but at least one c jet are labelled as $t\bar{t}+\geq 1c$. Finally, events not containing any heavy-flavour jets aside from the $t\bar{t}$ decay chain are labelled as $t\bar{t}+$ light. These three $t\bar{t}+$jets components receive separate treatments in many aspects of the analyses.

6.3.2 $t\bar{t}+\geq 1b$

Production of $t\bar{t}+\geq 1b$ at the LHC is dominated by the QCD-mediated $t\bar{t}+b\bar{b}$ process. At LO, the cross-section of $t\bar{t}+b\bar{b}$ production has a dependence on the fourth power of the strong coupling constant α_S, making it particularly sensitive to variations of the renormalisation scale [128]. Even at NLO, the production cross-section sees a 20-30% impact from varying this scale up and down by a factor two, which is a conventional way to estimate the uncertainty due to missing higher-order contributions. One of the challenges in calculations of the $t\bar{t}+b\bar{b}$ process is that it is a process characterised by two different energy scales: that of the $t\bar{t}$ system, at $\sim 500\,\text{GeV}$, and that of the $b\bar{b}$ system, at a few tens of GeV. This must be taken into account when choosing the renormalisation scale in order to avoid potentially large corrections beyond NLO. Different approaches may be used to generate $t\bar{t}+b\bar{b}$ events.

One possible approach is to use a $t\bar{t}$ ME at NLO in the 5FS. Additional b jets arise from $b\bar{b}$ pairs due to $g\to b\bar{b}$ splittings generated by the PS and, to a lesser extent, in the ME process $gb\to t\bar{t}b$, since the b quark is an available initial-state parton in the five flavour PDFs. Both cases are described by a $t\bar{t}+j$ ME, which is only LO-accurate in this prediction. Furthermore, the b jet observables depend largely on the modelling of the PS that governs the gluon splittings. The upside of this dependence is that PS models provide enough freedom to allow accurate tuning to data.

Another option is to use a $t\bar{t}+b\bar{b}$ ME at NLO in the 4FS. This approach avoids the large dependence on the PS because the $g\to b\bar{b}$ splitting is always included in the ME. Divergences due to gluon splittings are prevented by the non-zero b quark mass in the 4FS. It has been shown that $t\bar{t}+\geq 1b$ production is dominated by $t\bar{t}g$ production followed by gluon splittings into $b\bar{b}$, which supports the use of this prescription. This estimate covers the full phase-space of $t\bar{t} + \geq 1b$, with up to two additional b jets. It also provides NLO accuracy on observables involving the additional b jets. A practical advantage of this approach is that the bulk of generated events are in the $t\bar{t} + \geq 1b$ category, while in the previous prescriptions the whole $t\bar{t}$ + jets phase-space must be generated, out of which only a small fraction of events corresponds to $t\bar{t} + \geq 1b$. Figure 6.2 shows two example diagrams of $t\bar{t} + b\bar{b}$ production, highlighting the vertices and lines whose treatment depends on the prescription used.

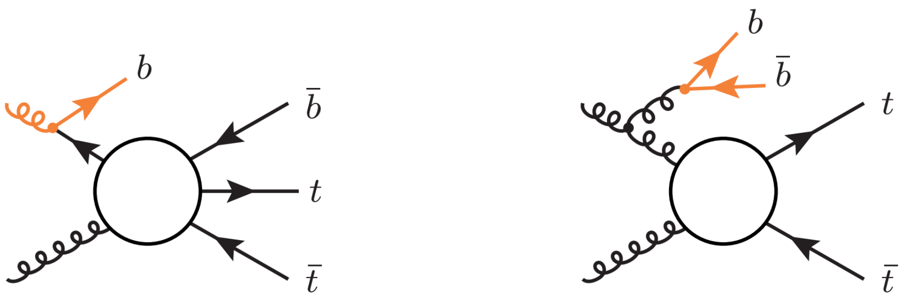

Figure 6.2: Example diagrams of $t\bar{t} + b\bar{b}$ production, with the $b\bar{b}$ pair resulting from initial-state (left) and final-state (right) gluon splittings [128]. In the $t\bar{t}$ NLO 5FS prescription, the ME provides the part of the process represented in black, while the elements in orange are generated by the PS. In the $t\bar{t} + b\bar{b}$ NLO 4FS prescription, both processes are fully covered by the ME.

Considering the theoretical arguments presented above, the Powheg-Box+Pythia8 $t\bar{t} + b\bar{b}$ 4FS sample is used as the nominal prediction for $t\bar{t} + \geq 1b$ in the analyses. This choice was also supported by comparisons between data and simulation in signal-depleted analysis regions. A BDT was trained to classify events as originating from either the $t\bar{t} + b\bar{b}$ sample or the $t\bar{t}$ inclusive sample. This resulted in significantly different predictions for the distribution of the BDT score, where the Powheg-Box+Pythia8 $t\bar{t} + b\bar{b}$ sample was found to agree better with the data. The normalisation of this sample is given directly by the cross-section predicted by the generator. However, this is only used as a reference: the normalisation of the $t\bar{t} + \geq 1b$ background is let free-floating in the fits, acquiring the value that best adjusts to data, without any prior constraint.

6.3.3 $t\bar{t}+$ light and $t\bar{t}+\geq 1c$

For $t\bar{t}+\geq 1c$ and $t\bar{t}+$ light events, the PowhegBox+Pythia8 $t\bar{t}$ 5FS sample is used. The $t\bar{t}+$ light prediction benefits from precise measurements in data of the $t\bar{t}+$jets process, of which $t\bar{t}+$ light is the dominant component. However, the smaller $t\bar{t}+\geq 1c$ component is relatively more important in the analyses discussed here, since $t\bar{t}+\geq 1c$ events are more likely to meet the b-tagging requirements made. For this reason, $t\bar{t}+\geq 1c$ and $t\bar{t}+$ light are treated as independent processes in the analysis, each with its own modelling uncertainties. The sample is normalised to a cross section of 832 pb, which is the central value of the predicted $t\bar{t}$ cross-section calculated at next-to-next-to leading order (NNLO) in QCD, including resummation of next-to-next-to-leading logarithmic (NNLL) soft gluon terms with top++2.0, for a top quark mass of 172.5 GeV [141, 142].

6.3.4 Other backgrounds

For the modelling of single top production (t-channel, s-channel and tW), the PowhegBox+Pythia8 samples are employed. These samples are normalised using the theory prediction calculated at NLO in QCD with Hathor [143, 144] for t- and s-channel, and using the theory prediction calculated at NLO in QCD with NNLL soft gluon corrections for tW production [145].

The $t\bar{t}V$, $t\bar{t}t\bar{t}$, tZq, and tWZ backgrounds are modelled using the MadGraph5_aMC@NLO+Pythia8 MC samples. The tH production process is considered as background in the cross-section analysis, and modelled using the MadGraph5_aMC@NLO+Pythia8 SM samples.

The single and pair production of vector bosons in association with jets is modelled using the Sherpa samples. The V+jets samples are normalised to an NNLO prediction [146]. The normalisation of the Z+jets sample is scaled to match the data in a region closer to the analysis regions, with a b jet requirement.

The estimation of the background due to fake and non-prompt leptons in the dilepton channel relies on the full set of nominal background samples. Events with fake and non-prompt leptons in those samples are subject to a data-driven correction, derived in regions with same-charge lepton pairs. In the single-lepton channel, this background was found to be negligible in the selected phase-space. This was done by verifying that the level of agreement between data and prediction, in regions sensitive to this background, does not depend on the lepton isolation criteria.

Higgs boson production processes other than those associated with top quarks were found to be negligible and are not considered.

6.4 Systematic uncertainties

Many sources of systematic uncertainty affect these analyses. Different sources may affect only the normalisation of the samples (total number of events in the phase-space selected by the analyses), only the shape (distribution of the events across the analysis regions and bins), or both. All the considered sources of experimental uncertainty, with the exception of the uncertainty on luminosity, affect both the normalisation and shape of samples. Regarding modelling uncertainties, the three kinds of sources exist: cross-section uncertainties affect normalisation only, uncertainties related to $t\bar{t} + \geq 1b$ modelling only affect shape, while all the other modelling uncertainty sources affect both shape and normalisation. Aside from cross-section uncertainties, modelling uncertainties are estimated in such a way as to not have an impact on the inclusive cross-section of the corresponding process. This does not mean that they will not have an impact in the normalisation, since the fraction of events accepted in the phase-space of the analysis is in general affected.

Unless explicitly specified, each uncertainty source has a correlated effect across all the analysis regions. Additionally, experimental uncertainty sources have their impact correlated across all samples.

There are differences in signal modelling uncertainties between the cross-section and the $\mathcal{CP}$ analyses and, for that reason, they are not detailed in this section, but rather in the chapter of the respective analysis.

6.4.1 Experimental

Luminosity and pile-up modelling

The uncertainty on the integrated luminosity only has an effect on normalisations. For the full Run 2 dataset, it is 1.7% [147]. The uncertainty in the ratio between predicted and measured pile-up is taken into account by a variation of the pile-up dependent weights used on simulated events.

Detector objects

Reconstruction of physics objects is not perfectly modelled by simulation. Thus, different efficiencies with respect to data are compensated by using scale factors as event weights in simulation. These scale factors are derived with uncertainties, which must be propagated. In these analyses, leptons have scale factor uncertainties associated with selection by the trigger, reconstruction, identification, and isolation. In total, there are 4 such components for electrons and 10 for muons. Jets have one scale factor uncertainty associated with JVT and 85 associated with *b*-tagging. The latter are divided into those related to the tagging of true *b* jets (45 sources) and those related to the *b*-(mis)tagging of *c* and light-flavour jets (20 sources each). The large number of sources is due to the use of PC *b*-tagging and the parameterisation of the scale factors as a function of jet p_T.

The energy or momentum scales of objects and their corresponding resolutions also behave differently between data and simulation. Corrections are applied on simulation to account for this, and the uncertainties on these corrections affect the analyses. In the case of energy or momentum scales, the impact is estimated by re-doing the event selection with the associated quantities affected by $\pm 1\sigma$. For jets, there are 31 sources of energy scale uncertainty, among which are those related to jet flavour, pile-up corrections, η dependence, and high-p_T jets. To account for energy/momentum resolution effects, the event selection is re-done after smearing the corresponding quantity in the event. Altogether, energy/momentum scales and resolutions account for 3 uncertainty components for electrons, 5 for muons, 40 for jets and 3 for the soft term of missing E_T.

6.4.2 Background modelling

$t\bar{t}$+jets

An uncertainty of $\pm 6\%$ is assumed for the $t\bar{t}+$ light cross-section based on the prediction at NNLO+NNLL for inclusive $t\bar{t}$ production. This value includes effects from varying the factorisation and renormalisation scales (μ_r and μ_f, respectively), the PDFs, α_S, and the top quark mass [148]. An uncertainty of 100% on the normalisation of the $t\bar{t}+\geq 1c$ sample is applied. No uncertainty on the normalisation of $t\bar{t}+\geq 1b$ is considered, since it is to be inferred from the data simultaneously with the signal properties. All the uncertainty sources in $t\bar{t}+$ jets modelling are decorrelated among the $t\bar{t}+\geq 1b$, $t\bar{t}+\geq 1c$ and $t\bar{t}+$ light processes.

Since the $t\bar{t}+\geq 1b$ normalisation is measured in the data, it is convenient to ensure that $t\bar{t}+\geq 1b$ modelling uncertainties only affect shape. In practice, the alternative predictions that are compared to the nominal for estimating uncertainties are normalised to the nominal before the comparison. It should be stressed that the full analysis phase-space is considered for this correction, such that $t\bar{t}+\geq 1b$ modelling uncertainties still impact the number of events in each of the analysis regions.

An uncertainty is assigned to the relative importance of the $t\bar{t}+1b$ and $t\bar{t}+\geq 2b$ subcomponents of the $t\bar{t}+\geq 1b$ background. The ratio between the $t\bar{t}+1b$ and $t\bar{t}+\geq 2b$ fractions in the analysis phase-space is given a relative uncertainty of 75% upwards and 49% downwards, resulting in a shape-only effect on $t\bar{t}+\geq 1b$. This relative variation is the largest one obtained when comparing any two $t\bar{t}+\geq 1b$ predictions. In particular, it results from the comparison between the PowhegBox+Pythia8 and PowhegBox+Herwig7 $t\bar{t}$ samples. Since this uncertainty in the $1b/2b$ ratio is included explicitly, a correction is applied to other modelling uncertainties of $t\bar{t}+\geq 1b$ such that they have no impact on this ratio.

Uncertainties associated with the modelling of $t\bar{t} + \geq 1b$, $t\bar{t} + \geq 1c$ and $t\bar{t} +$ light by the nominal MC samples are also considered, leading to 4 independent sources for each of these $t\bar{t} +$ jets components (12 in total). For uncertainties in the modelling of initial-state radiation (ISR) and final-state radiation (FSR), event weights are available in the nominal samples that provide predictions with varied scales. Up variations correspond to multiplying scales by a factor close to 0.5, while down variations correspond to factors close to 2. Decreasing a scale corresponds to increasing α_S in a certain component of the event generation, thus increasing the associated amount of radiation. The uncertainty due to ISR is estimated by simultaneously changing μ_r and μ_f in the ME and the renormalisation scale for ISR emissions (μ_r^{ISR}) in the PS. For the FSR, μ_r^{FSR} is changed in the PS. For the uncertainties due to the PS and hadronisation model and due to the NLO matching scheme, no alternative samples of 4FS $t\bar{t} + b\bar{b}$ were available. Therefore, in order to estimate these uncertainties on $t\bar{t} + \geq 1b$, comparisons are made between $t\bar{t} + \geq 1b$ estimates from 5FS $t\bar{t}$ samples, as is done for $t\bar{t} + \geq 1c$ and $t\bar{t} +$ light. The nominal PowhegBox+Pythia8 sample is compared to the PowhegBox+Herwig7 sample to assess the effect of the PS and hadronisation models, and to the MadGraph5_aMC@NLO+Pythia8 sample to assess the effect of the NLO matching technique.

Comparing the predictions from two 5FS $t\bar{t}$ setups to estimate the effects of PS and hadronisation model and NLO matching technique choices on $t\bar{t} + \geq 1b$ may be seen as inadequate. As discussed in Section 6.3.2, the observables on the additional b jets are described at NLO with the $t\bar{t} + b\bar{b}$ samples, while they are described by the PS in the $t\bar{t}$ samples. Therefore, the impact of NLO matching and PS modelling choice is expected to be larger in the $t\bar{t}$ predictions than in the $t\bar{t} + b\bar{b}$ predictions for the observables relevant for these analyses. Although not ideal, these uncertainty estimates may at least be regarded as conservative and were kept due to the lack of viable alternatives.

Additional systematic uncertainties are included for the dominant $t\bar{t} + \geq 1b$ background, depending on the analysis. In the cross-section analysis, the p_T distribution of the Higgs candidate b-jet pair ($p_T^{b\bar{b}}$) is used as an observable in the signal regions. Significant mismodelling of this distribution is observed, and for that reason an uncertainty is included in order to account for it. The upwards variation is derived in such a way as to bring the predicted binned distribution of $p_T^{b\bar{b}}$ to a perfect agreement with data. The derivation of the NLO matching and the PS and hadronisation from 5FS $t\bar{t}$ predictions does not provide enough confidence in the estimated correlation of their impact across regions. For this reason, both uncertainties are decorrelated between the single-lepton and the dilepton channels. Besides this, the uncertainty due to NLO matching is decorrelated between signal and control regions and, within the signal regions, it is decorrelated across the bins of $p_T^{b\bar{b}}$. In the $\mathcal{CP}$ analysis, an uncertainty due to the choice of prescription – ME and flavour scheme – is considered, by comparing the nominal 4FS $t\bar{t} + b\bar{b}$ sample to the 5FS PowhegBox+Pythia8 $t\bar{t}$ sample. This was found to be necessary because the difference between the two predictions in some of the distributions of $\mathcal{CP}$-discriminant observables was not covered by other uncertainties.

The different systematic uncertainties affecting the modelling of the $t\bar{t}$ + jets background are summarised in Table 6.1.

Table 6.1: Summary of the sources of systematic uncertainty for $t\bar{t}$ + jets modelling. The $t\bar{t} + \geq 1b$ uncertainties are evaluated in such a way as to have no impact on the normalisation of $t\bar{t} + \geq 1b$. Due to the inclusion of the uncertainty on the $1b/2b$ ratio, all other $t\bar{t} + \geq 1b$ uncertainties are corrected in order to have no impact on that ratio.

Uncertainty source	Description	Components
$t\bar{t}$ cross-section	Up or down by 6%	$t\bar{t}$ + light
$t\bar{t} + \geq 1c$ normalisation	Up or down by 100%	$t\bar{t} + \geq 1c$
$1b/2b$ ratio	Up by 75% or down by 49%	$t\bar{t} + \geq 1b$
ISR	Varying μ_R^{ISR} (PS), μ_R and μ_F (ME)	All
FSR	Varying μ_R^{FSR} (PS)	All
NLO matching	MadGraph5_aMC@NLO vs. PowhegBox	All
PS and hadronisation	Herwig7 vs. Pythia8	All
$p_T^{b\bar{b}}$ shape (cross-section analysis only)	Data-driven correction of $p_T^{b\bar{b}}$ shape	$t\bar{t} + \geq 1b$
ME and FS ($\mathcal{CP}$ analysis only)	$t\bar{t}$ (5FS) vs. $t\bar{t} + b\bar{b}$ (4FS)	$t\bar{t} + \geq 1b$

Other backgrounds

A ±5% uncertainty is considered for the cross-sections of the three single top production modes [149]. Uncertainties associated with the PS and hadronisation model and with the NLO matching scheme are evaluated by comparing, for each process, the nominal PowhegBox+Pythia8 sample to samples produced using PowhegBox+Herwig7 and MadGraph5_aMC@NLO+Pythia8, respectively. The uncertainty associated with the interference between tW and $t\bar{t}$ production at NLO is assessed by comparing the nominal sample produced using the diagram removal scheme to an alternative sample produced using the diagram subtraction scheme.

Modelling uncertainties on the $t\bar{t}V$ background are similar for the $t\bar{t}W$ and $t\bar{t}Z$ components, but decorrelated between the two. The uncertainty on the NLO cross-section prediction is 15% [150, 151], split into a PDF source and a QCD scales source. An additional $t\bar{t}V$ modelling uncertainty, simultaneously related to the choice of PS and hadronisation model and NLO matching scheme is assessed by comparing the nominal MadGraph5_aMC@NLO+Pythia8 samples with the alternative ones generated with Sherpa.

A total 50% normalisation uncertainty is considered for the $t\bar{t}t\bar{t}$ background, covering effects from varying μ_r and μ_f, PDFs and α_S. The small backgrounds from tZq and tWZ are each assigned cross-section uncertainties: for tZq, ±7.9% accounting for μ_r and μ_f variations and ±0.9% accounting for PDFs; for tWZ, a single uncertainty of ±50%.

An uncertainty of 40% is assumed for the W+jets cross-section, with an additional 30% normalisation uncertainty used for W + heavy-flavour jets, decorrelated between events with two and more than two heavy-flavour jets. These uncertainties are based on variations of μ_r and μ_f in the Sherpa samples. An uncertainty of 35% is applied to the Z+jets normalisation, to account for the effects of scale variations and for the uncertainty in deriving from data the normalisation of the heavy-flavour component. This uncertainty is decorrelated between the single-lepton and dilepton channels and between the 3-jet and $\geq$4-jet regions in the dilepton channel. A total 50% normalisation uncertainty in the diboson background is assumed, estimated from comparisons of cross-sections and jet multiplicity distributions obtained from different generators.

Table 6.2 summarises all the systematic uncertainties considered in the analyses, with a count of the independent components and the indication of whether they affect only the normalisation (N), only shapes (S), or both (NS). The signal uncertainties are included for completeness of the table, although they are only described in detail in the following chapters. In the cases where the number of components differs between the cross-section and $\mathcal{CP}$ analyses, they are both shown in the format $n_{\text{cross-section}}/n_{\mathcal{CP}}$.

6.5 Profile-likelihood fit

A binned profile-likelihood fit is used to perform the measurements. The observable inputs to the fit are absolute-frequency histograms of a discriminant variable for each of the analysis regions. The signal and background contributions are adjusted, such that the total prediction best fits the data. This fit is made by simultaneously varying parameters that affect shapes and normalisations of both signal and background processes.

A likelihood function is constructed to allow the fitting procedure [152]. It is proportional to the probability for a model with given parameter values to yield the observed data. This is realised by the product of Poisson probabilities over all bins considered in the analysis, each Poisson term having the form $P(n^{\text{obs}}|n^{\text{exp}})$, where the mean value n^{exp} is the expected number of events for that bin given the parameter values, and n^{obs} is the number of data events in that bin. The best-fit set of parameter values is estimated as the one which maximises the likelihood function.

The fit model includes free parameters $\vec{\phi}$ and constrained parameters $\vec{\theta}$. A constrained parameter is used for each source of systematic uncer-

Table 6.2: Summary of systematic uncertainties included in the analyses. Type 'N' only affects normalisation, type 'S' only affects shapes, and type 'SN' affects both. For the modelling uncertainties of $t\bar{t}H$, tH and $t\bar{t} + \geq 1b$, there are differences between the cross-section and the $\mathcal{CP}$ analyses and the number of components is given as $n_{\text{cross-section}}/n_{\mathcal{CP}}$.

Systematic uncertainty	Type	No. of components
Luminosity	N	1
Pile-up modelling	SN	1
Detector Objects		
Electrons	SN	7
Muons	SN	15
b-tagging	SN	85
Jet energy scale/resolution, JVT	SN	41
Missing E_T	SN	3
Signal modelling		
H branching fractions	N	3
$t\bar{t}H$ cross-section	N	2
$t\bar{t}H$ modelling	SN	9/4
tH modelling	SN	0/4
$t\bar{t}$+jets modelling		
$t\bar{t}$ + light cross-section	N	1
$t\bar{t} + \geq 1c$ normalisation	N	1
$t\bar{t}$ + light modelling	SN	4
$t\bar{t} + \geq 1c$ modelling	SN	4
$t\bar{t} + \geq 1b$ modelling	S	17/6
Other background modelling		
$t\bar{t}V$ cross-section	N	4
$t\bar{t}V$ modelling	SN	2
Single top cross-section	N	3
Single top modelling	SN	7
Rare top processes cross-section	N	4
V+jets, VV normalisation	N	7

tainty, to allow adjustments to the predictions that respect the size of the uncertainty considered. For each θ_i, the nominal prediction is mapped to the value 0, the predictions from the upwards and downwards variations of the corresponding source of uncertainty are mapped to ± 1, and all other values are obtained by interpolation/extrapolation. For systematic uncertainties defined by comparing two MC setups, the alternative setup is defined as the upwards variation, and the downwards variation is obtained by symmetrising its effect. The systematic uncertainty due to limited statistics of MC samples is accounted for by a set of constrained parameters, one for each analysis bin, affecting the total prediction in that bin by an amount equal to the sum in quadrature of the MC event weights in that bin. The θ_i should not vary freely, but rather in a constrained way, compatible with the size of the uncertainties. This is achieved with prior distributions – penalty factors – of the form $C(\theta_i)$. A Gaussian constraint is used for most constrained parameters, with mean value and standard deviation equal to 0 and 1, respectively. The exceptions are those related to the limited statistics of the MC samples, which are given Poisson constraints instead. The constraint terms strongly reduce the likelihood if there are large shifts in the respective parameters. In summary, the likelihood function may be written as

$$\mathcal{L}(\vec{\phi}, \vec{\theta}) = \prod_{i \in \text{bins}} P(n_i^{\text{obs}} | n_i^{\text{exp}}(\vec{\phi}, \vec{\theta})) \prod_{\theta_j} C(\theta_j), \tag{6.1}$$

which could be worded as the probability of the data given the parameters times the prior probability of the constrained parameters. The first factor, which includes the free parameters and the data, is purely frequentist. The second factor, regarding constrained parameters, is of a Bayesian nature, as it makes a statement about the probability distribution of parameter values, estimated from previous measurements or theoretical considerations.

In the context of analysis, the classification of parameters into parameters of interest and nuisance parameters is used. The parameters of interest are those that the analyses aim to measure and they are free parameters affecting the signal: the $t\bar{t}H$ signal strength μ, in the cross-section analysis, and the $\mathcal{CP}$-mixing angle α and the coupling modifier κ_t', in the $\mathcal{CP}$ analysis. The nuisance parameters include the free parameter $k(t\bar{t} + \geq 1b)$, which is the $t\bar{t} + \geq 1b$ normalisation factor, and all the constrained parameters corresponding to systematic uncertainties.

In practice, the problem of maximising the likelihood function is turned into the minimisation of the negative log-likelihood (NLL)

$-\ln \mathcal{L}(\vec{\phi}, \vec{\theta})$. This minimisation, in a space with number of dimensions of order 100, is performed iteratively: at each step, the gradient and the Hessian matrix of the NLL are computed through finite methods. A distance to the minimum is estimated, as well as a tentative direction towards it. A search for a minimum along that direction is performed, and the minimiser evolves to the position found. The process is repeated until the estimated distance to the minimum falls below a given threshold. At the end, the best-fit parameter values are returned. Besides that, the parameter uncertainties and a matrix of correlation coefficients are obtained from the Hessian matrix.

The frequentist factors in the likelihood disfavour disagreements between data and prediction. For this reason, the uncertainties on nuisance parameters may be constrained by data during the fit, becoming smaller than they are originally in the prior distributions. Thus, inclusion of control regions with high statistics in a profile-likelihood fit is an effective strategy for reducing the impact of systematic uncertainties on the measurement. The control region selections should not be too different from the signal region ones, since the validity of extrapolating parameters among regions is assumed.

6.5.1 Likelihood scans

The parameter uncertainties obtained from the Hessian matrix are only approximate and always symmetric around the best-fit value. The underlying assumption made is that, near the minimum, the NLL is quadratic in the parameters. In the $\mathcal{CP}$ analysis, this is a bad approximation for α. In the cross-section analysis, the approximation works better, but an assessment as accurate as possible of the uncertainty in μ is desirable. For these reasons, the actual NLL values away from the minimum are used to obtain the uncertainties in the parameters of interest, as well as in the normalisations of $t\bar{t} + \geq 1b$ and $t\bar{t} + \geq 1c$.

Considering some parameter p', which is a component of $\vec{\phi}$ or $\vec{\theta}$, a test statistic q_p is defined as:

$$q_p = -2 \ln \frac{\mathcal{L}(\hat{\hat{\vec{\phi}}}[p], \hat{\hat{\vec{\theta}}}[p])}{\mathcal{L}(\hat{\vec{\phi}}, \hat{\vec{\theta}})}, \tag{6.2}$$

where $\hat{\vec{\phi}}$ and $\hat{\vec{\theta}}$ are the values of the parameters that globally maximise the likelihood function, while $\hat{\hat{\vec{\phi}}}[p]$ and $\hat{\hat{\vec{\theta}}}[p]$ are the parameter values that maximise the likelihood function, under the constraint that the parameter p' is fixed to p. For likelihoods derived from sufficiently large numbers, it is shown in Wilks' theorem that, if p is the true value of p', the values of q_p, across an ensemble of measurements, are distributed as a χ^2 distribution with one degree-of-freedom (χ^2_1) [153]. Thus, a particular value p can be excluded with confidence level equal to the cumulative χ^2_1 distribution up to the observed q_p. Instead of using the probability to express a confidence level, a significance may be preferred. Given a probability, the corresponding significance is defined as the distance, in number of standard deviations (σ), of a number x to the mean value x_0 of a normal distribution, such that the two-sided integral from $x_0 - x$ to $x_0 + x$ of the normal distribution covers the same probability. The confidence interval of p' at a confidence level l is the (possibly disjoint) set of values of p' that cannot be excluded with a confidence level l or higher. The confidence intervals at $l = 68\%$ are used as the uncertainties on the parameters of interest and on the $t\bar{t} + \geq 1b$ and $t\bar{t} + \geq 1c$ normalisation factors. One-dimensional scans of q_p may be performed, in which all the other parameters are said to be profiled. In the case of α, studying the test statistic across the allowed α range $[-\pi, \pi]$ is necessary due to features such as the possibility of multiple local minima.

In the $\mathcal{CP}$ analysis, it is also interesting to simultaneously measure α and the coupling modifier κ'_t. The best-fit values are necessarily defined as before. But the test statistic now depends on two parameters. Analogously to the previous case, and naming the additional parameter r', it becomes

$$q_{p,r} = -2\ln \frac{\mathcal{L}(\hat{\hat{\vec{\phi}}}[p,r], \hat{\hat{\vec{\theta}}}[p,r])}{\mathcal{L}(\hat{\vec{\phi}}, \hat{\vec{\theta}})}. \tag{6.3}$$

From the theorem of Wilks, this test statistic is distributed as a χ^2_2 distribution (two degrees of freedom). The set of points that cannot be excluded with a confidence level l define a confidence region in the (p', r') plane, at a confidence level l. Two-dimensional scans of q_{α,κ'_t} are performed in the $\mathcal{CP}$ analysis. They are represented in the $(\kappa_t, \tilde{\kappa}_t)$ coordinates, where the boundaries of the confidence regions are represented as contours.

6.5.2 Asimov dataset

The expected results of the analyses are obtained from fits to Asimov datasets. The Asimov dataset is an artificial dataset built by making each of the measured observables exactly equal to its nominal expected value. The obtained best-fit parameter values from this fit are necessarily the nominal ones. Valuable information provided by fitting the Asimov dataset includes the expected uncertainty on the parameters of interest and the expected significances for hypothesis exclusion. Besides, it is useful to learn about the behaviour of systematic uncertainties: to what extent they are expected to be constrained by the data, how correlated they are among each other and how much impact they have on the parameters of interest.

6.5.3 Pruning, smoothing and symmetrisation of systematic uncertainties

As a measure to reduce the computational time of the minimisation procedure, a selective rejection of systematic uncertainties, called 'pruning', is employed. A systematic uncertainty is pruned from the fit if its size is below 0.5%. This evaluation and the pruning itself are done separately for each sample in the analysis, and separately for the shape and normalisation components within each region. It was verified that pruning with such a low threshold has no impact on the results.

In order to cope with statistical fluctuations in the MC samples used to estimate the systematic uncertainties, symmetrisation and smoothing strategies were applied. Symmetrisation replaces the magnitude of the upwards and downwards variations by the average of the original magnitudes, bin by bin. This makes use of the assumption that the nominal value should lie in the midpoint between the upwards and downwards variations, eliminating any asymmetries that could originate from fluctuations due to limited statistics. For smoothing, an algorithm is applied to the histogram of the relative size of each systematic uncertainty, for each of the analysis regions. The algorithm attempts to mitigate peaks and migrations between bins resulting from fluctuations, while keeping the physical effect of the uncertainty, assumed to have a smooth shape. The smoothing algorithms used start by merging neighbouring bins whose values are compatible within statistical uncertainties. The merging is followed by the application of running averages or medians in order to produce the desired smooth output.

Chapter 7

Common analysis strategy

The $t\bar{t}H(H \to b\bar{b})$ cross-section and $\mathcal{CP}$ analyses target the same final state and select the same phase-space, resulting in a large overlap in the analysis strategies. The common trunk of the two strategies is described in this chapter. Event selection and reconstruction of the $t\bar{t}H$ system are discussed in Sections 7.1 and 7.2, respectively. In Section 7.3, the multivariate methods used for signal/background classification are described.

7.1 Event selection

7.1.1 Trigger

The analysed events are recorded by the loosest unprescaled single-lepton triggers. Events are required to either pass the trigger with lowest p_T threshold and with a lepton isolation requirement, or triggers with higher thresholds but with looser identification criteria and without any isolation requirement. The lowest p_T threshold at trigger level used for muons is 20 (26) GeV, while for electrons the threshold is 24 (26) GeV in 2015 (2016-2018).

7.1.2 Pre-selection

Two main channels are targeted by the analyses: single lepton and dilepton. For both channels, events are required to have at least one reconstructed lepton (e or μ) with $p_T > 27$ GeV matching a lepton with the same flavour reconstructed by the trigger algorithm within $\Delta R < 0.15$. The lepton p_T cut ensures the full efficiency of the single-lepton triggers used. Events in the single-lepton channel must have exactly one lepton, while in the dilepton channel they must have exactly two leptons with opposite electric charge. In the ee and $\mu\mu$ categories of the dilepton channel, the dilepton invariant mass must be above 15 GeV and outside of the Z boson mass window between 83 GeV and 99 GeV. To maintain orthogonality with analyses of other $t\bar{t}H$ channels, events are vetoed if they contain one or more τ leptons in the dilepton channel or at least two τ leptons in the single-lepton channel. To improve the purity in dilepton and single-lepton events, leptons are further required to satisfy additional identification and isolation criteria, otherwise the corresponding events are removed.

Within the single-lepton channel, events are selected into the 'boosted' channel if they have at least one boosted Higgs candidate and at least two small-R jets b-tagged with the 77% WP that are not constituents of the Higgs candidate. Events failing the boosted selection are classified in the single-lepton 'resolved' channel if they have at least five jets, at least four of which b-tagged using the 70% WP. In the dilepton channel, which is also a resolved channel, events are required to have at least three jets, of which at least three must be b-tagged using the 70% WP.

7.1.3 Control regions and inclusive signal regions

After the pre-selection, the selected phase-space is dominated by background from $t\bar{t}$ events. In order to take advantage of the higher jet and b-jet multiplicities of the $t\bar{t}H$ signal process, events in the dilepton and single-lepton resolved channels are classified into analysis regions based on the total number of jets, as well as the number of b-tagged jets using the 70% and 60% WPs, in a way that ensures orthogonality between the regions. The definitions of the resolved regions into which the selected events are classified are summarised in Table 7.1 and described below.

Events in each of the resolved channels are first classified according to the number of jets: three or at least four in the dilepton channel and five or at least six in the single-lepton channel. Then, a region is defined in each channel from events in the highest jet multiplicity category and with at least four b-tagged jets at the 70% WP. These regions, where $t\bar{t}H$ and $t\bar{t} + \geq 1b$ are enhanced relative to the other backgrounds, are referred to as 'inclusive signal regions' (grey text in Table 7.1). The reason for the term 'inclusive' is that these regions are further split, in different ways, in the cross-section analysis and in the $\mathcal{CP}$ analysis. In the dilepton channel,

Table 7.1: Summary of the resolved region splitting common to the cross-section and $\mathcal{CP}$ analyses. These non-overlapping regions are defined by number of leptons, number of jets and number of b-tagged jets using the 60% and 70% WPs. Only events not passing the boosted selection are considered for the single-lepton resolved regions.

Region	No. of leptons	No. of jets	No. of b-tagged jets 70% WP	No. of b-tagged jets 60% WP
4j4b	$= 2$	≥ 4	≥ 4	-
4jhi			$= 3$	$= 3$
4jlo				< 3
3j		$= 3$		$= 3$
6j4b	$= 1$	≥ 6	≥ 4	-
5jlo		$= 5$		< 4
5jhi				≥ 4

the inclusive signal region is called '4j4b', and in the resolved single-lepton channel it is called '6j4b'. It is important to ensure that the analysis strategy is not biased by the observed data in these signal-enriched regions. To address that concern, a blinding procedure was adopted during the strategy definition and optimisation: in all comparisons and fits performed, data was only made available in regions or bins where the predicted signal-to-background ratio was below 7.7%.

Resolved regions with lower multiplicities of jets or b-tagged jets are referred to as 'control regions' (blue text in Table 7.1). In these regions that are signal-depleted, yet close to the signal regions, the data provides constraints on the background model during the fit procedure. There are 5 such regions, defined by number of jets and number of b-tagged jets using the 60% and 70% WPs. The labels of 'inclusive signal region' and 'control region' are only used to elucidate the main role of each region in the analyses, the two kinds of region are not treated any differently in the profile-likelihood fits.

In the dilepton channel, the '3j' region is defined by requiring exactly three jets in the event, all b-tagged with the 60% WP. Two additional control regions are defined from events with at least four jets but less than four b-tagged jets with the 70% WP, thus not selected into 4j4b. In the '4jlo' ('4jhi') control region, events are required to have exactly three b-tagged jets with the 70% WP and less than three (exactly three) jets b-tagged with the 60% WP[1].

In the single-lepton resolved channel, events in the '5jlo' and '5jhi' control regions are required to have exactly five jets, of which at least four should be b-tagged using the 70% WP. The separation into 'lo' and 'hi' corresponds to less than four or at least four b-tagged jets using the 60% WP, respectively.

For the profile-likelihood fit, the observables used from the dilepton control regions are the event yields in each of the regions. The large statistics in those regions is sufficient to constrain $t\bar{t}+$jets modelling systematic uncertainties. Besides, since only three b-tagged jets are selected, the proximity of this phase-space to the signal regions is not enough to ensure that shape information can be extrapolated from it. In each of the single-lepton control regions, a distribution with six bins is used. The distribution is that of $\Delta R_{bb}^{\text{avg}}$, the average ΔR separation between pairs of jets among the four jets with highest PC b-tagging score in the event. Here, since the number of b-tagged jets is the same as in the signal regions, the confidence in shape information is better motivated. This observable is a highly-ranked input variable to the BDT used in the 6j4b region to discriminate signal from backgrounds, such that any correction of shapes in the control regions is expected to improve the background modelling in the signal regions, where the BDT is used.

7.2 Kinematic reconstruction

Optimal separation between $t\bar{t}H$ signal and backgrounds, as well as separation between different $\mathcal{CP}$ scenarios, requires access to the kinematics of top quarks and Higgs bosons. The final state of the $t\bar{t}H$ ($H \to b\bar{b}$) process is composed of many jets resulting from the Higgs boson and top quark decay products, as well as from additional radiation. Many

[1] The terms 'lo' and 'hi' in the region names refer to "lower" and "higher" signal purity, respectively.

combinations of these jets are possible when attempting to reconstruct the signal event topology. Besides, the undetected neutrinos from the leptonic decays of the top quarks make it impossible to retrieve the full information of the event. The strategies used to address these challenges and to perform the full $t\bar{t}H$ system reconstruction are described in this section.

In the single-lepton resolved channel, the leptonically decaying W boson candidate is reconstructed from the lepton four-momentum p_ℓ and the neutrino four-momentum p_ν. The latter is built from the missing E_T plus a z component inferred by solving the equation $m_W^2 = (p_\ell + p_\nu)^2$, where m_W represents the W boson mass. This quadratic equation may have up to two solutions. If no real solutions exist, the discriminant of the quadratic equation is set to zero, giving a unique solution. In the dilepton channel, the missing E_T is also attributed to the neutrinos of the final state. To reconstruct the kinematics of the two leptonically decaying W boson candidates, the neutrino weighting method is used [154].

7.2.1 Reconstruction BDT

In the resolved channels, a 'combination' is defined by a choice of two jets to reconstruct the Higgs boson, the assignment of jets to the b and $\bar{b}$ quarks from the top and anti-top quark decays, a particular solution for the neutrinos and, in the single-lepton case, two jets to reconstruct the hadronically decaying W.

In a first step, b-tagging information is used to discard combinations containing assignments inconsistent with the correct parton candidate flavour. After that, a 'Reconstruction BDT' is used to select, in each event, the most likely correct combination. This BDT is employed in the inclusive signal regions and allows the reconstruction of Higgs boson and top quark candidates. The Reconstruction BDT was trained in simulated $\mathcal{CP}$-even $t\bar{t}H$ events, to distinguish between correct and incorrect combinations, using mostly invariant masses and angular separations as inputs. The full list of input variables to the Reconstruction BDT is given in Appendix B. The toolkit for multivariate analysis (TMVA) [155] within the ROOT framework [156] was used to train this BDT. For each simulated event, one combination labelled as correct was obtained by matching the detector-level objects to the truth-level partons. All other combinations enter the category of incorrect combinations for the training. When the BDT is applied, the combination with the highest (most correct-like) BDT score is picked to proceed with the reconstruction.

Two versions of the Reconstruction BDT are used, the difference between them being that in one version the information related to the Higgs boson candidate is not used. The motivation for this is to avoid a bias in background distributions, for example of the Higgs boson candidate invariant mass, that could ultimately lead to a loss in discrimination. Reconstructed observables given by both prescriptions are used in the analyses.

7.2.2 Boosted top reconstruction

In the boosted channel, after the Higgs candidate is found, additional large-R jets are considered as candidates for a boosted hadronically-decaying top quark, and a resolved leptonic top quark candidate is reconstructed as well. The boosted top quark candidates are required to have $p_T > 300\,\text{GeV}$ and pass a threshold of 0.3 on the DNN output $P(t)$. If more than one candidate is identified, the one with the mass closest to the top quark mass is selected. Afterwards, the leptonic top candidate is reconstructed. If a hadronic top candidate has been found, the reconstruction of the leptonic top is attempted using the lepton, neutrino and, in case it exists, the highest-p_T small-R jet (outside the jet cones of the Higgs and hadronic top candidates) that allows a reconstructed leptonic top mass in the window $[130, 200]\,\text{GeV}$. The neutrino solution chosen is the one that leads to a reconstructed leptonic top quark mass closest to 172.5 GeV. If the boosted hadronic top candidate is not found, small-R jets not overlapping with the Higgs candidate are used to attempt a simultaneous reconstruction of both top quarks. The mass of the hadronic top is required to be in the interval $[70, 195]$ GeV, while the invariant mass of the leptonic top must be within $[130, 200]$ GeV. If there is more than one viable combination, the one with minimum value of $|m_{\text{had. }t} - 172.5| + |m_{\text{lep. }t} - 172.5|$ is considered. In case there are no viable combinations, the hadronic top is reconstructed from the three highest-p_T jets (not overlapping with the Higgs candidate) and the leptonic top is reconstructed using only the lepton and neutrino.

7.3 Signal/background classification

In each of the inclusive signal regions, an additional BDT, called 'Classification BDT', is built to discriminate $t\bar{t}H$ signal from backgrounds, in particular $t\bar{t} + \geq 1b$. Binned distributions of the scores of these Classification BDTs are the observables used in the fit procedure in the cross-section analysis. In the $\mathcal{CP}$ analysis, the scores are used to split the resolved inclusive signal regions into signal-enriched regions, used to measure the signal properties, and signal-depleted regions, used to constrain systematic uncertainties.

The Classification BDTs were trained to discriminate between the $\mathcal{CP}$-even PowhegBox+Pythia8 $t\bar{t}H$ signal and the nominal backgrounds. In the dilepton channel, only the $t\bar{t} + \geq 1b$ process was used as background in the training. In the single-lepton resolved channel, $t\bar{t} + \geq 1c$ and $t\bar{t} +$ light were also included in the training, while in the single-lepton boosted channel, all backgrounds were considered. The Classification BDTs are built by combining several input variables that exploit the different kinematics of signal and background events, as well as the b-tagging information. The input variables include invariant masses and angular separations of pairs of jets and leptons and the PC b-tagging scores of the selected jets. Kinematics of the reconstructed top quarks and Higgs bosons are also used as input, as well as the scores of the Reconstruction BDTs in resolved channels and the DNN outputs in the boosted channel. In the single-lepton resolved channel, a likelihood discriminant (LHD) method – described below – is also used as input to the Classification BDT. The full list of input variables used in the Classification BDTs is given in Appendix B. The training of the Classification BDT was also performed using the TMVA package.

In the boosted channel, an additional requirement is made that events have a Classification BDT score greater than -0.05. In this way, the region of lowest signal purity is rejected, which eliminates most of the $t\bar{t}+$light background, while keeping the sensitivity to signal. The resulting region is also considered an inclusive signal region.

Likelihood discriminant

The main idea of the LHD is to discriminate signal from backgrounds by calculating, for each event, its compatibility with the signal and background hypotheses. Two likelihoods p^{sig} and p^{bkg} are estimated, proportional to the probability of obtaining the observed event under the signal or background hypothesis, respectively. The discriminant itself is defined as $\frac{p^{\text{sig}}}{p^{\text{sig}}+p^{\text{bkg}}}$. Each likelihood is computed using a product of one-dimensional probability density functions (pdfs), therefore not accounting for correlations between variables.

The pdfs used are distributions of invariant masses and angular distributions of systems made of jets, leptons and missing E_T, requiring the choice of a combination. The same variables are used for the signal and background pdfs, and the complete list is given in Appendix B. For building the pdfs, events from a $\mathcal{CP}$-even $t\bar{t}H$ sample were used for the signal hypothesis and $t\bar{t}+\geq 1b$ events were used for the background hypothesis. Only the correct combination of each event, obtained by truth-matching, was considered in this step. When evaluating the LHD, an average is made across all possible combinations, using weights based on b-tagging information to suppress combinations where that information is inconsistent with the assigned parton flavours.

7.4 Pre-fit modelling in control and inclusive signal regions

In this section, the prediction prior to the fit and its comparison with data are presented for the control regions and inclusive signal regions. Figure 7.1 shows the background composition in each of the regions in the form of pie charts, as well as the signal purity S/B and simplified significance $S/\sqrt{B}$, where S and B are the signal and background yields, respectively[2]. The $t\bar{t} + \geq 1b$ background dominates all regions. Moderate contributions from $t\bar{t} + \geq 1c$ exist in all dilepton control regions, in 5jlo and in the boosted region. In particular, a large contribution is present in 4jlo, which allows the normalisation of this background to be constrained. The largest expression of $t\bar{t} +$ light occurs in this region too, and is moderate in 5jlo and in the boosted region. The control region with highest signal purity is 5jhi, due to the requirement of four jets b-tagged at the tightest WP, while all other control regions have purities of at most 3%. The apparent contradiction that 5jhi is considered a control region and yet has a higher signal purity than 6j4b is only resolved after the splitting and binning of 6j4b in the analyses. After that, the purest bins from 6j4b are much more signal-enriched than any bin in 5jhi. The purest inclusive signal region is the boosted region, followed by 4j4b and finally 6j4b.

Figure 7.2 shows the comparison between data and prediction for the event yields in the control regions and inclusive signal regions, as well as the $\Delta R_{bb}^{\text{avg}}$ distributions used in the fit in the 5j regions. In the latter, the result of a χ^2 test is also shown as a metric for the agreement between data and prediction, in that distribution only, taking into account the effect of systematic uncertainties and their correlations. Normalised distributions of $t\bar{t}H$ signal in the $\mathcal{CP}$-even and $\mathcal{CP}$-odd scenarios are also shown, as overlaid dashed lines. Across all regions, there is a significant underestimation of data by the prediction. The nominal $t\bar{t} + \geq 1b$ normalisation is too small to describe the data, and will be increased by the

[2]Using the SM signal prediction as in the $\mathcal{CP}$ analysis, described in section 9.1. Differences with respect to the model used in the cross-section analysis are negligible.

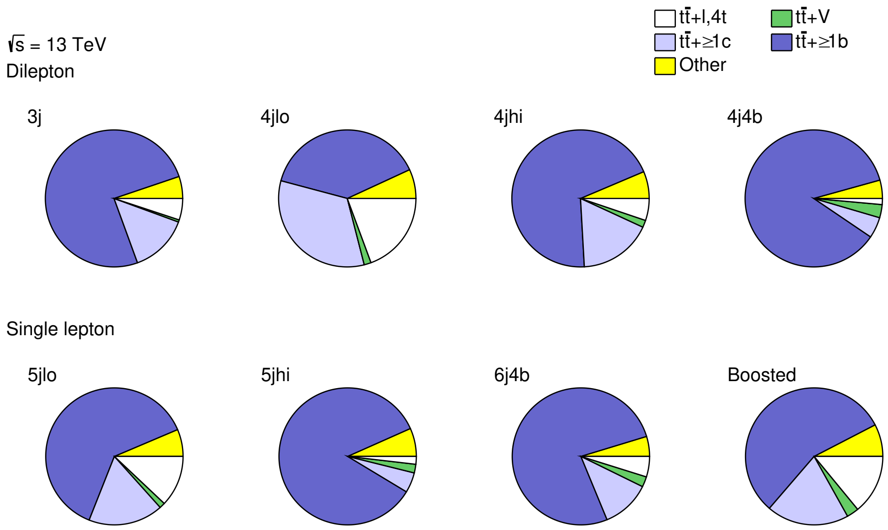

(a)

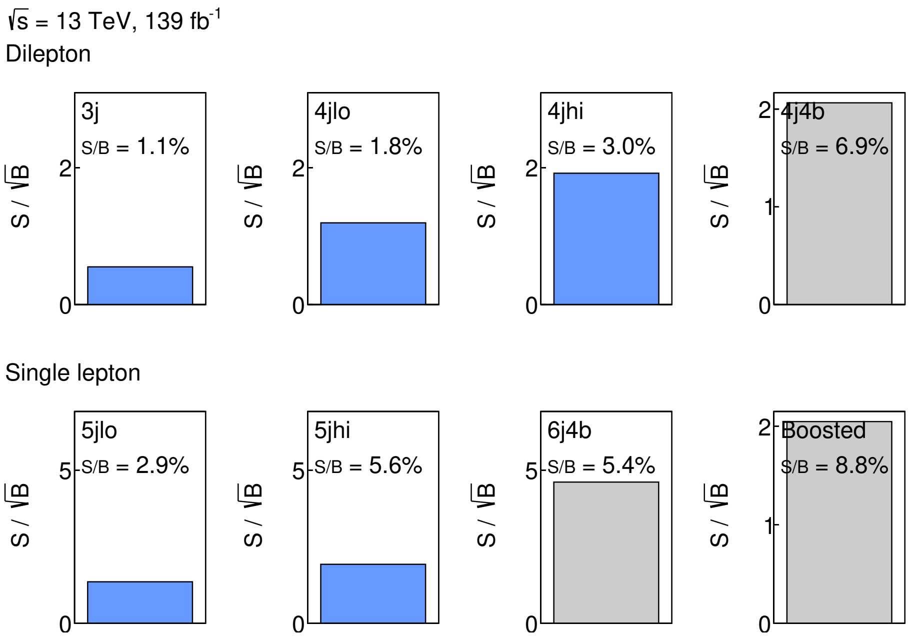

(b)

Figure 7.1: Composition of the control regions and inclusive signal regions. (a) Expected background fractions. (b) Signal purities S/B and simplified significances $S/\sqrt{B}$.

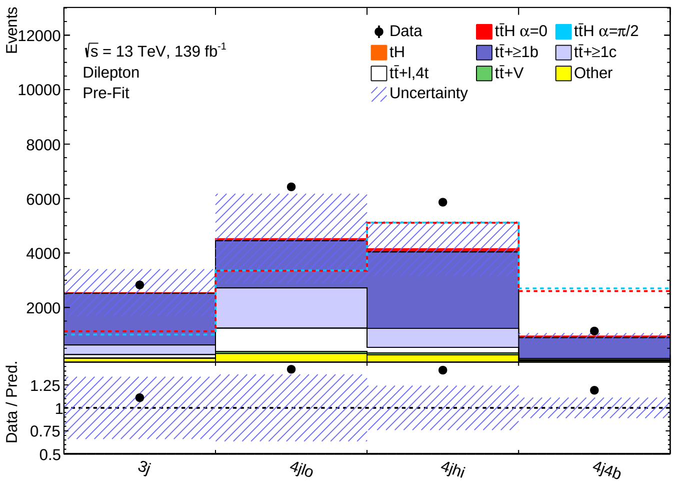

(a)

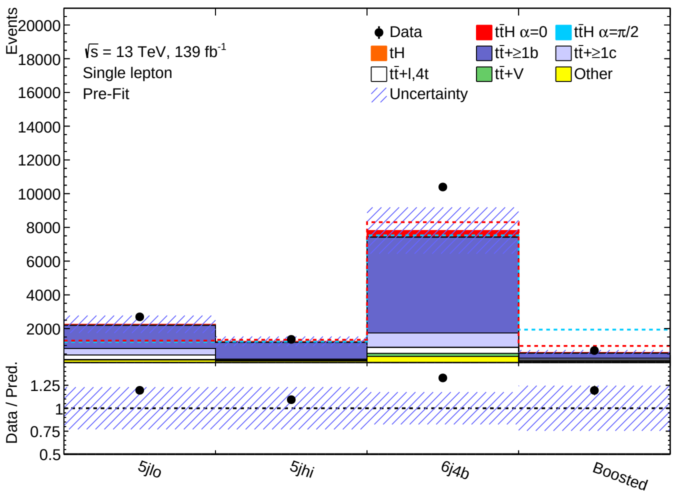

(b)

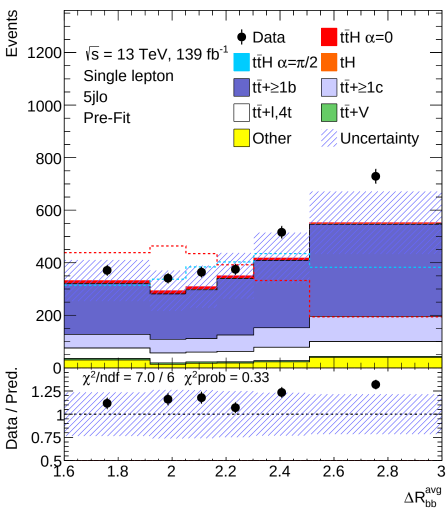

(c)

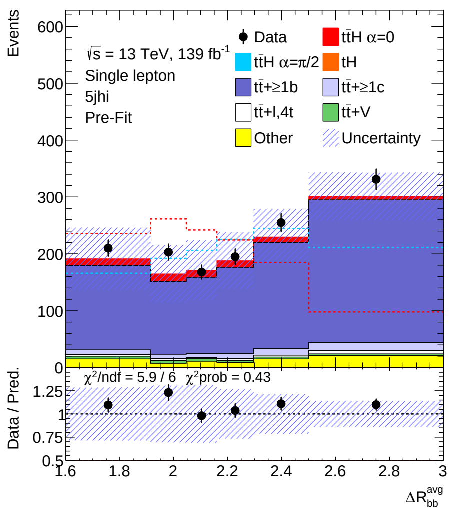

(d)

Figure 7.2: Pre-fit comparisons between data and prediction in the control regions and in the inclusive signal regions. (a) Dilepton channel. (b) Single-lepton channel. (c) $\Delta R_{bb}^{\text{avg}}$ distribution in 5jlo. (d) $\Delta R_{bb}^{\text{avg}}$ distribution in 5jhi.

profile-likelihood fit. Within each leptonic channel, the disagreement is worse for higher jet multiplicity. The $\Delta R_{bb}^{\text{avg}}$ shapes in data are reasonably well modelled by the prediction, considering the large pre-fit uncertainty bands. The different $\mathcal{CP}$ scenarios lead to similar distributions of the $t\bar{t}H$ signal across the control regions. As expected, there is a higher fraction of $t\bar{t}H$ events classified in the boosted region in the $\mathcal{CP}$-odd scenario than in the $\mathcal{CP}$-even scenario. The $\Delta R_{bb}^{\text{avg}}$ distribution also discriminates between the two signal hypotheses, although the $\mathcal{CP}$ analysis will draw most of its sensitivity from regions with higher signal purity. Tables 7.2 and 7.3 show the data and the pre-fit expected yields in the control regions of the dilepton and single-lepton channels, respectively.

Table 7.2: Data and expected pre-fit yields in the dilepton control regions. Predictions of $t\bar{t}H$ and tH are included for the $\mathcal{CP}$-even and $\mathcal{CP}$-odd (κ_t' =1) scenarios.

	3j	4jlo	4jhi
$t\bar{t}H, \alpha = 0$	26.4 $\pm$ 3.9	78.6 $\pm$ 7.9	120 $\pm$ 12
$tWH, \alpha = 0$	1.23 $\pm$ 0.14	1.00 $\pm$ 0.26	1.92 $\pm$ 0.38
$t\bar{t}H, \alpha = \pi/2$	10.6 $\pm$ 1.6	35.6 $\pm$ 3.6	54.1 $\pm$ 5.4
$tWH, \alpha = \pi/2$	5.92 $\pm$ 0.68	7.7 $\pm$ 2.0	11.8 $\pm$ 2.3
$t\bar{t} + \geq 1b$	1900 $\pm$ 780	1730 $\pm$ 430	2810 $\pm$ 660
$t\bar{t} + \geq 1c$	350 $\pm$ 360	1500 $\pm$ 1500	700 $\pm$ 710
$t\bar{t}$ + light, $4t$	128 $\pm$ 74	860 $\pm$ 350	210 $\pm$ 120
$t\bar{t}Z$	11.1 $\pm$ 1.8	51.7 $\pm$ 7.0	57.1 $\pm$ 7.4
$t\bar{t}W$	1.88 $\pm$ 0.58	21.5 $\pm$ 3.7	10.8 $\pm$ 1.6
Fake leptons	6.3 $\pm$ 1.8	56 $\pm$ 14	47 $\pm$ 12
Other	125 $\pm$ 35	251 $\pm$ 74	211 $\pm$ 62
Total prediction ($\alpha = 0$)	2540 $\pm$ 860	4500 $\pm$ 1600	4200 $\pm$ 1000
Data	2827	6429	5865

Table 7.3: Data and expected pre-fit yields in the single-lepton control regions. Predictions of $t\bar{t}H$ and tH are included for the $\mathcal{CP}$-even and $\mathcal{CP}$-odd (κ_t' =1) scenarios.

	5jlo	5jhi
$t\bar{t}H, \alpha = 0$	60.4 $\pm$ 8.7	63 $\pm$ 10
$tHjb, \alpha = 0$	2.22 $\pm$ 0.27	2.56 $\pm$ 0.34
$tWH, \alpha = 0$	0.84 $\pm$ 0.11	0.728 $\pm$ 0.098
$t\bar{t}H, \alpha = \pi/2$	27.8 $\pm$ 6.5	28.3 $\pm$ 6.2
$tHjb, \alpha = \pi/2$	12.1 $\pm$ 1.5	12.9 $\pm$ 1.7
$tWH, \alpha = \pi/2$	4.41 $\pm$ 0.58	3.72 $\pm$ 0.50
$t\bar{t}+ \geq 1b$	1370 $\pm$ 230	1000 $\pm$ 270
$t\bar{t}+ \geq 1c$	390 $\pm$ 400	56 $\pm$ 59
$t\bar{t}$ + light, $4t$	260 $\pm$ 120	22 $\pm$ 16
$t\bar{t}Z$	26.4 $\pm$ 3.7	23.5 $\pm$ 3.4
$t\bar{t}W$	2.53 $\pm$ 0.53	0.54 $\pm$ 0.13
Single top Wt	58 $\pm$ 32	27 $\pm$ 20
Other single top	41 $\pm$ 16	27 $\pm$ 11
V+jets, VV+jets	42 $\pm$ 18	24.2 $\pm$ 9.8
Total prediction ($\alpha = 0$)	2260 $\pm$ 520	1250 $\pm$ 290
Data	2696	1362

Chapter 8

Measurement of $t\bar{t}H$ production cross-section

This chapter addresses the inclusive cross-section measurement of $t\bar{t}H$ production in the final state with leptons and with $H \to b\bar{b}$, which has been published in Ref. [6]. In that publication, together with the inclusive cross-section measurement, an additional measurement was performed within the Simplified Template Cross-Section (STXS) framework [59]. For the sake of simplicity, the inclusive and STXS measurements were done in the same analysis regions and using the same modelling uncertainties. For that reason, although only the inclusive result will be discussed here, the specific needs of the STXS measurement are presented as motivation for choices in the analysis strategy.

Section 8.1 describes the procedure for signal modelling and associated uncertainties. The analysis strategy, including region definition and fitted observables, is presented in Section 8.2. The pre-fit modelling in the signal regions is shown in Section 8.2. Sections 8.4 and 8.5 show the expected and observed results, respectively. The comparison between data and post-fit prediction is made in Section 8.6.

8.1 Signal modelling

The $t\bar{t}H$ signal process is modelled using the samples described in Section 6.2.2. For the nominal model, the PowhegBox samples are used. The samples are normalised to a cross-section of 507 fb, which is the central value of the cross-section computed at NLO in QCD with electroweak corrections [59].

8.1.1 Uncertainties

Uncertainties from the theoretical calculation of the inclusive SM $t\bar{t}H$ cross-section value are considered: a 3.6% uncertainty due to PDFs and α_S, and a 9.2% uncertainty due to missing higher-order terms in QCD [59]. Theoretical uncertainties on the Higgs boson branching fractions are also considered, in particular a 2.2% uncertainty is used for the $b\bar{b}$ decay.

Uncertainties due to the modelling of $t\bar{t}H$ by MC samples are also included, for a total of four independent components, in a similar way to what is done for $t\bar{t}+$ jets. For the uncertainty due to NLO matching, the MadGraph5_aMC@NLO +Pythia8 sample is compared to the nominal PowhegBox+Pythia8 sample. The uncertainty due to ISR is estimated by simultaneously changing μ_r and μ_f in the ME and α_S^{ISR} in the PS, while the uncertainty due to FSR is estimated by changing α_S^{FSR} in the PS. These scale variations are done using event weights in the nominal samples. The PowhegBox+Pythia8 sample is compared to the PowhegBox+Herwig7 sample to assess the uncertainty due to PS and hadronisation.

In the STXS framework, cross-sections are measured in mutually exclusive phase-space regions, defined with the purpose of constraining scenarios of new physics, while reducing the theory dependence of the measurements. In this channel, the STXS regions were defined by the true (parton-level) Higgs boson p_T (p_T^H), with boundaries (in GeV) at $0, 120, 200, 300, 450$ and $+\infty$. For this reason, an additional uncertainty is included to account for possible effects of missing higher-order terms in QCD on migrations between p_T^H bins. This is estimated from the ISR downwards variation, which was found to have the largest impact on the p_T^H distribution among all variations of μ_r, μ_f, ISR and FSR. The uncertainty is split in five additional sources, each affecting a set of adjacent p_T^H bins in a way compatible with the migration of events across the bin boundaries. Depending on the p_T^H bin, the total uncertainty due to missing higher-orders in QCD – combining the inclusive and migration components – ranges from 11% to 17%.

8.2 Analysis strategy

In order to maximise sensitivity to the $t\bar{t}H$ signal in the different true p_T^H bins, the boundaries dictated by the STXS strategy were used to split the inclusive signal regions, according to the observable $p_T^{b\bar{b}}$: the p_T of the pair of b-tagged jets reconstructed as the Higgs boson candidate, as determined by the Reconstruction BDT in the resolved channels and by the Higgs tagger in the boosted channel.

The single-lepton resolved region 6j4b was split into five signal regions, one for each of the following intervals of $p_T^{b\bar{b}}$ (in GeV): $[0, 120[$, $[120, 200[$, $[200, 300[$, $[300, 450[$ and $[450, +\infty[$. These will be referred to as 6jXS^1, 6jXS^2, 6jXS^3, 6jXS^4 and 6jXS^5. The dilepton region 4j4b was also divided into signal regions in a similar way, with the exception that the 4th and 5th $p_T^{b\bar{b}}$ bins are merged into the single region 4jXS^{4+5}, due to the lack of statistics. The boosted region is split into the BoostedXS^4 and BoostedXS^5 signal regions, since the Higgs candidate selection requires $p_T^{b\bar{b}} > 300\,\text{GeV}$.

Figure 8.1 shows the S/B and $S/\sqrt{B}$ fractions for the signal regions used in the cross-section measurement. There is not a significant variation of signal purity across $p_T^{b\bar{b}}$ bins in the 4j4b and boosted inclusive signal regions. In 6j4b, however, the purity rises to a maximum in 6jXS^3, and then drops significantly for higher $p_T^{b\bar{b}}$. $S/\sqrt{B}$ is smaller in the higher $p_T^{b\bar{b}}$ bins, due to lower statistics. Background compositions are very similar across $p_T^{b\bar{b}}$ bins. The contribution from non-$t\bar{t}$ backgrounds is expected to increase in 6jXS^5, although remaining below 12% of the total background.

Figure 8.2 shows the comparison between data and prediction for the $p_T^{b\bar{b}}$ distribution in each of the inclusive signal regions. The bin boundaries match those used for defining the signal regions, such that bin contents correspond to event yields in each of the signal regions. A significant mismodelling of $p_T^{b\bar{b}}$ is visible, suggesting that the $b\bar{b}$ pairs produced in $t\bar{t} + \geq 1b$ have a harder p_T spectrum in the nominal model than in data. The same comparison is given in Tables 8.1, 8.2 and 8.3, for the dilepton, single-lepton resolved and single-lepton boosted channels, respectively.

In all the signal regions, the Classification BDT distribution is used as the fitted observable, except for 6jXS^5, where the event yield is used instead, due to the very low statistics. The separation between signal and background provided by the Classification BDT increases the sensitivity to the signal strength, in the signal-rich bins, and further constrains the background model, in signal-depleted bins.

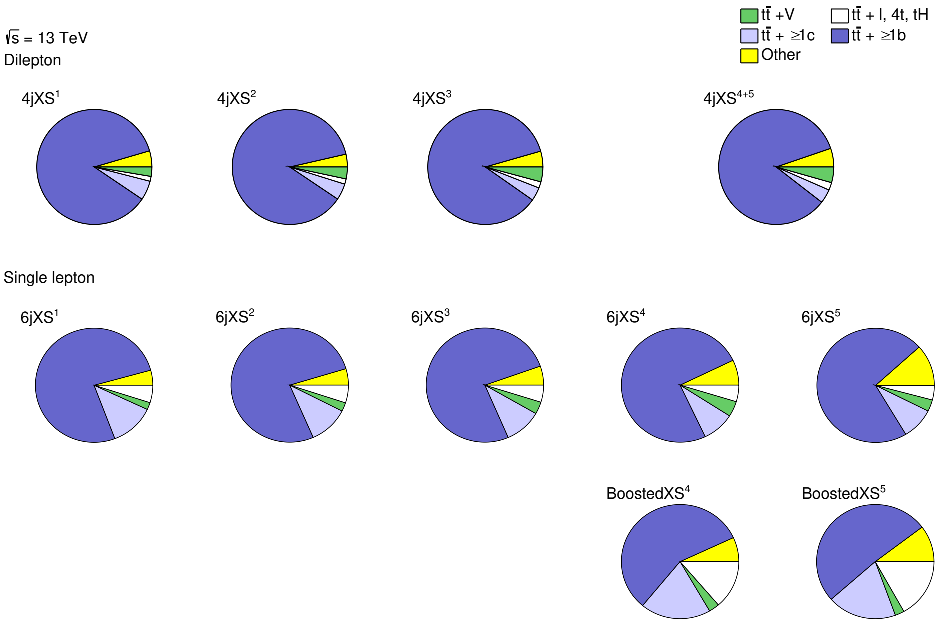

(a)

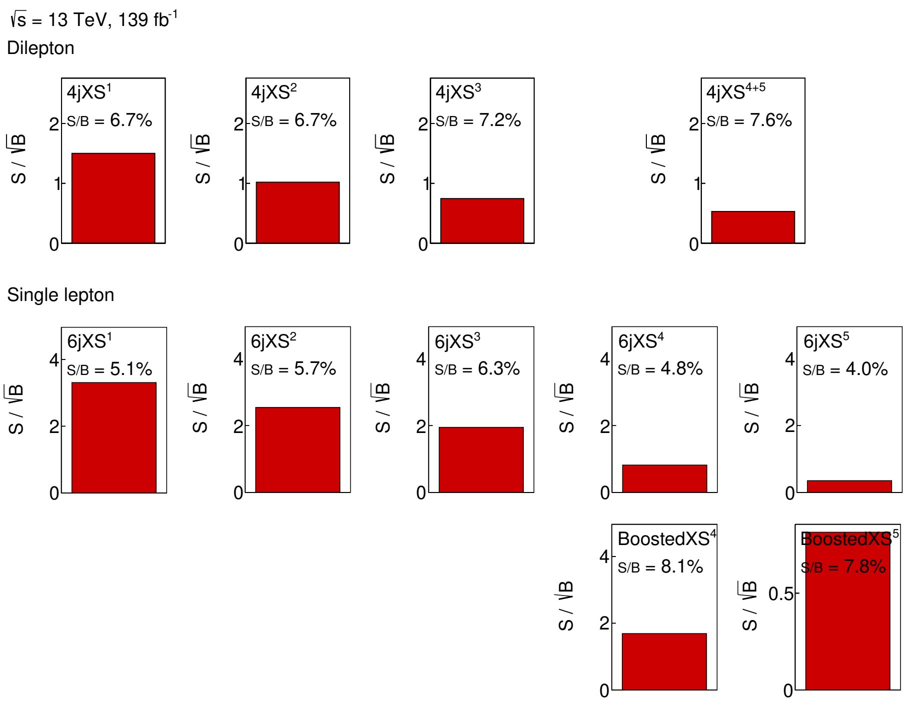

(b)

Figure 8.1: Composition of the signal regions used in the cross-section measurement. (a) Expected relative background contributions. (b) S/B and $S/\sqrt{B}$ fractions.

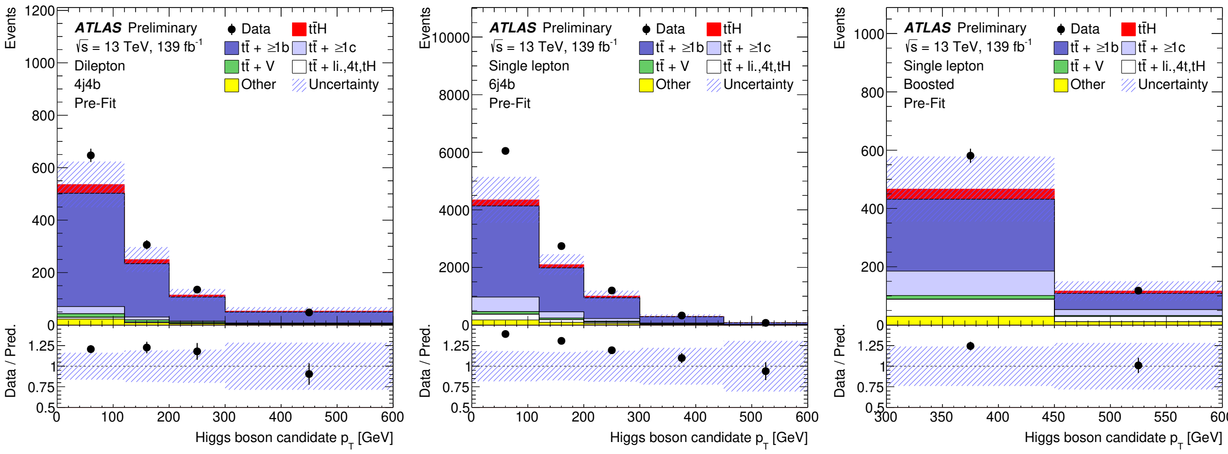

(a) (b) (c)

Figure 8.2: Comparison between data and pre-fit prediction of the $p_T^{b\bar{b}}$ distribution in each channel or, equivalently, of the event yields in each of the signal regions. (a) Dilepton, 4j4b. (b) Single lepton resolved, 6j4b. (c) Single lepton boosted.

Table 8.1: Data and pre-fit prediction for the event yields in the dilepton signal regions used in the cross-section measurement.

	4jXS^1	4jXS^2	4jXS^3	4jXS^{4+5}
$t\bar{t}H$	33.6 $\pm$ 4.1	15.6 $\pm$ 1.8	7.71 $\pm$ 0.90	3.72 $\pm$ 0.44
$t\bar{t} + \geq 1b$	432 $\pm$ 97	203 $\pm$ 53	92 $\pm$ 23	42 $\pm$ 16
$t\bar{t} + \geq 1c$	27 $\pm$ 29	11 $\pm$ 12	4.0 $\pm$ 4.2	1.9 $\pm$ 2.1
$t\bar{t}$ + light, $4t$, tH	6.9 $\pm$ 5.2	3.5 $\pm$ 2.5	1.9 $\pm$ 1.5	1.1 $\pm$ 1.2
$t\bar{t}Z$	12.5 $\pm$ 2.0	7.4 $\pm$ 1.6	4.18 $\pm$ 0.72	2.05 $\pm$ 0.45
$t\bar{t}W$	0.75 $\pm$ 0.31	0.38 $\pm$ 0.12	0.27 $\pm$ 0.12	0.124 $\pm$ 0.068
Fake leptons	3.7 $\pm$ 1.1	1.33 $\pm$ 0.51	0.40 $\pm$ 0.23	0.57 $\pm$ 0.30
Other	19.1 $\pm$ 6.9	7.1 $\pm$ 4.4	4.3 $\pm$ 4.0	2.0 $\pm$ 1.5
Total prediction	540 $\pm$ 100	249 $\pm$ 55	114 $\pm$ 24	53 $\pm$ 16
Data	647	306	135	48

Table 8.2: Data and pre-fit prediction for the event yields in the single-lepton resolved signal regions used in the cross-section measurement.

	6jXS[1]	6jXS[2]	6jXS[3]	6jXS[4]	6jXS[5]
$t\bar{t}H$	213 $\pm$ 29	113 $\pm$ 15	59.9 $\pm$ 7.8	13.9 $\pm$ 2.0	3.09 $\pm$ 0.49
$t\bar{t}+\geq 1b$	3160 $\pm$ 500	1530 $\pm$ 240	720 $\pm$ 140	215 $\pm$ 60	55 $\pm$ 26
$t\bar{t}+\geq 1c$	510 $\pm$ 540	220 $\pm$ 230	100 $\pm$ 100	26 $\pm$ 27	6.9 $\pm$ 7.5
$t\bar{t}+\text{light}, 4t, tH$	200 $\pm$ 120	100 $\pm$ 59	46 $\pm$ 24	13.5 $\pm$ 7.9	3.2 $\pm$ 2.2
$t\bar{t}Z$	77 $\pm$ 11	44.6 $\pm$ 6.6	30.1 $\pm$ 4.9	11.5 $\pm$ 2.4	2.05 $\pm$ 0.64
$t\bar{t}W$	7.0 $\pm$ 1.2	4.31 $\pm$ 0.90	2.47 $\pm$ 0.52	1.05 $\pm$ 0.32	0.47 $\pm$ 0.15
Single top Wt	71 $\pm$ 40	40 $\pm$ 26	17.9 $\pm$ 7.6	8.5 $\pm$ 7.9	6.0 $\pm$ 5.3
Other single top	46 $\pm$ 24	23 $\pm$ 16	13 $\pm$ 10	4.3 $\pm$ 2.8	1.08 $\pm$ 0.55
V+jets, VV+jets	60 $\pm$ 24	29 $\pm$ 11	19.7 $\pm$ 8.3	7.8 $\pm$ 3.4	1.90 $\pm$ 0.88
Total prediction	4350 $\pm$ 820	2100 $\pm$ 370	1000 $\pm$ 190	301 $\pm$ 71	80 $\pm$ 28
Data	6047	2742	1199	331	75

Table 8.3: Data and pre-fit prediction for the event yields in the single-lepton boosted signal regions used in the cross-section measurement.

	BoostedXS[4]	BoostedXS[5]
$t\bar{t}H$	35.0 $\pm$ 4.1	8.5 $\pm$ 1.1
$t\bar{t}+\geq 1b$	246 $\pm$ 46	55 $\pm$ 23
$t\bar{t}+\geq 1c$	84 $\pm$ 90	21 $\pm$ 23
$t\bar{t}+\text{light}, 4t, tH$	59 $\pm$ 26	18 $\pm$ 10
$t\bar{t}Z$	10.7 $\pm$ 2.1	2.21 $\pm$ 0.60
$t\bar{t}W$	1.86 $\pm$ 0.39	0.55 $\pm$ 0.18
Single top Wt	13.1 $\pm$ 8.0	6.1 $\pm$ 5.8
Other single top	4.3 $\pm$ 3.2	0.80 $\pm$ 0.78
V+jets, VV+jets	12.4 $\pm$ 5.7	4.3 $\pm$ 2.3
Total prediction	470 $\pm$ 110	117 $\pm$ 37
Data	581	118

8.3 Pre-fit modelling in analysis regions

In this section, pre-fit comparisons between data and prediction are shown for the signal regions of the cross-section measurement.

8.3.1 Observable distributions

Figure 8.3 shows a comparison between data and prediction for the observables used in the fit in the dilepton signal regions. Figure 8.4 shows the same for the single-lepton signal regions. Apart from the already mentioned disagreement in $t\bar{t} + \geq 1b$ normalisation between data and simulation, the shape differences seem to be covered by the uncertainty bands. In the regions of highest $p_T^{b\bar{b}}$ in all channels, a slope is apparent in the data-to-prediction ratio of the classification BDT histograms. This suggests that in the high $p_T^{b\bar{b}}$ range, data has more background-like events than what is predicted by simulation.

8.3.2 Classification BDT input variables

In order to validate the use of the Classification BDT, the modelling of its input variables is also checked against the data. Figure 8.5 compares data and the pre-fit prediction for distributions of the most relevant input variables to the dilepton Classification BDT, in the regions 4jXS^1, 4jXS^3 and 4jXS^{4+5}. The variables are $\Delta\eta_{bb}^{\text{avg}}$ (average $\Delta\eta$ between pairs of jets b-tagged with the 70% WP), $N_{bb}^{\text{Higgs 30}}$ (number of pairs of jets b-tagged with the 70% WP and with invariant mass within 30 GeV of the Higgs boson mass) and the output of the Reconstruction BDT that uses Higgs boson information. Similar distributions are shown in Figure 8.6, for the single-lepton regions 6jXS^1, 6jXS^3, 6jXS^4, BoostedXS^4 and BoostedXS^5. The variables shown are the LHD and $\Delta R_{bb}^{\text{avg}}$ in the 6j4b regions, and the DNN output $P(H)$ in the boosted regions. In the dilepton channel, all the shapes are well modelled in 4jXS^1, and do not show significant signs of mismodelling in the regions of higher $p_T^{b\bar{b}}$, where the large statistical uncertainties can accomodate the disagreements observed. In the

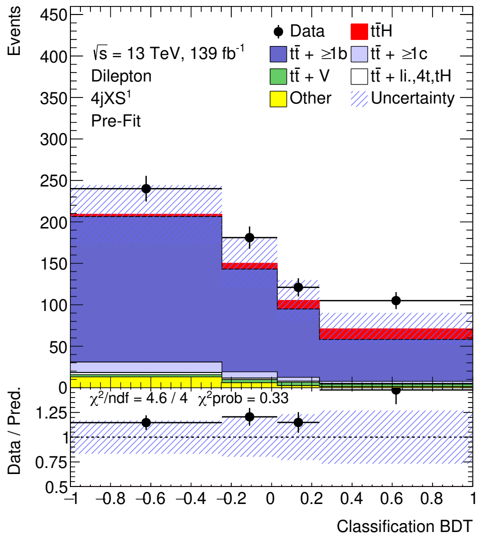

(a)

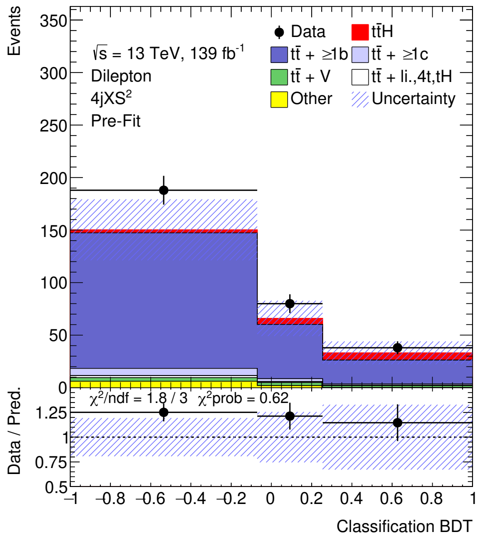

(b)

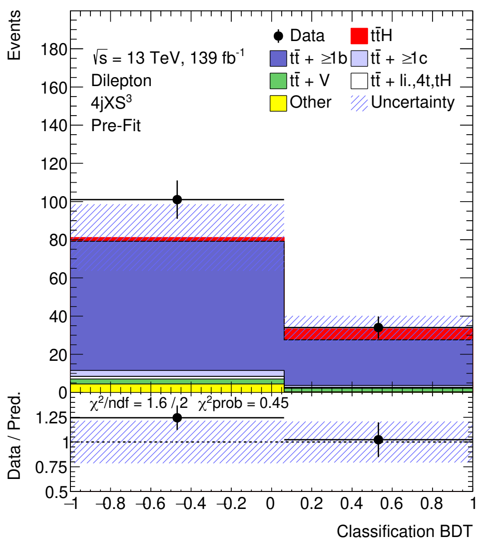

(c)

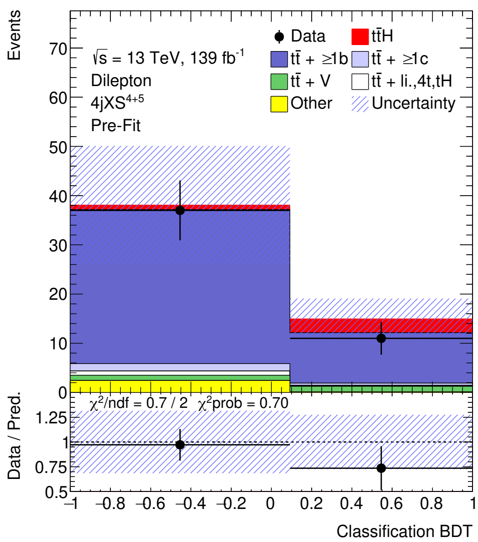

(d)

Figure 8.3: Pre-fit comparisons between data and prediction of the observables used in the fit in dilepton signal regions. (a) 4jXS^1. (b) 4jXS^2. (c) 4jXS^3. (d) 4jXS^{4+5}.

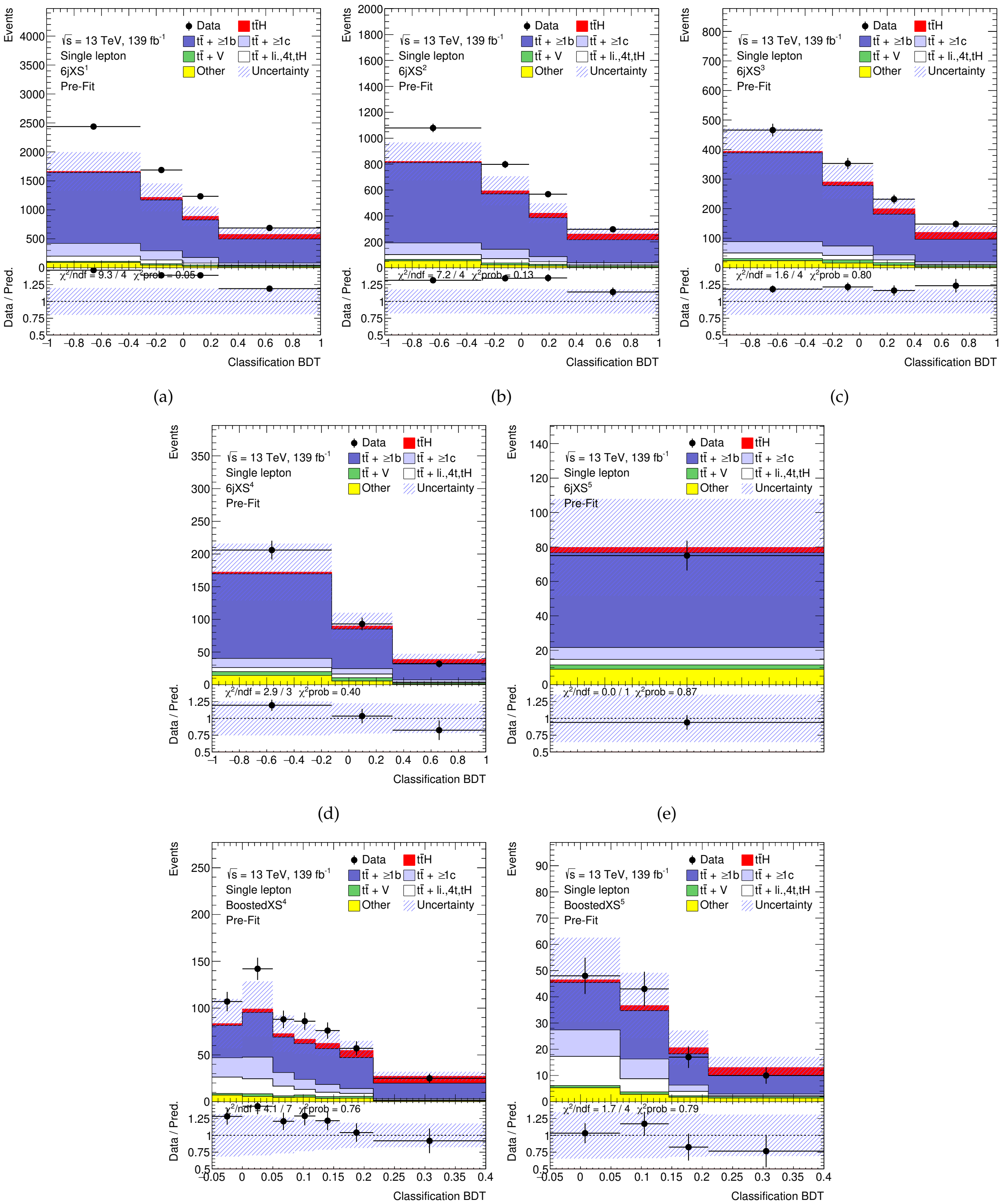

(a) (b) (c)

(d) (e)

(f) (g)

Figure 8.4: Pre-fit comparisons between data and prediction of the observables used in the fit in the single-lepton signal regions. (a) 6jXS^1. (b) 6jXS^2. (c) 6jXS^3. (d) 6jXS^4. (e) 6jXS^5. (f) BoostedXS^4. (g) BoostedXS^5.

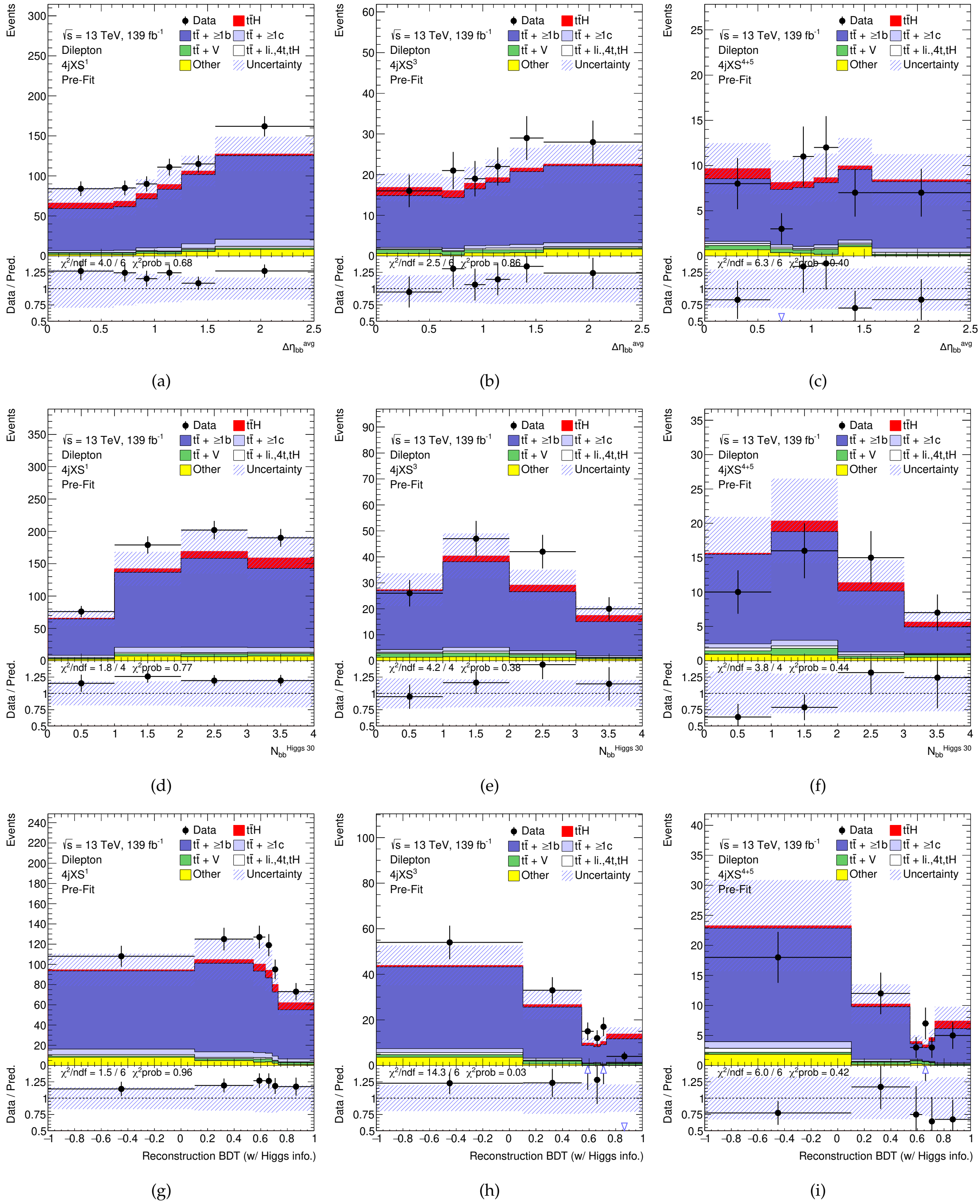

Figure 8.5: Distributions of data and pre-fit prediction for the most relevant input variables to the dilepton Classification BDT, in the regions 4jXS^1 (left), 4jXS^3 (middle) and 4jXS^{4+5} (right). (a,b,c) $\Delta\eta_{bb}^{\text{avg}}$. (d,e,f) $N_{bb}^{\text{Higgs 30}}$. (g,h,i) Reconstruction BDT output with Higgs boson information.

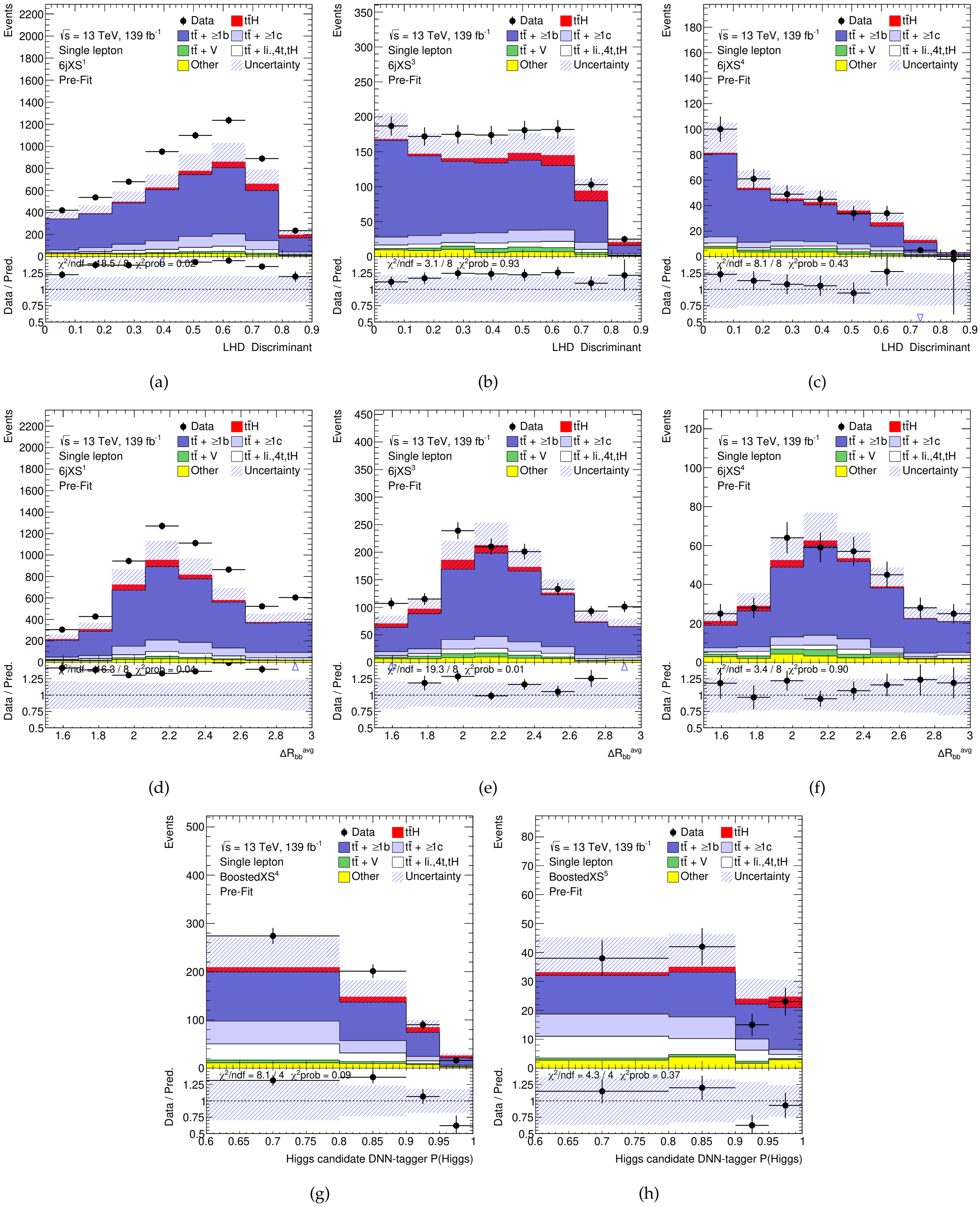

Figure 8.6: Distributions of data and pre-fit prediction for the most relevant input variables to the single-lepton Classification BDTs, in the regions 6jXS^1 (left), 6jXS^3 (middle), 6jXS^4 (right), BoostedXS^4 (bottom-left) and BoostedXS^5 (bottom-right). (a,b,c) LHD. (d,e,f) $\Delta R_{bb}^{\text{avg}}$. (g,h) $P(H)$.

single-lepton channel, the higher statistics reveal a clear mismodelling of the shapes, nevertheless mostly with a spread in ratio smaller than the systematic uncertainty band. A tendency is observed in $6jXS^4$ and in $BoostedXS^4$, where the data are distributed more towards background-like bins than in the prediction.

8.4 Expected results

Expected results are obtained by fitting an Asimov dataset, using simultaneously all signal and control regions. Uncertainties are separated into statistical and systematic components. The statistical component is obtained as the uncertainty on the signal strength μ in a fit with all nuisance parameters fixed to their best-fit value, which corresponds to removing all sources of systematic uncertainty. The systematic component is estimated by subtracting, in quadrature, the statistical component from the total uncertainty. In order to gauge the relative importance of the different channels (dilepton, single lepton resolved and single lepton boosted) to the overall sensitivity of the analysis, a fit is performed with three decorrelated signal strengths, each affecting the signal yield in the corresponding channel.

Figure 8.7 shows the obtained best-fit values and uncertainties on the signal strengths for the combined fit and for the fit with one signal strength per channel. This measurement is dominated by systematic uncertainties. The most sensitive channel is single lepton resolved and the least sensitive is the dilepton channel. The single-lepton boosted channel is the only single channel not dominated by systematic uncertainties, which are on par with the statistical uncertainty. The expected significance for exclusion of the background-only hypothesis ($\mu = 0$) is 3.4σ.

The expected uncertainty on the normalisation factor for the $t\bar{t} + \geq 1b$ background $k(t\bar{t} + \geq 1b)$ is ± 0.07. Uncertainties on other nuisance parameters are represented in Figure 8.8. This is a reduced set of nuisance parameters, including only those related to $t\bar{t}$ modelling or displaying

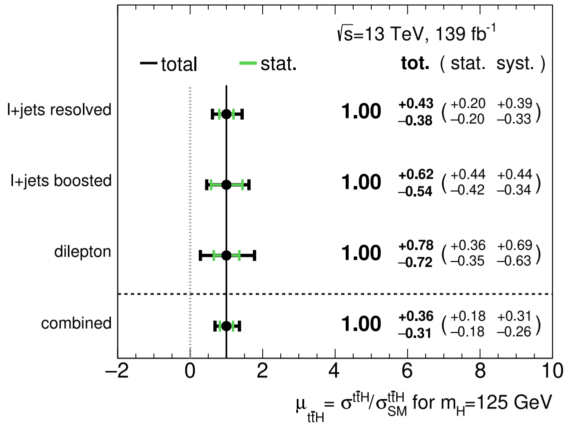

Figure 8.7: Fitted signal strength in the fit to the Asimov dataset, with uncertainties broken into statistical and systematic components. Besides the combined result, signal strengths from individual channels are also shown.

significant constraints or pulls in the expected or observed results. The results on the full set of nuisance parameters are given in Appendix C. Strong constraints from the data are expected on most $t\bar{t} + \geq 1b$ modelling parameters, as well as on the normalisation of $t\bar{t} + \geq 1c$. This is a consequence of the large impact that a variation of these parameters has on the prediction. Mild constraints are expected in other $t\bar{t}$ + jets modelling nuisance parameters, on Wt modelling, on the jet energy scale uncertainty related to jet flavour composition, and on the main components of uncertainty in the b-tagging scale factors for c and light-flavour jets. Correlation coefficients between the various parameters are shown, in %, in the matrix of Figure 8.9. The strongest correlations are expected among $t\bar{t} + \geq 1b$ modelling uncertainties, which contribute to reducing the impact of such uncertainties on μ. In particular, there are three correlation coefficients with absolute value above 50%: between the NLO matching in the single-lepton control regions and the PS and hadronisation uncertainty in the single-lepton channel, between the $1b/2b$ ratio and the $t\bar{t} + \geq 1b$ ISR, and between the $1b/2b$ ratio and the NLO matching in the dilepton control regions. There is a strong correlation between the $t\bar{t} + \geq 1c$ normalisation and the main uncertainty on light-flavour jet b-tagging. The nuisance parameters most strongly correlated with μ are

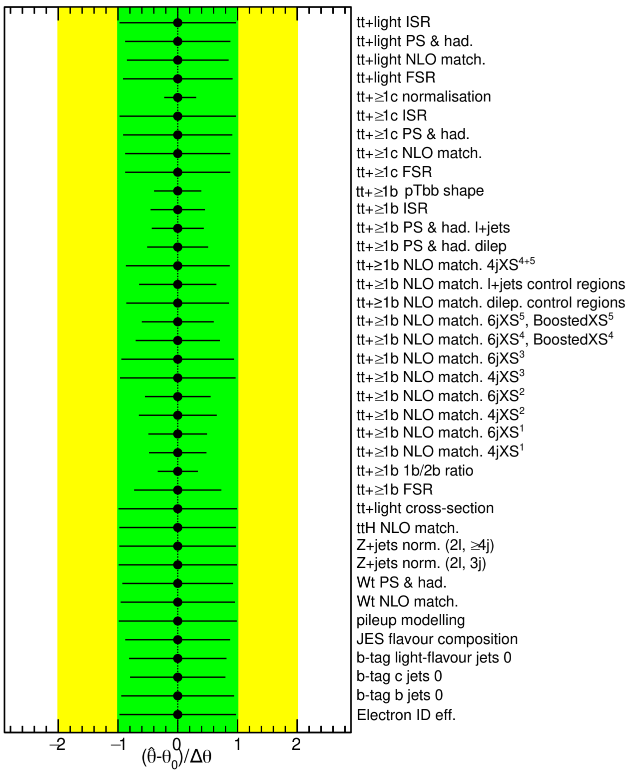

Figure 8.8: Expected uncertainties on nuisance parameters from the fit to the Asimov dataset. Black bars correspond to the post-fit constraint, while the prior constraint on all nuisance parameters is ±1 (green band).

the NLO matching uncertainties on $t\bar{t} + \geq 1b$ in the regions 6jXS^1 and 6jXS^2.

The impact of systematic uncertainties on the measured μ is estimated by running several fits to the Asimov dataset. For each nuisance parameter, two fits are run, with the parameter fixed to the value on the upper and lower edges of its post-fit uncertainty. The impact of the corresponding uncertainty on μ is taken as the difference between the best-fit values of μ obtained in the two fits. Figure 8.10 shows the impact on μ of the 20 systematic uncertainties with highest impact (ranked by their impact). The impact computed using the pre-fit uncertainties is also shown. Uncertainties on $t\bar{t} + \geq 1b$ and $t\bar{t}H$ modelling are the ones expected to impact μ the most. Among the $t\bar{t} + \geq 1b$ modelling uncertainties, NLO matching and PS and hadronisation are the leading ones, precisely

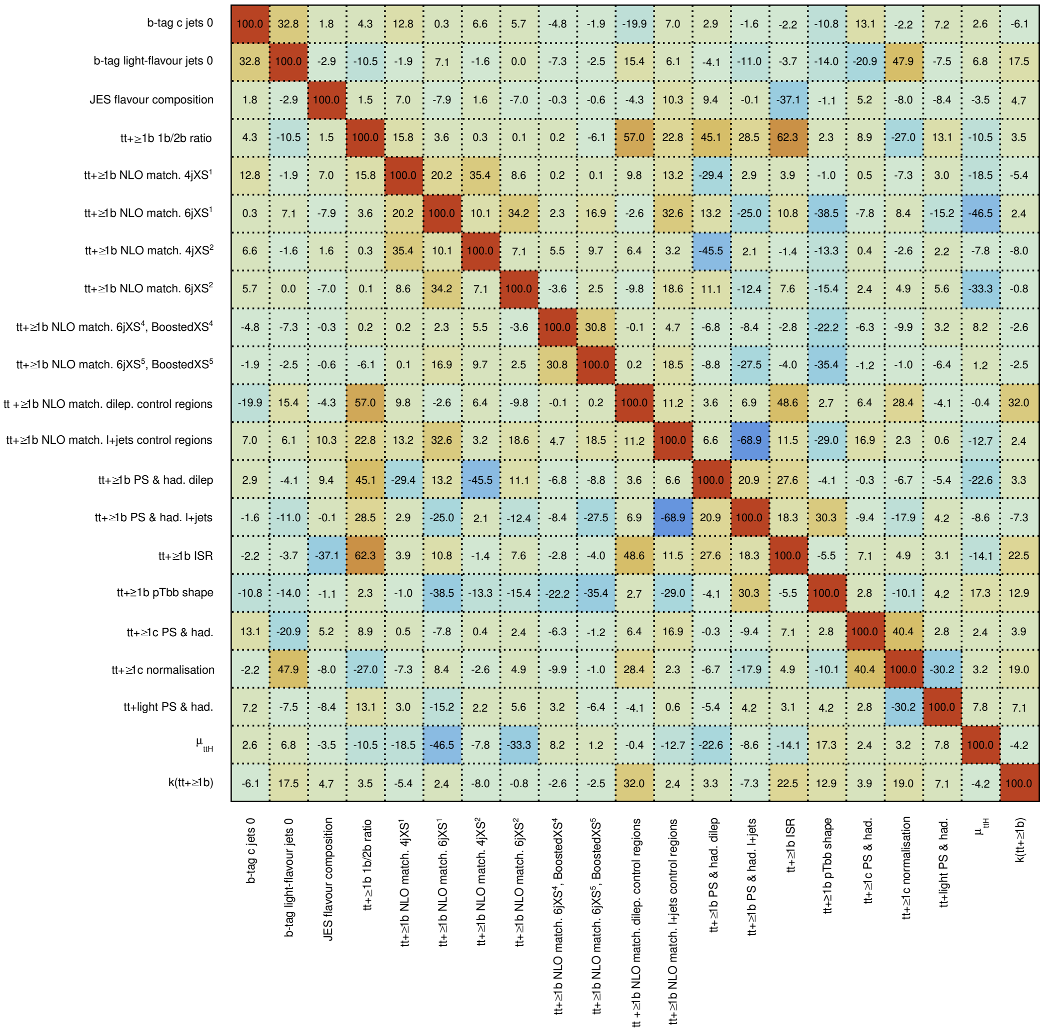

Figure 8.9: Correlation coefficients, in %, between the parameters in the fit to the Asimov dataset.

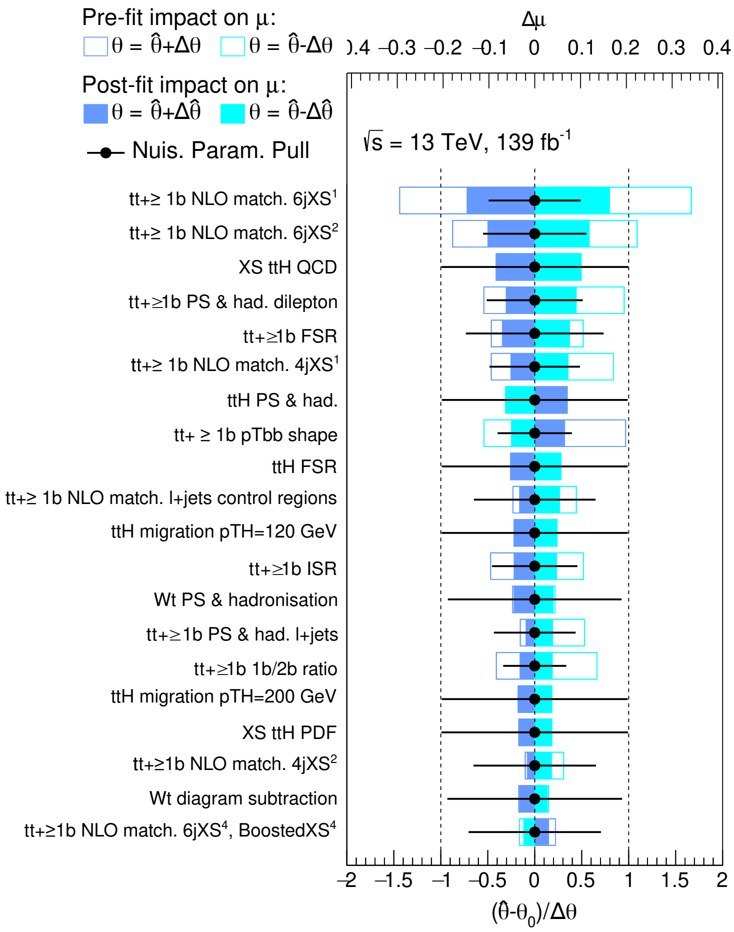

Figure 8.10: Pre- and post-fit impacts on μ of the 20 nuisance parameters with the largest post-fit impact on μ in the fit to the Asimov dataset.

the ones estimated using a ME and flavour scheme different from the nominal, in the conservative approach discussed in Section 6.4.2. The differences between the pre- and post-fit impacts of these uncertainties show that the constraints from data contribute to an important reduction of the impact. There are no uncertainties from experimental sources among the 20 leading ones.

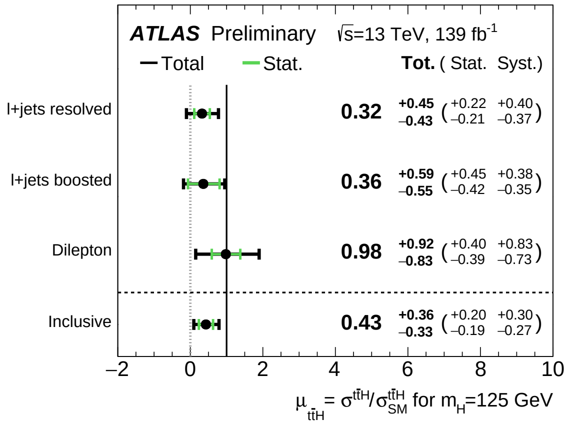

Figure 8.11: Observed signal strength in the fit to data [6]. Besides the combined μ, signal strengths observed in individual channels are also shown.

8.5 Observed results

The observed results are obtained by fitting the data. The observed μ is shown in Figure 8.11, together with the observed signal strengths fitted separately in the different analysis channels [6]. The observed best-fit value for μ is 0.43. The uncertainty on this value is $^{+0.36}_{-0.33}$, dominated by the component from systematic sources, in agreement with expectation. This means that the result is not compatible with the SM prediction at the level of 1σ, a result that may be attributed to the single-lepton channels, which both measure a μ below 0.4. The signal strengths measured in the individual channels are compatible with each other and their relative importance to the global sensitivity is close to expectation, although the dilepton channel sees an increase in systematic uncertainty and becomes less sensitive than expected. The observed significance for excluding the background-only hypothesis is 1.3σ.

A $t\bar{t} + \geq 1b$ normalisation factor of $1.26^{+0.09}_{-0.09}$ is measured, which is consistent with the ratios between data and predicted yields observed in pre-fit comparisons (see Figure 7.2). Figure 8.12 shows the most relevant fitted nuisance parameters. The results on the full set of nuisance parameters are given in Appendix C. The post-fit constraints on all nuisance parameters are consistent with the expected ones. The largest observed

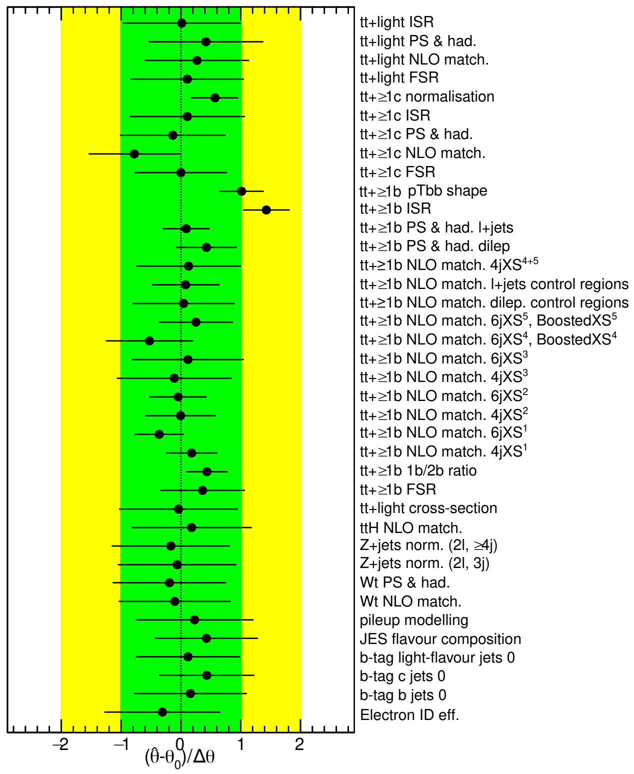

Figure 8.12: Observed nuisance parameters in the fit to data. Black dots and bars represent the best-fit values and constraints of the parameters, respectively. For all nuisance parameters, the nominal values are 0 and the prior constraint is ± 1 (green band).

pull is on the $t\bar{t} + \geq 1b$ ISR uncertainty. The variation favoured by the data corresponds to smaller μ_r and μ_f in the ME and thus leads to an increased amount of radiation and higher jet multiplicities. This pull has been shown to improve the modelling of the jet multiplicity distribution, by comparing data to predictions before and after the application of the $t\bar{t} + \geq 1b$ ISR pull. In fact, a re-scaling of μ_r in $t\bar{t} + b\bar{b}$ calculations, based on theoretical grounds, has been recently proposed [157]. It was shown that a re-scaling by a factor of $1/1.6$ with respect to the standard choice (used for the nominal prediction in this analysis) provides better convergence between different MC setups and better agreement with NLO calculations of $t\bar{t} + b\bar{b}j$. The observed pull in $t\bar{t} + \geq 1b$ ISR provides experimental motivation for the adoption of the re-scaling. The second largest pull occurs for the p_T^{bb} shape nuisance parameter, at $+1$. This is reassuring, since that uncertainty was introduced precisely such that the upwards variation would correct the mismodelling of the $p_T^{b\bar{b}}$ distribution in the signal regions. The normalisation of $t\bar{t} + \geq 1c$ background is also pulled up, resulting in a normalisation factor of 1.5. Mild pulls occur in other $t\bar{t}$ modelling systematic uncertainties, in the jet energy scale uncertainty due to jet flavour composition and in the leading component of uncertainty in the b-tagging scale factors for c jets. Observed correlations between the fit parameters are shown in the matrix of Figure 8.13. The

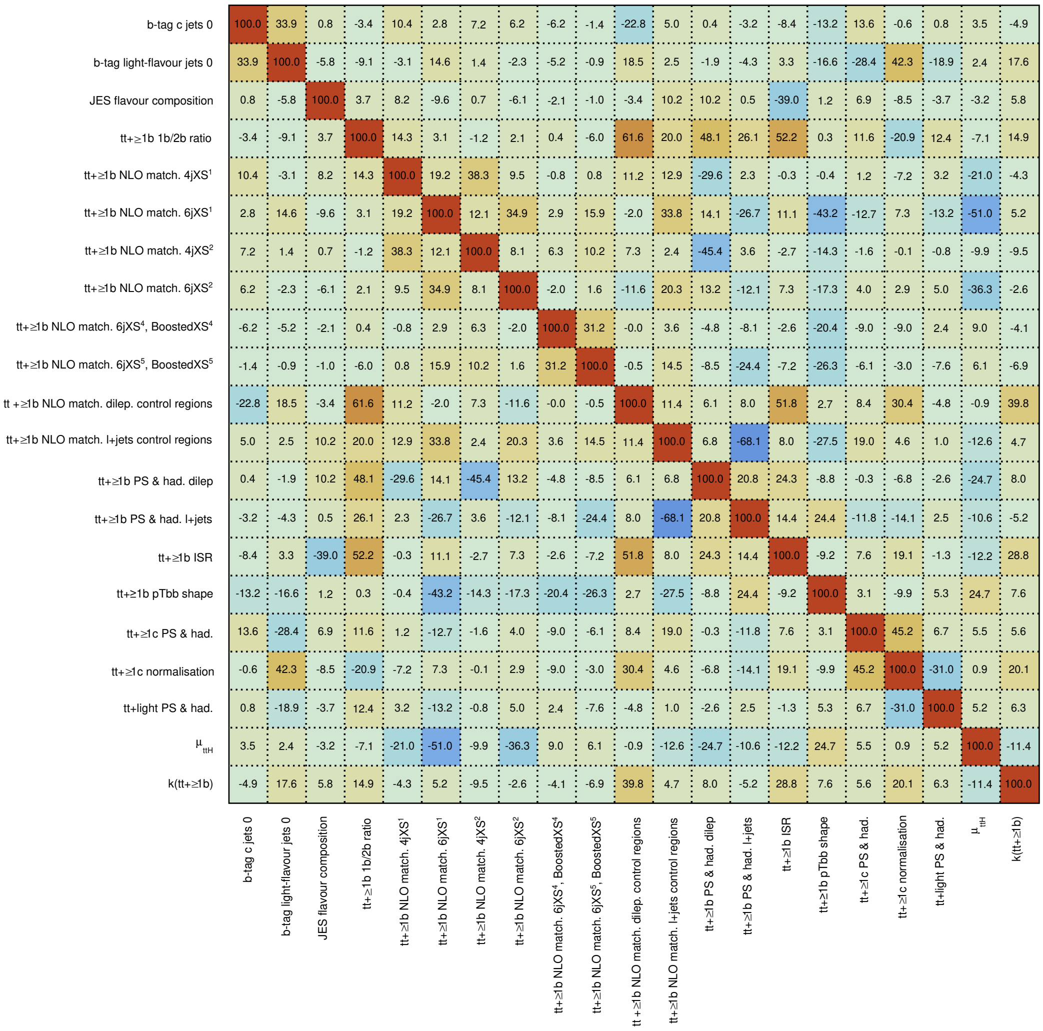

Figure 8.13: Correlation coefficients, in %, between the parameters in the fit to data.

observed pattern of correlations is very similar to the expected.

Observed impacts on μ are shown in Figure 8.14 for the 20 nuisance parameters with the largest post-fit impact. The most relevant difference

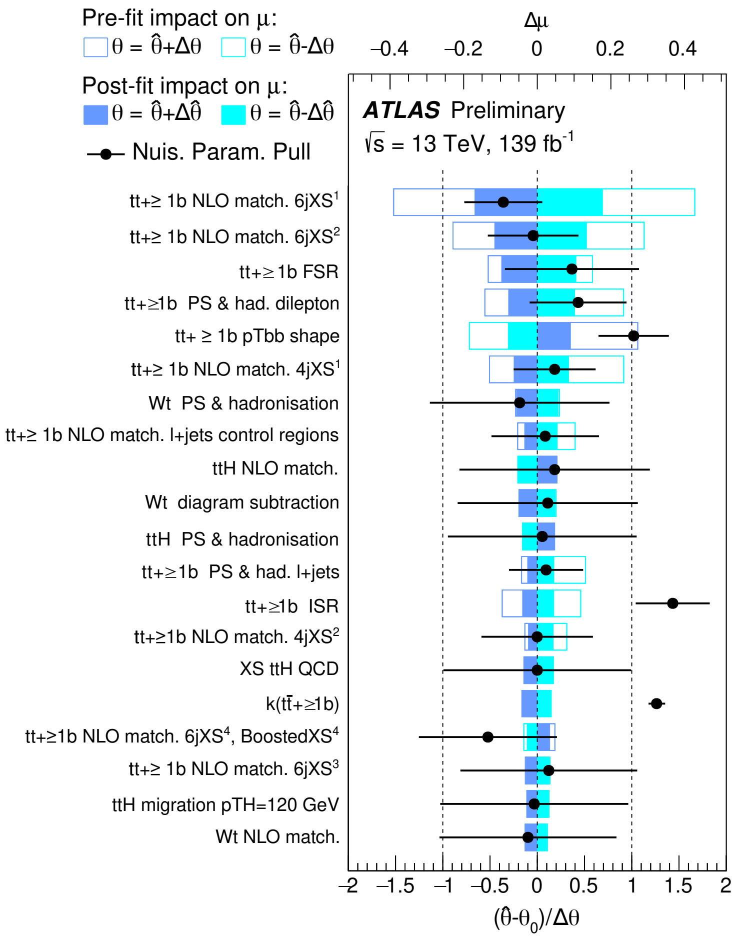

Figure 8.14: Observed impacts on μ of the 20 nuisance parameters with the largest post-fit impact on μ.

with respect to the expected impacts is in the $t\bar{t}H$ modelling uncertainties, for which the observed impact is much smaller. This is due to the observed value of μ being significantly below 1. Since the $t\bar{t}H$ modelling uncertainties are relative uncertainties on the signal, their impact on the absolute value of μ scales with μ itself.

Another possibility to estimate the impact of a systematic uncertainty on the uncertainty in μ is to perform the fit with the corresponding nuis-

Table 8.4: Observed impacts of grouped uncertainty sources on the uncertainty in μ.

Uncertainty Source	$\Delta\mu$	
$t\bar{t}+\geq 1b$ modelling	+0.25	-0.24
$t\bar{t}H$ modelling	+0.14	-0.06
Single top Wt modelling	+0.08	-0.08
b-tagging	+0.05	-0.05
Limited statistics in MC samples	+0.05	-0.05
Jet energy scale and resolution	+0.03	-0.03
$t\bar{t}+\geq 1c$ modelling	+0.03	-0.03
$t\bar{t}$+light modelling	+0.02	-0.02
Luminonsity	+0.01	-0.00
Other sources	+0.03	-0.03
Total systematic uncertainty	+0.30	-0.27
Total statistical uncertainty	+0.20	-0.19
$t\bar{t}+\geq 1b$ normalisation	+0.03	-0.05
Total uncertainty	+0.36	-0.33

ance parameter fixed to its best-fit value. The resulting uncertainty on μ will be smaller, and an impact estimate may be obtained by subtracting in quadrature that uncertainty on μ from the one obtained in the full fit. This procedure can be extended to evaluate the combined impact of a set of uncertainty sources. Impacts of grouped uncertainties are summarised in Table 8.4. Consistently with what is seen in the impact plots of individual sources, the measurement is dominated by $t\bar{t}+\geq 1b$ modelling uncertainties and has a significant impact from $t\bar{t}H$ modelling. All other sources are of minor importance. Among the experimental uncertainties, the most relevant ones are those related to b-tagging scale factors.

8.6 Post-fit modelling in analysis regions

Figure 8.15 shows a comparison between data and post-fit prediction of the $p_T^{b\bar{b}}$ distributions in each of the inclusive signal regions. The binning matches the definition of signal regions, such that the bin contents correspond to the observed and predicted event yields in each of the signal regions. The mismodelling of $p_T^{b\bar{b}}$ that was visible pre-fit is corrected by

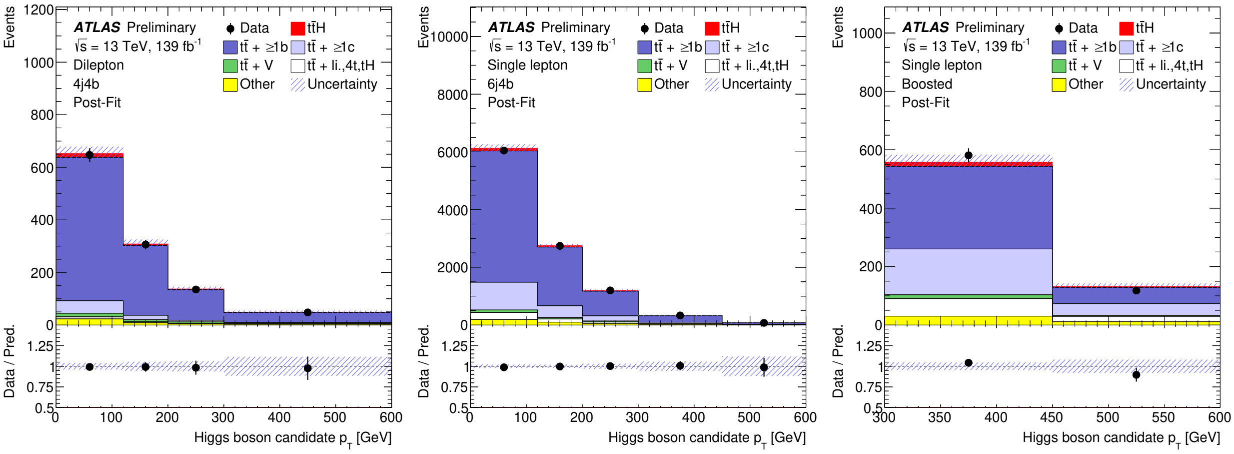

(a) (b) (c)

Figure 8.15: Comparison between data and post-fit prediction of the $p_T^{b\bar{b}}$ distribution in each inclusive signal region. The binning used matches the definition of the signal regions. (a) Dilepton, 4j4b. (b) Single lepton resolved, 6j4b. (c) Single lepton boosted.

the fit, as expected. Tables 8.5, 8.6 and 8.7 show the event yields for data and post-fit prediction in the signal regions of the dilepton, single-lepton resolved and single-lepton boosted channels, respectively. Tables 8.8 and 8.9 show the same information for the dilepton and single-lepton control regions, respectively.

Table 8.5: Event yields for data and post-fit prediction in the dilepton signal regions.

	4jXS^1	4jXS^2	4jXS^3	4jXS^{4+5}
$t\bar{t}H$	14 $\pm$ 12	6.7 $\pm$ 5.3	3.3 $\pm$ 2.6	1.6 $\pm$ 1.2
$t\bar{t} + \geq 1b$	557 $\pm$ 28	265 $\pm$ 17	117.6 $\pm$ 9.6	37.4 $\pm$ 5.6
$t\bar{t} + \geq 1c$	48.7 $\pm$ 9.5	14.4 $\pm$ 4.4	6.2 $\pm$ 1.4	3.9 $\pm$ 1.0
$t\bar{t}$ + light, $4t$, tH	7.9 $\pm$ 5.8	4.2 $\pm$ 2.8	2.1 $\pm$ 1.5	1.4 $\pm$ 1.3
$t\bar{t}Z$	12.5 $\pm$ 2.0	7.6 $\pm$ 1.6	4.15 $\pm$ 0.71	2.03 $\pm$ 0.44
$t\bar{t}W$	0.75 $\pm$ 0.31	0.41 $\pm$ 0.12	0.27 $\pm$ 0.11	0.128 $\pm$ 0.069
Fake leptons	3.6 $\pm$ 1.1	1.32 $\pm$ 0.51	0.40 $\pm$ 0.23	0.57 $\pm$ 0.30
Other	19.0 $\pm$ 6.7	7.7 $\pm$ 4.2	4.4 $\pm$ 4.0	2.0 $\pm$ 1.5
Total prediction	664 $\pm$ 24	307 $\pm$ 16	138.5 $\pm$ 8.9	48.9 $\pm$ 5.1
Data	647	306	135	48

Table 8.6: Event yields for data and post-fit prediction in the single-lepton resolved signal regions.

	6jXS[1]	6jXS[2]	6jXS[3]	6jXS[4]	6jXS[5]
$t\bar{t}H$	93 $\pm$ 74	49 $\pm$ 39	26 $\pm$ 21	5.9 $\pm$ 4.6	1.3 $\pm$ 1.0
$t\bar{t}+\geq 1b$	4450 $\pm$ 160	2040 $\pm$ 85	855 $\pm$ 43	234 $\pm$ 20	43.4 $\pm$ 8.2
$t\bar{t}+\geq 1c$	960 $\pm$ 210	404 $\pm$ 87	179 $\pm$ 38	46 $\pm$ 11	12.9 $\pm$ 3.3
$t\bar{t}+$ light, $4t$, tH	250 $\pm$ 140	105 $\pm$ 57	52 $\pm$ 26	15.4 $\pm$ 8.8	3.5 $\pm$ 2.2
$t\bar{t}Z$	79 $\pm$ 10	46.0 $\pm$ 6.4	31.1 $\pm$ 4.9	11.8 $\pm$ 2.3	2.12 $\pm$ 0.64
$t\bar{t}W$	7.3 $\pm$ 1.1	4.46 $\pm$ 0.87	2.54 $\pm$ 0.48	1.09 $\pm$ 0.31	0.48 $\pm$ 0.14
Single top Wt	80 $\pm$ 43	44 $\pm$ 27	18.7 $\pm$ 7.8	9.5 $\pm$ 9.0	6.1 $\pm$ 5.4
Other single top	48 $\pm$ 25	24 $\pm$ 16	14 $\pm$ 10	4.5 $\pm$ 2.7	1.09 $\pm$ 0.54
V+jets, VV+jets	63 $\pm$ 24	30 $\pm$ 11	20.6 $\pm$ 8.2	8.1 $\pm$ 3.4	1.92 $\pm$ 0.84
Total prediction	6026 $\pm$ 84	2747 $\pm$ 52	1198 $\pm$ 31	336 $\pm$ 15	72.8 $\pm$ 7.0
Data	6047	2742	1199	331	75

Table 8.7: Event yields for data and post-fit prediction in the single-lepton boosted signal regions.

	BoostedXS[4]	BoostedXS[5]
$t\bar{t}H$	15 $\pm$ 12	3.6 $\pm$ 2.8
$t\bar{t}+\geq 1b$	297 $\pm$ 27	51.0 $\pm$ 9.8
$t\bar{t}+\geq 1c$	157 $\pm$ 37	40 $\pm$ 11
$t\bar{t}+$ light, $4t$, tH	62 $\pm$ 25	16.9 $\pm$ 7.6
$t\bar{t}Z$	11.0 $\pm$ 2.1	2.34 $\pm$ 0.60
$t\bar{t}W$	1.89 $\pm$ 0.36	0.57 $\pm$ 0.17
Single top Wt	14.0 $\pm$ 8.3	4.9 $\pm$ 4.3
Other single top	4.4 $\pm$ 3.0	0.88 $\pm$ 0.78
V+jets, VV+jets	13.1 $\pm$ 5.6	4.2 $\pm$ 2.0
Total prediction	575 $\pm$ 23	124.4 $\pm$ 9.7
Data	581	118

Table 8.8: Event yields for data and post-fit prediction in the dilepton control regions.

	3j		4jlo		4jhi	
$t\bar{t}H$	10.5	$\pm$ 8.4	33	$\pm$ 27	51	$\pm$ 41
$t\bar{t} + \geq 1b$	2030	$\pm$ 130	2540	$\pm$ 170	4080	$\pm$ 210
$t\bar{t} + \geq 1c$	520	$\pm$ 130	2500	$\pm$ 500	1190	$\pm$ 260
$t\bar{t}$ + light, $4t, tH$	123	$\pm$ 66	920	$\pm$ 360	220	$\pm$ 130
$t\bar{t}Z$	10.7	$\pm$ 1.7	52.5	$\pm$ 6.8	57.4	$\pm$ 7.3
$t\bar{t}W$	1.83	$\pm$ 0.55	22.0	$\pm$ 3.5	10.9	$\pm$ 1.6
Fake leptons	6.3	$\pm$ 1.8	56	$\pm$ 14	46	$\pm$ 12
Other	126	$\pm$ 34	254	$\pm$ 71	208	$\pm$ 60
Total prediction	2835	$\pm$ 54	6429	$\pm$ 82	5861	$\pm$ 79
Data	2827		6429		5865	

Table 8.9: Event yields for data and post-fit prediction in the single-lepton control regions.

	5jlo		5jhi	
$t\bar{t}H$	26	$\pm$ 20	26	$\pm$ 21
$t\bar{t}+ \geq 1b$	1595	$\pm$ 80	1102	$\pm$ 51
$t\bar{t}+ \geq 1c$	630	$\pm$ 140	90	$\pm$ 23
$t\bar{t}$ + light, $4t, tH$	270	$\pm$ 100	26	$\pm$ 16
$t\bar{t}Z$	25.9	$\pm$ 3.5	22.8	$\pm$ 3.1
$t\bar{t}W$	2.62	$\pm$ 0.46	0.53	$\pm$ 0.12
Single top Wt	60	$\pm$ 32	28	$\pm$ 20
Other single top	41	$\pm$ 16	28	$\pm$ 11
V+jets, VV+jets	43	$\pm$ 15	24.9	$\pm$ 8.8
Total prediction	2700	$\pm$ 52	1348	$\pm$ 38
Data	2696		1362	

8.6.1 Observable distributions

An evaluation is made of the global goodness of fit to the observed data distributions, using a saturated fit model [158]. In this model, one free parameter is added to the fit for each analysis bin, that scales the content of the prediction in that bin. Thus, the fit with the saturated model always results in perfect agreement between data and prediction, without pulling any parameters with a prior constraint. The resulting NLL obtained from this fit corresponds to the absolute minimum attainable for the observed data, provided a model with ideal flexibility. This NLL value is compared to the one from the regular fit. Using Wilks' theorem, the difference between the NLLs can be converted into a p-value for the level of post-fit agreement between data and prediction. The observed p-value was 86%, of which a valid interpretation is: if the post-fit prediction were the true model, a level of disagreement with data at least as large as what is observed would be expected 86% of the time.

Data and post-fit predictions for the distributions used in the fit are shown in Figure 8.16 for the control regions, in Figure 8.17 for the dilepton signal regions, and in Figure 8.18 for the single-lepton signal regions. Good post-fit modelling is observed in all regions. In the higher $p_T^{b\bar{b}}$ regions 4jXS^3, 4jXS^{4+5} and 6jXS^4, the slope visible at pre-fit is still present, although mitigated. As these are regions with relatively low statistics, this moderate mismodelling does not penalise the goodness of the fit. A deficit of the prediction is visible in the most signal-rich bin of 4jXS^1, which is the dilepton signal region with highest statistics. This is consistent with the observed higher signal strength in the dilepton channel when decorrelating signal strengths.

8.6.2 Classification BDT input variables

The fit to data is not expected to correct the modelling of any observable to the same degree as it does for the observables used in the fit. Nevertheless, the strongest parameter pulls and constraints were interpreted under physical arguments, such that an improvement in the modelling of

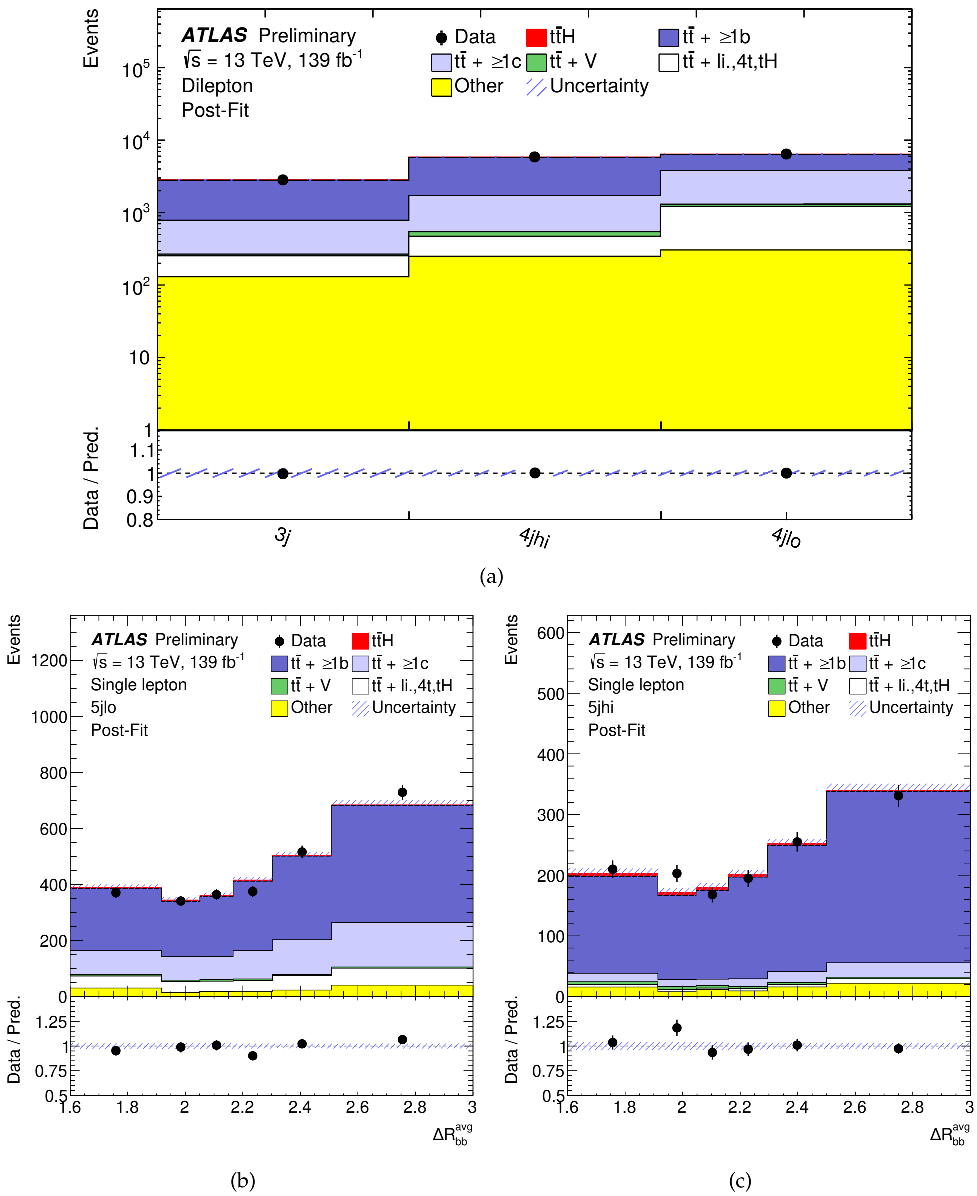

Figure 8.16: Data and post-fit predictions for the fitted distributions in the control regions. (a) Dilepton control regions. (b) 5jlo. (c) 5jhi.

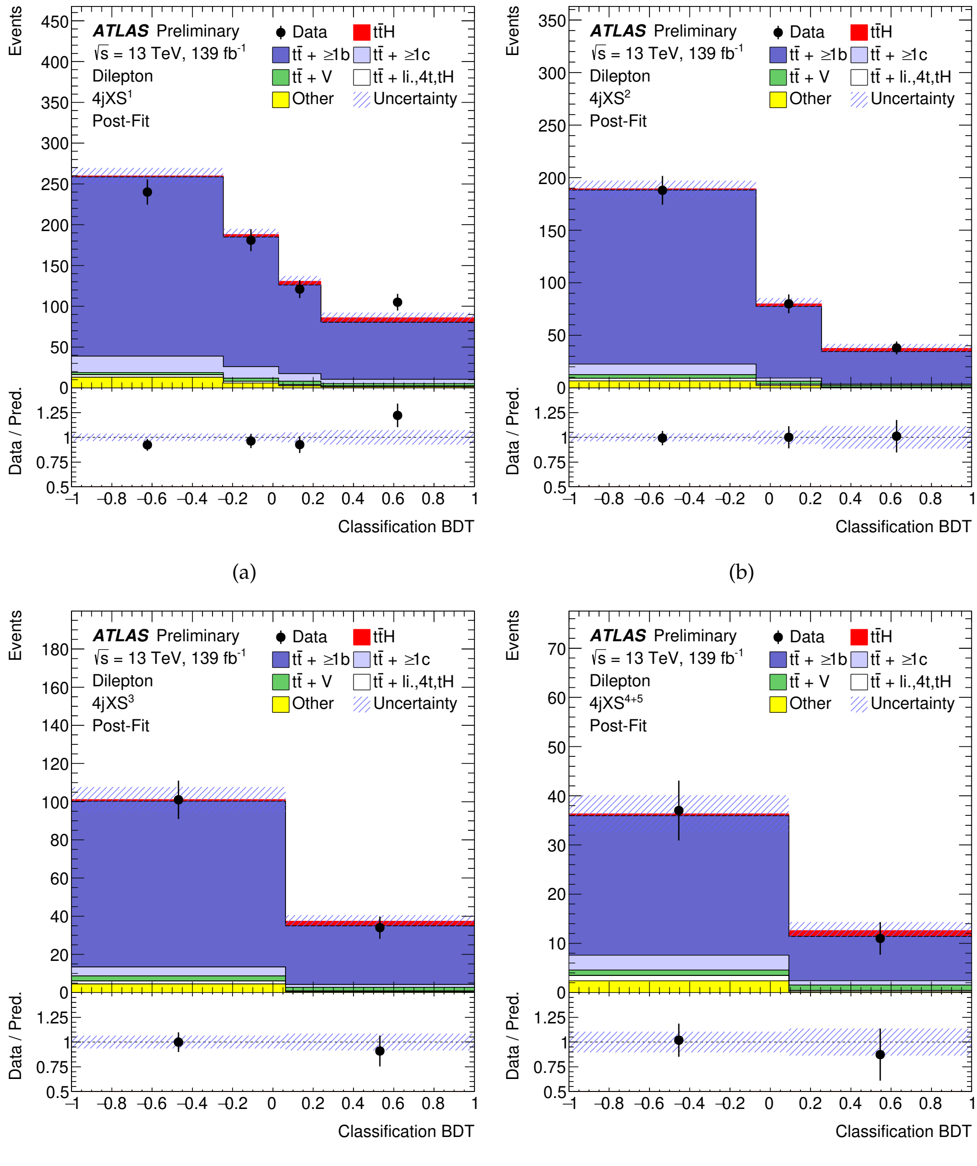

Figure 8.17: Data and post-fit predictions for the fitted distributions in the dilepton signal regions. (a) 4jXS^1. (b) 4jXS^2. (c) 4jXS^3. (d) 4jXS^{4+5}.

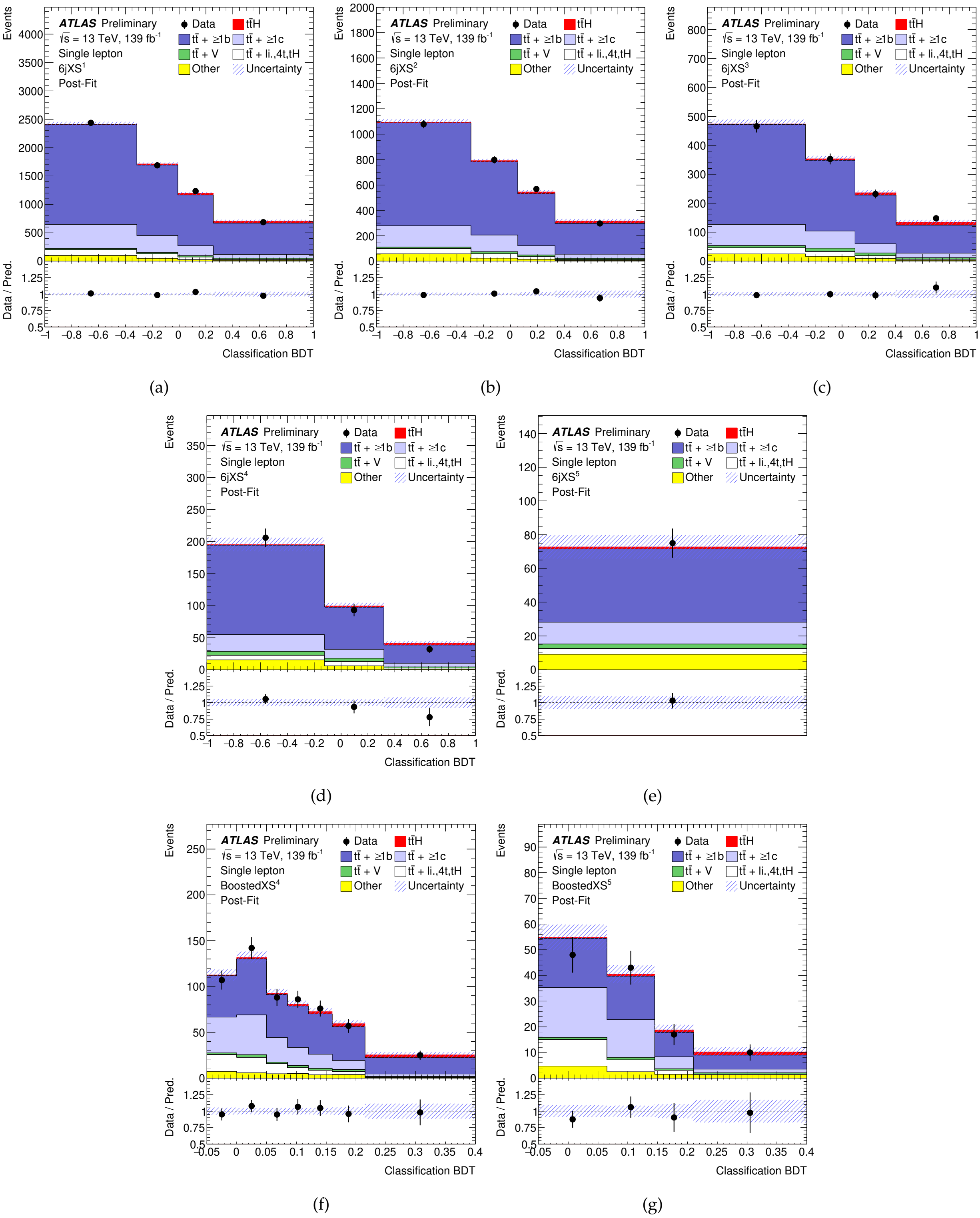

Figure 8.18: Data and post-fit predictions for the fitted distributions in the single-lepton signal regions. (a) 6jXS^1. (b) 6jXS^2. (c) 6jXS^3. (d) 6jXS^4. (e) 6jXS^5. (f) BoostedXS^4. (g) BoostedXS^5.

observables not directly used in the fit should occur, to a certain degree. Such an improvement should be most evident in the highest-ranked input variables to the Classification BDT, as they are correlated with the BDT score, whose distribution is used in the fit. Post-fit predictions are compared to data in distributions of the main Classification BDT input variables in Figure 8.19 for the dilepton regions 4jXS^1, 4jXS^3 and 4jXS^{4+5}, and in Figure 8.20 for the single-lepton regions 6jXS^1, 6jXS^3, 6jXS^4, BoostedXS^4 and BoostedXS^5. Overall, the agreement between data and prediction improves significantly with respect to pre-fit. This is mostly due to the normalisation within each region. Shapes of distributions only suffer mild corrections, most visible in the single-lepton resolved regions, which have higher statistics. In the dilepton region 4jXS^{4+5} the modelling is worse than in the pre-fit comparison. The adjustment of the prediction is small in that region, whereas there is a strong constraint of systematic uncertainties that make the prediction less compatible with data.

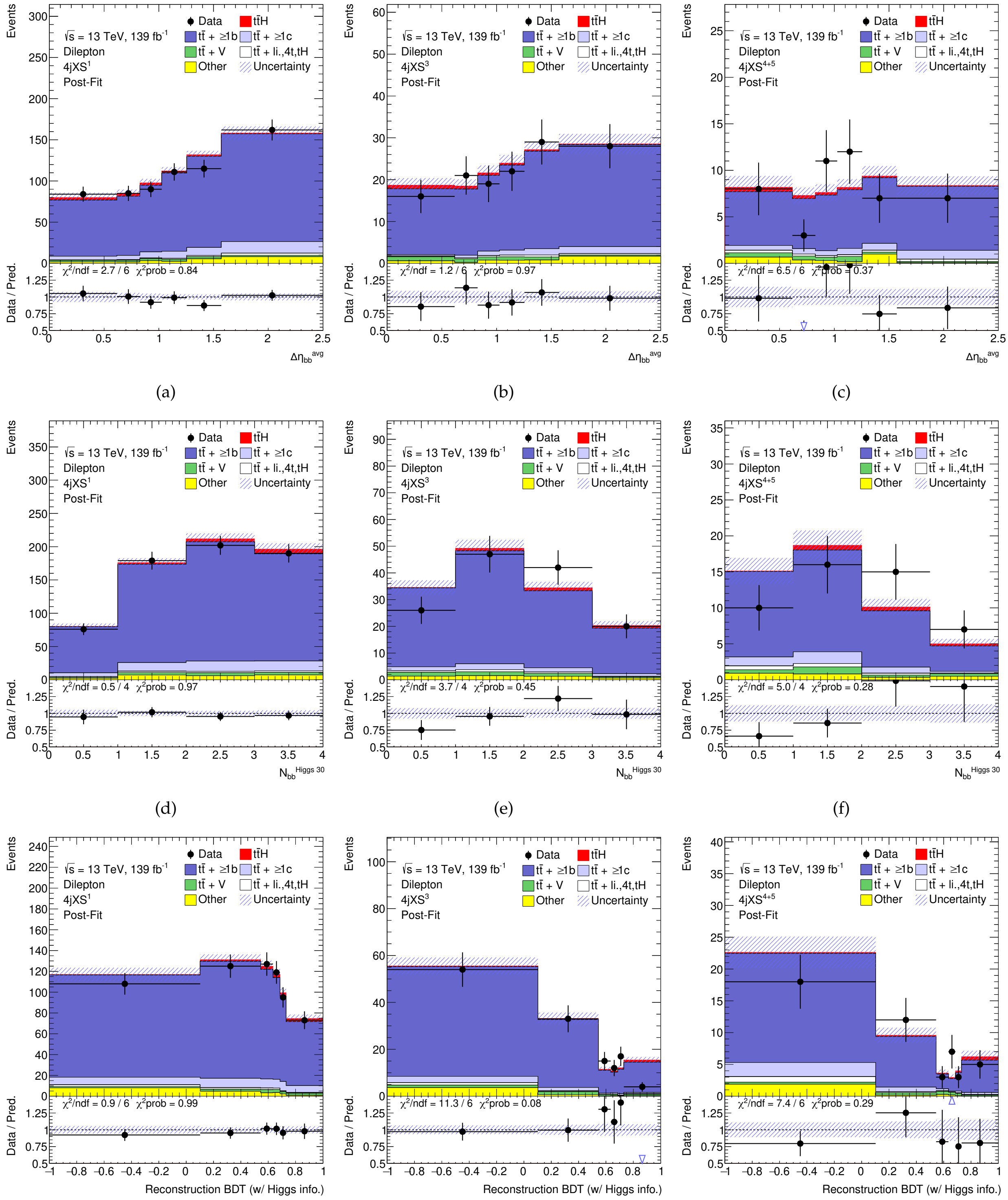

(a) (b) (c)

(d) (e) (f)

(g) (h) (i)

Figure 8.19: Distributions of data and post-fit prediction for the most relevant input variables to the dilepton Classification BDT, in the regions 4jXS^1 (left), 4jXS^3 (middle) and 4jXS^{4+5} (right). (a,b,c) $\Delta\eta_{bb}^{\text{avg}}$. (d,e,f) $N_{bb}^{\text{Higgs 30}}$. (g,h,i) Reconstruction BDT output with Higgs boson information.

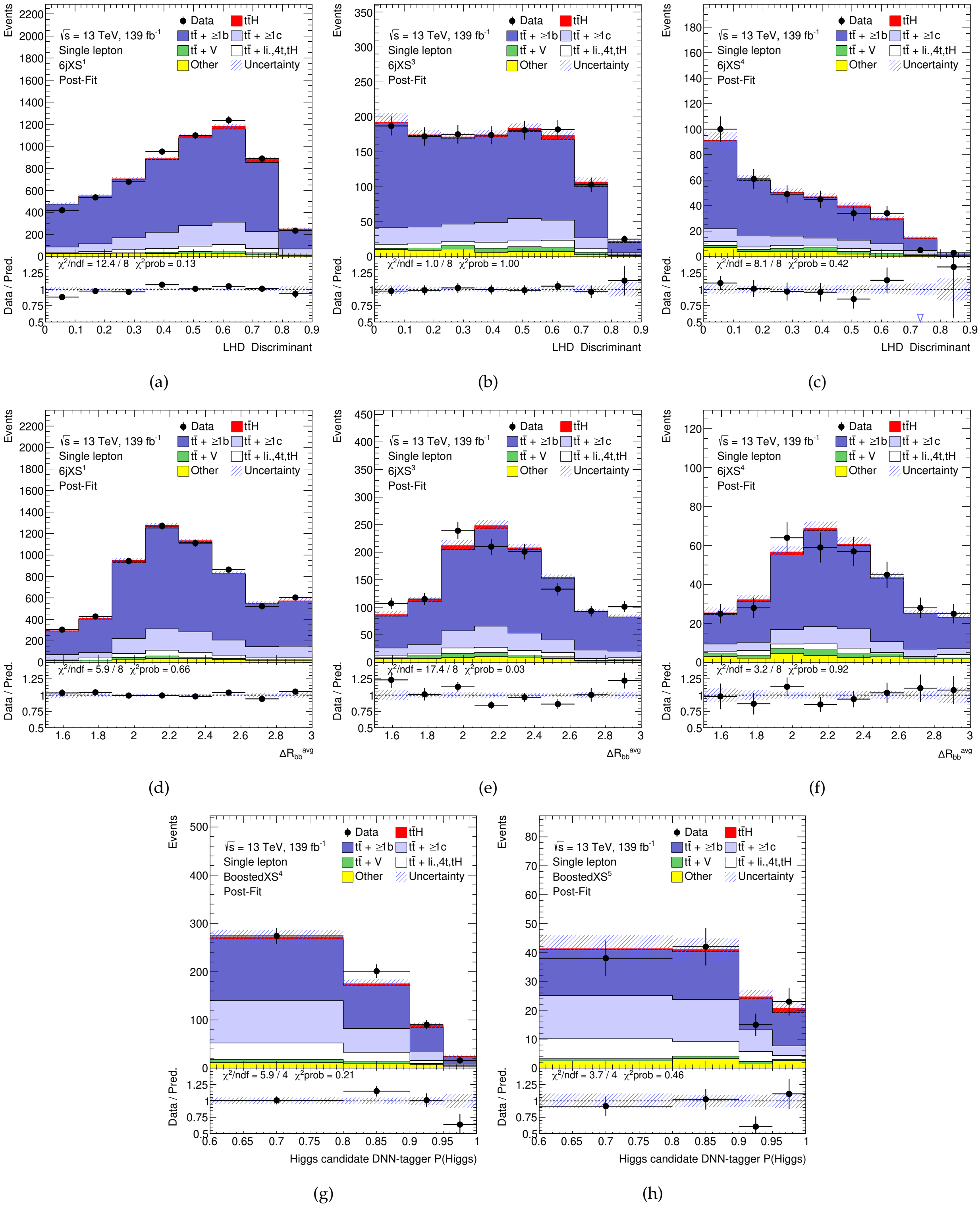

Figure 8.20: Distributions of data and post-fit prediction for the most relevant input variables to the single-lepton Classification BDTs, in the regions 6jXS[1] (left), 6jXS[3] (middle), 6jXS[4] (right), BoostedXS[4] (bottom-left) and BoostedXS[5] (bottom-right). (a,b,c) LHD. (d,e,f) $\Delta R_{bb}^{\text{avg}}$. (g,h) $P(H)$.

Chapter 9

Measurement of the top-Higgs coupling $\mathcal{CP}$

This chapter describes and presents the results of the measurement of the $\mathcal{CP}$ properties of the top quark Yukawa coupling in $t\bar{t}H$ events with leptons and with $H \to b\bar{b}$. The same phase-space is selected as in the cross-section measurement analysis, but inclusive signal regions are split differently, into '$\mathcal{CP}$-dedicated' regions. The signal model is made to depend on the parameters of interest in the fit: the $\mathcal{CP}$-mixing angle in the coupling, α, and the coupling modifier κ_t'.

Section 9.1 describes the signal model and associated uncertainties used in this measurement. Section 9.2 discusses the observables used in the analysis for discriminating between $\mathcal{CP}$ scenarios. The analysis strategy, including region definitions and the corresponding fitted observables, is explained in Section 9.3. Comparisons between data and the pre-fit prediction are shown in Section 9.4. In Sections 9.5 and 9.6, the expected and observed results are discussed, respectively. Post-fit comparisons between predictions and data are given in Section 9.7.

9.1 Signal modelling

9.1.1 $t\bar{t}H$

For the nominal $t\bar{t}H$ model, the MadGraph5_aMC@NLO samples described in Section 6.2.2 for the pure $\mathcal{CP}$-even and pure $\mathcal{CP}$-odd scenarios are used. As in the cross-section analysis, the SM sample is normalised to a cross-section of 507 fb, the central value of the cross-section computed at NLO in QCD with electroweak corrections [59]. This corresponds to a 1.1 K-factor with respect to the prediction by MadGraph5_aMC@NLO in the event generation. The same K-factor of 1.1 is also applied to the pure $\mathcal{CP}$-odd sample.

The expected $t\bar{t}H$ yield in a given analysis bin, for a point in parameter space $(\kappa_t, \tilde{\kappa}_t)$, is parameterised as:

$$y(\kappa_t, \tilde{\kappa}_t) = \kappa_t^2 y_{\text{even}} + \tilde{\kappa}_t{}^2 y_{\text{odd}},$$

where y_{even} and y_{odd} are the expected yields, for that same bin, from the pure $\mathcal{CP}$-even and pure $\mathcal{CP}$-odd $t\bar{t}H$ predictions, respectively. Any possible interference between the $\mathcal{CP}$-even and $\mathcal{CP}$-odd processes is neglected. This was shown to be a good approximation by comparing results at truth level from this parameterisation to the ones obtained from the sample generated in the maximal mixing scenario. This agreement is observed using the cross-sections from MadGraph5_aMC@NLO for the $\mathcal{CP}$-even and $\mathcal{CP}$-odd predictions, which motivates the use of the same K-factor for these samples. Examples of distributions used for the validation of this procedure are shown in Figure 9.1. The decay of the Higgs boson is performed by Pythia8 and is kept to be SM-like, regardless of the $\mathcal{CP}$ parameters of the top-Higgs coupling.

9.1.2 *tH*

In tH production, there is destructive interference between the amplitudes proportional to the top-Higgs coupling and those proportional to the W-Higgs coupling (see Figure 2.6a). This results in a large dependence of the tH cross-section on the coupling parameters. In order to capture this effect, tH yields are parameterised in terms of κ_t and $\tilde{\kappa}_t$ [159]. The parameterisation is separately obtained for the $tHjb$ and tWH processes, and for each analysis bin, as:

$$\frac{y(\kappa_t, \tilde{\kappa}_t)}{y_{\text{even}}} = A\kappa_t^2 + B\tilde{\kappa}_t^2 + C\kappa_t + D\tilde{\kappa}_t + E\kappa_t\tilde{\kappa}_t + F.$$

The coefficients A through F are obtained by fitting the polynomial above to the 11 samples generated for each process, corresponding to the 11 different values of the coupling parameters listed in Section 6.2.2. In the dilepton channel, the $tHjb$ process is found to have a negligible contribution, even in the coupling scenarios in which its cross-section is most enhanced. For this reason, only the tWH process is considered in that channel. Figures 9.2 and 9.3 show the fitted coefficient values and their uncertainties in each of the analysis bins in the single-lepton and dilepton

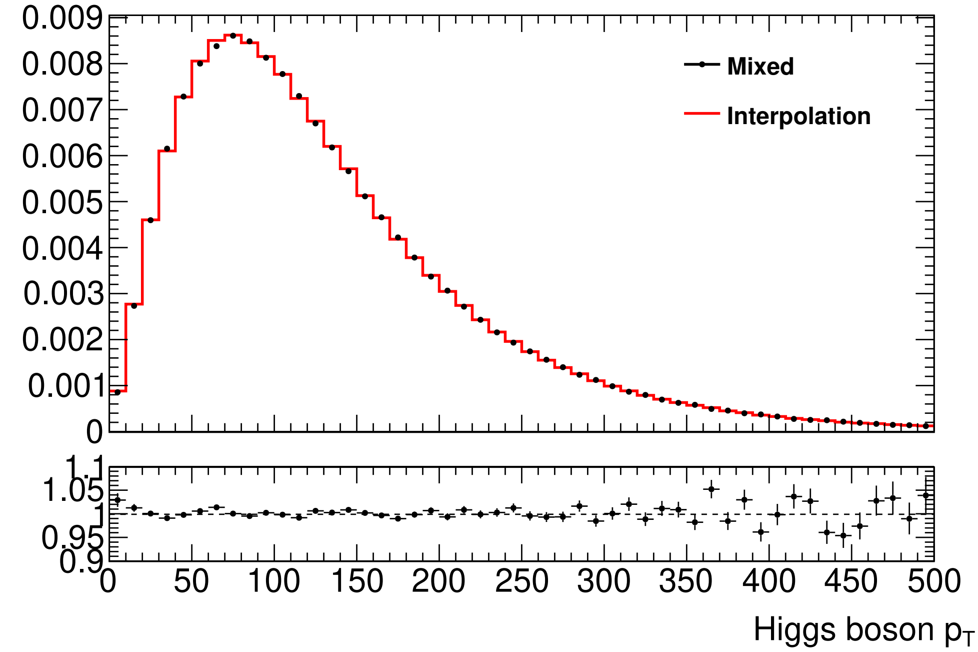

(a)

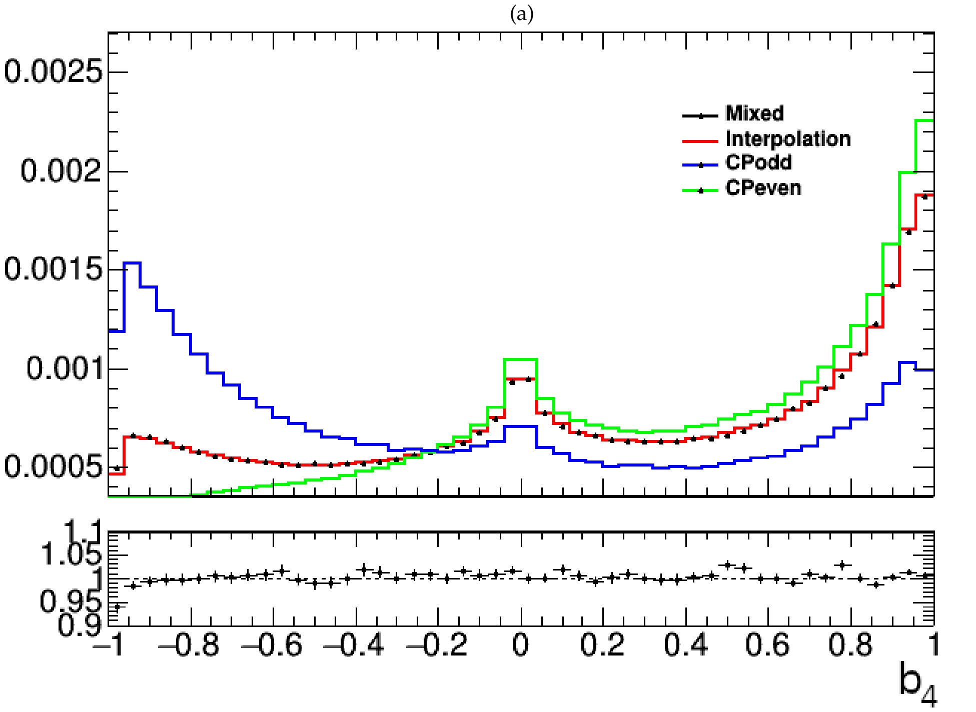

(b)

Figure 9.1: Examples of distributions used for validating the parameterisation of $\mathcal{CP}$-mixed $t\bar{t}H$. Truth-level observables are compared between the parameterised prediction – 'interpolation' – and the sample generated in the $\mathcal{CP}$-mixed scenario – 'mixed'. (a) p_T of the Higgs boson in the single-lepton channel. (b) b_4 in the dilepton channel, with the distributions of the pure $\mathcal{CP}$-even and pure $\mathcal{CP}$-odd samples also shown.

regions, respectively.

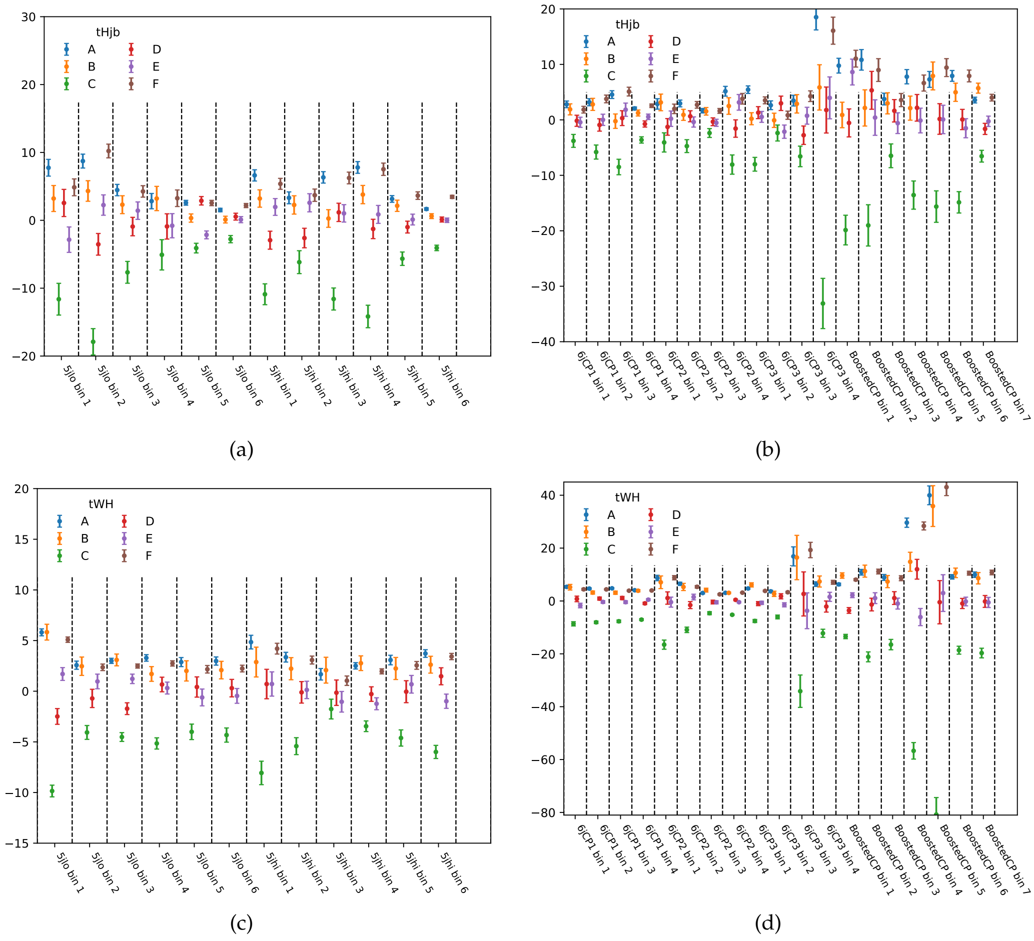

Figure 9.2: Best-fit values and uncertainties for the coefficients A through F in the single-lepton channel. (a) $tHjb$ coefficients in single-lepton control regions. (b) $tHjb$ coefficients in single-lepton $\mathcal{CP}$-dedicated regions. (c) tWH coefficients in single-lepton control regions. (d) tWH coefficients in single-lepton $\mathcal{CP}$-dedicated regions.

The full definition of the analysis bins is only given later, in Section 9.3. Nevertheless, a few remarks can be made about the coefficients at this point. The fact that the coefficient values vary across bins confirms the need to have such a parameterisation in place, that takes into account shape effects across bins. As expected, the A, B and F coefficients, which can be naively associated with production via the $\mathcal{CP}$-even top-Higgs, $\mathcal{CP}$-odd top-Higgs, and W-Higgs couplings, respectively, have a positive sign. The C coefficient, which is associated with the destructive inter-

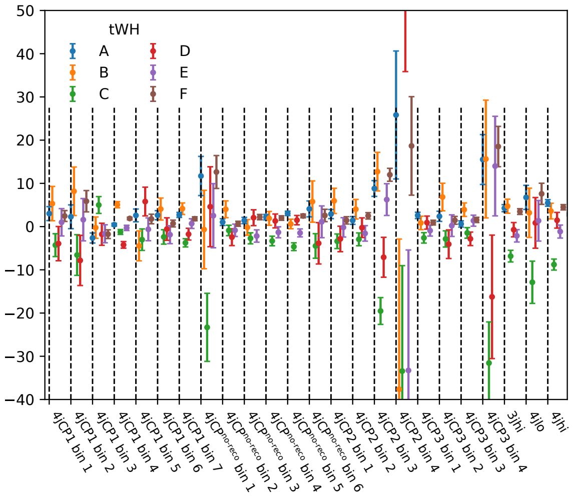

(a)

Figure 9.3: Best-fit values and uncertainties for the coefficients A through F in the dilepton channel. Only the tWH process is considered in the dilepton channel.

ference term, takes negative values, while D and E, included to account for possible interference terms between $\mathcal{CP}$-odd and $\mathcal{CP}$-even contributions arising at NLO, are compatible with zero in the majority of the bins. Validation of this parameterisation was done at the reconstruction level: parameterised yields were compared to those obtained directly from MC for every bin of the analysis and for all the generated points in parameter space. Figure 9.4 shows examples of validation plots for two analysis bins.

As in $t\bar{t}H$, the Higgs boson decay is always SM-like. The W-Higgs coupling, which is relevant in tH production, is also fixed to its SM value.

9.1.3 Uncertainties

For all signal processes, the modelling uncertainties are estimated for the SM scenario, and the obtained relative variations are applied across the full space of coupling parameters.

Two uncertainty sources are considered for the $t\bar{t}H$ cross-section: a 3.6% uncertainty due to PDFs and α_S, and a 9.2% uncertainty due to miss-

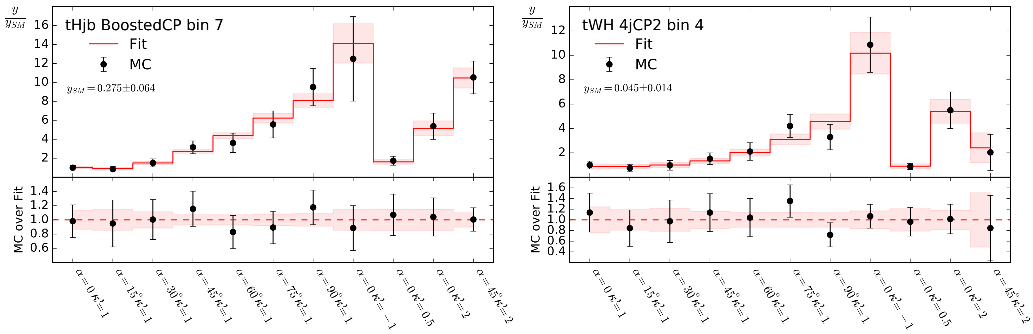

(a) (b)

Figure 9.4: Examples of distributions used for validating the parameterised modelling of tH. Yields in each analysis bin obtained from the available MC samples – 'MC' – are compared to the corresponding parameterised prediction – 'Fit'. (a) $tHjb$ yields in the most signal-rich bin in the boosted region of the single-lepton channel. (b) tWH yields in the most $\mathcal{CP}$-odd enriched bin in one of the dilepton regions.

ing higher-order terms in QCD [59]. The uncertainty due to the choice of NLO matching scheme in $t\bar{t}H$ is obtained by comparing the PowhegBox samples to the nominal MadGraph5_aMC@NLO ones. It is the same comparison as in the cross-section analysis, with a swap between the nominal and alternative predictions. For the uncertainties due to PS and hadronisation, ISR and FSR, the PowhegBox+Pythia8 sample is taken as a reference and compared to the same alternatives as in the cross-section analysis. The resulting relative variations are taken as the relative uncertainty in the $t\bar{t}H$ prediction.

For the modelling of tH production with MC samples, two sources of uncertainty are considered for each process ($tHjb$ and tWH). Unlike what is done for other samples, the impact of these modelling uncertainties on the inclusive cross-section is not removed, and instead they are used to accommodate the cross-section uncertainty. For one source, which is the uncertainty in the PDFs, 100 PDF sets are available through event weights in the nominal samples. The associated uncertainty is defined as the standard deviation of the expected yields, per bin, obtained with the different PDF sets. The other source, due to missing higher-order QCD contributions, is estimated by comparing two alternative predictions, also available as event weights, obtained by coherently varying μ_r and μ_f. The uncertainty on the parameterised yields due to limited MC statistics in the tH samples is obtained from error propagation, through uncertainties on the coefficients.

9.2 $\mathcal{CP}$-even/$\mathcal{CP}$-odd classification

The sensitivity of a measurement to the $\mathcal{CP}$ properties of $t\bar{t}H$ depends on the ability to include observables in the fit that provide discrimination between the $\mathcal{CP}$-even and $\mathcal{CP}$-odd scenarios. In the dilepton channel, a BDT ($\mathcal{CP}$ BDT) is used for this effect. It was trained on $t\bar{t}H$ events in 4j4b for which the reconstruction of top quarks was successful. The training targeted discrimination between the pure $\mathcal{CP}$-even and the pure $\mathcal{CP}$-odd scenarios. The input variables were selected from an extensive list including global event variables (e.g. centrality, aplanarity, H_T), angular separations (between leptons, jets, leptons and jets, reconstructed particles), invariant masses of various composite systems, transverse momenta of b-tagged jet pairs, the output from the Reconstruction BDT, b_4 and products of sines and co-sines of angles evaluated in boosted reference frames. The selection followed several criteria: first, only the ~ 30 variables showing the highest separation between the distributions of the two signal hypotheses were included in a preliminary training. Then, in iterated trainings, the lowest-ranked input variable to the BDT was removed. The process was stopped in the step where a significant drop in the BDT performance was observed, and the training from the immediately preceding step was used. For the remaining variables, the distributions in data and prediction were compared, and the variables displaying the worst modelling were also removed. The final training of the $\mathcal{CP}$ BDT used only b_4 (defined in Section 3.2.3) and products of sines and co-sines of angles evaluated in boosted reference frames (discussed in Section 3.2.5), where the reconstructed particles rely on the assignment made by the Reconstruction BDT with Higgs boson information.

The prescription from Ref. [9] for defining angles in boosted reference frames was extended to generate a larger and better motivated set of possible angles and products of their sines and co-sines. Instead of specifying a top quark and its decay chain by the charge of the corresponding lepton, the label A is used for the top quark which is the least separated in ΔR from the Higgs boson direction. For the top quark which is the most separated from the Higgs boson direction, the label B is used. All particles in the top decay chains inherit the label from their parent top quark. The motivation for specifying the top quarks by proximity to the Higgs boson comes from the relationship between the $\mathcal{CP}$ scenarios and the relative importances of internal and external diagrams in t-channel $t\bar{t}H$ production, as discussed in Section 3.1. In the external diagrams, the Higgs boson is radiated off by one of the external top quark lines and some of that information is expected to be passed on to the ΔR separation between the Higgs boson and the top quarks. For the b jets resulting from the Higgs boson decay, the labels 1 and 2 are used for the leading and subleading jets in p_T, respectively. Two types of angles are used: $\theta(p)$ and $\phi(p_1, p_2, p_3)$. The angle $\theta(p)$ is measured between the momentum of particle p, in the $t\bar{t}H$ rest frame, and the $t\bar{t}H$ momentum in the lab frame. The angle $\phi(p_1, p_2, p_3)$ is measured between the momentum of particle p_1, in the rest frame of particle p_2, and the momentum of particle p_2 in the rest frame of the composite system $p_2 + p_3$.

The input variables to the $\mathcal{CP}$ BDT are summarised in Table 9.1, ranked from most to least important for the BDT output. All the variables used require the successful reconstruction of the $t\bar{t}H$ system. This is not always possible in the dilepton channel, even in 4j4b. For the events in which the reconstruction attempt fails, the discriminant used is $\Delta\eta_{\ell\ell}$.

In the single-lepton channel, the observable b_2 is used as a discriminant between $\mathcal{CP}$ scenarios, and is computed in the $t\bar{t}H$ rest frame to enhance its discrimination power, as argued in Section 3.2.4. The possibility of using a $\mathcal{CP}$ BDT combining several variables was also studied in the single-lepton channel. However, it resulted in a slight decrease in sensitivity with respect to the use of the distribution of b_2, and for that reason the latter was kept, adding the benefit of a simpler analysis

Table 9.1: $\mathcal{CP}$ BDT input variables, ranked from most to least important to the BDT score.

Input variable
b_4
$\sin\theta(t_B)\sin\phi(b_1, t_A, H)$
$\sin\phi(b_A, H, t_A)\sin\phi(W_A, H, t_A)$
$\cos\theta(t_B)\cos\phi(b_2, t_B, H)$
$\sin\theta(t_B)\sin\phi(b_A, H, t_A)$
$\sin\theta(t_B)\sin\phi(b_2, t_A, H)$
$\sin\theta(t_A)\sin\phi(b_2, t_A, H)$
$\sin\theta(t_B)\sin\phi(b_1, t_B, H)$

strategy. This loss in sensitivity with the BDT was attributed to the fact that the background model and uncertainties were not taken into account in the training. The impact of background uncertainties on the BDT may be larger than that on the single variable, or otherwise have an effect on the background distribution that makes it more compatible with either of the signal hypotheses. In that case, in a channel dominated by background uncertainties, it is plausible that the improvement in separation between signal scenarios does not translate into an increase sensitivity. In the dilepton channel, where statistical uncertainty is more important, a significant improvement from using the BDT with respect to the best single variable was observed.

9.3 Analysis strategy

This analysis must provide the ability to constrain simultaneously the rate of signal and its shape in $\mathcal{CP}$-discriminating distributions. In the resolved channels, this is accomplished by a two-step splitting of the inclusive signal regions. The first step divides the inclusive signal regions into new regions, aiming at a better separation between signal and backgrounds. These new regions are referred to as '$\mathcal{CP}$-dedicated' regions. The second step consists of using a $\mathcal{CP}$-discriminant distribution in each of the $\mathcal{CP}$-dedicated regions as input to the fit.

Prior to the first splitting, events in 4j4b for which the reconstruction of the $t\bar{t}H$ system is not successful are classified into a region labelled '4jCP$^{\text{no-reco}}$'. Then, each inclusive signal region is split according to the output of the Classification BDT. The resulting regions in the dilepton channel are 4jCP^1, 4jCP^2 and 4jCP^3, and in the single-lepton channel they are 6jCP^1, 6jCP^2 and 6jCP^3. These regions are numbered in increasing order of signal-to-background ratio.

Unlike in the cross-section analysis, the boosted region is not split further in the $\mathcal{CP}$ analysis. Still, in this context, it is referred to as BoostedCP and included in the category of $\mathcal{CP}$-dedicated regions. A summary of the definition of the $\mathcal{CP}$-dedicated regions is shown in Table 9.2.

Table 9.2: Summary of the definition of $\mathcal{CP}$-dedicated regions from the inclusive signal regions. In the resolved channels, a selection based on the Classification BDT score is used to obtain signal-depleted and signal-enriched regions. In the dilepton channel, events with failed reconstruction are classified in their own region prior to the split.

Inclusive signal region	$\mathcal{CP}$-dedicated region	Classification BDT interval
4j4b	4jCP$^{\text{no-reco}}$	-
	4jCP^1	$[-1, -0.086[$
	4jCP^2	$[-0.086, 0.186[$
	4jCP^3	$[0.186, 1]$
6j4b	6jCP^1	$[-1, -0.128[$
	6jCP^2	$[-0.128, 0.249[$
	6jCP^3	$[0.249, 1]$
Boosted	BoostedCP	-

Background compositions for the $\mathcal{CP}$-dedicated regions, as well as the expected S/B and $S/\sqrt{B}$ ratios for both the $\mathcal{CP}$-even and $\mathcal{CP}$-odd scenarios, in both cases with κ_t' =1, are presented in Figure 9.5. Across the dilepton regions, the background composition is very similar, with relatively larger contributions from $t\bar{t}+V$ in 4jCP^3 and from non-$t\bar{t}$ sources in 4jCP$^{\text{no-reco}}$. In the single-lepton regions, the $t\bar{t}+\geq 1b$ fraction increases as the regions become more enriched in signal. Signal purities are in

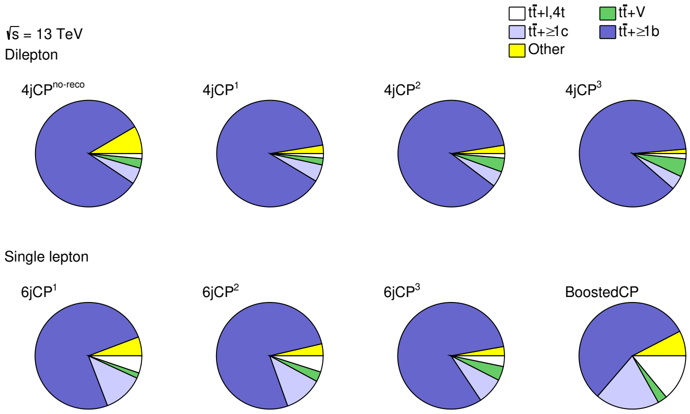

(a)

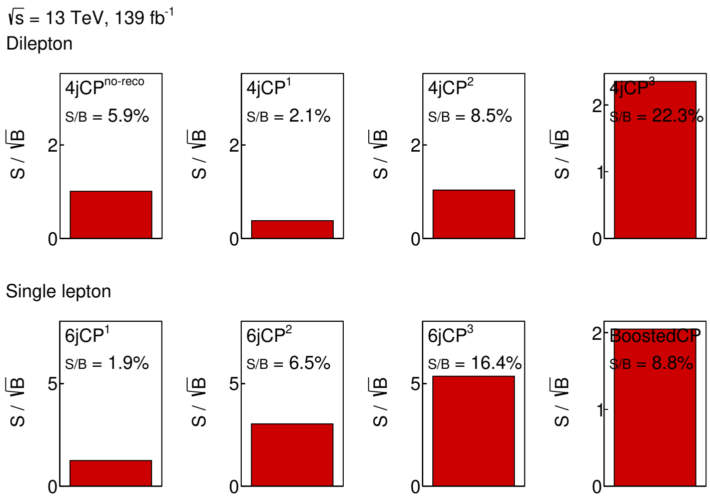

(b)

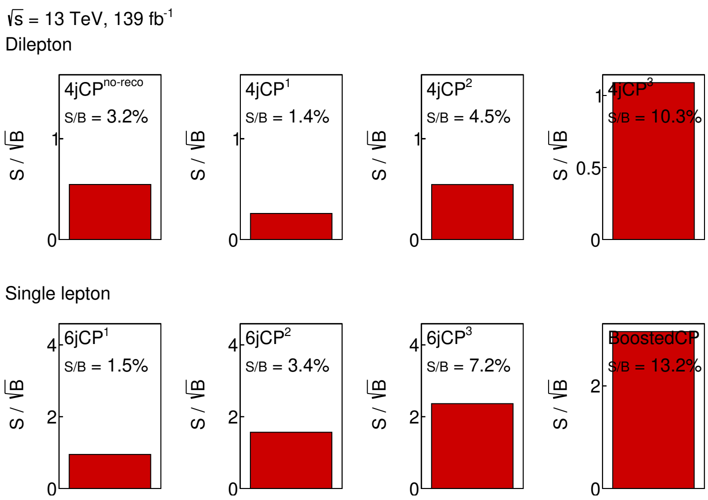

(c)

Figure 9.5: Composition of the $\mathcal{CP}$-dedicated regions. (a) Expected relative background contributions. (b) Signal purities S/B and simplified significances $S/\sqrt{B}$ in the $\mathcal{CP}$-even scenario (κ_t' =1). (c) S/B and $S/\sqrt{B}$ in the $\mathcal{CP}$-odd scenario (κ_t' =1).

general smaller for the $\mathcal{CP}$-odd scenario, because it predicts a lower production cross-section of $t\bar{t}H$. One remarkable exception to this is BoostedCP, where the purity is actually higher in the $\mathcal{CP}$-odd scenario. Two effects contribute to this. One is that the tH contribution, which has its highest relevance in this region, is greatly enhanced in the $\mathcal{CP}$-odd scenario. The other is that the rate of $t\bar{t}H$ events remains approximately the same, because the cross-section suppression in the $\mathcal{CP}$-odd scenario occurs only for low Higgs boson p_T. The rate of increase of S/B from signal-depleted to signal-enriched regions is slightly smaller in the $\mathcal{CP}$-odd scenario. This is because the Classification BDT was trained to discriminate between backgrounds and $\mathcal{CP}$-even $t\bar{t}H$ signal, thus not being so effective in doing the same in the $\mathcal{CP}$-odd case.

Figure 9.6 shows the comparison between data and prediction for the event yields in the $\mathcal{CP}$-dedicated regions. The $\mathcal{CP}$-even scenario is used for the signal, but a normalised distribution of $t\bar{t}H$ in the $\mathcal{CP}$-odd scenario is also shown. From this comparison, aside from the overall underestimation of the $t\bar{t}+\geq 1b$ background, some mismodelling is visible in the distribution of events across single-lepton regions: in 6j4b, data is more distributed towards the background-like regions of the Classification BDT than the prediction and, comparing 6j4b and BoostedCP, the ratio between events in the two categories is also mismodelled, with a lower fraction of boosted events in data. In the dilepton channel, the modelling of the Classification BDT shape is good, as is that of the fraction of dilepton events failing reconstruction. Tables 9.3 and 9.4 provide the same information in numeric format for the dilepton and single-lepton $\mathcal{CP}$-dedicated regions, respectively, with the addition of $t\bar{t}H$ and tH event yields also for the $\mathcal{CP}$-odd scenario. The enhancement of tH in the $\mathcal{CP}$-odd scenario is visible: it is most pronounced in the boosted region, where the tH contribution is 15 times larger than in the $\mathcal{CP}$-even scenario and makes up for more than a third of the total signal.

In the resolved $\mathcal{CP}$-dedicated regions, the distributions of the $\mathcal{CP}$ discriminants discussed above are used as observables in the fit. This means that the $\mathcal{CP}$ BDT output is used in the dilepton regions, except

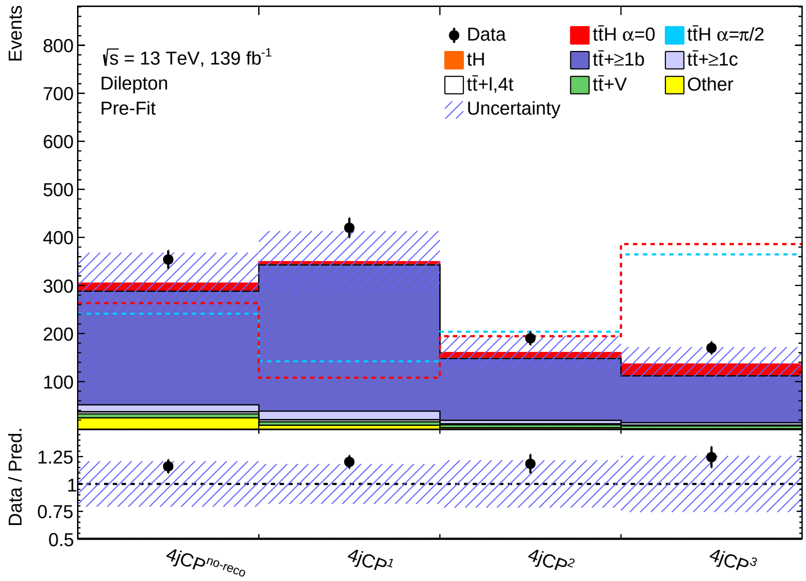

(a)

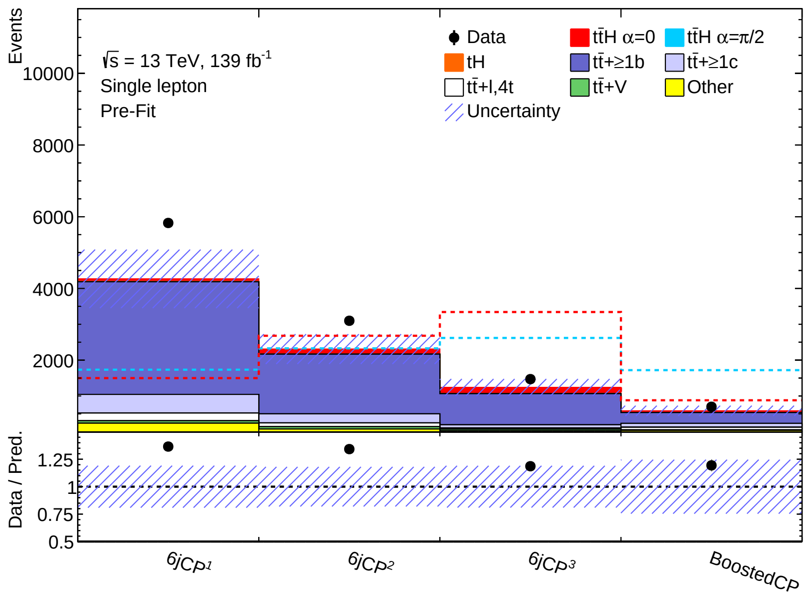

(b)

Figure 9.6: Comparison between data and $\mathcal{CP}$-even pre-fit prediction for the event yields in $\mathcal{CP}$-dedicated regions. (a) Dilepton channel. (b) Single-lepton channel.

Table 9.3: Data and pre-fit prediction for the event yields in the dilepton $\mathcal{CP}$-dedicated regions. Signal predictions are included for the $\mathcal{CP}$-even and $\mathcal{CP}$-odd scenarios (with $\kappa_t' = 1$).

	4jCP$^{\text{no-reco}}$	4jCP^1	4jCP^2	4jCP^3
$t\bar{t}H, \alpha = 0$	16.9 $\pm$ 2.2	6.9 $\pm$ 1.1	12.5 $\pm$ 1.5	24.8 $\pm$ 3.0
$tWH, \alpha = 0$	0.213 $\pm$ 0.088	0.097 $\pm$ 0.038	0.107 $\pm$ 0.034	0.093 $\pm$ 0.067
$t\bar{t}H, \alpha = \pi/2$	7.24 $\pm$ 0.92	4.27 $\pm$ 0.63	6.11 $\pm$ 0.72	10.9 $\pm$ 1.3
$tWH, \alpha = \pi/2$	2.03 $\pm$ 0.83	0.51 $\pm$ 0.20	0.52 $\pm$ 0.17	0.57 $\pm$ 0.41
$t\bar{t} + \geq 1b$	237 $\pm$ 59	304 $\pm$ 59	129 $\pm$ 33	98 $\pm$ 34
$t\bar{t} + \geq 1c$	14 $\pm$ 16	18 $\pm$ 19	7.1 $\pm$ 7.6	4.8 $\pm$ 5.2
$t\bar{t}$ + light, $4t$	4.5 $\pm$ 3.9	4.6 $\pm$ 3.8	2.0 $\pm$ 1.7	1.8 $\pm$ 1.5
$t\bar{t}Z$	7.6 $\pm$ 1.5	6.7 $\pm$ 1.5	5.9 $\pm$ 1.1	5.8 $\pm$ 1.2
$t\bar{t}W$	0.59 $\pm$ 0.15	0.39 $\pm$ 0.14	0.29 $\pm$ 0.17	0.26 $\pm$ 0.17
Fake leptons	2.34 $\pm$ 0.77	2.15 $\pm$ 0.75	0.62 $\pm$ 0.30	0.85 $\pm$ 0.38
Other	22 $\pm$ 11	6.7 $\pm$ 3.6	3.2 $\pm$ 2.3	0.69 $\pm$ 0.86
Total prediction ($\alpha = 0$)	305 $\pm$ 63	350 $\pm$ 64	161 $\pm$ 35	137 $\pm$ 35
Data	354	420	190	170

Table 9.4: Data and pre-fit prediction for the event yields in the single-lepton $\mathcal{CP}$-dedicated regions. Signal predictions are included for the $\mathcal{CP}$-even and $\mathcal{CP}$-odd scenarios (with $\kappa_t' = 1$).

	6jCP^1	6jCP^2	6jCP^3	BoostedCP
$t\bar{t}H, \alpha = 0$	78 $\pm$ 11	139 $\pm$ 19	174 $\pm$ 27	45.7 $\pm$ 5.7
$tHjb, \alpha = 0$	1.88 $\pm$ 0.35	1.30 $\pm$ 0.38	0.72 $\pm$ 0.24	1.15 $\pm$ 0.23
$tWH, \alpha = 0$	1.05 $\pm$ 0.24	0.78 $\pm$ 0.34	0.46 $\pm$ 0.31	0.54 $\pm$ 0.15
$t\bar{t}H, \alpha = \pi/2$	45 $\pm$ 11	61 $\pm$ 12	68 $\pm$ 16	44.7 $\pm$ 6.1
$tHjb, \alpha = \pi/2$	7.6 $\pm$ 1.4	5.6 $\pm$ 1.6	4.0 $\pm$ 1.3	14.1 $\pm$ 2.8
$tWH, \alpha = \pi/2$	8.7 $\pm$ 2.0	6.8 $\pm$ 2.9	5.0 $\pm$ 3.3	12.1 $\pm$ 3.3
$t\bar{t}+ \geq 1b$	3140 $\pm$ 480	1660 $\pm$ 260	870 $\pm$ 200	302 $\pm$ 57
$t\bar{t}+ \geq 1c$	520 $\pm$ 550	250 $\pm$ 270	86 $\pm$ 91	100 $\pm$ 110
$t\bar{t}$ + light, $4t$	220 $\pm$ 130	106 $\pm$ 59	34 $\pm$ 23	76 $\pm$ 34
$t\bar{t}Z$	61.4 $\pm$ 9.2	60.2 $\pm$ 8.5	43.4 $\pm$ 6.8	12.9 $\pm$ 2.5
$t\bar{t}W$	7.6 $\pm$ 1.5	5.23 $\pm$ 0.98	2.48 $\pm$ 0.48	2.41 $\pm$ 0.53
Single top Wt	99 $\pm$ 54	32 $\pm$ 20	13.2 $\pm$ 9.7	19 $\pm$ 11
Other single top	61 $\pm$ 32	21 $\pm$ 17	6.2 $\pm$ 3.4	5.1 $\pm$ 3.7
V+jets, VV+jets	82 $\pm$ 36	26 $\pm$ 12	10.4 $\pm$ 5.3	16.7 $\pm$ 8.2
Total prediction ($\alpha = 0$)	4270 $\pm$ 820	2310 $\pm$ 420	1240 $\pm$ 240	590 $\pm$ 140
Data	5826	3098	1470	699

for 4jCP$^{\text{no-reco}}$, where $\Delta\eta_{\ell\ell}$ is used instead. In the resolved single-lepton regions, b_2 is used. This provides sensitivity to the $\mathcal{CP}$-odd coupling and allows the background modelling of the $\mathcal{CP}$ discriminants to be adjusted, using the higher statistics in the regions of lower signal purity. Figure 9.7 shows two-dimensional distributions of the Classification and $\mathcal{CP}$ BDTs in 4j4b (after removing events falling into 4jCP$^{\text{no-reco}}$), separately for the $t\bar{t}+\text{jets}$, $\mathcal{CP}$-even $t\bar{t}H$ and $\mathcal{CP}$-odd $t\bar{t}H$ processes. The boundaries used for the region splitting and binning are also represented, as well as the correlation coefficients between the two variables. Figure 9.8 shows similar distributions for the single-lepton channel, in which the $\mathcal{CP}$ discriminant b_2 is used instead of a $\mathcal{CP}$ BDT.

In BoostedCP, the distribution of the Classification BDT is used as input to the fit. No distribution of a $\mathcal{CP}$ discriminant is used. However, as already discussed, the fraction of high-p_T ($\gtrsim$ 200 GeV) Higgs bosons in $t\bar{t}H$ is expected to be much higher in the $\mathcal{CP}$-odd scenario than in $\mathcal{CP}$-even. This means that the amount of signal in the boosted region with respect to that in the resolved regions is enough to add sensitivity to the presence of a $\mathcal{CP}$-odd coupling.

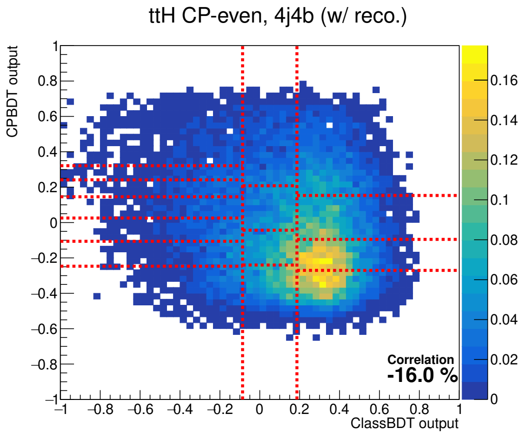

(a)

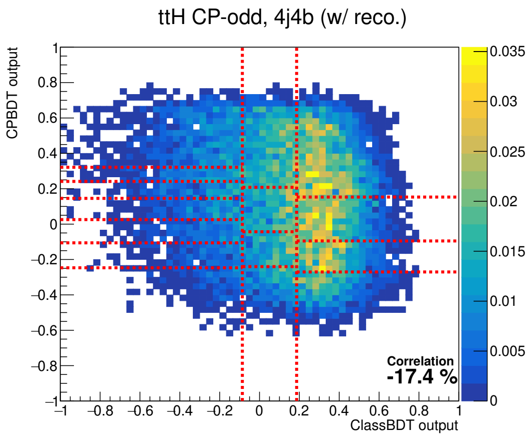

(b)

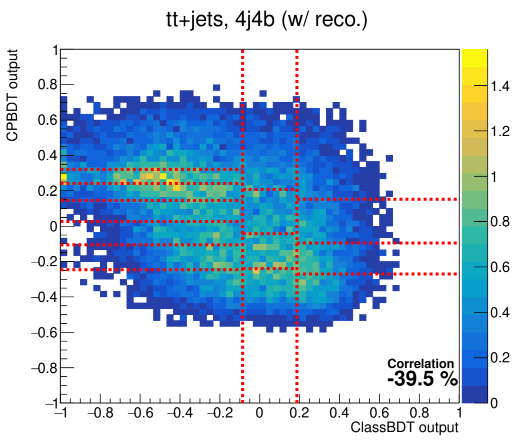

(c)

Figure 9.7: Two-dimensional distributions of the Classification and $\mathcal{CP}$ BDTs in the dilepton region 4j4b, after removing events with failed reconstruction. (a) $\mathcal{CP}$-even $t\bar{t}H$. (b) $\mathcal{CP}$-odd $t\bar{t}H$. (c) $t\bar{t}+$jets. The boundaries along which the inclusive signal region is split are represented as dashed lines, as well as the bin edges used in the $\mathcal{CP}$ BDT distribution.

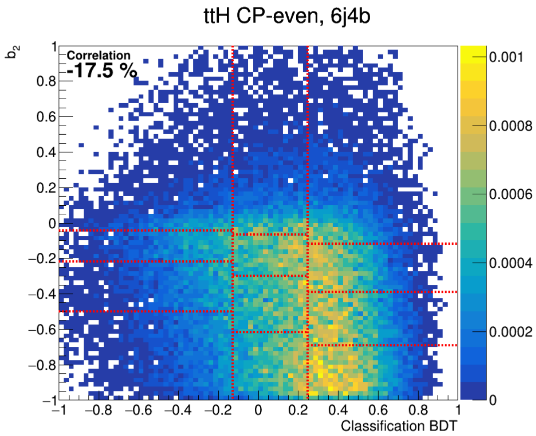

(a)

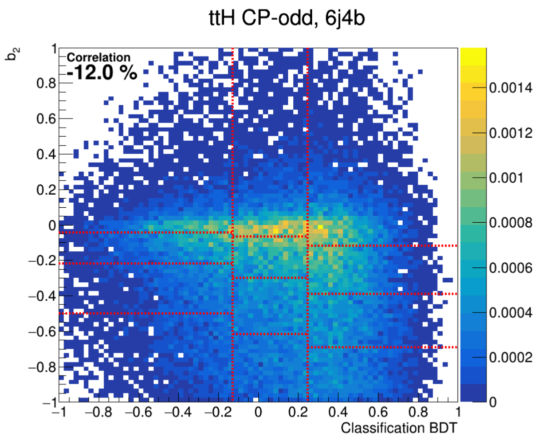

(b)

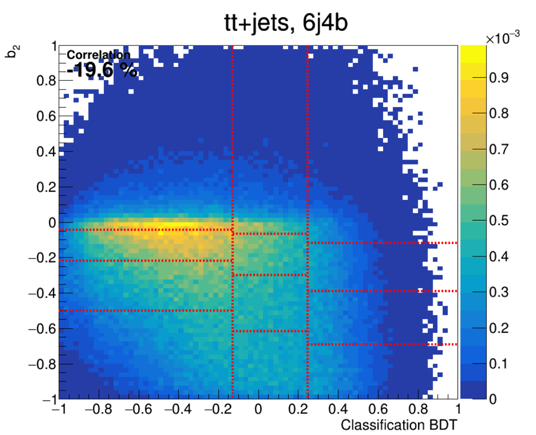

(c)

Figure 9.8: Two-dimensional distributions of the Classification BDT and b_2 in the single-lepton region 6j4b. (a) $\mathcal{CP}$-even $t\bar{t}H$. (b) $\mathcal{CP}$-odd $t\bar{t}H$. (c) $t\bar{t}+$jets. The boundaries along which the inclusive signal regions are split are represented as dashed lines, as well as the bin edges in b_2.

9.4 Pre-fit modelling in analysis regions

This section presents comparisons of distributions between data and pre-fit prediction, for the $\mathcal{CP}$-dedicated regions.

9.4.1 Observable distributions

Figures 9.9 and 9.10 show the data and pre-fit prediction for the distributions that are used in the fit in the dilepton and single-lepton channels, respectively. The $\mathcal{CP}$-even signal prediction is used, but the shape of $\mathcal{CP}$-odd $t\bar{t}H$ is shown as well. Overall, a decent modelling of the shapes is observed already at pre-fit, taking into account the large pre-fit uncertainty. In the $\mathcal{CP}$ BDT distributions, the first bin (the most $\mathcal{CP}$-even like) shows a consistent peak in the data-to-prediction ratio across regions. The data in 6jCP^3 is distributed more towards the $\mathcal{CP}$-odd-like bins of the b_2 distribution than the prediction. From the signal shapes, the significant discrimination between $\mathcal{CP}$ scenarios provided by the distributions of b_2 and of the $\mathcal{CP}$ BDT is evident.

9.4.2 $\mathcal{CP}$ BDT input variables

Figure 9.11 shows data and pre-fit predictions for distributions of the three most important variables used as inputs to the $\mathcal{CP}$ BDT, in the dilepton regions where the $\mathcal{CP}$ BDT is used. Some mismodelling of the distribution shapes is visible, which is nevertheless covered by the statistical uncertainty on the data and the pre-fit systematic uncertainty.

9.5 Expected results

Results from fits to Asimov datasets are presented in this section. Two Asimov datasets were used to perform the fits, one using the SM signal prediction and another using a pure $\mathcal{CP}$-odd prediction with $\kappa_t' = 1$. The parameters of interest fitted are α and κ_t'.

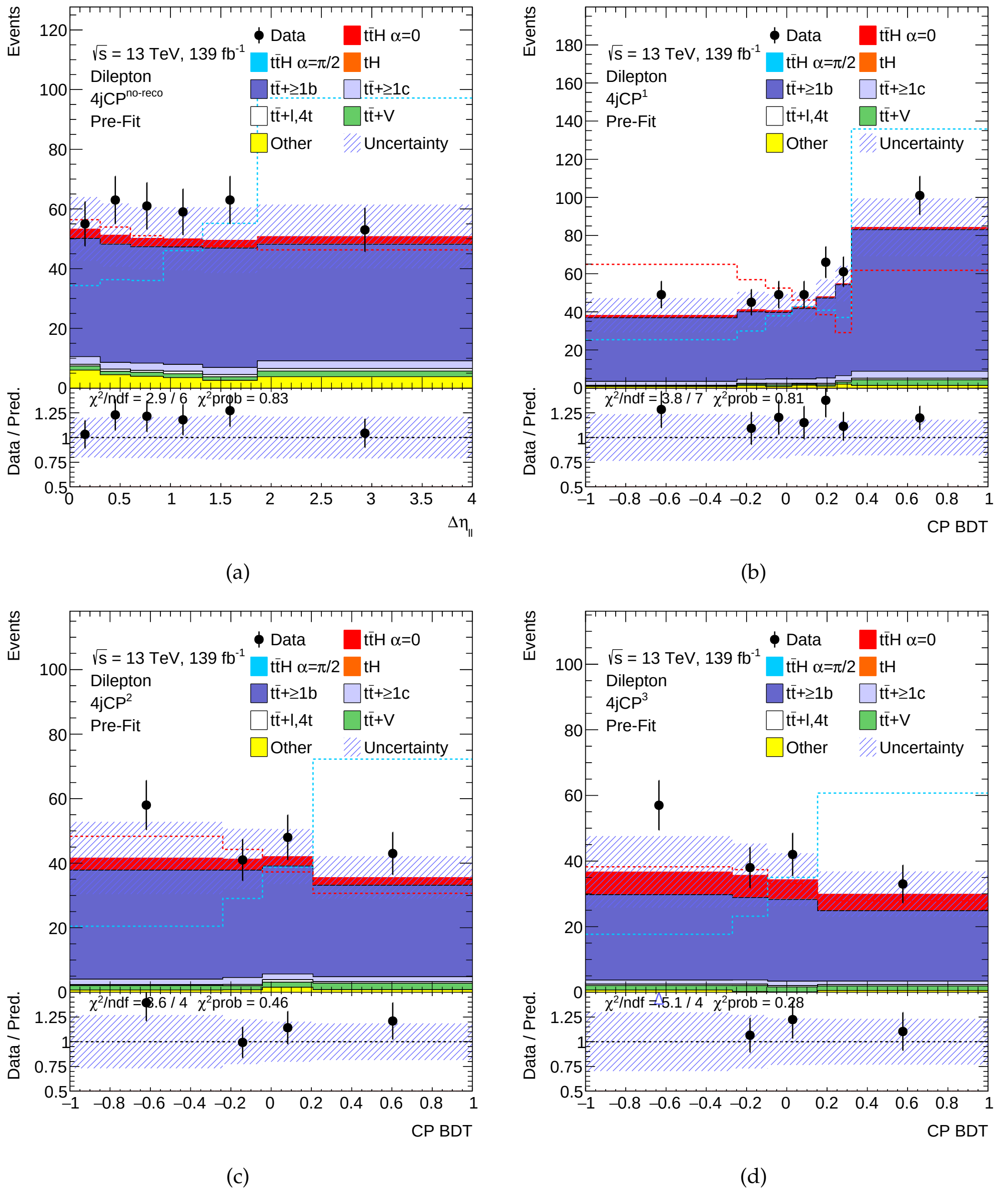

Figure 9.9: Comparison between data and pre-fit prediction of the distributions used in the fit in each of the dilepton $\mathcal{CP}$-dedicated regions. (a) 4jCP$^{\text{no-reco}}$. (b) 4jCP^1. (c) 4jCP^2. (d) 4jCP^3.

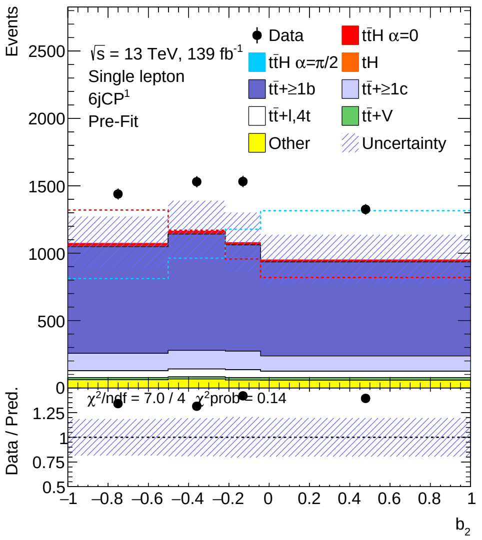

(a)

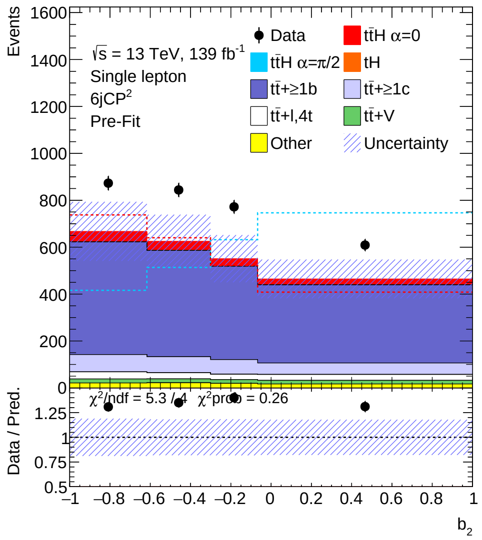

(b)

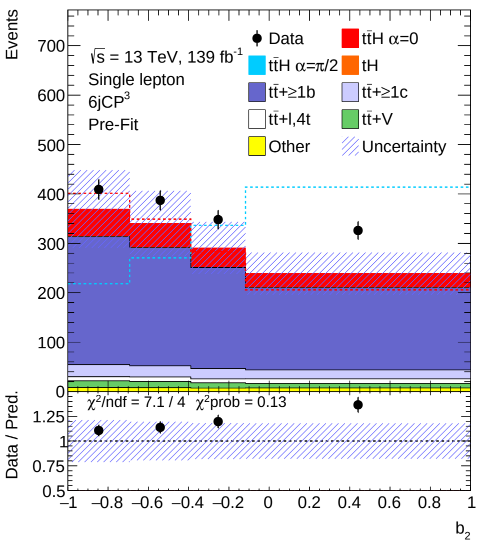

(c)

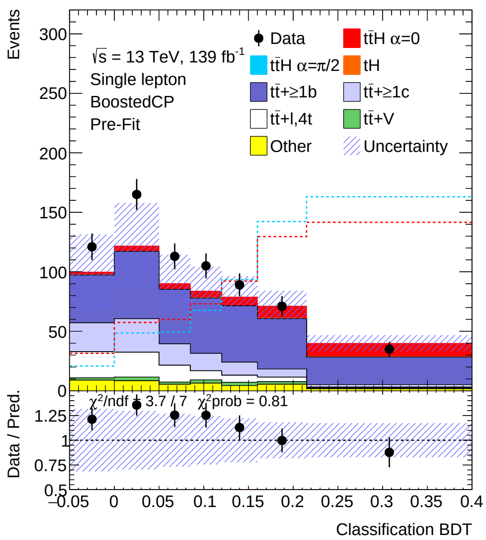

(d)

Figure 9.10: Comparison between data and pre-fit prediction of the distributions used in the fit in each of the single-lepton $\mathcal{CP}$-dedicated regions. (a) 6jCP^1. (b) 6jCP^2. (c) 6jCP^3. (d) BoostedCP.

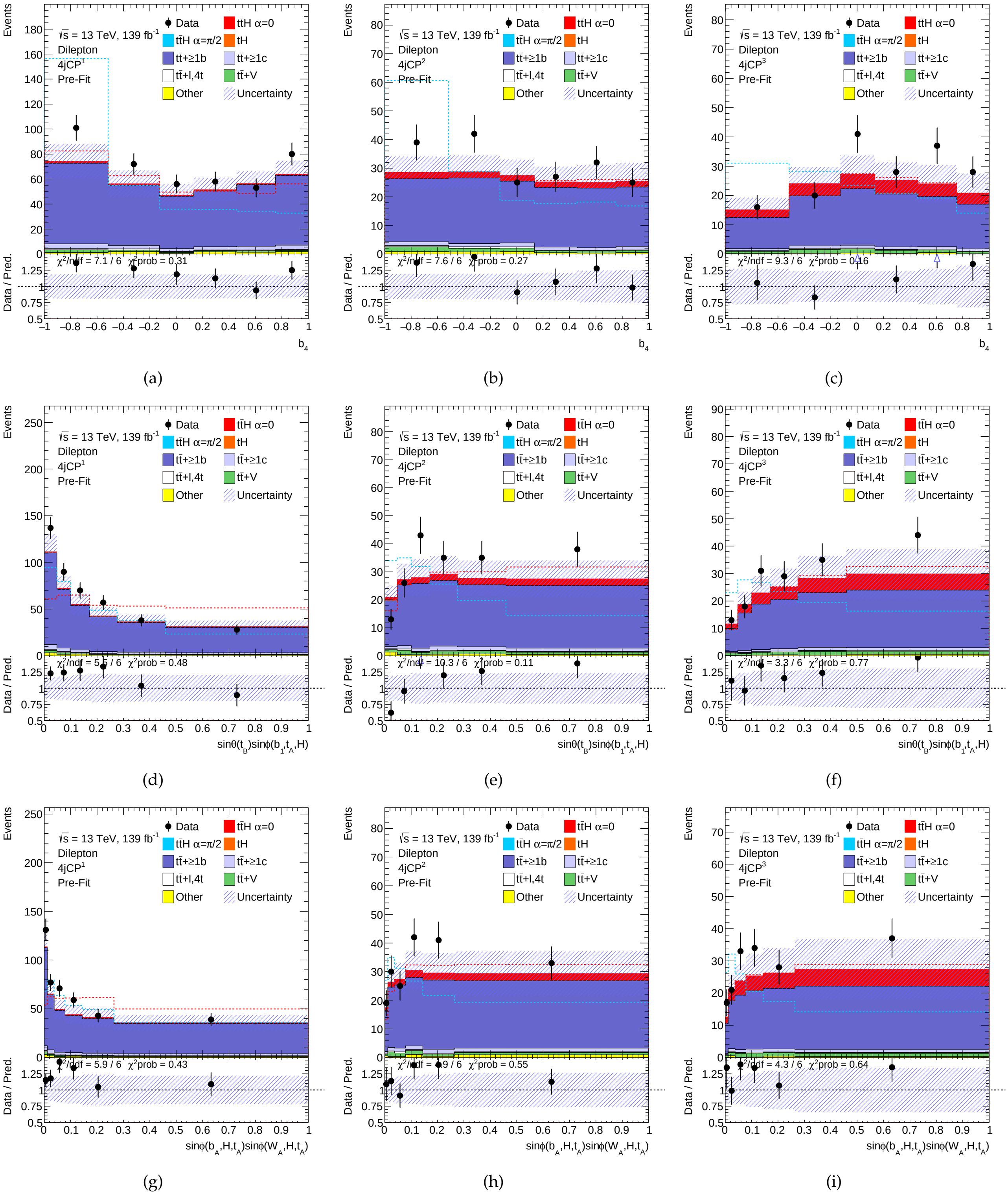

Figure 9.11: Comparison between data and pre-fit prediction of the distributions of the most important input variables to the $\mathcal{CP}$ BDT, in 4jCP^1 (left), 4jCP^2 (middle), and 4jCP^3 (right). (a,b,c) b_4. (d,e,f) $\sin\theta(t_B)\sin\phi(b_1,t_A,H)$. (g,h,i) $\sin\phi(b_A,H,t_A)\sin\phi(W_A,H,t_A)$.

The expected results for α are shown in Figure 9.12. The NLL scan in α is shown, for the combined regions, but also separately for the single-lepton and dilepton channels. Unlike in the cross-section analysis, where the individual channel results correspond to multiple signal strengths in a single fit to all regions, here the individual channel results come from separate fits, each using the regions of the corresponding channel. Using the NLL scan, the best-fit value and 1σ intervals for α are derived, as well as the exclusion significances of the $\mathcal{CP}$-odd scenario for the $\mathcal{CP}$-even Asimov and of the $\mathcal{CP}$-even scenario for the $\mathcal{CP}$-odd Asimov. These significances refer to the exclusion of the corresponding α values regardless of κ_t', which is profiled. Essentially, the signal rate information is not used to discriminate between $\mathcal{CP}$ scenarios. The expected uncertainty on α in a measured signal, assuming the SM scenario, is ${}^{+0.28\pi}_{-0.27\pi}$, or ${}^{+50^\circ}_{-49^\circ}$. In that case, the $\alpha = \pm\pi$ scenario ($\mathcal{CP}$-even with negative κ_t) is excluded at 1.1σ. In the pure $\mathcal{CP}$-odd scenario, the expected uncertainty around the best-fit value of α is ${}^{+0.33\pi}_{-0.25\pi}$, or ${}^{+59^\circ}_{-45^\circ}$. The $\mathcal{CP}$-even scenario with negative κ_t is not as excluded as the one with the SM coupling, due to the enhancement of the tH cross-section, which contributes to the yield in BoostedCP, making it more compatible with the $\mathcal{CP}$-odd Asimov. Another minimum exists for negative α, with barely higher NLL value. In practice, this measurement has no sensitivity to the sign of α, or equivalently, to the sign of $\tilde{\kappa}_t$. Overall, the sensitivity is driven by the single-lepton channel, and this is especially the case for the $\mathcal{CP}$-odd Asimov.

Expected results on κ_t' and on the normalisation factor of $t\bar{t} + \geq 1b$ are shown in Figure 9.13. The uncertainty in κ_t' is ${}^{+0.21}_{-0.23}$ in the $\mathcal{CP}$-even Asimov fit, which corresponds to an uncertainty in signal strength of ${}^{+0.46}_{-0.41}$, considerably larger than in the cross-section measurement. This is expected because two parameters of interest are fitted instead of a single one. In the dilepton channel and in the combined result, the uncertainty in κ_t' is larger in the $\mathcal{CP}$-odd Asimov fit, due to the smaller signal rate. In particular, the dilepton result is compatible with the background-only hypothesis ($\kappa_t' = 0$) within 1σ. In both $\mathcal{CP}$ scenarios, the single-lepton channel is much more sensitive to this parameter. The uncertainty in the

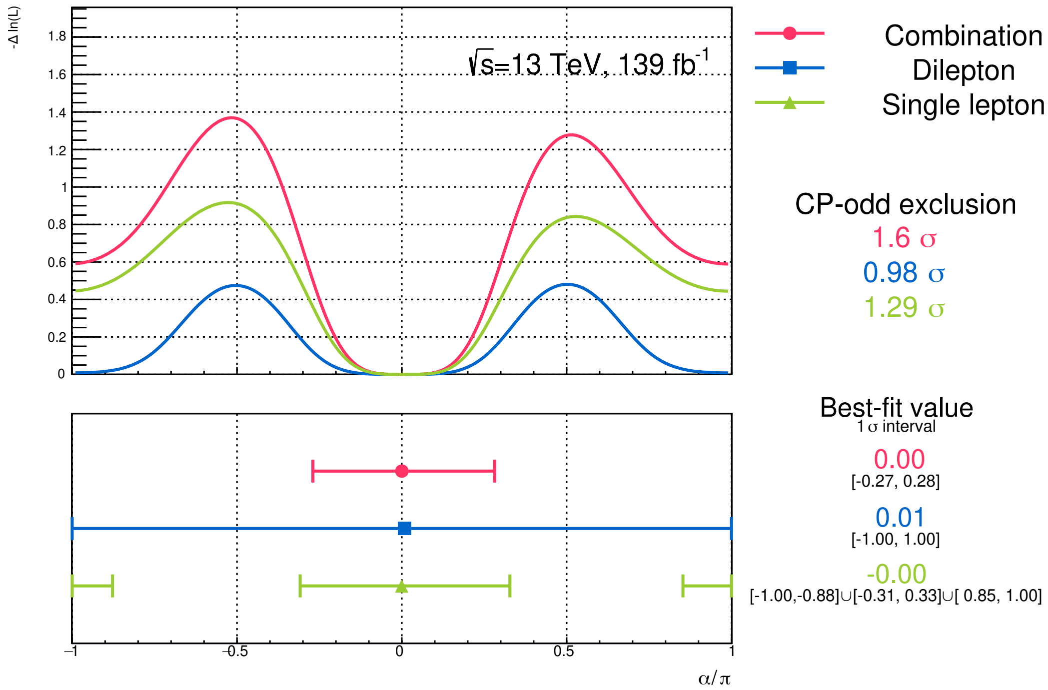

(a)

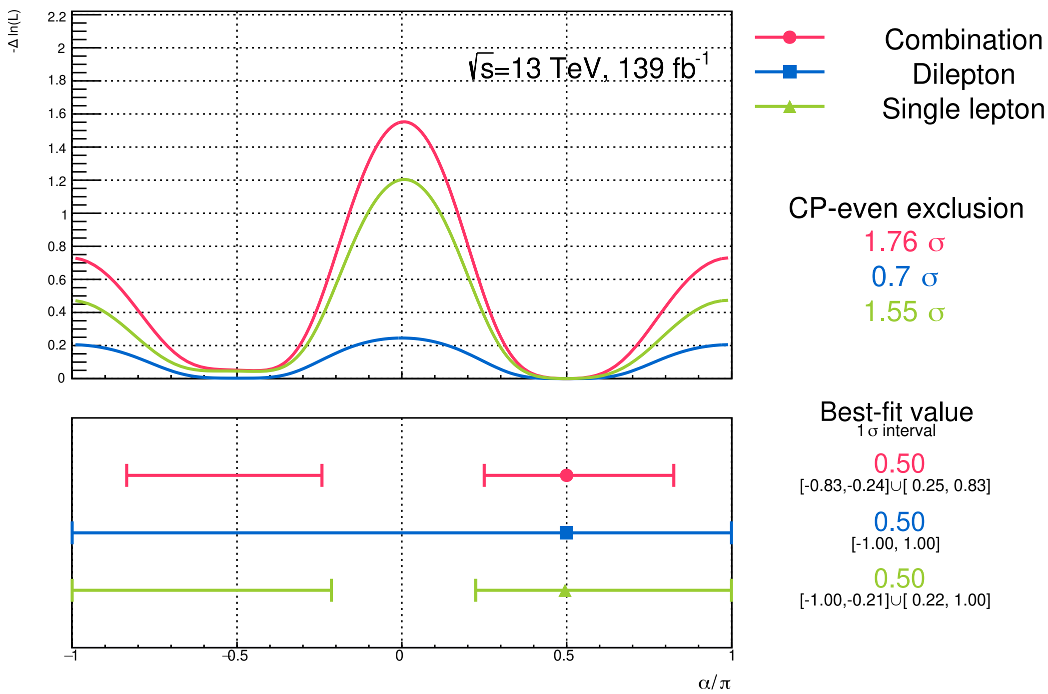

(b)

Figure 9.12: Expected results for α from the combined fit and from fits to the single-lepton or dilepton regions separately. Besides the NLL scan, also the 1σ intervals and the exclusion significance of the 'opposite' $\mathcal{CP}$ scenario are shown. (a) $\mathcal{CP}$-even Asimov dataset. (b) $\mathcal{CP}$-odd Asimov dataset.

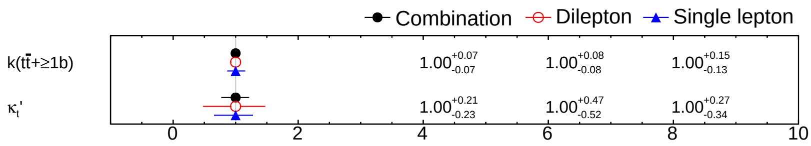

(a)

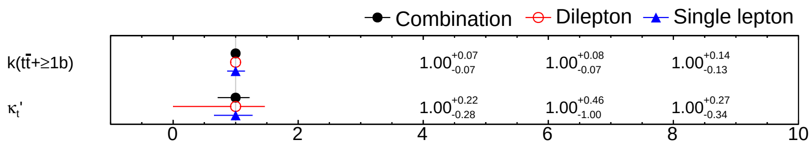

(b)

Figure 9.13: Expected results on κ_t' and on the $t\bar{t} + \geq 1b$ normalisation factor. (a) $\mathcal{CP}$-even Asimov dataset. (b) $\mathcal{CP}$-odd Asimov dataset.

$t\bar{t} + \geq 1b$ normalisation factor is the same in the two scenarios and equal to the expected one in the cross-section analysis.

The expected two-dimensional NLL scans on the $(\kappa_t, \tilde{\kappa}_t)$ plane are shown in Figure 9.14 for the $\mathcal{CP}$-even and $\mathcal{CP}$-odd Asimov datasets. The results on α and κ_t' discussed previously are reflected here, respectively in the constraints on the angular and radial coordinates. An interesting feature that only becomes visible in this representation is the fact that, in the minima close to the $\mathcal{CP}$-even scenario with negative κ_t, the preferred value of κ_t' is between 0.7 and 0.8, and not 1. This is due to the enhancement of tH in this region: since the rate of tH is larger than in the SM, the Asimov dataset is better fitted by bringing the $t\bar{t}H$ and tH rates down through κ_t'.

Expected constraints on the most relevant nuisance parameters are presented in Figure 9.15, for the combined fit as well as for the fits to the individual channels. The results on the full set of nuisance parameters are given in Appendix C. The expected constraints are compatible with those expected in the cross-section measurement. A strong constraint is expected in the additional $t\bar{t} + \geq 1b$ uncertainty related to the choice of ME and flavour scheme. For uncertainties which are separated into multiple com-

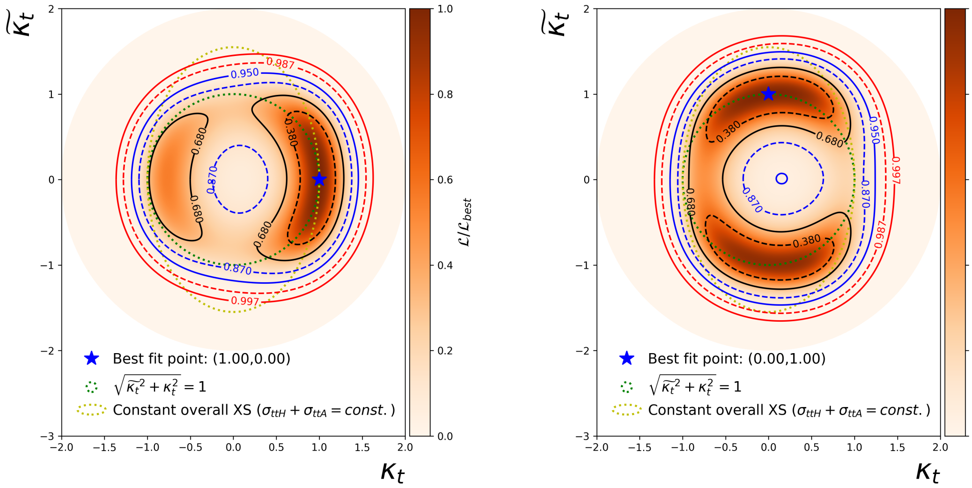

(a) (b)

Figure 9.14: Expected two-dimensional NLL scans on the $(\kappa_t, \tilde{\kappa}_t)$ plane. The solid contours are lines of equal exclusion significance: 1σ in black, 2σ in blue, 3σ in red. (a) $\mathcal{CP}$-even Asimov dataset. (b) $\mathcal{CP}$-odd Asimov dataset.

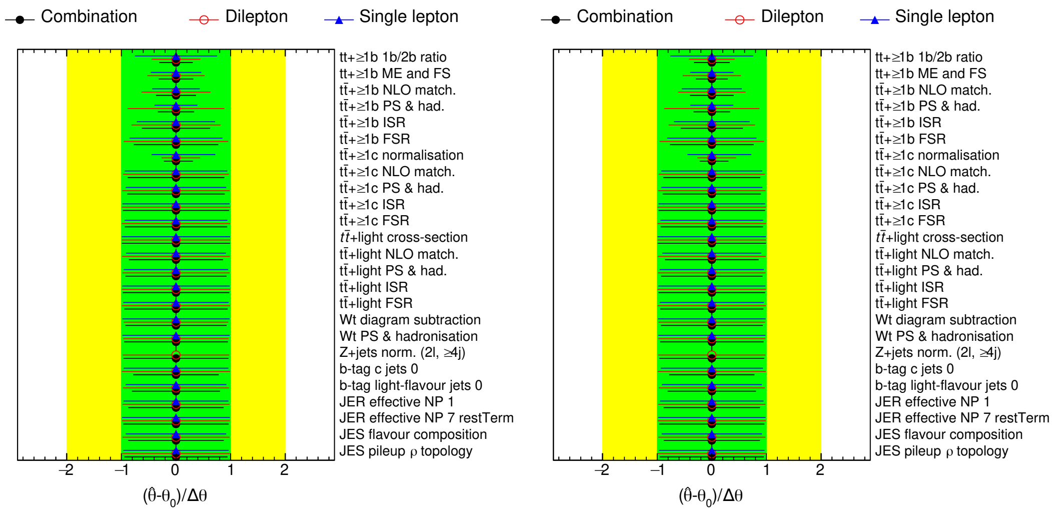

(a) (b)

Figure 9.15: Expected constraints on nuisance parameters in the combined fit and in the fits to single-lepton or dilepton regions only. (a) $\mathcal{CP}$-even Asimov dataset. (b) $\mathcal{CP}$-odd Asimov dataset.

ponents in the cross-section analysis, such as the ones due to $t\bar{t} + \geq 1b$ NLO matching and PS and hadronisation, the corresponding single parameter in the $\mathcal{CP}$ analysis is expected to be more strongly constrained. The $t\bar{t} + \geq 1b$ ISR uncertainty is not expected to be as constrained in this analysis as in the cross-section analysis. In terms of comparisons between channels, the constraints on the normalisation of the $t\bar{t} + \geq 1c$ background and on the $1b/2b$ ratio of $t\bar{t} + \geq 1b$ are dominated by the dilepton channel, owing to the control regions with 3 b-tagged jets. The single-lepton regions bring most of the sensitivity to the $t\bar{t} + \geq 1b$ PS and hadronisation model.

The expected correlation coefficients (in %) between the nuisance parameters are presented in the matrices of Figure 9.16. The correlation coefficients are obtained from the Hessian matrix assuming a quadratic dependence of the NLL on the parameters near the minimum. In the case of α, the NLL has a quartic dependence on it near the minimum. For that reason, the correlation coefficients between α and the other parameters are not available. As in the cross-section measurement, the strongest correlations occur among parameters related to $t\bar{t} + \geq 1b$ modelling uncertainties. A direct comparison between the two analyses is difficult to make for $t\bar{t} + \geq 1b$ modelling uncertainties in particular, due to their different definitions. However, the correlations between other $t\bar{t}$ modelling parameters and the instrumental ones are similar between the two analyses. The uncertainty related to choice of ME and flavour scheme, exclusive to the $\mathcal{CP}$ analysis, becomes highly anti-correlated with $t\bar{t} + \geq 1b$ ISR. This correlation contributes to the weaker constraint on $t\bar{t} + \geq 1b$ ISR in the $\mathcal{CP}$ analysis. One of the strongest correlations in the cross-section analysis, between $t\bar{t} + \geq 1b$ $1b/2b$ ratio and ISR, is no longer present. There are moderate differences between the correlation matrices from the $\mathcal{CP}$-even and $\mathcal{CP}$-odd Asimov fits. The most relevant one is a 0.27 increase in the correlation between the $t\bar{t} + \geq 1b$ ME and flavour scheme and the NLO matching scheme.

The expected impact on the uncertainty in α due to other fit parameters – nuisance parameters or κ_t' – is assessed by performing multiple fits,

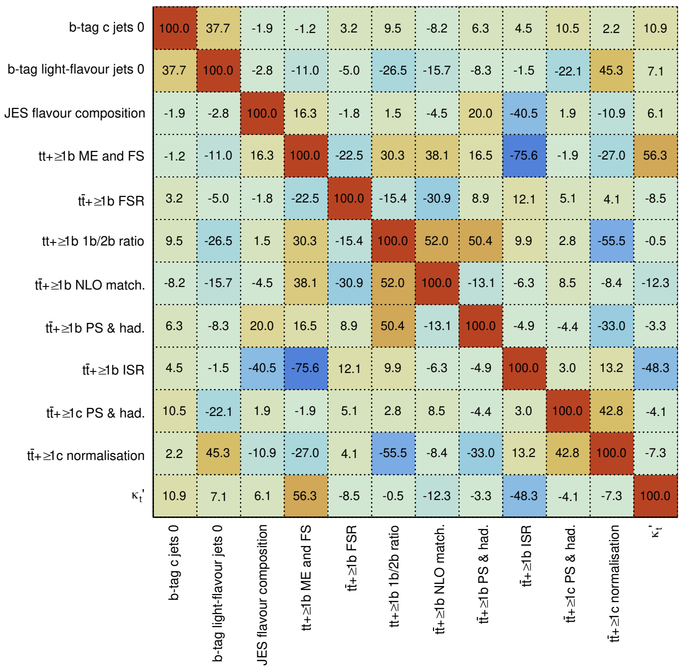

(a)

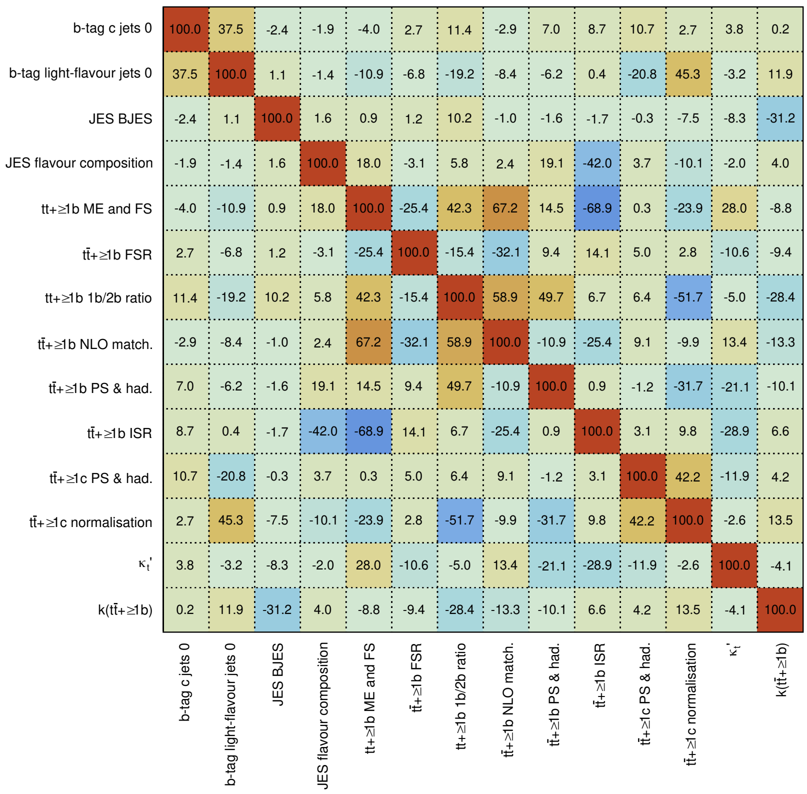

(b)

Figure 9.16: Expected correlation coefficients between the nuisance parameters, in %. (a) $\mathcal{CP}$-even Asimov dataset. (b) $\mathcal{CP}$-odd Asimov dataset.

each with one parameter fixed to its best-fit value. Using the 1σ intervals of α in those fits, the impact of a particular parameter on the uncertainty in α is defined as the subtraction, in quadrature, of the length of the (possibly disjoint) interval in the fit with that parameter fixed from the length of the interval in the normal fit. The expected impact of the most impactful parameters is shown in Figure 9.17 for the $\mathcal{CP}$-even scenario. The values on the horizontal axis give the impact on α/π. As in the cross-section

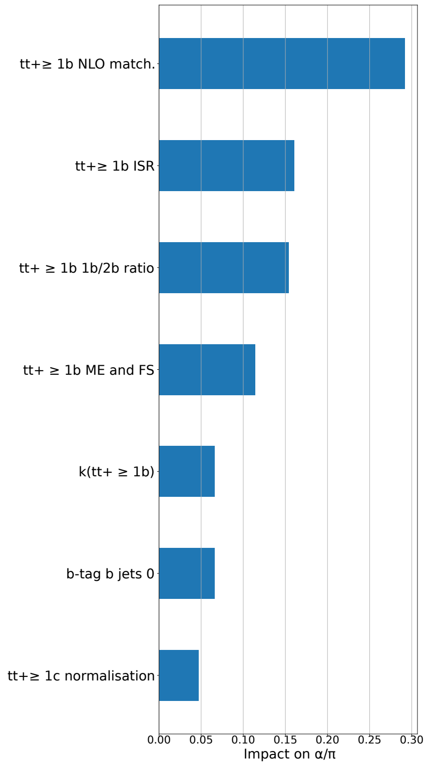

Figure 9.17: Expected impact on α/π of the systematic uncertainties with the largest impact.

measurement, the source of uncertainty with largest impact is the choice of NLO matching scheme for the $t\bar{t}+\geq 1b$ prediction. The measurement of α is not as sensitive to signal uncertainties as the measurement of μ, since the main effect of those is on signal rate. The $t\bar{t}+\geq 1b$ ME and flavour scheme choice uncertainty added for the $\mathcal{CP}$ analysis appears high in the ranking by impact.

9.6 Observed results

Observed results are obtained by fitting data. The observed parameters of interest and the normalisation factor of $t\bar{t} + \geq 1b$ are shown in Figure 9.18, for the combined fit and for fits in the single-lepton and dilepton channels separately. For α, not only the best-fit value and 1σ intervals are given, but also the full NLL scan and the exclusion significance of the $\mathcal{CP}$-odd scenario. The observed best-fit value of α is 0.02π, or $4°$, and the 1σ interval is $[-0.31\pi, 0.31\pi]$, or $[-56°, 56°]$. This result is very compat-

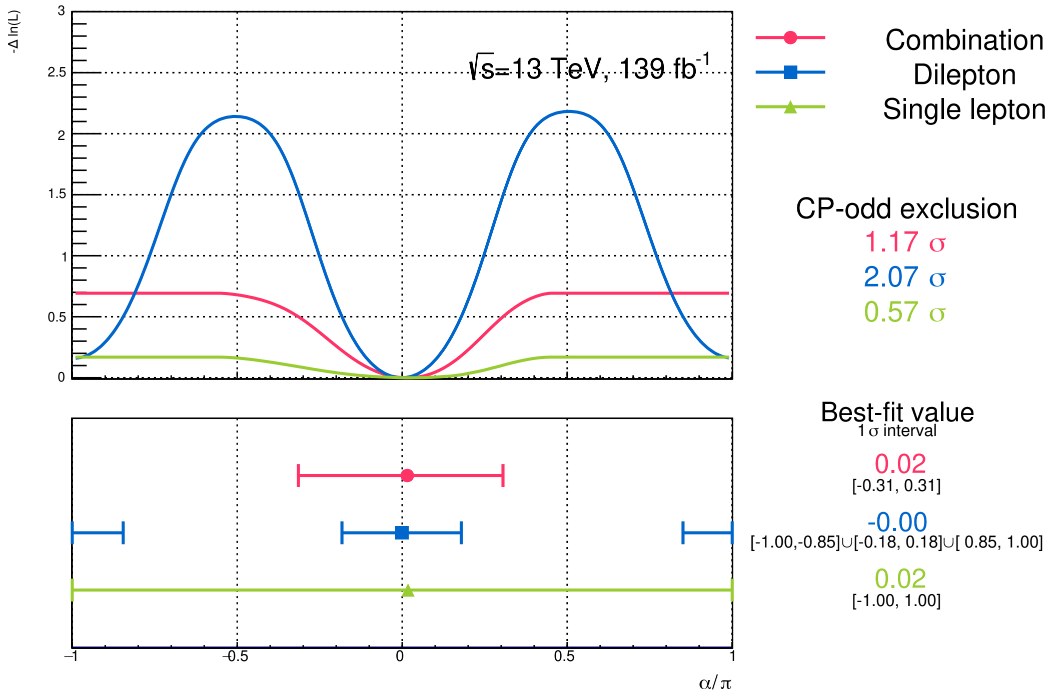

(a)

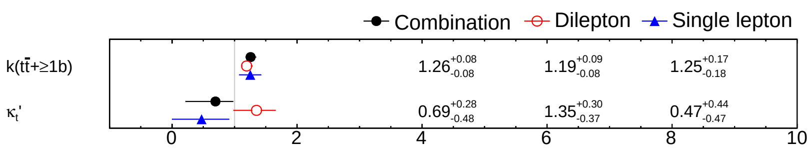

(b)

Figure 9.18: Observed parameters of interest and $t\bar{t} + \geq 1b$ normalisation factor, for the combined fit and for fits in the single-lepton and dilepton channels separately. (a) α: NLL scan, best-fit value, 1σ intervals, exclusion significance of $\mathcal{CP}$-odd scenario. (b) κ_t' and $t\bar{t} + \geq 1b$ normalisation factor.

ible with the $\mathcal{CP}$-even scenario. The pure $\mathcal{CP}$-odd scenario is excluded with a significance of 1.17σ, while the $\mathcal{CP}$-even scenario with negative κ_t is excluded with a significance of 1.18σ. Each channel individually also measures α very close to 0. Unlike what was expected, the single-lepton channel alone is much less sensitive than the dilepton channel alone. This may be explained by the difference in the best-fit values of κ_t' in each of the channels: 1.35 in dilepton and 0.47 in single-lepton. These correspond to signal strengths of 1.82 and 0.22, respectively. The measured κ_t' in the dilepton channel is compatible with the SM value $\kappa_t' = 1$ within one standard deviation, while the one observed in single-lepton is slightly more incompatible. The higher signal rate measured in the dilepton channel alone provides a better constraint on the signal properties: α is more constrained even than in the combination, and the $\mathcal{CP}$-odd scenario is excluded at more than 2σ. The measured coupling modifier κ_t' in the combination is 0.69, with uncertainty $^{+0.28}_{-0.48}$. This corresponds to a signal strength of $0.48^{+0.46}_{-0.43}$, compatible with what is measured in the cross-section analysis, with a larger uncertainty, as expected. Although κ_t' is measured with larger uncertainty in the single-lepton channel fit than in dilepton, the combined result is closer to that of the single-lepton fit. The observed $t\bar{t} + \geq 1b$ normalisation factor is very similar to what is observed in the cross-section measurement.

The observed two-dimensional NLL scan on the $(\kappa_t, \tilde{\kappa}_t)$ plane is shown in Figure 9.19. The same general conclusions may be drawn from this representation. The observed signal rate is smaller than expected, such that the $(0, 0)$ point lies within the 1σ region. That being the case, a strong exclusion of any value of α while profiling κ_t' is not possible, because the region close to the $(0, 0)$ point is available to the fit for any value of α. This also explains why the observed one-dimensional NLL becomes constant for α outside $[-0.5\pi, 0.4\pi]$: there, the fit obtains the model most compatible with data simply by bringing κ_t' to 0. The SM point $(1, 0)$ lies within the 1σ region. The inverted coupling scenario at $(-1, 0)$ is excluded at over 2σ, as is the $\mathcal{CP}$-odd scenario at $(0, 1)$, while the $\mathcal{CP}$-odd scenario in which $t\bar{t}H$ has the same inclusive cross-section as in the $\mathcal{CP}$-

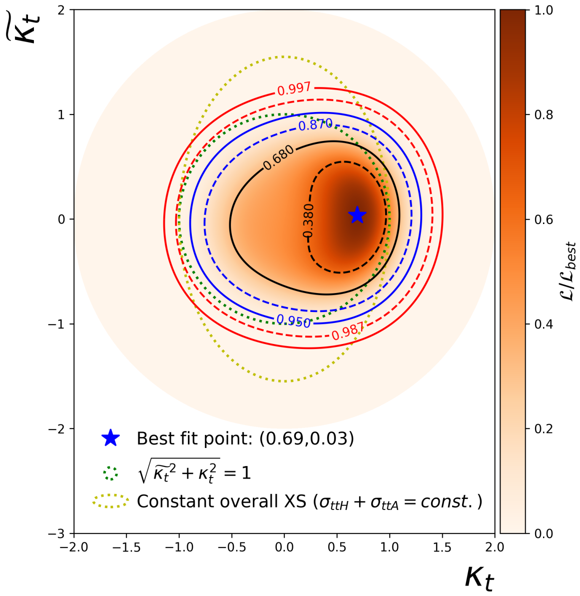

Figure 9.19: Observed two-dimensional NLL scan on the $(\kappa_t, \tilde{\kappa}_t)$ plane. The solid contours are lines of equal exclusion significance: 1σ in black, 2σ in blue, 3σ in red.

even scenario is excluded at over 3σ. These three particular BSM scenarios are excluded more strongly than expected: they are less compatible with a $\mathcal{CP}$-even-like signal with low rate (as observed) than with a signal with the SM-expected rate (as in the $\mathcal{CP}$-even Asimov).

Observed pulls and constraints on the most relevant nuisance parameters are presented in Figure 9.20, for the combined fit as well as for the fits to the individual channels. The results on the full set of nuisance parameters are given in Appendix C. Overall the pulls are small and compatible between the two channels. The largest observed pull is on $t\bar{t} + \geq 1b$ ISR, which is known from the cross-section analysis to correct the modelling of jet multiplicity. The normalisation of $t\bar{t} + \geq 1c$ is pulled up by 42%. The observed constraints are compatible with the expected ones, being slightly stronger on the $t\bar{t} + \geq 1b$ modelling parameters, possibly due to the larger number of $t\bar{t} + \geq 1b$ events in data than in the pre-fit prediction. The observed correlation coefficients (in %) between the nuisance parameters are presented in the matrix of Figure 9.21. In general,

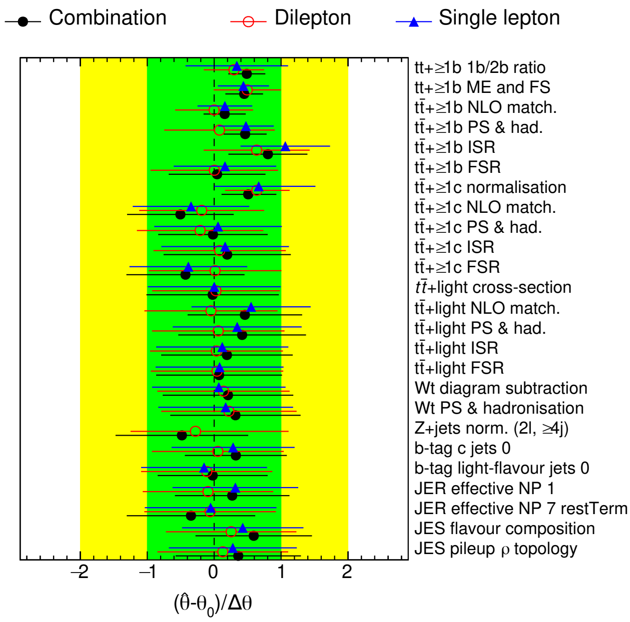

Figure 9.20: Observed pulls and constraints on nuisance parameters in the combined fit and in the fits to single-lepton and dilepton channels separately.

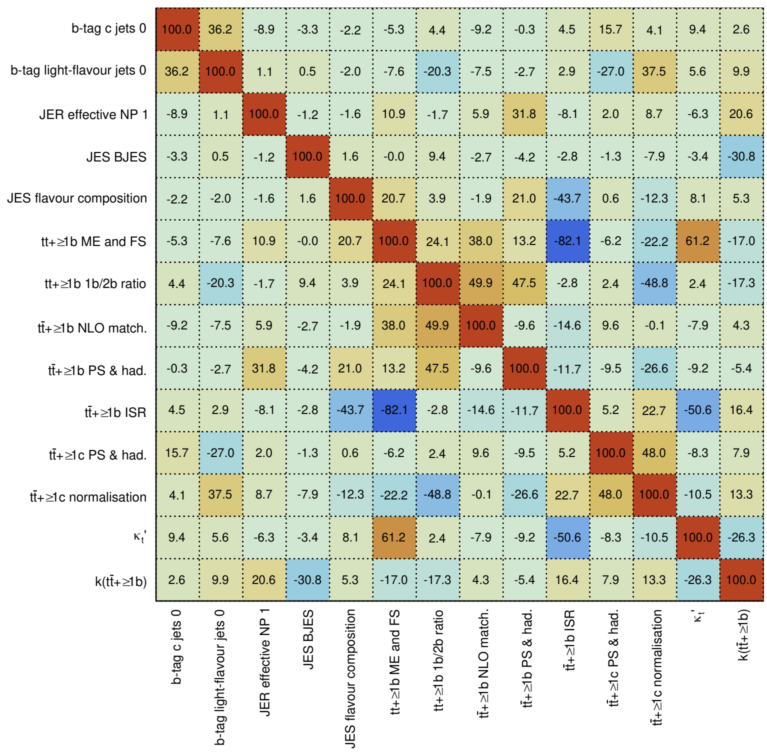

	b-tag c jets 0	b-tag light-flavour jets 0	JER effective NP 1	JES BJES	JES flavour composition	tt+≥1b ME and FS	tt+≥1b 1b/2b ratio	tt̄+≥1b NLO match.	tt̄+≥1b PS & had.	tt̄+≥1b ISR	tt̄+≥1c PS & had.	tt̄+≥1c normalisation	κ_t'	k(tt̄+≥1b)
b-tag c jets 0	100.0	36.2	-8.9	-3.3	-2.2	-5.3	4.4	-9.2	-0.3	4.5	15.7	4.1	9.4	2.6
b-tag light-flavour jets 0	36.2	100.0	1.1	0.5	-2.0	-7.6	-20.3	-7.5	-2.7	2.9	-27.0	37.5	5.6	9.9
JER effective NP 1	-8.9	1.1	100.0	-1.2	-1.6	10.9	-1.7	5.9	31.8	-8.1	2.0	8.7	-6.3	20.6
JES BJES	-3.3	0.5	-1.2	100.0	1.6	-0.0	9.4	-2.7	-4.2	-2.8	-1.3	-7.9	-3.4	-30.8
JES flavour composition	-2.2	-2.0	-1.6	1.6	100.0	20.7	3.9	-1.9	21.0	-43.7	0.6	-12.3	8.1	5.3
tt+≥1b ME and FS	-5.3	-7.6	10.9	-0.0	20.7	100.0	24.1	38.0	13.2	-82.1	-6.2	-22.2	61.2	-17.0
tt+≥1b 1b/2b ratio	4.4	-20.3	-1.7	9.4	3.9	24.1	100.0	49.9	47.5	-2.8	2.4	-48.8	2.4	-17.3
tt̄+≥1b NLO match.	-9.2	-7.5	5.9	-2.7	-1.9	38.0	49.9	100.0	-9.6	-14.6	9.6	-0.1	-7.9	4.3
tt̄+≥1b PS & had.	-0.3	-2.7	31.8	-4.2	21.0	13.2	47.5	-9.6	100.0	-11.7	-9.5	-26.6	-9.2	-5.4
tt̄+≥1b ISR	4.5	2.9	-8.1	-2.8	-43.7	-82.1	-2.8	-14.6	-11.7	100.0	5.2	22.7	-50.6	16.4
tt̄+≥1c PS & had.	15.7	-27.0	2.0	-1.3	0.6	-6.2	2.4	9.6	-9.5	5.2	100.0	48.0	-8.3	7.9
tt̄+≥1c normalisation	4.1	37.5	8.7	-7.9	-12.3	-22.2	-48.8	-0.1	-26.6	22.7	48.0	100.0	-10.5	13.3
κ_t'	9.4	5.6	-6.3	-3.4	8.1	61.2	2.4	-7.9	-9.2	-50.6	-8.3	-10.5	100.0	-26.3
k(tt̄+≥1b)	2.6	9.9	20.6	-30.8	5.3	-17.0	-17.3	4.3	-5.4	16.4	7.9	13.3	-26.3	100.0

Figure 9.21: Observed correlation coefficients between the nuisance parameters, in %.

the observed correlation coefficients are very similar to the expected ones for the $\mathcal{CP}$-even Asimov dataset.

The observed impact on the uncertainty in α due to other fit parameters is assessed, as it was for the expected impact. The observed impact is shown in Figure 9.22 for the parameters with the largest impact. The values on the horizontal axis give the impact on α/π. The highest-ranked

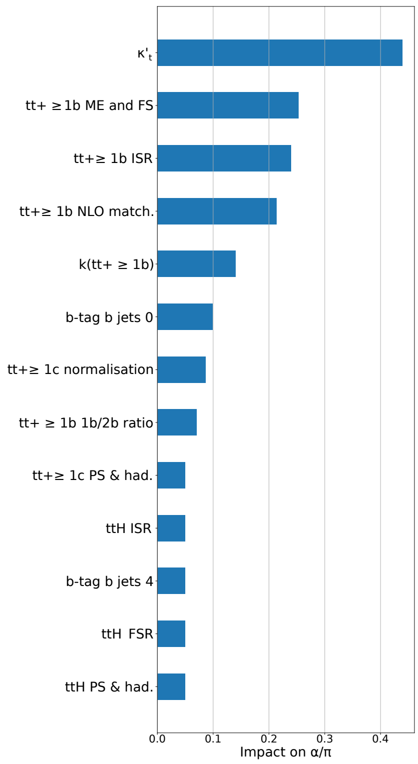

Figure 9.22: Observed impact on α/π of the other fit parameters with the largest impact.

parameter is κ_t', as expected from the discussion above. If the freedom to adjust κ_t' is removed from the fit to data, the range of allowed α values at 1σ is largely reduced. The highest ranked systematic uncertainties are the ones related to $t\bar{t}+\geq 1b$ modelling, as expected, although the NLO matching uncertainty does not stand out with respect to the ISR and the ME and flavour scheme ones. Unlike in the expected results, $t\bar{t}H$ modelling uncertainties have a sizeable impact.

9.7 Post-fit modelling in analysis regions

Figure 9.23 shows data and post-fit prediction comparisons for the event yields in the $\mathcal{CP}$-dedicated regions. Across the 4j4b regions, the data-to-prediction ratio increases as the signal purity increases, indicating that data is more distributed towards signal-like bins of the Classification BDT than the post-fit prediction, consistently with the high signal rate obtained in fit to dilepton regions only. Nevertheless, this is a slight effect, and overall the yields in all regions are well modelled, showing that the fit corrected the shape of the Classification BDT in 6j4b and the ratio between yields in boosted and resolved channels, which showed mismodelling in pre-fit comparisons. The post-fit comparison of event yields in the $\mathcal{CP}$-dedicated regions is given in Tables 9.5 and 9.6, for the dilepton and single-lepton channels, respectively. Tables 9.7 and 9.8 show the same information for the dilepton and single-lepton control regions, respectively.

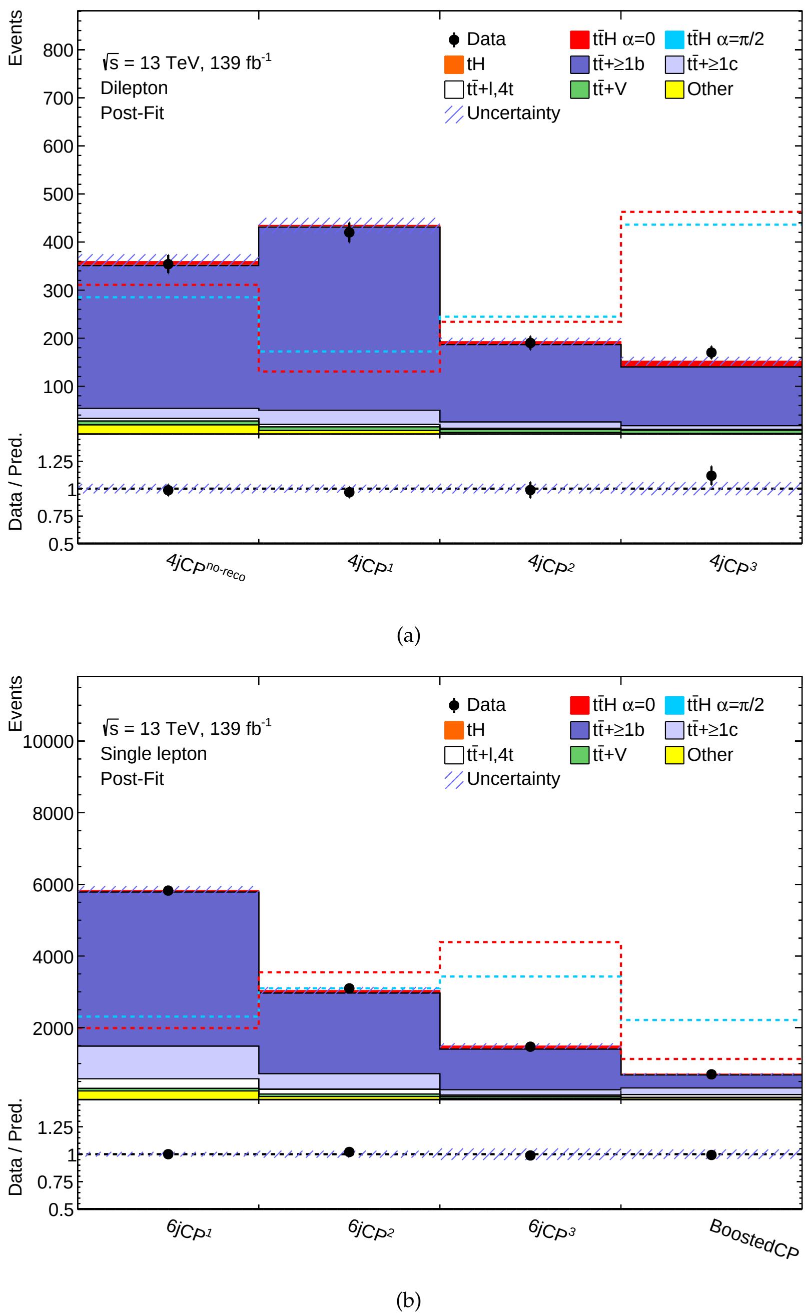

Figure 9.23: Comparison between data and post-fit prediction of event yields in the $\mathcal{CP}$-dedicated regions. (a) Dilepton channel. (b) Single-lepton channel.

Table 9.5: Data and post-fit prediction for the event yields in the $\mathcal{CP}$-dedicated dilepton regions.

	$4\mathrm{jCP}^{no-reco}$	$4\mathrm{jCP}^1$	$4\mathrm{jCP}^2$	$4\mathrm{jCP}^3$
$t\bar{t}H$	8.1 ± 1.0	3.39 ± 0.51	6.08 ± 0.72	12.0 ± 1.4
tWH	0.20 ± 0.12	0.098 ± 0.053	0.087 ± 0.057	0.107 ± 0.091
$t\bar{t} + \geq 1b$	297 ± 16	381 ± 16	160.9 ± 8.5	122.3 ± 8.9
$t\bar{t} + \geq 1c$	20.5 ± 5.6	29.4 ± 5.5	12.8 ± 3.1	7.5 ± 1.9
$t\bar{t} + \text{light}, 4t$	5.7 ± 4.3	5.3 ± 3.8	2.9 ± 2.2	2.0 ± 1.5
$t\bar{t}Z$	7.5 ± 1.5	7.1 ± 1.6	6.0 ± 1.1	6.3 ± 1.2
$t\bar{t}W$	0.64 ± 0.15	0.40 ± 0.14	0.29 ± 0.16	0.28 ± 0.18
Fake leptons	2.34 ± 0.77	2.15 ± 0.75	0.62 ± 0.30	0.85 ± 0.38
Other	17.0 ± 8.1	5.6 ± 3.0	2.8 ± 2.0	0.75 ± 0.88
Total prediction	359 ± 16	434 ± 16	192.5 ± 8.5	152.1 ± 9.1
Data	354	420	190	170

Table 9.6: Data and post-fit prediction for the event yields in the single-lepton $\mathcal{CP}$-dedicated regions.

	$6\mathrm{jCP}^1$	$6\mathrm{jCP}^2$	$6\mathrm{jCP}^3$	BoostedCP
$t\bar{t}H$	38.6 ± 5.2	68.8 ± 8.6	85 ± 13	21.9 ± 2.6
$tHjb$	2.0 ± 1.1	1.02 ± 0.61	0.70 ± 0.44	1.59 ± 0.72
tWH	1.09 ± 0.60	0.88 ± 0.57	0.60 ± 0.50	1.06 ± 0.52
$t\bar{t}+ \geq 1b$	4300 ± 160	2250 ± 110	1135 ± 80	362 ± 30
$t\bar{t}+ \geq 1c$	910 ± 190	429 ± 90	146 ± 31	181 ± 41
$t\bar{t} + \text{light}, 4t$	270 ± 130	137 ± 67	44 ± 25	80 ± 28
$t\bar{t}Z$	65.2 ± 9.1	62.1 ± 8.3	45.8 ± 6.8	13.8 ± 2.6
$t\bar{t}W$	8.1 ± 1.4	5.41 ± 0.88	2.52 ± 0.45	2.51 ± 0.49
Single top Wt	84 ± 46	29 ± 20	9.9 ± 7.6	16.1 ± 9.0
Other single top	62 ± 32	21 ± 18	6.4 ± 3.3	5.5 ± 3.9
V+jets, VV+jets	88 ± 36	29 ± 13	10.9 ± 5.0	18.1 ± 8.1
Total prediction	5830 ± 130	3036 ± 98	1487 ± 78	704 ± 31
Data	5826	3098	1470	699

Table 9.7: Data and post-fit prediction for the event yields in the dilepton control regions.

	3j	4jlo	4jhi
$t\bar{t}H$	12.0 ± 1.7	38.5 ± 3.8	58.3 ± 5.7
tWH	0.92 ± 0.93	0.95 ± 0.98	1.7 ± 1.7
$t\bar{t} + \geq 1b$	2030 ± 130	2630 ± 160	4180 ± 210
$t\bar{t} + \geq 1c$	490 ± 130	2400 ± 480	1090 ± 240
$t\bar{t}$ + light, $4t$	132 ± 66	1010 ± 350	240 ± 120
$t\bar{t}Z$	10.6 ± 1.7	53.6 ± 7.0	58.3 ± 7.4
$t\bar{t}W$	1.78 ± 0.53	22.4 ± 3.5	11.0 ± 1.6
Fake leptons	6.3 ± 1.8	56 ± 14	47 ± 12
Other	119 ± 34	227 ± 60	188 ± 53
Total prediction	2803 ± 66	6430 ± 140	5880 ± 130
Data	2827	6429	5865

Table 9.8: Data and post-fit prediction for the event yields in the single-lepton control regions.

	5jlo	5jhi
$t\bar{t}H$	28.0 ± 4.0	28.8 ± 4.8
$tHjb$	2.4 ± 1.2	3.1 ± 1.6
tWH	0.69 ± 0.30	0.59 ± 0.26
$t\bar{t}+ \geq 1b$	1641 ± 86	1133 ± 53
$t\bar{t}+ \geq 1c$	590 ± 130	83 ± 21
$t\bar{t}$ + light, $4t$	284 ± 94	26 ± 17
$t\bar{t}Z$	25.7 ± 3.5	22.4 ± 3.1
$t\bar{t}W$	2.58 ± 0.45	0.53 ± 0.12
Single top Wt	49 ± 27	20 ± 17
Other single top	42 ± 17	27 ± 10
V+jets, VV+jets	43 ± 17	25.4 ± 9.8
Total prediction	2712 ± 68	1370 ± 47
Data	2696	1362

9.7.1 Observable distributions

Data and post-fit predictions for the observables used in the fit are shown in Figures 9.24, 9.25 and 9.26, respectively for the control regions, the dilepton $\mathcal{CP}$-dedicated regions and the single-lepton $\mathcal{CP}$-dedicated regions. Overall, the post-fit prediction provides good modelling of all the distributions. The shape mismodelling in the $\mathcal{CP}$ BDT that was visible pre-fit, with the first bin having a higher fraction of data than predicted, is not corrected by the fit, although the tension from this disagreement is small, due to considerable statistical uncertainty.

9.7.2 $\mathcal{CP}$ BDT input variables

Figure 9.27 shows data and post-fit predictions for distributions of the three most important variables used as inputs to the $\mathcal{CP}$ BDT, in the dilepton regions where the $\mathcal{CP}$ BDT is used. They show significantly improved modelling with respect to pre-fit, not only of the normalisation component, but also of the distribution shapes. The uncertainty bands are constrained with respect to the pre-fit comparison, but still the χ^2 values obtained are compatible with a good model of data.

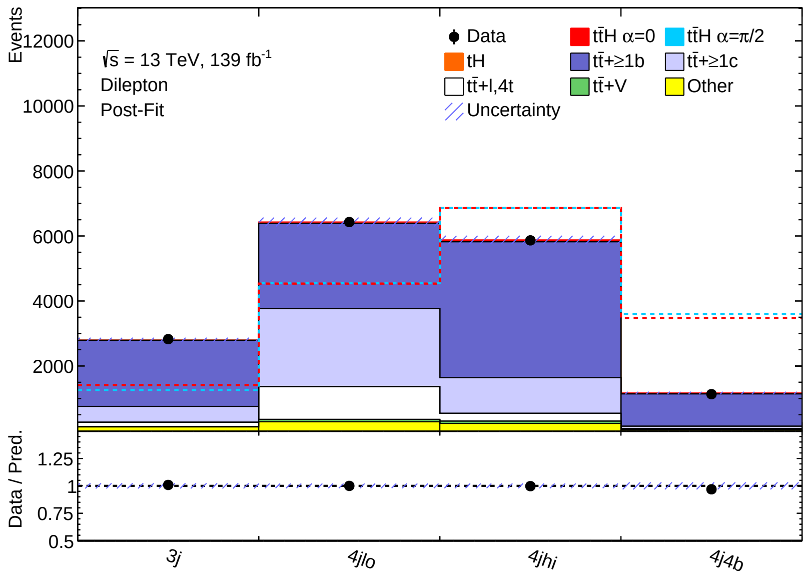

(a)

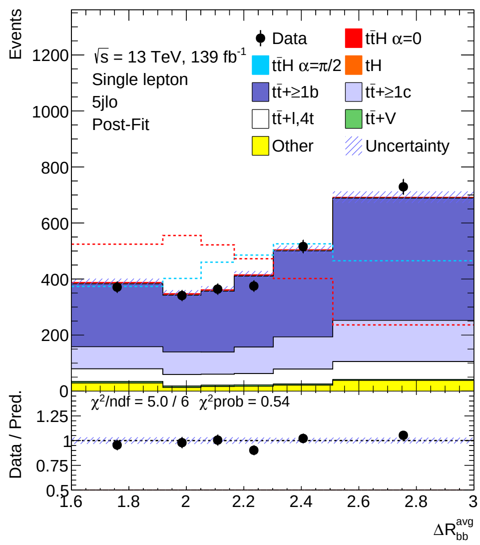

(b)

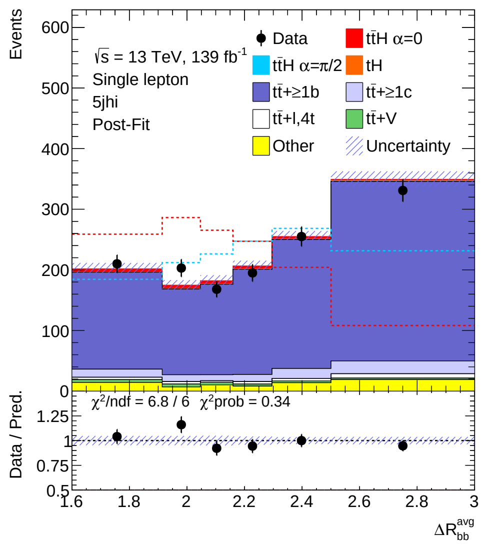

(c)

Figure 9.24: Comparison between data and post-fit prediction of the observables used in the fit in each of the control regions. (a) Dilepton channel (4j4b also shown). (b) 5jlo. (c) 5jhi.

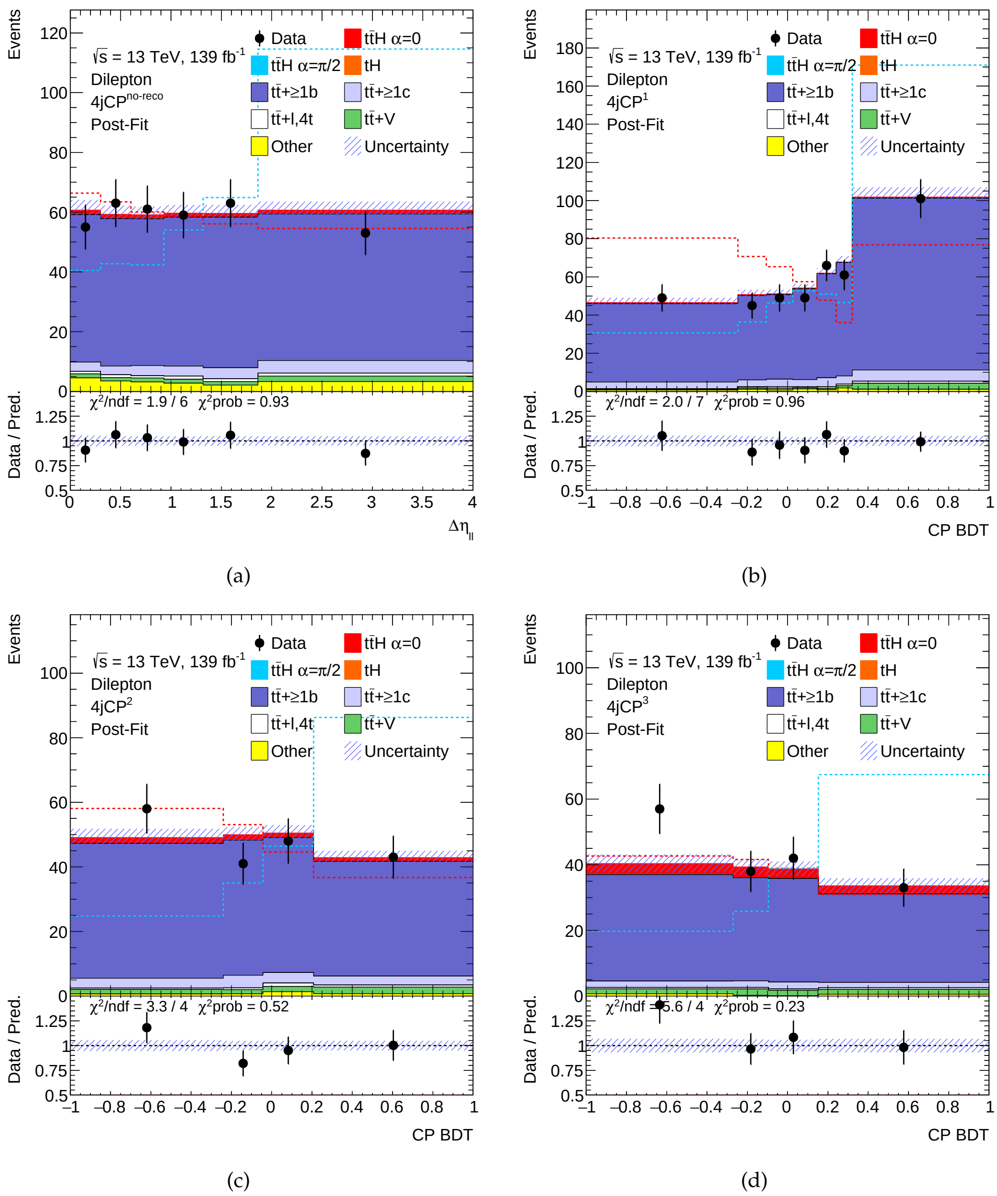

Figure 9.25: Comparison between data and post-fit prediction of the distributions used in the fit in each of the dilepton $\mathcal{CP}$-dedicated regions. (a) 4jCP$^{\text{no-reco}}$. (b) 4jCP^1. (c) 4jCP^2. (d) 4jCP^3.

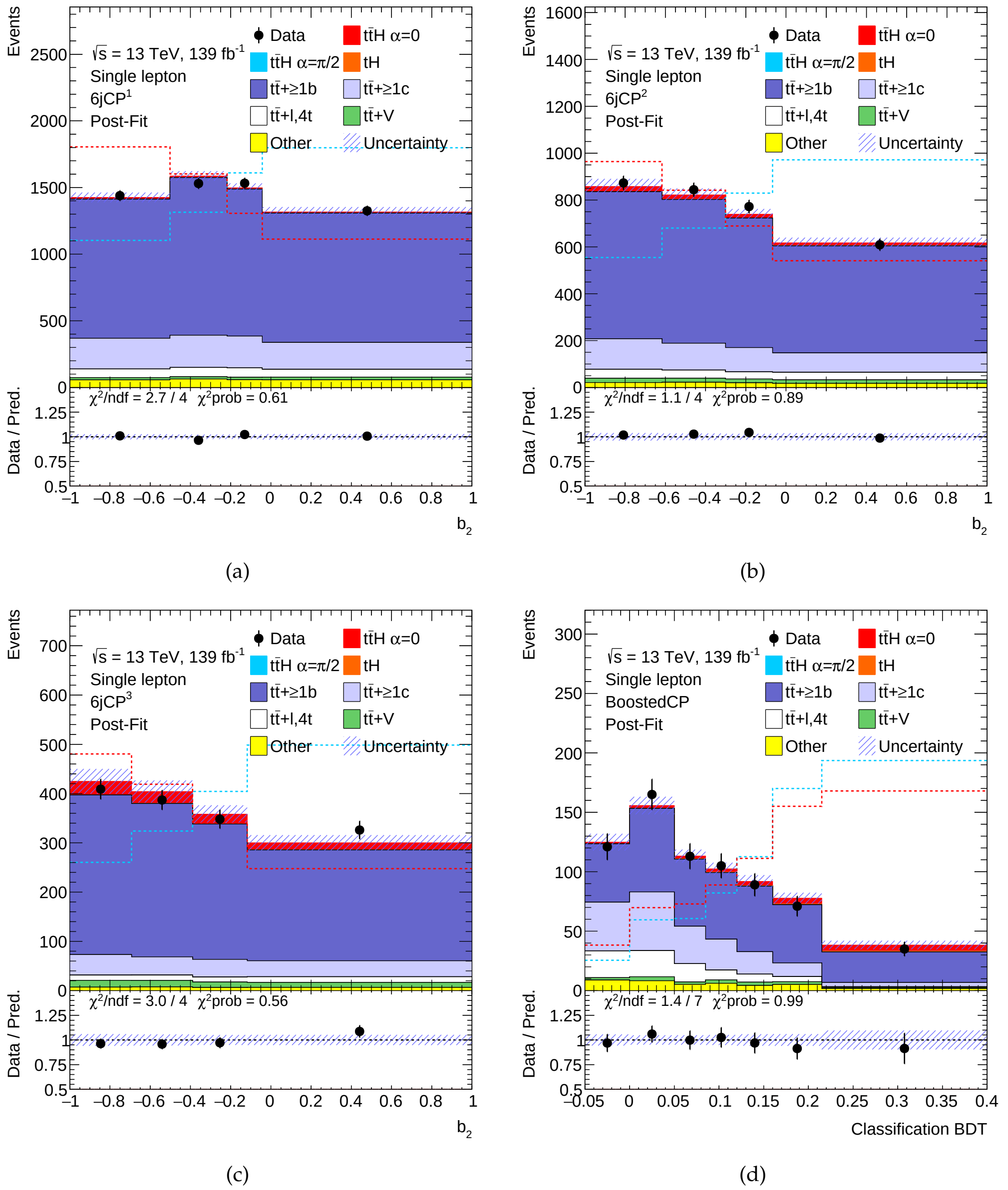

Figure 9.26: Comparison between data and post-fit prediction of the distributions used in the fit in each of the single-lepton $\mathcal{CP}$-dedicated regions. (a) 6jCP^1. (b) 6jCP^2. (c) 6jCP^3. (d) BoostedCP.

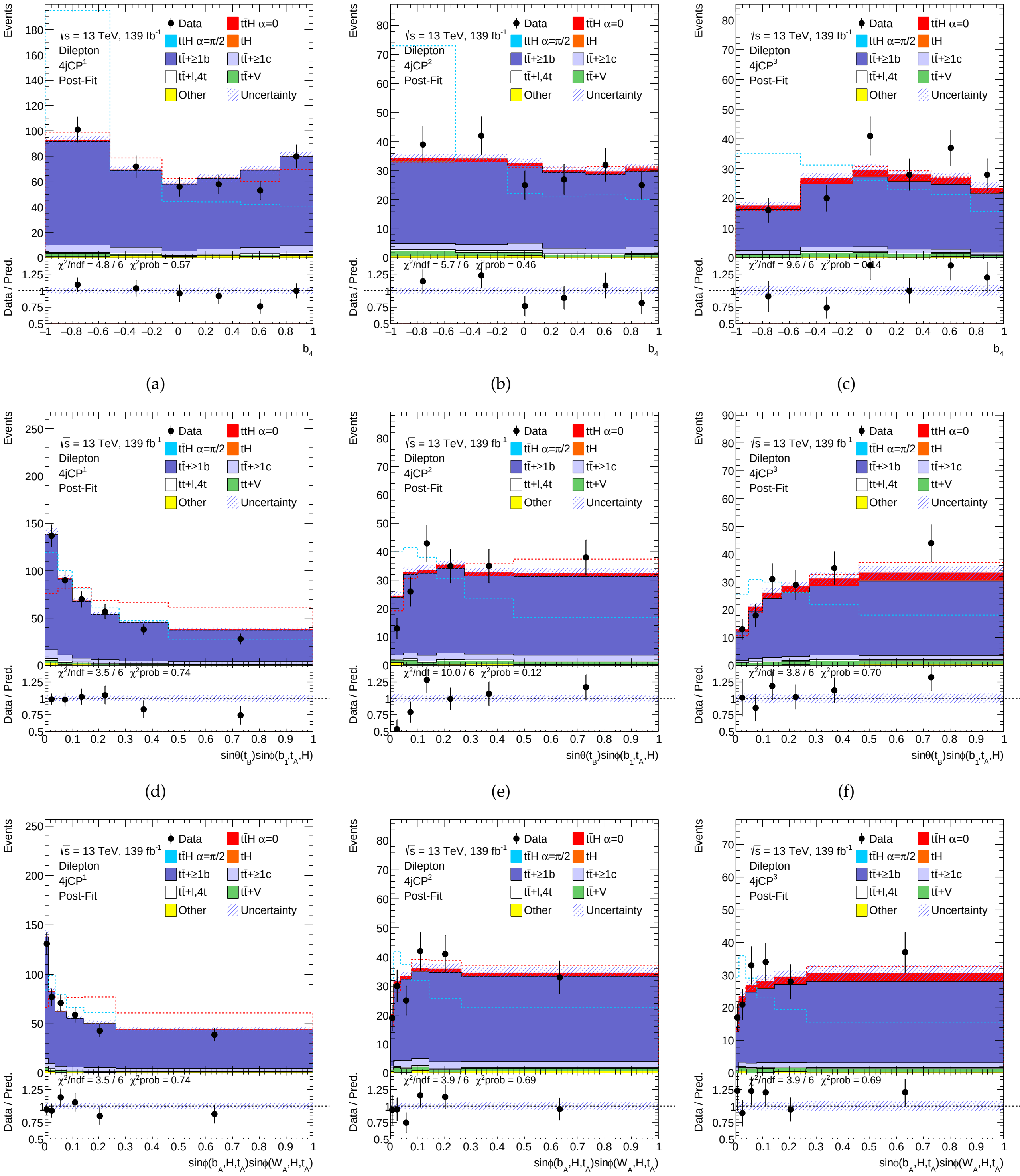

(a) (b) (c)

(d) (e) (f)

(g) (h) (i)

Figure 9.27: Comparison between data and post-fit prediction for the distributions of the most important input variables to the $\mathcal{CP}$ BDT, in 4jCP^1 (left), 4jCP^2 (middle), and 4jCP^3 (right). (a,b,c) b_4. (d,e,f) $\sin\theta(t_B)\sin\phi(b_1,t_A,H)$. (g,h,i) $\sin\phi(b_A,H,t_A)\sin\phi(W_A,H,t_A)$.

Chapter 10

Conclusions

The properties of the 125 GeV Higgs boson are currently a subject under intense investigation at the LHC, using the Run 2 dataset. At any moment, these measurements of unprecedented precision could reveal effects of new physics. The theoretical puzzles posed by the SM seem to require a more fundamental underlying theory, a need further motivated by observational facts that clash with the SM predictions, such as the baryon asymmetry in the Universe. Necessary to the emergence of this asymmetry is the occurrence of $\mathcal{CP}$ violation at a rate higher than that predicted by the SM. Soon after the Higgs boson discovery, its $\mathcal{CP}$ properties were investigated, by excluding the negative parity hypothesis, as well as constraining anomalous $\mathcal{CP}$-odd couplings to vector bosons. However, measurements of $\mathcal{CP}$ properties of Yukawa couplings had to wait for the full Run 2 dataset, and only recently started being carried out. These are essentially different from the couplings to vector bosons, because a $\mathcal{CP}$-odd state does not couple at tree level to vector bosons, while it does couple at tree level to fermions. Among all fermions, the top quark stands as the most accessible candidate for such studies, due to its large mass. In addition to that, the top quark Yukawa coupling plays a central role in open questions of particle physics, as it governs the leading radiative corrections to the Higgs boson mass and to the Higgs quartic coupling.

There are several measurements sensitive to the top quark Yukawa coupling, even at low energy scales, such as the EDM of the electron. Indirect measurements often provide much stronger constraints than direct measurements, given some set of assumptions. This is of invaluable importance for model builders, since they may learn that reasonable assumptions in their favourite models greatly shrink the available parameter space. However, an indirect measurement cannot replace a direct one, and the two approaches should be seen as complementary efforts, rather than competitive. An example of perfect complementarity would be for a direct measurement to observe a scenario previously excluded by an indirect measurement. Necessarily, some of the assumptions made in the indirect measurement would be wrong. Only from the confrontation of both measurements would this be possible to conclude, not from either one separately. In this sense, it is not wise for experiments to abandon the pursuit of direct probes to scenarios that are indirectly excluded. By construction, that would leave the underlying assumptions untested.

Production of $t\bar{t}H$ at the LHC is the best direct probe currently available of the top quark Yukawa coupling. Using the full Run 2 dataset collected by ATLAS, two measurements of this process were performed, by analysing events in final states with leptons and with the Higgs boson decaying to $b\bar{b}$. In the measurement of the inclusive cross-section, a signal strength of $0.43^{+0.36}_{-0.33}$ was observed, corresponding to a cross-section of 220^{+180}_{-170} fb. The background-only hypothesis was excluded with a significance of 1.3σ (3.4σ expected). The uncertainty is dominated by the $t\bar{t} + \geq 1b$ modelling uncertainties, in particular those due to the choice of NLO matching scheme. Analysis regions were defined in bins of $p_T^{b\bar{b}}$ to enable the STXS measurement. However, this forced the decorrelation of the $t\bar{t} + \geq 1b$ NLO matching uncertainty across regions, which is necessarily detrimental to the sensitivity of the inclusive measurement. A possible improvement in this respect would be to revert the split in $p_T^{b\bar{b}}$ bins, performing the fit to the Classification BDT distribution in each of the inclusive signal regions. The impact of the mismodelling of the $p_T^{b\bar{b}}$ distribution on this fit would be smaller, but should be accounted for by an uncertainty if necessary.

In the measurement of the $\mathcal{CP}$ structure of the top quark Yukawa coupling, the coupling modifier κ_t' and the $\mathcal{CP}$-mixing angle α were simultaneously probed. This means that the determination of α relied on signal shape information only, since the signal rate was adjusted by profiling κ_t'. The angle α was measured to be 0.02π, or 4°, and the observed 1σ interval was $[-0.31\pi, 0.31\pi]$, or $[-56^\circ, 56^\circ]$, in agreement with the $\mathcal{CP}$-even SM prediction. A pure $\mathcal{CP}$-odd scenario was excluded with a significance of 1.17σ. The measured κ_t' was $0.69^{+0.28}_{-0.48}$, corresponding to a signal strength of $0.48^{+0.46}_{-0.43}$, compatible with the one measured in the cross-section analysis. Due to the observed low signal rate, driven by the single-lepton channel, a strong exclusion of any value of α was not possible. In the (κ_t,$\tilde{\kappa}_t$) plane, the SM point $(1,0)$ lies within the 1σ region, while there are other scenarios with $\kappa_t' = 1$ excluded with significances above 2σ, such as the inverted coupling scenario at $(-1,0)$ and the $\mathcal{CP}$-odd scenario at $(0,1)$. The $\mathcal{CP}$-odd scenario in which $t\bar{t}H$ has the same inclusive cross-section as in the SM is excluded with significance above 3σ.

The choice of observables used in the $\mathcal{CP}$ analysis was largely influenced by the phenomenological studies carried out in Refs. [3, 9]. The conclusion that the observable b_2 saw significantly enhanced discrimination power when evaluated in the $t\bar{t}H$ rest frame was particularly important, as this observable became the best $\mathcal{CP}$ discriminant in the single-lepton resolved channel. Variables used in the $\mathcal{CP}$ BDT of the dilepton channel included b_4 and products of sines and co-sines of angles measured in different rest frames. In the analysis, the labelling of top quarks in the calculation of the angles was changed with respect to the initial proposal, drawing motivation from the difference in diagram contributions to the different signal scenarios, which resulted in enhanced separation power. The Higgs boson candidate p_T was also used in the analysis as a discriminant, through the separation into boosted and resolved regions, and showed significant pre-fit mismodelling. However, all the other discriminants are reasonably modelled before the fit. Generically, the latter can be expressed as ratios of components of momenta, where systematic shifts in energy cancel out. This feature and the use of boosted reference frames make these observables particularly robust with respect to the modelling of additional radiation by the MC generators, which is not the case for the Higgs boson p_T.

In future installments of the $\mathcal{CP}$ analysis, one possible improvement would be to replace the two sequential binary classifications – signal against backgrounds and $\mathcal{CP}$-even against $\mathcal{CP}$-odd – by a multi-class discriminator. The output scores of such a discriminator could be used to more efficiently define bins enriched in each of the processes, exploiting correlations better than the currently used rectangular edges (see Figures 9.7 and 9.8). No $\mathcal{CP}$-odd observables were explored in this analysis.

That would be an interesting addition in the future, since it could probe $\mathcal{CP}$ violation in $t\bar{t}H$ production, resolve the degeneracy in the sign of α and enhance sensitivity to small values of $\tilde{\kappa}_t$.

From both analyses, it became evident that it is worth reconstructing the top quarks and the Higgs boson in $t\bar{t}H$ events, even if there is some reconstruction inefficiency and a high rate of combinatorial mistakes. For discrimination of signal against backgrounds, as well as for discrimination between the $\mathcal{CP}$ scenarios, observables built from reconstructed particles provide information otherwise inaccessible.

The reach of both analyses is limited by the current ability to model $t\bar{t} + \geq 1b$ production. At the pre-fit level, the disagreement is large in the normalisation, in the shape of the $p_T^{b\bar{b}}$ distribution and in the jet multiplicity. The observed $t\bar{t} + \geq 1b$ normalisation factor of 1.26, as well as the pull in $t\bar{t} + \geq 1b$ ISR support the use of a lower renormalisation scale in future event generations of this process. The uncertainties used to account for choices of NLO matching and PS and hadronisation model are expected to be conservative, but are not satisfactory, as they relied on samples where the ME and flavour scheme were different from the nominal ones.

When systematic uncertainties dominate, there is limited room for improvement from just repeating analyses with a larger dataset. For that reason, important gains in future versions of the discussed analyses depend on qualitative improvements to the analysis strategies. Boosted regions are a corner of phase-space not yet so dominated by systematic uncertainties and have high signal purity. The inclusion of a boosted dilepton selection would be beneficial for these analyses, with the added benefit of enhanced spin correlations that could contribute to the sensitivity of the $\mathcal{CP}$ analysis.

The use of alternative samples of $t\bar{t} + b\bar{b}$ generated in the 4FS to estimate uncertainties on the $t\bar{t} + \geq 1b$ background is another expected improvement. On first principles only, $t\bar{t} + b\bar{b}$ 4FS samples should give a more accurate description of data. However, this is not necessarily the case in the full $t\bar{t} + \geq 1b$ phase-space, as the tuning of PDFs and PS in the $t\bar{t}$ 5FS provide enough flexibility to match that sample to data. The use of

$t\bar{t}$ samples where $t\bar{t}$ 5FS and $t\bar{t}+b\bar{b}$ 4FS predictions are merged according to the regions of phase-space where each of them gives a more accurate prediction would make it unnecessary to keep the comparison between the two as a systematic uncertainty. Although these changes would result in smaller modelling uncertainties, a more precise prediction is not necessarily a more accurate one. For example, the mismodelling of the $p_T^{b\bar{b}}$ distribution was not initially covered by any of the modelling uncertainties, including the conservative ones, and it had to be accounted for by an additional, purely empirical, uncertainty. If the accuracy of $t\bar{t}+b\bar{b}$ MC generators does not improve substantially, there are two possible approaches to improve the nominal $t\bar{t}+\geq 1b$ prediction. One would be to use reweighting, for example of the truth-level $p_T^{b\bar{b}}$ distribution, to match the highest-order theoretical prediction available. The other would be to rely on data-driven methods, in which the MC distributions would be corrected to match the data in a control region, and the corrections would be extrapolated to the signal regions. In this approach, only the ratio from control regions to signal regions is taken from the MC, in principle resulting in reduced impact of modelling uncertainties. On the other hand, the validity of extrapolating from one region to the other should be ensured by a low correlation between the variables used to define regions and those used for the distributions.

In both analyses, machine learning methods (in particular BDTs) are employed for classification tasks. In the training of these classifiers, optimisation is only made for the separation between nominal hypotheses, with no regard to whether the alternative background predictions used for estimating uncertainties are classified in a similar way as the nominal. In a measurement limited by statistics this may be good enough, but in measurements limited by systematic uncertainties, it could be more advantageous to ensure that the classifiers have similar responses for all the alternative background predictions, even at the cost of some separation power. This could be achieved during the training by penalising the classifier for its ability to discriminate among the background models used.

For the profile-likelihood fit, binned likelihoods were used in both analyses, which in principle are always surpassed by unbinned ones in terms of sensitivity. Binned likelihoods may be regarded as unbinned likelihoods in which the most basic probability density estimators – histograms – are used. The use of histograms and the associated choice of binning may be motivated by the low statistics of MC samples. However, binning truncates the separation provided by the highly optimised methods for classifying events. Exploring continuous probability density estimators, with a degree of sophistication matching that of the classifiers would be an interesting route for any analysis currently depending on histograms.

The best direct measurement of the $\mathcal{CP}$ properties of the top-Higgs coupling would come from the combination of dedicated analyses in as many $t\bar{t}H$ and tH final states as possible. Currently, only the $t\bar{t}H$ final states where the Higgs decays to $b\bar{b}$, $\gamma\gamma$ and 4ℓ have been explored for this effect. Among the multilepton final states, the next best candidate would be the category with two hadronic τ leptons. This is purely populated with $H \to \tau\tau$ events, making it compatible with reconstruction of the Higgs boson and possibly of the top quarks. Other multilepton final states would be much more challenging, since each final state gets large contributions from different Higgs and top quark decays, with up to four W bosons decaying leptonically in the event, making neutrino reconstruction unfeasible. The $\mathcal{CP}$ structure of Yukawa couplings other than that of the top quark should be investigated. In particular, results for all fermions of the third generation would constrain multi-Higgs models where the various scalar fields couple differently to up-type quarks, down-type quarks, and leptons.

In the medium-term future, data collected during the whole HL-LHC programme will allow the Yukawa couplings of fermions of the third generation and of muons to be measured at the 2%-4% level [160]. Even then, coupling properties will not necessarily be available for all of them: in the Higgs boson decays to b quarks or muons, used as precise probes of the magnitude of the respective couplings, the spin information of the final state is not available, and an approach similar to that used with τ leptons is not possible. In the long-term future, the top quark Yukawa coupling will be measured with nearly 1% precision at the Future Circular Collider (FCC), which is the preferred option put forward in the latest Update of the European Strategy for Particle Physics [161] for the next large collider at CERN. This represents an improvement of one order of magnitude with respect to the current measurements, which is the most modest among all Yukawa couplings. Such an improvement in precision, although remarkable and desirable, is not certainly one of the strongest motivations for the FCC programme. This is evident in face of a naive comparison to the LHC programme, which during its first decade of operation accomplished the discovery of the Higgs boson, the direct observation of Yukawa couplings and the measurement of those couplings with 10% precision. As a consequence of this expected slow rate of improvement in the top-Higgs coupling precision, $t\bar{t}H$ production measurements from the Run 2 of the LHC will remain relevant for several years.

Bibliography

[1] ATLAS Collaboration. Observation of a new particle in the search for the Standard Model Higgs boson with the ATLAS detector at the LHC. *Phys. Lett. B*, (716):1, 2012. URL `http://dx.doi.org/10.1016/j.physletb.2012.08.020`.

[2] CMS Collaboration. Observation of a new boson at a mass of 125 GeV with the CMS experiment at the LHC. *Phys. Lett. B*, (716):30, 2012. URL `http://dx.doi.org/10.1016/j.physletb.2012.08.021`.

[3] A Ferroglia, M. C. N. Fiolhais, E. Gouveia, and A. Onofre. Role of the $t\bar{t}h$ rest frame in direct top-quark Yukawa coupling measurements. *Phys. Rev. D*, 100(7):075034, Oct 2019. URL `https://link.aps.org/doi/10.1103/PhysRevD.100.075034`.

[4] E. Gouveia, R. Gonçalo, A. Onofre, and D. Azevedo. Measuring the CP structure of the top Yukawa coupling in $t\bar{t}H$ events at the LHC. In *11th International Workshop on Top Quark Physics*, Feb 2019. URL `https://arxiv.org/abs/1902.00298`.

[5] M. Cepeda et al. *Report from Working Group 2: Higgs Physics at the HL-LHC and HE-LHC*, volume 7, pages 221–584. 12 2019. URL `https://e-publishing.cern.ch/index.php/CYRM/article/view/952`.

[6] ATLAS Collaboration. Measurement of the Higgs boson decaying to b-quarks produced in association with a top-quark pair in pp collisions at $\sqrt{s} = 13$ TeV with the ATLAS detector. Technical Report ATLAS-CONF-2020-058, CERN, Geneva, Nov 2020. URL `https://cds.cern.ch/record/2743685`.

[7] ATLAS Collaboration. Search for the standard model Higgs boson produced in association with top quarks and decaying into a $b\bar{b}$ pair in pp collisions at $\sqrt{s}$ = 13 TeV with the ATLAS detector. *Phys. Rev. D*, 97(7):072016, 2018. doi: 10.1103/PhysRevD.97.072016.

[8] J. de Favereau et al. DELPHES 3, A modular framework for fast simulation of a generic collider experiment. *JHEP*, 02:057, 2014. doi: 10.1007/JHEP02(2014)057.

[9] S. P. Amor dos Santos et al. Probing the CP nature of the Higgs coupling in $t\bar{t}h$ events at the LHC. *Phys. Rev. D*, 96:013004, Jul 2017. URL `https://link.aps.org/doi/10.1103/PhysRevD.96.013004`.

[10] F. Halzen and Alan D. Martin. *QUARKS AND LEPTONS: AN INTRODUCTORY COURSE IN MODERN PARTICLE PHYSICS*. 1984. New York, USA: Wiley (1984) 396p.

[11] M. Tanabashi et al. Review of Particle Physics. *Phys. Rev. D*, 98(3):030001, 2018. doi: 10.1103/PhysRevD.98.030001.

[12] Andrej Arbuzov. Quantum Field Theory and the Electroweak Standard Model. *CERN Yellow Rep. School Proc.*, 3:1–35, 2018. doi: 10.23730/CYRSP-2018-003.1.

[13] User:MissMJ. Standard Model of Elementary Particles. *Wikimedia Commons, Creative Commons license CC-BY-3.0*. URL `https://upload.wikimedia.org/wikipedia/commons/0/00/Standard_Model_of_Elementary_Particles.svg`.

[14] Carl D. Anderson. The positive electron. *Phys. Rev.*, 43:491–494, Mar 1933. URL `https://link.aps.org/doi/10.1103/PhysRev.43.491`.

[15] Y. Nambu and G. Jona-Lasinio. Dynamical Model of Elementary Particles Based on an Analogy with Superconductivity. I. *Phys. Rev.*, (122):345, 1967. URL `http://dx.doi.org/10.1103/PhysRev.122.345`.

[16] Jeffrey Goldstone. Field theories with "Superconductor" solutions. *Nuovo cimento*, (19):154, 1961. URL `http://dx.doi.org/10.1007/BF02812722`.

[17] Jeffrey Goldstone, Abdus Salam, and Steven Weinberg. Broken symmetries. *Phys. Rev.*, (127):965, 1962. URL `http://dx.doi.org/10.1103/PhysRev.127.965`.

[18] P.W. Higgs. Broken symmetries, massless particles and gauge fields. *Phys. Lett.*, (12):132, 1964. URL `http://dx.doi.org/10.1016/0031-9163(64)91136-9`.

[19] P.W. Higgs. Broken symmetries and the masses of gauge bosons. *Phys. Rev. Lett.*, (13):508, 1964. URL `http://dx.doi.org/10.1103/PhysRevLett.13.508`.

[20] P.W. Higgs. Spontaneous symmetry breakdown without massless bosons. *Phys. Rev.*, (145):1156, 1966. URL `http://dx.doi.org/10.1103/PhysRev.145.1156`.

[21] F. Englert and R. Brout. Broken symmetry and the mass of gauge vector mesons. *Phys. Rev. Lett.*, (13):321, 1964. URL `http://dx.doi.org/10.1103/PhysRevLett.13.321`.

[22] G. S. Guralnik, C. R. Hagen, and T. W. B. Kibble. Global conservation laws and massless particles. *Phys. Rev. Lett.*, (13):585, 1964. URL `http://dx.doi.org/10.1103/PhysRevLett.13.585`.

[23] T. W. B. Kibble. Symmetry breaking in non-Abelian gauge theories. *Phys. Rev.*, (155):1554, 1967. URL `http://dx.doi.org/10.1103/PhysRev.155.1554`.

[24] Abdus Salam. Weak and Electromagnetic Interactions. *Conf. Proc.*, C680519:367–377, 1968.

[25] Steven Weinberg. A model of leptons. *Phys. Rev. Lett.*, (19):1264, 1967. URL `http://dx.doi.org/10.1103/PhysRevLett.19.1264`.

[26] Sheldon L. Glashow. Partial-symmetries of weak interaction. *Nucl. Phys.*, (22):579, 1961. URL `http://dx.doi.org/10.1016/0029-5582(61)90469-2`.

[27] G. 't Hooft and M. Veltman. Regularization and renormalization of gauge fields. *Nuclear Physics B*, 44(1):189 – 213, 1972. URL `http://www.sciencedirect.com/science/article/pii/0550321372902799`.

[28] The Nobel Foudation. The Nobel Prize in Physics 2015. *Nobelprize.org. Nobel Media*, 2020. URL `https://www.nobelprize.org/prizes/physics/2015/press-release/`.

[29] Alessandro Strumia and Francesco Vissani. Neutrino masses and mixings and... (hep-ph/0606054), Jun 2006.

[30] Peter Minkowski. $\mu \to e\gamma$ at a rate of one out of 109 muon decays? *Physics Letters B*, 67(4):421 – 428, 1977. URL `http://www.sciencedirect.com/science/article/pii/037026937790435X`.

[31] Tatsumi Aoyama, Toichiro Kinoshita, and Makiko Nio. Revised and Improved Value of the QED Tenth-Order Electron Anomalous Magnetic Moment. *Phys. Rev. D*, 97(3):036001, 2018. doi: 10.1103/PhysRevD.97.036001.

[32] D. Hanneke, S. Fogwell Hoogerheide, and G. Gabrielse. Cavity Control of a Single-Electron Quantum Cyclotron: Measuring the Electron Magnetic Moment. *Phys. Rev. A*, 83:052122, 2011. doi: 10.1103/PhysRevA.83.052122.

[33] Ken-ichi Aoki et al. Electroweak Theory: Framework of On-Shell Renormalization and Study of Higher-Order Effects. *Progress of Theoretical Physics Supplement*, 73:1–226, 1982. URL `http://ptps.oxfordjournals.org/content/73/1.abstract`.

[34] Stephen P. Martin. A Supersymmetry primer. *Adv. Ser. Direct. High Energy Phys.*, 21:1–153, 2010. doi: 10.1142/9789812839657_0001.

[35] Kenneth D. Lane. An Introduction to technicolor. In *Theoretical Advanced Study Institute (TASI 93) in Elementary Particle Physics: The Building Blocks of Creation - From Microfermius to Megaparsecs*, pages 381–408, 6 1993. doi: 10.1142/9789814503785_0010.

[36] Nima Arkani-Hamed, Savas Dimopoulos, and G. R. Dvali. The Hierarchy problem and new dimensions at a millimeter. *Phys. Lett.*, B429:263–272, 1998. doi: 10.1016/S0370-2693(98)00466-3.

[37] Werner Bernreuther. CP violation and baryogenesis. *Lect. Notes Phys.*, 591:237–293, 2002.

[38] Mark Trodden. Electroweak baryogenesis: A Brief review. In *Proceedings, 33rd Rencontres de Moriond 98 electroweak interactions and unified theories: Les Arcs, France, Mar 14-21, 1998*, pages 471–480, 1998. URL `https://inspirehep.net/record/470220/files/Pages_from_C98-03-14_471.pdf`.

[39] Gustavo C. Branco, Luis Lavoura, and Joao P. Silva. CP Violation. *Int. Ser. Monogr. Phys.*, 103:1–536, 1999.

[40] C. S. Wu et al. Experimental Test of Parity Conservation in Beta Decay. *Phys. Rev.*, 105:1413–1415, Feb 1957. URL `https://link.aps.org/doi/10.1103/PhysRev.105.1413`.

[41] J. H. Christenson, J. W. Cronin, V. L. Fitch, and R. Turlay. Evidence for the 2π decay of the k_2^0 meson. *Phys. Rev. Lett.*, 13:138–140, Jul 1964. URL `https://link.aps.org/doi/10.1103/PhysRevLett.13.138`.

[42] Makoto Kobayashi and Toshihide Maskawa. CP-Violation in the renormalizable theory of weak interaction. *Prog. Theor. Phys.*, (49 (2)):652, 1973. URL `http://dx.doi.org/10.1143/PTP.49.652`.

[43] Maki, Ziro and Nakagawa, Masami and Sakata, Shoichi. Remarks on the Unified Model of Elementary Particles. *Progress of Theoretical Physics*, 28(5):870–880, 1962. URL `http://dx.doi.org/10.1143/PTP.28.870`.

[44] Nicola Cabibbo. Unitary symmetry and leptonic decays. *Phys. Rev. Lett.*, 10:531–533, Jun 1963. URL `https://link.aps.org/doi/10.1103/PhysRevLett.10.531`.

[45] C. Jarlskog. Commutator of the quark mass matrices in the standard electroweak model and a measure of maximal CP nonconservation. *Phys. Rev. Lett.*, 55:1039–1042, Sep 1985. URL `https://link.aps.org/doi/10.1103/PhysRevLett.55.1039`.

[46] G. C. Branco et al. Theory and phenomenology of two-Higgs-doublet models. *Phys. Rept.*, 516:1–102, 2012. doi: 10.1016/j.physrep.2012.02.002.

[47] Duarte Fontes, Jorge C. Romão, João P. Silva, and Rui Santos. Large pseudo-scalar components in the C2HDM. In *2nd Toyama International Workshop on Higgs as a Probe of New Physics (HPNP2015) Toyama, Japan, February 11-15, 2015*, 2015. URL `https://inspirehep.net/record/1374236/files/arXiv:1506.00860.pdf`.

[48] CDF Collaboration. Observation of top quark production in $\bar{p}p$ collisions with the collider detector at Fermilab. *Phys. Rev. Lett.*, (74):2626, 1995. URL `http://dx.doi.org/10.1103/PhysRevLett.74.2626`.

[49] D∅ Collaboration. Observation of the top quark. *Phys. Rev. Lett.*, (74):2632, 1995. URL `http://dx.doi.org/10.1103/PhysRevLett.74.2632`.

[50] ATLAS Collaboration. Measurement of the top quark mass in the $t\bar{t} \to$ lepton+jets channel from $\sqrt{s} = 8$ TeV ATLAS data and combination with previous results. *Eur. Phys. J. C*, 79(4):290, 2019. doi: 10.1140/epjc/s10052-019-6757-9.

[51] CMS Collaboration. Measurement of the top quark mass using proton-proton data at $\sqrt{(s)}$ = 7 and 8 TeV. *Phys. Rev.*, D93(7):072004, 2016. doi: 10.1103/PhysRevD.93.072004.

[52] Martin Beneke et al. Top Quark Physics. (hep-ph/0003033. CERN-TH-2000-100):111 p, Mar 2000. URL `http://cds.cern.ch/record/429963`.

[53] ATLAS Collaboration. Measurements of top-quark pair spin correlations in the $e\mu$ channel at $\sqrt{s} = 13$ TeV using pp collisions in the ATLAS detector. *Eur. Phys. J. C*, 80(8):754, 2020. doi: 10.1140/epjc/s10052-020-8181-6.

[54] CMS Collaboration. Measurement of the top quark polarization and $\mathrm{t\bar{t}}$ spin correlations using dilepton final states in proton-proton collisions at $\sqrt{s} = 13$ TeV. *Phys. Rev. D*, 100(7):072002, 2019. doi: 10.1103/PhysRevD.100.072002.

[55] Arnd Behring et al. Higher order corrections to spin correlations in top quark pair production at the LHC. *Phys. Rev. Lett.*, 123(8):082001, 2019. doi: 10.1103/PhysRevLett.123.082001.

[56] Lyndon Evans and Philip Bryant. LHC Machine. *JINST*, (3):S08001, 2008. URL `http://dx.doi.org/10.1088/1748-0221/3/08/S08001`.

[57] ATLAS Collaboration. The ATLAS experiment at the CERN Large Hadron Collider. *JINST*, (3):S08003, 2008. URL `http://iopscience.iop.org/1748-0221/3/08/S08003`.

[58] CMS Collaboration. The CMS experiment at the CERN LHC. *JINST*, (3):S08004, 2008. URL `http://iopscience.iop.org/1748-0221/3/08/S08004`.

[59] D. de Florian et al. Handbook of LHC Higgs Cross Sections: 4. Deciphering the Nature of the Higgs Sector. Technical Report CERN-2017-002-M, CERN-2017-002, Oct 2016.

[60] The Nobel Foudation. The Nobel Prize in Physics 2013. *Nobelprize.org. Nobel Media*, 2020. URL `https://www.nobelprize.org/prizes/physics/2013/press-release/`.

[61] ATLAS Collaboration. Measurement of the Higgs boson mass in the $H \to ZZ^* \to 4\ell$ decay channel with $\sqrt{s} = 13$ TeV pp collisions using the ATLAS detector at the LHC. Apr 2020. ATLAS-CONF-2020-005.

[62] CMS Collaboration. A measurement of the Higgs boson mass in the diphoton decay channel. *Phys. Lett. B*, 805:135425, 2020. doi: 10.1016/j.physletb.2020.135425.

[63] ATLAS Collaboration. A combination of measurements of Higgs boson production and decay using up to 139 fb^{-1} of proton–proton collision data at $\sqrt{s} = 13$ TeV collected with the ATLAS experiment. Aug 2020. ATLAS-CONF-2020-027.

[64] CMS Collaboration. Combined Higgs boson production and decay measurements with up to 137 fb-1 of proton-proton collision data at $\sqrt{s}$ = 13 TeV. Jan 2020. CMS-PAS-HIG-19-005.

[65] ATLAS Collaboration. Study of the spin and parity of the Higgs boson in diboson decays with the ATLAS detector. *Eur. Phys. J.*, C75(10):476, 2015. doi: 10.1140/epjc/s10052-015-3685-1,10.1140/epjc/s10052-016-3934-y. [Erratum: Eur. Phys. J.C76,no.3,152(2016)].

[66] CMS Collaboration. Constraints on the spin-parity and anomalous HVV couplings of the Higgs boson in proton collisions at 7 and 8 TeV. *Phys. Rev. D*, 92:012004, Jul 2015. URL `http://link.aps.org/doi/10.1103/PhysRevD.92.012004`.

[67] ATLAS Collaboration. Measurements of Higgs boson properties in the diphoton decay channel with 36 fb^{-1} of pp collision data at $\sqrt{s} = 13$ TeV with the ATLAS detector. *Phys. Rev. D*, 98:052005, 2018. doi: 10.1103/PhysRevD.98.052005.

[68] ATLAS Collaboration. Higgs boson production cross-section measurements and their EFT interpretation in the 4ℓ decay channel at $\sqrt{s}$ =13 TeV with the ATLAS detector. *Eur. Phys. J. C*, 80(10):957, 2020. doi: 10.1140/epjc/s10052-020-8227-9.

[69] CMS Collaboration. Combined search for anomalous pseudoscalar HVV couplings in VH(H $\to b\bar{b}$) production and H $\to$ VV decay. *Phys. Lett. B*, 759:672–696, 2016. doi: 10.1016/j.physletb.2016.06.004.

[70] CMS Collaboration. Constraints on anomalous HVV couplings from the production of Higgs bosons decaying to τ lepton pairs. *Phys. Rev. D*, 100(11):112002, 2019. doi: 10.1103/PhysRevD.100.112002.

[71] CMS Collaboration. Constraints on anomalous Higgs boson couplings to vector bosons and fermions in production and decay in the $H \to 4\ell$ channel. Aug 2020. CMS-PAS-HIG-19-009.

[72] Fawzi Boudjema, Rohini M. Godbole, Diego Guadagnoli, and Kirtimaan A. Mohan. Lab-frame observables for probing the top-Higgs interaction. *Phys. Rev.*, D92(1):015019, 2015. doi: 10.1103/PhysRevD.92.015019.

[73] CMS Collaboration. Analysis of the CP structure of the Yukawa coupling between the Higgs boson and τ leptons in proton-proton collisions at $\sqrt{s} = 13$ TeV. Aug 2020. CMS-PAS-HIG-20-006.

[74] ATLAS Collaboration. Observation of Higgs boson production in association with a top quark pair at the LHC with the ATLAS detector. *Phys. Lett. B*, 784:173–191, 2018. doi: 10.1016/j.physletb.2018.07.035.

[75] CMS Collaboration. Observation of $\mathrm{t\bar{t}H}$ production. *Phys. Rev. Lett.*, 120(23):231801, 2018. doi: 10.1103/PhysRevLett.120.231801.

[76] ATLAS Collaboration. CP Properties of Higgs Boson Interactions with Top Quarks in the $t\bar{t}H$ and tH Processes Using $H \to \gamma\gamma$ with the ATLAS Detector. *Phys. Rev. Lett.*, 125(6):061802, 2020. doi: 10.1103/PhysRevLett.125.061802.

[77] CMS Collaboration. Measurements of $\mathrm{t\bar{t}H}$ production and the CP structure of the Yukawa interaction between the Higgs boson and top quark in the diphoton decay channel. *Phys. Rev. Lett.*, 125(6):061801, 2020. doi: 10.1103/PhysRevLett.125.061801.

[78] Bednyakov, A. V. and Kniehl, B. A. and Pikelner, A. F. and Veretin, O. L. Stability of the Electroweak Vacuum: Gauge Independence and Advanced Precision. *Phys. Rev. Lett.*, 115:201802, Nov 2015. URL `http://link.aps.org/doi/10.1103/PhysRevLett.115.201802`.

[79] Joachim Brod, Ulrich Haisch, and Jure Zupan. Constraints on CP-violating Higgs couplings to the third generation. *JHEP*, 11:180, 2013. doi: 10.1007/JHEP11(2013)180.

[80] V. Andreev et al. Improved limit on the electric dipole moment of the electron. *Nature*, 562(7727): 355–360, 2018. doi: 10.1038/s41586-018-0599-8.

[81] John Ellis, Dae Sung Hwang, Kazuki Sakurai, and Michihisa Takeuchi. Disentangling Higgs-Top Couplings in Associated Production. *JHEP*, 04:004, 2014. doi: 10.1007/JHEP04(2014)004.

[82] Saurabh D. Rindani, Pankaj Sharma, and Ambresh Shivaji. Unraveling the CP phase of top-Higgs coupling in associated production at the LHC. *Phys. Lett.*, B761:25–30, 2016. doi: 10.1016/j.physletb.2016.08.002.

[83] CMS Collaboration. Search for associated production of a Higgs boson and a single top quark in proton-proton collisions at $\sqrt{s} = 13$ TeV. *Phys. Rev. D*, 99(9):092005, 2019. doi: 10.1103/PhysRevD.99.092005.

[84] ATLAS Collaboration. Constraints on Higgs boson properties using $WW^{*}(\to e\nu\mu\nu)\ jj$ production in 36.1fb^{-1} of $\sqrt{s} = 13TeV$ pp collisions with the ATLAS detector. Nov 2020. ATLAS-CONF-2020-055.

[85] ATLAS Collaboration. Evidence for $t\bar{t}t\bar{t}$ production in the multilepton final state in proton-proton collisions at $\sqrt{s}$=13 TeV with the ATLAS detector. Jul 2020. CERN-EP-2020-111.

[86] CMS Collaboration. Search for production of four top quarks in final states with same-sign or multiple leptons in proton-proton collisions at $\sqrt{s} = 13$ TeV. *Eur. Phys. J. C*, 80(2):75, 2020. doi: 10.1140/epjc/s10052-019-7593-7.

[87] Qing-Hong Cao et al. Limiting top quark-Higgs boson interaction and Higgs-boson width from multi-top productions. *Phys. Rev. D*, 99(11):113003, 2019. doi: 10.1103/PhysRevD.99.113003.

[88] CMS Collaboration. Measurement of the top quark Yukawa coupling from $\mathrm{t\bar{t}}$ kinematic distributions in the dilepton final state at $\sqrt{s} = 13$ TeV. (CMS-PAS-TOP-19-008), May 2020. URL `http://cds.cern.ch/record/2718943`.

[89] P.S. Bhupal Dev et al. Determining the CP properties of the Higgs boson. *Phys. Rev. Lett.*, 100:051801, 2008. doi: 10.1103/PhysRevLett.100.051801.

[90] J. Alwall et al. The automated computation of tree-level and next-to-leading order differential cross sections, and their matching to parton shower simulations. *JHEP*, 07:079, 2014. doi: 10.1007/JHEP07(2014)079.

[91] Priscila de Aquino and Kentarou Mawatari. Characterising a Higgs-like resonance at the LHC. In *1st Toyama International Workshop on Higgs as a Probe of New Physics 2013*, Jul 2013. URL `https://arxiv.org/abs/1307.5607`.

[92] P. Artoisenet et al. A framework for Higgs characterisation. *JHEP*, 11:043, 2013. doi: 10.1007/JHEP11(2013)043.

[93] John N. Ng and Pierre Zakarauskas. Qcd-parton calculation of conjoined production of higgs bosons and heavy flavors in $p\overline{p}$ collisions. *Phys. Rev. D*, 29:876–886, Mar 1984. URL `https://link.aps.org/doi/10.1103/PhysRevD.29.876`.

[94] Xiao-Gang He, Guan-Nan Li, and Ya-Juan Zheng. Probing Higgs boson CP properties with ttH at the LHC and the 100 TeV pp collider. *International Journal of Modern Physics A*, 30(25):1550156, 2015. URL `http://www.worldscientific.com/doi/abs/10.1142/S0217751X15501560`.

[95] John F. Gunion and Xiao-Gang He. Determining the CP nature of a neutral Higgs boson at the LHC. *Phys. Rev. Lett.*, 76:4468–4471, 1996. doi: 10.1103/PhysRevLett.76.4468.

[96] Federico Demartin et al. Higgs characterisation at nlo in qcd: Cp properties of the top-quark yukawa interaction. *The European Physical Journal C*, 74(9):3065, Sep 2014. URL `https://doi.org/10.1140/epjc/s10052-014-3065-2`.

[97] Jinmian Li, Zong-guo Si, Lei Wu, and Jason Yue. Central-edge asymmetry as a probe of Higgs-top coupling in $t\bar{t}h$ production at the LHC. *Phys. Lett. B*, 779:72–76, 2018. doi: 10.1016/j.physletb.2018.02.009.

[98] Buckley, Matthew R. and Gonçalves, Dorival. Boosting the Direct *CP* Measurement of the Higgs-Top Coupling. *Phys. Rev. Lett.*, 116:091801, Mar 2016. URL `https://link.aps.org/doi/10.1103/PhysRevLett.116.091801`.

[99] Pierre Artoisenet, Rikkert Frederix, Olivier Mattelaer, and Robbert Rietkerk. Automatic spin-entangled decays of heavy resonances in Monte Carlo simulations. *JHEP*, 03:015, 2013. doi: 10.1007/JHEP03(2013)015.

[100] D. Azevedo, A. Onofre, F. Filthaut, and R. Gonçalo. CP tests of Higgs couplings in $t\bar{t}h$ semileptonic events at the LHC. *Phys. Rev. D*, 98(3):033004, 2018. doi: 10.1103/PhysRevD.98.033004.

[101] Johannes Erdmann et al. A likelihood-based reconstruction algorithm for top-quark pairs and the KLFitter framework. *Nucl. Instrum. Meth. A*, 748:18–25, 2014. doi: 10.1016/j.nima.2014.02.029.

[102] CERN. Long shutdown 1: Exciting times ahead, 2013. URL `http://home.cern/about/updates/2013/02/long-shutdown-1-exciting-times-ahead`.

[103] CERN. CERN announces LHC restart schedule, 2014. URL `http://home.cern/about/updates/2014/06/cern-announces-lhc-restart-schedule`.

[104] ATLAS Collaboration. Luminosity Public Results, 2020. URL `https://twiki.cern.ch/twiki/bin/view/AtlasPublic/LuminosityPublicResultsRun2`.

[105] CMS Collaboration. Luminosity Public Results, 2020. URL `https://twiki.cern.ch/twiki/bin/view/CMSPublic/LumiPublicResults`.

[106] ATLAS Collaboration. Detector & Technology, 2020. URL `https://atlas.cern/discover/detector`.

[107] M Capeans et al. ATLAS Insertable B-Layer Technical Design Report. Technical Report CERN-LHCC-2010-013. ATLAS-TDR-19, CERN, Geneva, Sep 2010. URL `http://cds.cern.ch/record/1291633`.

[108] ATLAS Collaboration. Performance of the ATLAS Trigger System in 2015. *Eur. Phys. J. C*, 77(5):317, 2017. doi: 10.1140/epjc/s10052-017-4852-3.

[109] ATLAS Collaboration. Operation of the ATLAS trigger system in Run 2. *JINST*, 15(10):P10004, 2020. doi: 10.1088/1748-0221/15/10/P10004.

[110] ATLAS Collaboration. The performance of the jet trigger for the ATLAS detector during 2011 data taking. *Eur. Phys. J. C*, 76:526, 2016. doi: 10.1140/epjc/s10052-016-4325-0.

[111] ATLAS Collaboration. Trigger Menu in 2017. ATL-DAQ-PUB-2018-002, 2018. URL `https://cds.cern.ch/record/2625986`.

[112] Matteo Cacciari, Gavin P. Salam, and Gregory Soyez. The Anti-k(t) jet clustering algorithm. *JHEP*, 04:063, 2008. doi: 10.1088/1126-6708/2008/04/063.

[113] ATLAS Collaboration. Jet energy scale measurements and their systematic uncertainties in proton–proton collisions at $\sqrt{s} = 13\,\text{TeV}$ with the ATLAS detector. *Phys. Rev. D*, 96:072002, 2017. doi: 10.1103/PhysRevD.96.072002.

[114] ATLAS Collaboration. Calibration of light-flavour b-jet mistagging rates using ATLAS proton–proton collision data at $\sqrt{s} = 13$ TeV. ATLAS-CONF-2018-006, 2018. URL `https://cds.cern.ch/record/2314418`.

[115] ATLAS Collaboration. Tagging and suppression of pileup jets with the ATLAS detector. ATLAS-CONF-2014-018, 2014. URL `https://cds.cern.ch/record/1700870`.

[116] M. Shochet et al. Fast TracKer (FTK) Technical Design Report. Jun 2013. CERN-LHCC-2013-007, ATLAS-TDR-021.

[117] ATLAS Collaboration. Topological cell clustering in the ATLAS calorimeters and its performance in LHC Run 1. *Eur. Phys. J. C*, 77:490, 2017. doi: 10.1140/epjc/s10052-017-5004-5.

[118] ATLAS Collaboration. ATLAS b-jet identification performance and efficiency measurement with $t\bar{t}$ events in pp collisions at $\sqrt{s} = 13\,\text{TeV}$. 2019. 1907.05120 [hep-ex], CERN-EP-2019-132.

[119] Benjamin Nachman et al. Jets from jets: re-clustering as a tool for large radius jet reconstruction and grooming at the LHC. *JHEP*, 02:075, 2015. doi: 10.1007/JHEP02(2015)075.

[120] ATLAS Collaboration. The ATLAS Simulation Infrastructure. *Eur. Phys. J. C*, 70:823, 2010. doi: 10.1140/epjc/s10052-010-1429-9.

[121] S. Agostinelli et al. GEANT4 – a simulation toolkit. *Nucl. Instrum. Meth. A*, 506:250, 2003. doi: 10.1016/S0168-9002(03)01368-8.

[122] ATLAS Collaboration. The simulation principle and performance of the ATLAS fast calorimeter simulation FastCaloSim. ATL-PHYS-PUB-2010-013, 2010. URL `https://cds.cern.ch/record/1300517`.

[123] Torbjörn Sjöstrand et al. An introduction to PYTHIA 8.2. *Comput. Phys. Commun.*, 191:159, 2015. doi: 10.1016/j.cpc.2015.01.024.

[124] Rikkert Frederix, Emanuele Re, and Paolo Torrielli. Single-top t-channel hadroproduction in the four-flavour scheme with POWHEG and aMC@NLO. *JHEP*, 09:130, 2012. doi: 10.1007/JHEP09(2012)130.

[125] Simone Alioli, Paolo Nason, Carlo Oleari, and Emanuele Re. A general framework for implementing NLO calculations in shower Monte Carlo programs: the POWHEG BOX. *JHEP*, 06:043, 2010. doi: 10.1007/JHEP06(2010)043.

[126] Heribertus B. Hartanto, Barbara Jager, Laura Reina, and Doreen Wackeroth. Higgs boson production in association with top quarks in the POWHEG BOX. *Phys. Rev. D*, 91(9):094003, 2015. doi: 10.1103/PhysRevD.91.094003.

[127] Johannes Bellm et al. Herwig 7.0/Herwig++ 3.0 release note. *Eur. Phys. J. C*, 76(4):196, 2016. doi: 10.1140/epjc/s10052-016-4018-8.

[128] Tomáš Ježo, Jonas M. Lindert, Niccolo Moretti, and Stefano Pozzorini. New NLOPS predictions for $t\bar{t}+b$ -jet production at the LHC. *Eur. Phys. J. C*, 78(6):502, 2018. doi: 10.1140/epjc/s10052-018-5956-0.

[129] Federico Buccioni et al. OpenLoops 2. *Eur. Phys. J. C*, 79(10):866, 2019. doi: 10.1140/epjc/s10052-019-7306-2.

[130] Fabio Cascioli, Philipp Maierhofer, and Stefano Pozzorini. Scattering Amplitudes with Open Loops. *Phys. Rev. Lett.*, 108:111601, 2012. doi: 10.1103/PhysRevLett.108.111601.

[131] Ansgar Denner, Stefan Dittmaier, and Lars Hofer. Collier: a fortran-based Complex One-Loop LIbrary in Extended Regularizations. *Comput. Phys. Commun.*, 212:220–238, 2017. doi: 10.1016/j.cpc.2016.10.013.

[132] Tomas Jezo. Powheg-box-res ttbb source code, 2019. URL `https://gitlab.cern.ch/tjezo/powheg-box-res_ttbb/`.

[133] S. Frixione et al. A positive-weight next-to-leading-order Monte Carlo for heavy flavour hadroproduction. *JHEP*, 09:126, 2007. doi: 10.1088/1126-6708/2007/09/126.

[134] Simone Alioli, Paolo Nason, Carlo Oleari, and Emanuele Re. NLO single-top production matched with shower in POWHEG: s- and t-channel contributions. *JHEP*, 09:111, 2009. doi: 10.1007/JHEP02(2010)011,10.1088/1126-6708/2009/09/111. [Erratum: JHEP02,011(2010)].

[135] Emanuele Re. Single-top Wt-channel production matched with parton showers using the POWHEG method. *Eur. Phys. J. C*, 71:1547, 2011. doi: 10.1140/epjc/s10052-011-1547-z.

[136] Stefano Frixione et al. Single-top hadroproduction in association with a W boson. *JHEP*, 07:029, 2008. doi: 10.1088/1126-6708/2008/07/029.

[137] S. Catani, F. Krauss, R. Kuhn, and B. R. Webber. QCD matrix elements + parton showers. *JHEP*, 11:063, 2001. doi: 10.1088/1126-6708/2001/11/063.

[138] Stefan Höche, Frank Krauss, Steffen Schumann, and Frank Siegert. QCD matrix elements and truncated showers. *JHEP*, 05:053, 2009. doi: 10.1088/1126-6708/2009/05/053.

[139] Tanju Gleisberg and Stefan Höche. Comix, a new matrix element generator. *JHEP*, 12:039, 2008. doi: 10.1088/1126-6708/2008/12/039.

[140] Stefan Höche, Frank Krauss, Marek Schonherr, and Frank Siegert. A critical appraisal of NLO+PS matching methods. *JHEP*, 09:049, 2012. doi: 10.1007/JHEP09(2012)049.

[141] Michal Czakon, Paul Fiedler, and Alexander Mitov. The total top quark pair production cross-section at hadron colliders through $O(\alpha_S^4)$. *Phys. Rev. Lett.*, 110:252004, 2013. doi: 10.1103/PhysRevLett.110.252004.

[142] Michal Czakon and Alexander Mitov. Top++: A Program for the Calculation of the Top-Pair Cross-Section at Hadron Colliders. *Comput. Phys. Commun.*, 185:2930, 2014. doi: 10.1016/j.cpc.2014.06.021.

[143] M. Aliev et al. HATHOR: HAdronic Top and Heavy quarks crOss section calculatoR. *Comput. Phys. Commun.*, 182:1034–1046, 2011. doi: 10.1016/j.cpc.2010.12.040.

[144] P. Kant et al. HatHor for single top-quark production: Updated predictions and uncertainty estimates for single top-quark production in hadronic collisions. *Comput. Phys. Commun.*, 191:74–89, 2015. doi: 10.1016/j.cpc.2015.02.001.

[145] Nikolaos Kidonakis. Two-loop soft anomalous dimensions for single top quark associated production with a W- or H-. *Phys. Rev. D*, 82:054018, 2010. doi: 10.1103/PhysRevD.82.054018.

[146] Charalampos Anastasiou, Lance J. Dixon, Kirill Melnikov, and Frank Petriello. High precision QCD at hadron colliders: Electroweak gauge boson rapidity distributions at NNLO. *Phys. Rev. D*, 69:094008, 2004. doi: 10.1103/PhysRevD.69.094008.

[147] ATLAS Collaboration. Luminosity determination in pp collisions at $\sqrt{s} = 13\,\text{TeV}$ using the ATLAS detector at the LHC. ATLAS-CONF-2019-021, 2019. URL `https://cds.cern.ch/record/2677054`.

[148] LHCTopWG. ATLAS-CMS recommended predictions for top-quark-pair cross sections, 2015. URL `https://twiki.cern.ch/twiki/bin/view/LHCPhysics/TtbarNNLO`.

[149] LHCTopWG. ATLAS-CMS recommended predictions for single-top cross sections, 2017. URL `https://twiki.cern.ch/twiki/bin/view/LHCPhysics/SingleTopRefXsec`.

[150] LHCHXSWG1. Recommended predictions for $\mathrm{t\bar{t}V}$ cross sections, 2015. URL `https://twiki.cern.ch/twiki/bin/view/LHCPhysics/ProposaltTV`.

[151] John M. Campbell and R. Keith Ellis. $t\bar{t}W^{+-}$ production and decay at NLO. *JHEP*, 07:052, 2012. doi: 10.1007/JHEP07(2012)052.

[152] Kyle Cranmer. Practical Statistics for the LHC. In *2011 European School of High-Energy Physics*, pages 267–308, 2014. doi: 10.5170/CERN-2014-003.267.

[153] S.S. Wilks. The Large-Sample Distribution of the Likelihood Ratio for Testing Composite Hypotheses. *Annals Math. Statist.*, 9(1):60–62, 1938. doi: 10.1214/aoms/1177732360.

[154] ATLAS Collaboration. Measurements of top-quark pair differential cross-sections in the $e\mu$ channel in pp collisions at $\sqrt{s} = 13\,\text{TeV}$ using the ATLAS detector. *Eur. Phys. J. C*, 77:292, 2017. doi: 10.1140/epjc/s10052-017-4821-x.

[155] Andreas Hoecker et al. TMVA: Toolkit for Multivariate Data Analysis. *PoS*, ACAT:040, 2007.

[156] R. Brun and F. Rademakers. ROOT: An object oriented data analysis framework. *Nucl. Instrum. Meth.*, A389:81–86, 1997. doi: 10.1016/S0168-9002(97)00048-X.

[157] Federico Buccioni, Stefan Kallweit, Stefano Pozzorini, and Max F. Zoller. NLO QCD predictions for $t\bar{t}b\bar{b}$ production in association with a light jet at the LHC. *JHEP*, 12:015, 2019. doi: 10.1007/JHEP12(2019)015.

[158] Robert D. Cousins. Generalization of chisquare goodness-of-fit test for binned data using saturated models, with application to histograms. URL `http://www.physics.ucla.edu/~cousins/stats/cousins_saturated.pdf`.

[159] Luis Falda Coelho. Study of the CP nature of the top-Higgs coupling in $t\bar{t}H$ events at the LHC., Oct 2020. URL `https://cds.cern.ch/record/2746812`.

[160] J. de Blas et al. Higgs Boson Studies at Future Particle Colliders. *JHEP*, 01:139, 2020. doi: 10.1007/JHEP01(2020)139.

[161] 2020 Update of the European Strategy for Particle Physics (Brochure). Technical Report CERN-ESU-015, Geneva, 2020. URL `https://cds.cern.ch/record/2721370`.

[162] Richard D. Ball et al. Parton distributions for the LHC Run II. *JHEP*, 04:040, 2015. doi: 10.1007/JHEP04(2015)040.

[163] D. J. Lange. The EvtGen particle decay simulation package. *Nucl. Instrum. Meth. A*, 462:152, 2001. doi: 10.1016/S0168-9002(01)00089-4.

[164] ATLAS Collaboration. ATLAS Pythia 8 tunes to 7 TeV data. ATL-PHYS-PUB-2014-021, 2014. URL `https://cds.cern.ch/record/1966419`.

[165] L.A. Harland-Lang, A.D. Martin, P. Motylinski, and R.S. Thorne. Parton distributions in the LHC era: MMHT 2014 PDFs. *Eur. Phys. J. C*, 75(5):204, 2015. doi: 10.1140/epjc/s10052-015-3397-6.

[166] Steffen Schumann and Frank Krauss. A parton shower algorithm based on Catani–Seymour dipole factorisation. *JHEP*, 03:038, 2008. doi: 10.1088/1126-6708/2008/03/038.

[167] Jan-Christopher Winter, Frank Krauss, and Gerhard Soff. A Modified cluster hadronization model. *Eur. Phys. J. C*, 36:381–395, 2004. doi: 10.1140/epjc/s2004-01960-8.

[168] J. Pumplin et al. New Generation of Parton Distributions with Uncertainties from Global QCD Analysis. *JHEP*, 07:012, 2002. doi: 10.1088/1126-6708/2002/07/012.

[169] Vernon D. Barger, J. Ohnemus, and R. J. N. Phillips. Event shape criteria for single lepton top signals. *Phys. Rev. D*, 48:R3953–R3956, 1993. doi: 10.1103/PhysRevD.48.R3953.

Appendix A

Sample details

In this appendix, technical details about sample generation are provided.

In all samples with top quarks, the top quark mass is set to 172.5 GeV. The mass of the b quarks from the top quark decays and from the $t\bar{t} + b\bar{b}$ ME is set to 4.95 GeV. In samples with Higgs bosons, the Higgs boson mass is set to 125.0 GeV and, for the Higgs boson decay into $b\bar{b}$, the b quark mass is set to 4.80 GeV or 4.50 GeV, for samples using Pythia8 or Herwig7, respectively. For all samples generated at NLO in QCD using MadGraph5_aMC@NLO for the ME, the shower starting scale has the functional form $H_{\mathrm{T}}/2$, where H_{T} is defined as the scalar sum of the p_T of all outgoing partons. Table A.1 shows a list of processes generated with PowhegBox and MadGraph5_aMC@NLO, with the corresponding PDF sets used [162], functional forms of the renormalisation and factorisation scales and the h_{damp} parameter (for Powheg only)[1].

In all MC samples for which the PS, hadronisation, and multi-parton interactions are done either with Pythia8 or Herwig7, the decays of b and c hadrons are simulated using the EvtGen v1.6.0 program [163]. For Pythia8, the A14 [164] set of parameters is always used, with the `NNPDF2.3lo` PDF set, except for the modelling of pile-up interactions. For Herwig7, the H7UE set of tuned parameters [127] is always used, with the `MMHT2014 LO` PDF set [165]. All Sherpa samples use the Sherpa parton shower [166], based on Catani-Seymour dipoles, and the cluster hadronisation model [167]. The PS is employed with a set of tuned parameters developed by the Sherpa authors, based on the `NNPDF3.0nnlo` PDF set.

[1]The h_{damp} parameter controls the p_T of the first additional emission beyond the leading-order Feynman diagram in the PS and therefore regulates the high-p_T emission against which the ME final-state system recoils.

Table A.1: PDF sets [162], nominal renormalisation and factorisation scales, and h_{damp} parameter (when applicable) used in the sample generation. The transverse mass of a particle is defined as $m_T = \sqrt{m^2 + p_T^2}$. Sums with unspecified subscript i run over all the particles in the ME final state.

<table>
<tr><th>Process</th><th>PDF set</th><th>Renormalisation scale</th><th>Factorisation scale</th><th>h_{damp}</th></tr>
<tr><td>$t\bar{t}H$ MadGraph5_aMC@NLO</td><td>NNPDF3.0nlo</td><td colspan="2" rowspan="2">$\sqrt[3]{m_{T,t} m_{T,\bar{t}} m_{T,H}}$</td><td>-</td></tr>
<tr><td>$t\bar{t}H$ PowhegBox</td><td>NNPDF3.0nlo</td><td>$3/4(m_t + m_{\bar{t}} + m_H)$</td></tr>
<tr><td>$tHjb$</td><td>NNPDF3.0nlonf4</td><td colspan="2" rowspan="2">$1/2 \sum_i m_{T,i}$</td><td>-</td></tr>
<tr><td>tWH</td><td>NNPDF3.0nlo</td><td>-</td></tr>
<tr><td>$t\bar{t} + b\bar{b}$</td><td>NNPDF3.0nlonf4</td><td>$\sqrt[4]{m_{T,t} m_{T,\bar{t}} m_{T,b} m_{T,\bar{b}}}$</td><td>$\frac{1}{2}\Sigma_{i=t,\bar{t},b,\bar{b},j} m_{\text{T},i}$</td><td>$\frac{1}{2}\Sigma_i m_{\text{T},i}$</td></tr>
<tr><td>$t\bar{t}$</td><td>NNPDF3.0nlo</td><td colspan="2">$m_{T,t}$ (in $t\bar{t}$ rest frame)</td><td>$3/4(m_t + m_{\bar{t}})$</td></tr>
<tr><td>t-channel single top</td><td>NNPDF3.0nlonf4</td><td colspan="2">$m_{T,b}$</td><td>-</td></tr>
<tr><td>s-channel single top</td><td>NNPDF3.0nlo</td><td colspan="2" rowspan="3">m_t</td><td>-</td></tr>
<tr><td>tW PowhegBox</td><td>NNPDF3.0nlo</td><td>-</td></tr>
<tr><td>tW MadGraph5_aMC@NLO</td><td>CT10nlo</td><td>-</td></tr>
<tr><td>$t\bar{t}V$ MadGraph5_aMC@NLO</td><td>NNPDF3.0nlo</td><td colspan="2">$1/2 \sum_i m_{T,i}$</td><td>-</td></tr>
<tr><td>$t\bar{t}t\bar{t}$</td><td>NNPDF3.1nlo</td><td colspan="2">$1/4 \sum_i m_{T,i}$</td><td>-</td></tr>
<tr><td>tZq</td><td>CTEQ6L1 [168]</td><td colspan="2">$4m_{T,b}$ (b from gluon splitting)</td><td>-</td></tr>
<tr><td>tWZ</td><td>NNPDF3.0nlo</td><td colspan="2">m_t</td><td>-</td></tr>
</table>

Appendix B

Input variables of multivariate techniques

This appendix lists all the input variables used in the multivariate methods common to the cross-section and $\mathcal{CP}$ analyses.

B.1 Reconstruction BDTs

Tables B.1 and B.2 give the list of input variables to the Reconstruction BDTs in the dilepton and single-lepton resolved channels, respectively.

Table B.1: List of input variables to the Reconstruction BDTs in the dilepton channel. The variables listed in the first section use topological information from the $t\bar{t}$ system and the ones in the second section use information from the Higgs boson candidate. The top and anti-top candidates are built from one lepton and one b jet.

Variable	BDT w/ Higgs info.	BDT w/o Higgs info.
Mass of top	✓	✓
Mass of anti-top	✓	✓
Mass difference between top and anti-top	✓	✓
$\Delta R(\ell, b)$ from top	✓	✓
$\Delta R(\ell, b)$ from anti-top	✓	✓
$\lvert \Delta R(\ell, b)$ from top - $\Delta R(\ell, b)$ from anti-top $\rvert$	–	✓
$\Delta R(b$ from top, b from anti-top)	✓	–
$\Delta\phi(b$ from top, b from anti-top)	–	✓
p_T b from top	–	✓
p_T b from anti-top	–	✓
Min. $\Delta\eta(\ell, b$ from top or anti-top)	–	✓
Max. ΔR(Higgs, b from top or anti-top)	✓	–
Mass of Higgs	✓	–
$\Delta R(\text{Higgs}, t\bar{t})$	✓	–
$\Delta R(b_1$ from Higgs, b_2 from Higgs)	✓	–

B.2 Classification BDTs

B.2.1 Resolved channels

Tables B.3 and B.4 give the list of input variables to the Classification BDTs in the dilepton and single-lepton resolved channels, respectively.

Table B.2: List of input variables to the Reconstruction BDTs in the single-lepton resolved channel. The variables listed in the first section use topological information from the $t\bar{t}$ system and the ones in the second section use information from the Higgs boson candidate. The subscript had (lep) indicates the hadronically (leptonically) decaying W boson or the corresponding top quark candidate. The symbol b_i refers to b-tagged jets from the Higgs decay, sorted by p_T. The symbol q_i refers to jets from the hadronic W decay, also sorted by p_T.

Variable	BDT w/ Higgs info.	BDT w/o Higgs info.
Mass of $\mathrm{top_{lep}}$	✓	✓
Mass of $\mathrm{top_{had}}$	✓	✓
Mass of W_{had}	✓	✓
Mass of W_{had} and b from $\mathrm{top_{lep}}$	✓	✓
Mass of W_{lep} and b from $\mathrm{top_{had}}$	✓	✓
$\Delta R(W_{\mathrm{had}}, b \text{ from } \mathrm{top_{had}})$	✓	✓
$\Delta R(W_{\mathrm{had}}, b \text{ from } \mathrm{top_{lep}})$	✓	✓
$\Delta R(\ell, b \text{ from } \mathrm{top_{lep}})$	✓	✓
$\Delta R(\ell, b \text{ from } \mathrm{top_{had}})$	✓	✓
$\Delta R(b \text{ from } \mathrm{top_{lep}}, b \text{ from } \mathrm{top_{had}})$	✓	✓
$\Delta R(q_1 \text{ from } W_{\mathrm{had}}, q_2 \text{ from } W_{\mathrm{had}})$	✓	✓
$\Delta R(b \text{ from } t_{\mathrm{had}}, q_1 \text{ from } W_{\mathrm{had}})$	✓	✓
$\Delta R(b \text{ from } t_{\mathrm{had}}, q_2 \text{ from } W_{\mathrm{had}})$	✓	✓
Min. $\Delta R(b \text{ from } \mathrm{top_{had}}, q_i \text{ from } W_{\mathrm{had}})$	✓	✓
$\Delta R(\text{lep}, b \text{ from } \mathrm{top_{lep}}) - \text{min. } \Delta R(b \text{ from } \mathrm{top_{had}}, q_i \text{ from } W_{\mathrm{had}})$	✓	✓
Mass of Higgs	✓	–
Mass of Higgs and q_1 from W_{had}	✓	–
$\Delta R(b_1 \text{ from Higgs}, b_2 \text{ from Higgs})$	✓	–
$\Delta R(b_1 \text{ from Higgs, lepton})$	✓	–

Table B.3: Variables used in the Classification BDTs in the dilepton channel. The first section lists kinematic variables not using $t\bar{t}H$ reconstruction, while the second section lists variables using the output of the Reconstruction BDT. For variables depending on b-tagged jets, only jets b-tagged using the 70% WP are considered. Unless otherwise specified in the list, the Reconstruction BDT without Higgs boson information is used.

Variable	Definition
m_{bb}^{min}	Minimum invariant mass of a b-tagged jet pair
$m_{bb}^{\mathrm{min}\ \Delta R}$	Invariant mass of the b-tagged jet pair with minimum ΔR
$m_{\mathrm{jj}}^{\mathrm{max}\ p_{\mathrm{T}}}$	Invariant mass of the jet pair with maximum p_T
$m_{bb}^{\mathrm{max}\ p_{\mathrm{T}}}$	Invariant mass of the b-tagged jet pair with maximum p_T
$\Delta\eta_{bb}^{\mathrm{avg}}$	Average $\Delta\eta$ for all b-tagged jet pairs
$N_{bb}^{\mathrm{Higgs}\ 30}$	Number of b-tagged jet pairs with invariant mass within 30 GeV of the Higgs boson mass
BDT output	Output of the Reconstruction BDT for the combination selected by the Reconstruction BDT, using both versions of the Reconstruction BDT
m_{bb}^{Higgs}	Higgs candidate mass
$\Delta R_{H,t\bar{t}}$	ΔR between Higgs candidate and $t\bar{t}$ candidate system, using the Reconstruction BDT w/ Higgs info.
$\Delta R_{H,\ell}^{\mathrm{min}}$	Minimum ΔR between Higgs candidate and lepton
$\Delta R_{H,b}^{\mathrm{min}}$	Minimum ΔR between Higgs candidate and b-jet from top

Table B.4: Input variables to the Classification BDTs in the single-lepton resolved channel. The first section lists kinematic variables not using $t\bar{t}H$ reconstruction, the second section lists variables using the output of the Reconstruction BDT, while the third section lists variables related to b-tagging information. For variables depending on b-tagged jets, jets are sorted by their PC b-tagging score, and by their p_T when they have the same score. Unless otherwise specified in the list, the Reconstruction BDT without Higgs boson information is used.

Variable	Definition
$\Delta R_{bb}^{\text{avg}}$	Average ΔR for all b-tagged jet pairs
$\Delta R_{bb}^{\text{max } p_{\text{T}}}$	ΔR between the two b-tagged jets with the largest vector sum p_T
$\Delta\eta_{\text{jj}}^{\text{max}}$	Maximum $\Delta\eta$ between any two jets
$m_{bb}^{\text{min } \Delta R}$	Mass of the combination of two b-tagged jets with the smallest ΔR
$N_{bb}^{\text{Higgs 30}}$	Number of b-tagged jet pairs with invariant mass within 30 GeV of the Higgs-boson mass
Aplanarity	$1.5\lambda_2$, where λ_2 is the second eigenvalue of the momentum tensor [169] built with all jets
H_1	Second Fox–Wolfram moment computed using all jets and the lepton
BDT output	Output of the Reconstruction BDT w/ Higgs info.
m_{bb}^{Higgs}	Higgs candidate mass
$m_{H,b_{\text{lep top}}}$	Mass of Higgs candidate and b-jet from leptonic top candidate
$\Delta R_{bb}^{\text{Higgs}}$	ΔR between b-jets from the Higgs candidate
$\Delta R_{H,t\bar{t}}$	ΔR between Higgs candidate and $t\bar{t}$ candidate system, using the Reconstruction BDT w/ Higgs info.
$\Delta R_{H,\text{lep top}}$	ΔR between Higgs candidate and leptonic top candidate
$w_{b\text{-tag}}^{\text{Higgs}}$	Sum of PC b-tagging discriminants of jets from best Higgs candidate from the Reconstruction BDT
B_{jet}^{3}	3$^{\text{rd}}$ largest jet PC b-tagging discriminant
B_{jet}^{4}	4$^{\text{th}}$ largest jet PC b-tagging discriminant
B_{jet}^{5}	5$^{\text{th}}$ largest jet PC b-tagging discriminant
LHD	Likelihood discriminant

Likelihood discriminant

Table B.5 shows the input variables used for the definition of the signal and background pdfs used in the LHD method. The angle $\theta^*_{p,q}$, designed to be sensitive to the spin of decaying resonances, is defined as the angle between the direction of particle p, in the rest frame of q and the direction of q in the lab rest frame.

Table B.5: Variables used in the calculation of the signal and background pdfs used in the LHD. The symbols t_h and t_l represent the hadronically and leptonically decaying top quark candidates, respectively. The symbols b_1 and b_2 represent the jets from the Higgs boson candidate in the signal hypothesis and the additional jets produced in association with $t\bar{t}$ in the $t\bar{t} + \geq 1b$ hypothesis. The symbols b_h and b_l represent the b jets from the decay of the top quarks and q_1 represents the jet with the largest p_T from the W boson decay.

Variable
$M_H(b_1, b_2)$
$M_{t_l}(l, \nu, b_l)$
$M_{t_h}(b_h, q_1)$
$[M_{t_h t_l} - M_{t_h} - M_{t_l}](l, \nu, b_l, b_h, q_1)$
$[M_{t_h t_l b_1 b_2} - M_{t_l t_h} - M_H](l, \nu, b_l, b_h, q_1, b_1, b_2)$
$\cos\theta^*_{b,H}(b_1, b_2)$
$\cos\theta^*_{b_1 b_2, t_h t_l b_1 b_2}(l, \nu, b_l, b_h, q_1, b_1, b_2)$

B.2.2 Boosted channel

Table B.6 gives the list of input variables to the Classification BDT in the single-lepton boosted channel. In particular, $\eta^{\text{lep}}_{\text{Higgs}}$ is defined as the pseudorapidity of the Higgs candidate multiplied by the sign of the lepton pseudorapidity. This is the same for $\eta^{\text{lep}}_{\text{hadTop}}$ variable. These variables are constructed this way to account for the symmetry with respect to the transverse plane at $z = 0$.

Table B.6: Input variables to the Classification BDT in the boosted single-lepton region. For variables depending on b-tagged jets, jets are sorted by their PC b-tagging score, and by their p_T when they have the same b-tagging score. Moreover, the i index goes from zero to two.

Variable	Description
m_{Higgs}	Higgs candidate mass
$p_T{}^{\text{Higgs}}$	Higgs candidate transverse momentum
$\eta^{\text{lep}}_{\text{Higgs}}$	η of the Higgs candidate relative to the lepton
$\text{P(H)}_{\text{Higgs}}$	DNN Higgs probability for the Higgs candidate
m_{hadTop}	Hadronic top candidate mass
$p_T{}^{\text{hadTop}}$	Hadronic top candidate transverse momentum
$\eta^{\text{lep}}_{\text{hadTop}}$	η of the hadronic top candidate relative to the lepton
$\text{PCB}^{\text{jet}_\text{i}}_{\text{hadTop}}$	PC b-tagging score of the i^{th} jet associated to the hadronic top
m_{lepTop}	Leptonic top candidate mass
$p_T{}^{\text{lepTop}}$	Leptonic top candidate transverse momentum
$\text{PCB}^{\text{jet}}_{\text{lepTop}}$	PC b-tagging score of the jet associated to the leptonic top
n_{jets}	Small-R jets multiplicity
$\Delta R(\text{Higgs}, \text{hadTop})$	ΔR between the Higgs and the hadronic top candidates
$\Delta R(\text{Higgs}, \text{lepTop})$	ΔR between the Higgs and the leptonic top candidates
$\Delta R(\text{hadTop}, \text{lepTop})$	ΔR between the hadronic top and the leptonic top candidates
$p_T{}^{t\bar{t}H}$	Transverse momentum of the $t\bar{t}H$ system
$p_T{}^{t\bar{t}}$	Transverse momentum of the $t\bar{t}$ system
PCB^{sum}	PC b-tagging score sum of the jets associated to $t\bar{t}H$
$\text{PCB}^{\text{add jet}}$	PC b-tagging score of the additional jet in the event

Appendix C

Results on the full set of nuisance parameters

In the main text, the results on expected and observed nuisance parameters were restricted to those related to $t\bar{t}$ modelling or otherwise showing significant pulls or constraints. This appendix shows expected and observed results for the full set of nuisance parameters. Figures C.1 and C.2 show the expected and observed results, respectively, for the cross-section analysis. Figures C.3 and C.4 show the expected results for the $\mathcal{CP}$ analysis, in the $\mathcal{CP}$-even and $\mathcal{CP}$-odd scenarios, respectively. The observed results for that analysis are given in C.5.

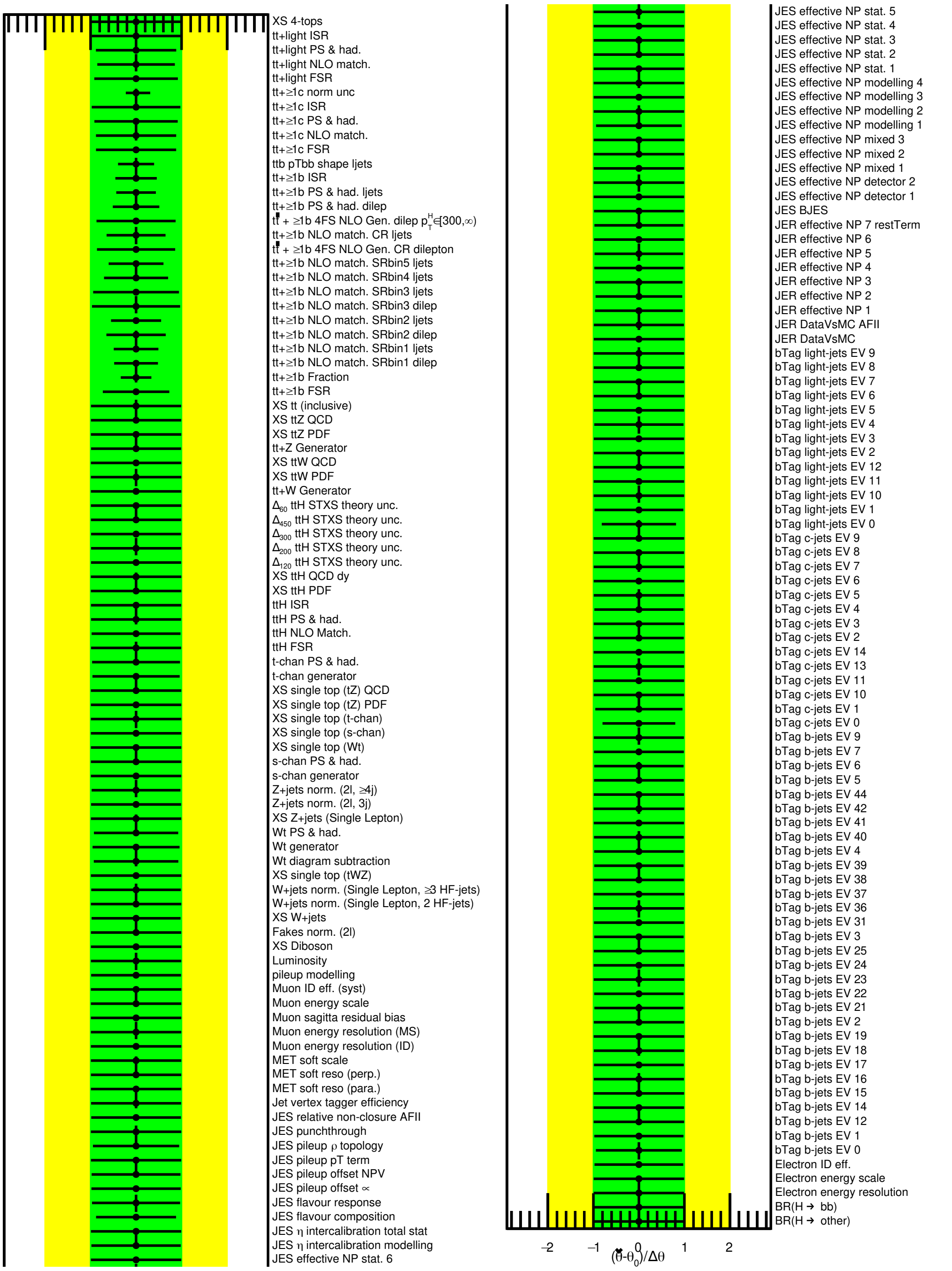

(a) (b)

Figure C.1: Expected pulls and constraints on the full set of nuisance parameters in the cross-section analysis.

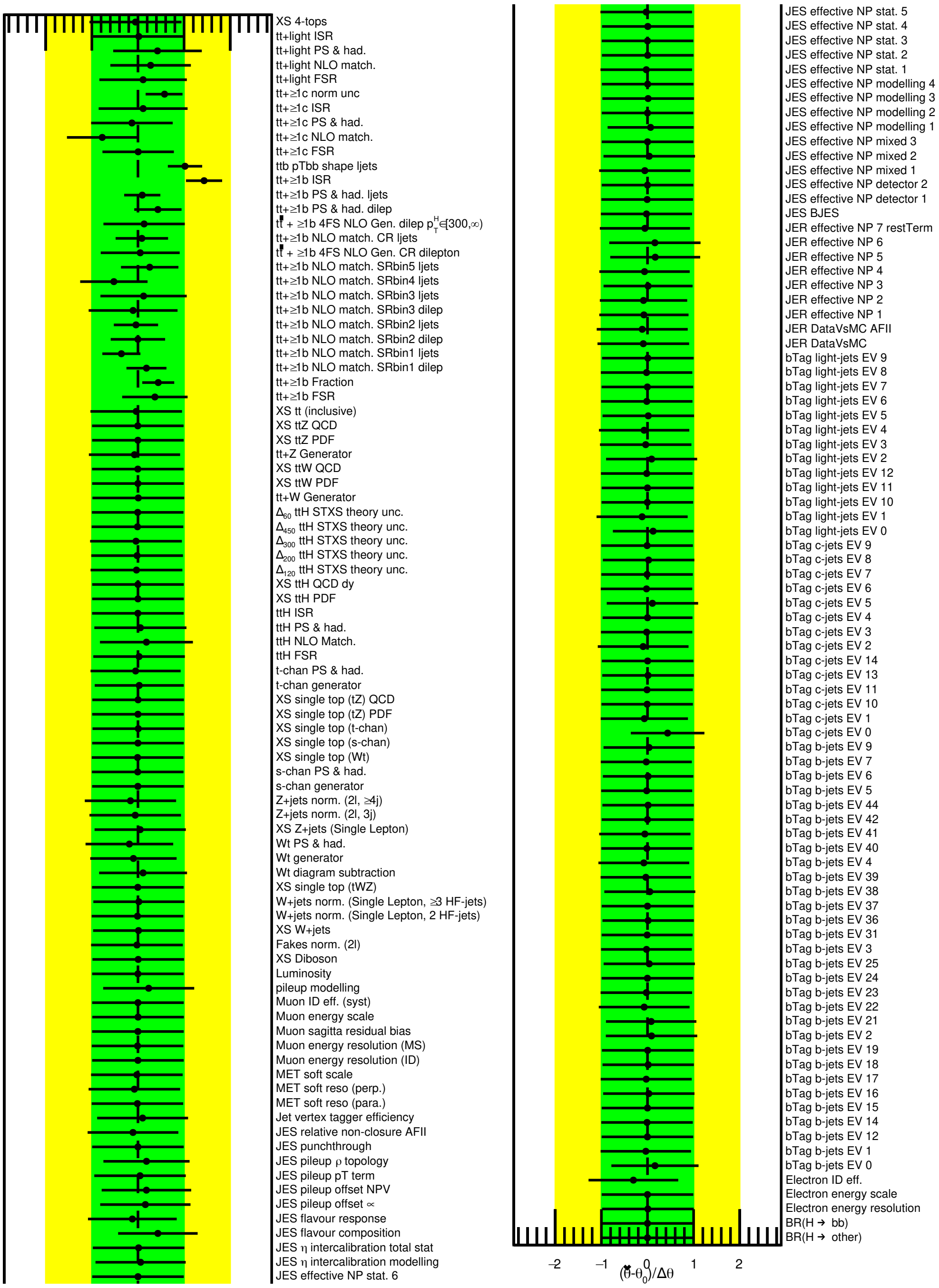

(a) (b)

Figure C.2: Observed pulls and constraints on the full set of nuisance parameters in the cross-section analysis.

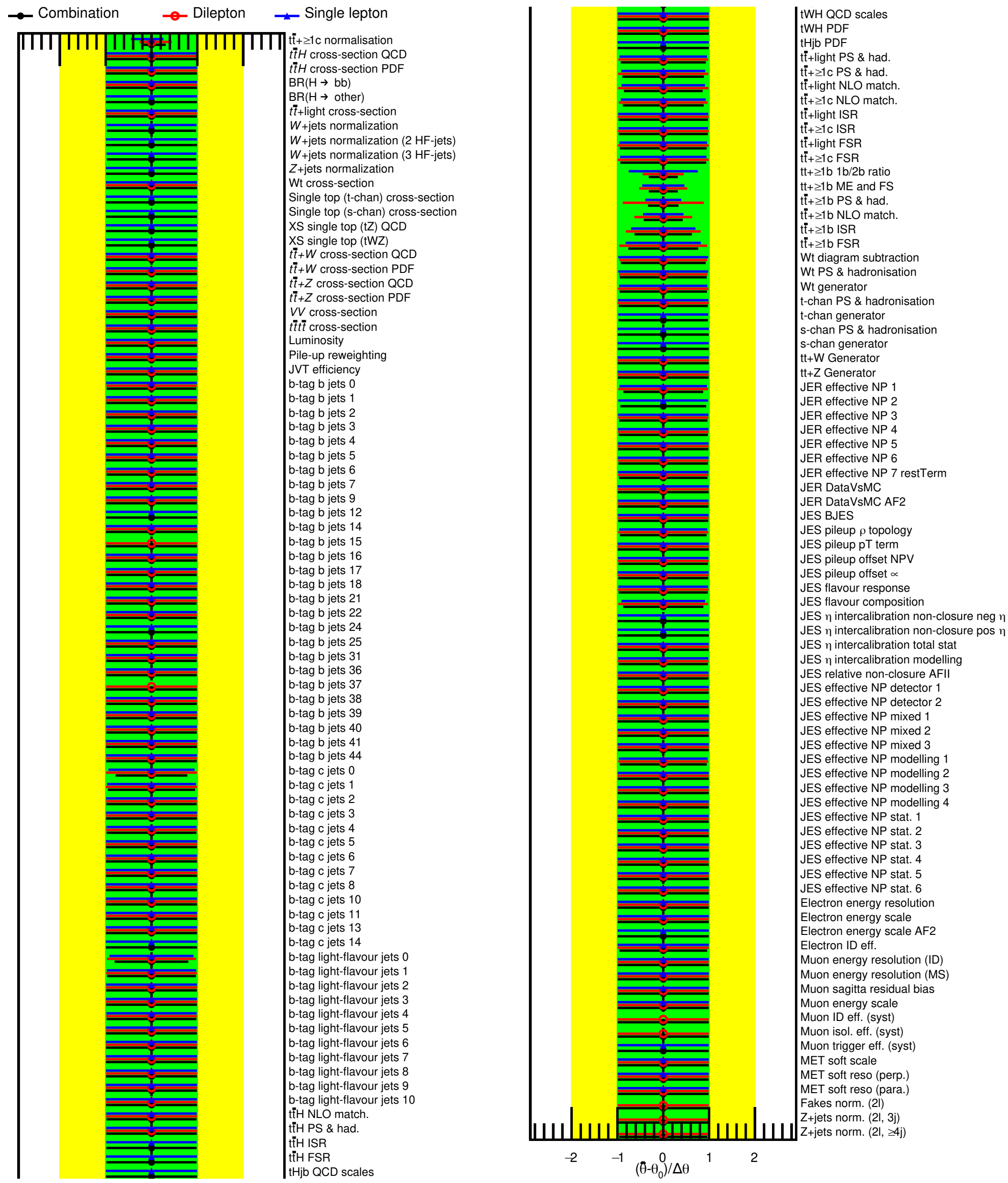

(a) (b)

Figure C.3: Expected pulls and constraints on the full set of nuisance parameters in the $\mathcal{CP}$ analysis, from the fit to the $\mathcal{CP}$-even Asimov dataset.

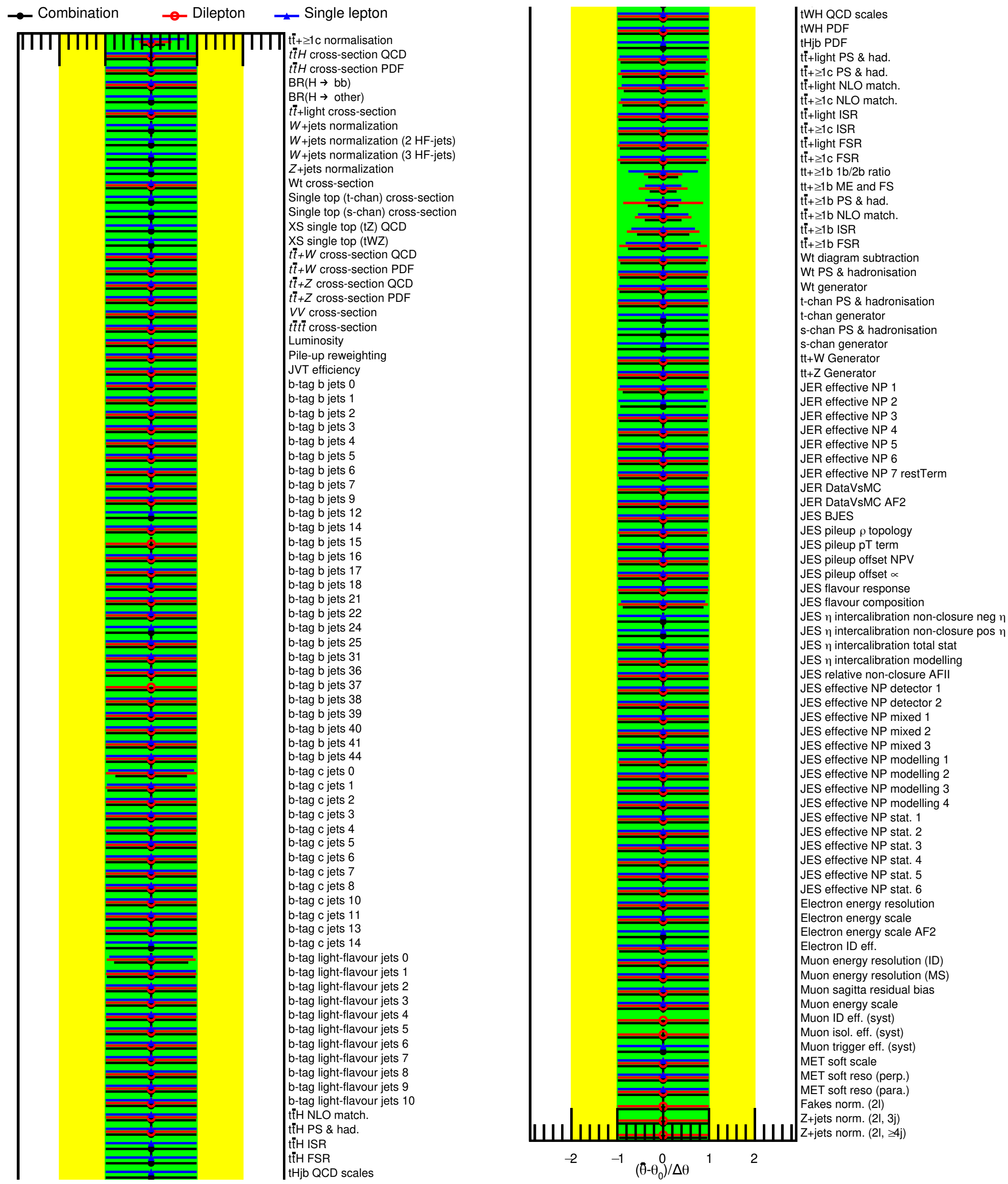

(a) (b)

Figure C.4: Expected pulls and constraints on the full set of nuisance parameters in the $\mathcal{CP}$ analysis, from the fit to the $\mathcal{CP}$-odd Asimov dataset.

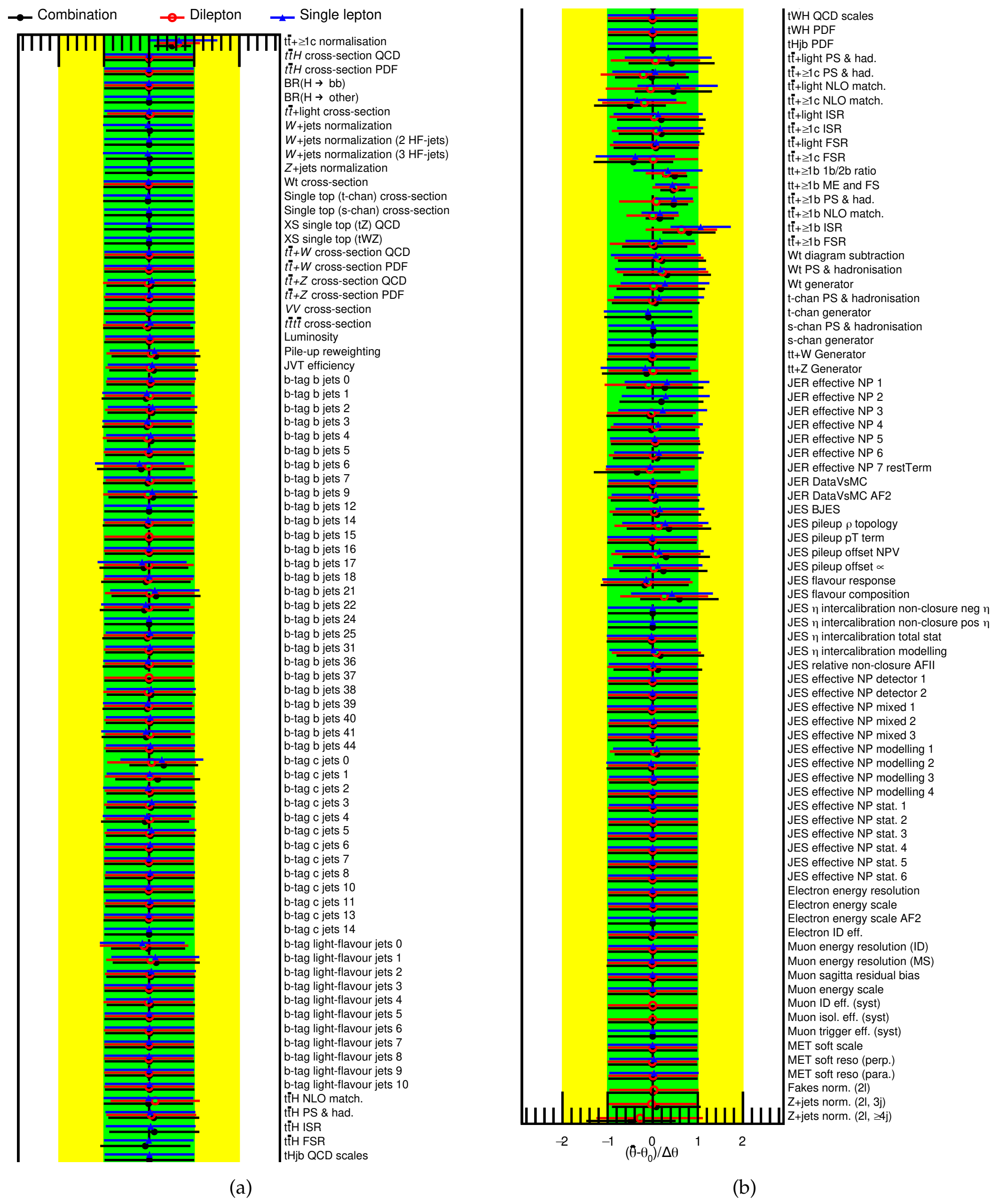

Figure C.5: Observed pulls and constraints on the full set of nuisance parameters in the $\mathcal{CP}$ analysis.